



From cellular variability to shape reproducibility : mechanics and morphogenesis of *Arabidopsis thaliana* sepal

Mathilde Dumond

► To cite this version:

Mathilde Dumond. From cellular variability to shape reproducibility : mechanics and morphogenesis of *Arabidopsis thaliana* sepal. Morphogenesis. Université de Lyon, 2017. English. NNT : 2017LY-SEN047 . tel-01650126

HAL Id: tel-01650126

<https://theses.hal.science/tel-01650126>

Submitted on 28 Nov 2017

HAL is a multi-disciplinary open access archive for the deposit and dissemination of scientific research documents, whether they are published or not. The documents may come from teaching and research institutions in France or abroad, or from public or private research centers.

L'archive ouverte pluridisciplinaire **HAL**, est destinée au dépôt et à la diffusion de documents scientifiques de niveau recherche, publiés ou non, émanant des établissements d'enseignement et de recherche français ou étrangers, des laboratoires publics ou privés.



Numéro National de Thèse : 2017LYSEN047

THÈSE de DOCTORAT DE L'UNIVERSITÉ DE LYON

opérée par

l'École Normale Supérieure de Lyon

École Doctorale N°340

Biologie Moléculaire Intégrative et Cellulaire (BMIC)

Spécialité de doctorat : Biologie

Soutenue publiquement le 15/09/2017, par :

Mathilde Dumond

**From cellular variability to shape reproducibility:
mechanics and morphogenesis of *Arabidopsis*
thaliana sepal.**

**De la variabilité cellulaire à la reproductibilité des
organes : étude de la mécanique de la morphogénèse
du sépale d'*Arabidopsis thaliana*.**

Devant le jury composé de :

FLECK, Christian	Professeur	WUR	Rapporteur
VERNHETTES, Samantha	Directrice de Recherche INRA	IJPB	Rapporteur
PERONNET, Frédérique	Directrice de Recherche CNRS	IBPS	Examinatrice
SÉMON, Marie	Maître de Conférences ENS de Lyon	LBMC	Examinatrice
LABOUESSE, Michel	Directeur de Recherche CNRS	IBPS	Examineur
BOUDAUD, Arezki	Professeur ENS de Lyon	RDP	Directeur de thèse
HAMANT, Olivier	Directeur de Recherche INRA	RDP	Co-encadrant de thèse

De la variabilité cellulaire à la reproductibilité des formes : étude de la mécanique de la morphogenèse chez le sépale d'*Arabidopsis thaliana*

RÉSUMÉ EN FRANÇAIS

La robustesse du développement est la capacité à produire le même phénotype au cours du développement malgré des perturbations intrinsèques ou de l'environnement. Chez toutes les espèces, la taille des organes est en général plutôt constante, alors que le comportement de leurs cellules est très variable.

Les voies de régulation de la taille et de la forme des organes ont été largement étudiées, cependant la régulation de la reproductibilité, de la taille et de la forme reste à élucider. Chaque plante d'*Arabidopsis thaliana* produit plus de 100 fleurs, rendant possible la mesure de la distribution statistique des tailles au sein d'un organisme individuel.

Les sépales, organes externes de la fleur, nous permettent d'étudier la robustesse dans le développement, car leur taille et leur forme doit être strictement régulée tout au long de leur développement pour protéger les organes reproducteurs. De plus, les tailles des cellules des sépales sont très variables.

Chez les plantes, les cellules sont entourées par une paroi pecto-cellulosique. Leurs formes résultent de l'équilibre entre la pression osmotique interne et la rigidité de la paroi. Les propriétés mécaniques de la paroi ayant un fort impact sur la forme finale des cellules, mon projet de thèse vise à élucider leur rôle dans la reproductibilité des formes. Précédemment, mon laboratoire de thèse avait montré que les cellules végétales peuvent percevoir les forces mécaniques qu'elles subissent, et modifier les propriétés mécaniques de leur paroi pour y résister. Comme l'anisotropie mécanique de la paroi module la direction de croissance, nous avons cherché à déterminer si le niveau de cette réponse cellulaire aux forces pouvait influencer la forme finale de l'organe en combinant approches théoriques et expérimentales.

J'ai d'abord développé un modèle purement mécanique, tenant compte des contraintes mécaniques, de la croissance anisotropique, ainsi que de la boucle de rétroaction mécanique liant contraintes et direction de croissance.

Grâce à ce modèle, j'ai pu prédire que le niveau de contraintes engendrées par le ralentissement de la croissance de la pointe du sépale associées à une forte rétroaction mécanique pouvait modifier la forme du sépale.

Cette prédiction a été confirmée expérimentalement par un autre étudiant en thèse de mon équipe.

Le consensus jusqu'à présent est que la forme des organes est dictée par des molécules appelées morphogènes qui dictent aux cellules où et quand croître. Cette étude suggère que la forme des organes résulte d'une synergie entre de tels morphogènes et les contraintes mécaniques générées par les différentiels de croissance.

Lorsque j'ai mesuré les propriétés mécaniques de sépales en utilisant un microscope à force atomique, j'ai trouvé qu'elles étaient fortement variables spatialement. J'ai alors rendu la

rigidité variable spatialement dans le modèle ce qui a rendu les formes moins reproductibles entre différentes simulations. Pour obtenir des formes reproductibles, j'ai dû ajouter une variabilité temporelle à la variabilité spatiale des propriétés mécaniques. Dans ce cas, la variabilité temporelle permettait de lisser les différences spatiales au cours du temps et d'augmenter la reproductibilité des formes finales.

Les hypothèses suggérées par le modèle ont ensuite été testées expérimentalement. Lors d'un crible génétique pour des mutants ayant des sépales moins reproductibles, nos collaborateurs à Cornell University ont isolé le mutant *ftsh4*. Nous avons montré que la variabilité spatiale était réduite dans le mutant comparé à la plante sauvage. J'ai confirmé en utilisant le microscope à force atomique que la variabilité spatiale de la rigidité de la paroi était aussi réduite chez le mutant.

Les expériences ont ainsi validé l'une des deux hypothèses formulées grâce au modèle : augmenter la variabilité spatiale des propriétés mécaniques augmente la reproductibilité des formes. La plupart des travaux portant sur la taille et la forme des organes se sont concentrés sur l'impact du gène étudié sur la taille moyenne des organes. De plus, la variabilité à l'échelle cellulaire est peu étudiée chez les organismes multicellulaires, et est souvent considérée comme désavantageuse. Nous montrons ici que la variabilité au niveau cellulaire peut au contraire permettre à l'organe de se développer correctement, et c'est la réduction de cette variabilité qui est délétère pour l'organisme.

ABSTRACT

Developmental robustness is the ability to produce the same phenotype despite environmental variability. Indeed, organisms produce similar organs despite a large cellular variability. Regulation of organ size and shape has been widely studied, but the regulation of reproducibility of organ size and shape is yet to be elucidated.

Arabidopsis thaliana sepals, external organs of the flower, can be used to study developmental robustness, because each plant produces more than 100 flowers, allowing the robust measurement of variability. Their size is tightly regulated all along the flower development to protect the reproductive organs.

In plants, cells are surrounded by a stiff cell wall. Cells modulate cell wall stiffness and mechanical anisotropy to control their growth. My PhD project aims at understanding the role of mechanical properties on organ shape reproducibility.

It had previously been shown that plant cells sense their physical environment and accordingly adjust their cell wall mechanical properties. We first studied whether the strength of this adjustment, or feedback, could influence the final shape of the organ. Using a modeling approach, I showed that the decrease of the growth rate observed at the tip of the sepal could modify the shape of the tip when the feedback was strong. This prediction has been experimentally demonstrated by another PhD student of the team.

This study suggests that organ shape results from a synergy between morphogens and the mechanical cues generated by growth. Using again a modeling approach, I showed that when mechanical properties were not variable, the shape of the organ was perfectly reproducible. This project hence suggest that not only morphogen influence organ shapes, but that mechanical feedback has a direct impact on shapes.

However, atomic force microscopy measurements showed that mechanical properties were highly spatially variable. When this variability was implemented in the model, the organ shapes were not reproducible. To produce reproducible shapes, I increased the temporal variability of the mechanical properties, which smoothed the spatial variability over time. Moreover, a decrease of the spatial variability lead to a decrease of organ shape reproducibility. These theoretical results suggest that spatial and temporal variability influence shape robustness.

The hypotheses raised by the model were experimentally tested: our collaborators identified a mutant displaying less robust sepal shapes. We showed that the spatial variability was reduced in this mutant. I confirmed using an atomic force microscope that spatial variability was reduced as well in the mutant, thus confirming one of the two hypotheses raised by the model: spatial variability of mechanical properties influence organ shape variability.

Most of the work on organ shape and size focused on the role of the gene of interest of the mean size of organs. Moreover, the variability at the scale of the cell is rarely studied in multicellular organisms and considered unfavorable. We show here that the variability at the cellular scale can enable the proper development of the organ, and it is the decrease of this variability which is deleterious for the organism.

Contents

1	Introduction	1
1.1	Variability in biology	2
1.1.1	What can vary in biology?	2
1.1.2	Sources of variability	2
1.1.3	What should vary but actually does not	3
1.1.4	Buffering mechanisms	4
1.1.5	Spatiotemporal averaging as a buffering mechanism	5
1.1.6	Is variability always detrimental?	5
1.2	The cell wall and its regulators	7
1.2.1	The composition and biosynthesis of the cell wall	7
	Cell wall composition	7
	Cell wall biosynthesis	11
1.2.2	The extension of the plant cell wall	12
	Mechanical properties of cell wall components	12
	Phytohormones	13
	Signaling molecules	13
	Mechanical stresses	13
	Wall regulators	14
1.3	Mechanics and morphogenesis	17
1.3.1	Turgor pressure and growth	17
1.3.2	Measuring turgor pressure	18
1.3.3	Measuring cell wall stiffness	18
1.3.4	Forces in plants and during morphogenesis	19
1.4	Growth of an organ	20
1.4.1	Describing morphogenesis	21
1.4.2	Modeling morphogenesis	22
1.4.3	Some case studies	24
	Morphogenesis of an isolated plant cell	24
	Curving an elongated organ: tropisms	24
	Shaping a sheet-like organ	25
	Feedback through mechanical signals	26

	Variability and morphogenesis	26
1.5	Why choosing the sepal as a model system	27
1.6	Main questions	28
2	Variable Cell Growth Yields Reproducible Organ Development through Spatiotemporal Averaging	29
2.1	Summary	30
2.2	Introduction	30
2.3	Results	32
2.3.1	<i>vos1</i> Mutants Have Increased Variability in Sepal Size and Shape	32
2.3.2	Mechanical Modeling Shows that Spatiotemporal Averaging of Cellular Variability Can Produce Organ Regularity	34
2.3.3	Reduced Local Spatial Variability in the Cell Growth of <i>vos1</i> Sepals Underlies Irregular Sepal Shape	38
2.3.4	Wild-Type Sepals Undergo Spatiotemporal Averaging of the Principal Direction of Growth, Resulting in Regularity, which Is Disrupted in <i>vos1</i> Mutants	41
2.3.5	<i>vos1</i> Is a Mutant of the FtsH4 Mitochondrial Protease	42
2.3.6	The Increased Irregularity in <i>ftsh4</i> Sepals Is Caused by Increased ROS Levels	42
2.3.7	ROS Act as a Growth Regulator in Wild-Type Sepals, Promoting Maturation and Termination of Growth	44
2.3.8	<i>ftsh4</i> Sepals Exhibit Cellular Characteristics of Maturation Earlier than Wild-Type	45
2.3.9	<i>ftsh4</i> Sepals Are Stiffer Than Wild-Type	46
2.3.10	Reduced Cellular Variability and Spatiotemporal Averaging Correlate with ROS Accumulation in Maturing Wild-Type Sepal Tips	46
2.3.11	Spatiotemporal Averaging Combined with a Maturation Gradient Regulated by ROS Produce Sepal Regularity	46
2.4	Discussion	49
2.4.1	Spatiotemporal Averaging as a General Mechanism to Deal with Stochasticity	50
2.4.2	ROS as a Signal that Promotes Cellular Maturation and Growth Arrest	51
2.5	Experimental procedures	52
2.5.1	Plant Material and Treatment	52
2.5.2	Microscopy and Image Analysis	52
2.5.3	Computational Modeling	53
2.6	Supplemental Experimental Procedures	53

3	A Mechanical Feedback Restricts Sepal Growth and Shape in Arabidopsis	70
3.1	Summary	71
3.2	Introduction	71
3.3	Results	73
3.3.1	The abaxial sepal exhibits a stereotypical growth pattern	73
3.3.2	The tip of the sepal exhibits a stereotypical cortical microtubule pattern .	73
3.3.3	The sepal growth pattern prescribes a mechanical stress pattern	76
3.3.4	CMTs align along maximal tensile stress in growing sepals	77
3.3.5	A mechanical feedback may channel sepal shape	78
3.4	Discussion	82
3.5	Experimental procedures	83
3.5.1	Plant material and growth conditions	83
3.5.2	Live imaging of the growing abaxial sepal	83
3.5.3	Mechanical perturbations	83
3.5.4	Image analysis	84
3.5.5	Computational Modeling	84
3.6	Supplemental Experimental Procedures	85
4	Discussion	90
4.1	Variability may have beneficial effects during development	91
4.2	Morphogens act in parallel to mechanical signals during morphogenesis	92
4.2.1	Mechanical sensing influences morphogenesis	92
4.2.2	Cell wall sensing could play a role in compensation	92
4.3	Mechanics and robustness of morphogenesis	93
4.3.1	Cell wall biochemistry and robustness	93
4.3.2	Mechanosensing and robustness	94
4.4	General conclusion	95
5	Appendix	128
5.1	Mechanical isolation of rapidly growing cell buffers growth heterogeneity and contributes to organ shape reproducibility	128

Acknowledgments

La fin de cette thèse est l'occasion de remercier tous les acteurs qui l'ont rendue possible. En premier lieu, je souhaite exprimer ma gratitude à mon directeur de thèse Arezki. Tu m'as encouragée à revenir à l'issue de mon stage de master 1, en me décrivant un projet super intéressant dans une collaboration - potentielle, à l'époque - de très haut niveau. Le projet était à la hauteur de tes promesses et c'est une réelle chance d'avoir pu en faire partie et de travailler sur des projets aussi chouettes.

De mon point de vue, tu as trouvé le bon compromis entre autonomie et soutien, avec une porte toujours ouverte et du temps à me consacrer, malgré ton emploi du temps de ministre. Tu n'as pas hésité à m'encourager à prendre des vacances et à me reposer quand tu as vu que c'était nécessaire, et ton attention a permis à cette thèse de rester une excellente expérience.

Je voudrais aussi remercier mon co-encadrant, Olivier, pour ta positivité et ton soutien, tes feedbacks et tes nouvelles idées incessantes. La prochaine fois je penserai aux ablations.

I would like to thank the jury of my thesis for having accepted to read my manuscript and for their useful comments. Pareillement, je remercie les membres de mon comité, qui ont su remettre en perspective ce projet lorsqu'il en avait le plus besoin. Leurs conseils ont été précieux pour amener mes projets à maturité.

As I already mentioned, this PhD was part of a collaboration, between labs around the world, with whom the Skypes (and the visits!) really rythmed these years. I am truly aware how lucky I am to have had the chance to interact so often with talented scientists from such diverse backgrounds. I am really proud of the research we have conducted together. In particular, I had the chance to spend a few month in Cornell in one of those labs, and work with Adrienne and Lilan. It was a great human and scientific experience.

Je souhaite remercier toutes les personnes du RDP qui donnent cette ambiance chaleureuse au labo, et plus particulièrement Nelly, qui a pris *beaucoup* de photos de sépales avec moi, mais aussi les autres, avec qui on a pris *beaucoup* de café, Stéphane (gardien attitré du chat), Thomas, Long, Kat, Marion.

Je remercie ma famille, qui, de loin, a su me soutenir quand il y en avait besoin.

Finalement, je remercie surtout Nicolas, toujours présent à mes côtés quand ça ne marche pas, et aussi quand ça marche, bref, tout le temps, je n'y serais pas arrivée sans toi.

1

Introduction

TWO INDIVIDUALS IN THE SAME SPECIES or population have similar sizes and shapes, and especially organs such as ears or hands are remarkably similar within a single individual. Even with the tremendous recent work on morphogenesis, how two organs such as hands have such remarkable reproducibility is still a mystery. Indeed, studies usually focus on the mechanisms making organs bigger or smaller, but how the organ can sense its shape and regulate it can be studied only by measuring variability of shapes. *Arabidopsis thaliana* flowers are a suitable tool for this study because each plant has dozens of flowers, allowing a robust estimation of shape variability.

Plant cells are surrounded by a stiff cell wall in tension from the internal pressure. The cell wall mechanical properties are central to cell growth regulation, and in turn play an important role in organ growth and ultimate shape. Because morphogenesis is at the interplay of intricate actors such as genetic regulation, cell growth and physics, using models is mandatory to get an understanding of the process.

The first part of the introduction will be focused on the study of variability in biology; I will then describe the cell wall biochemistry and the implication of its mechanical properties on growth. In a third part I will introduce the different ways to model plant morphogenesis, and lastly explain why the sepal is a suitable model organ.

1.1 Variability in biology

1.1.1 What can vary in biology?

There are many scales in biology: from populations to subcellular compartments, and every scale displays variability.

Individuals of a population can develop and behave differently, even in monoclonal populations such as bacteria populations.

Indeed, in a given organism, organs such as hands, ears, or plant leaves, can have varying sizes and shapes from 1 to 10% depending on the organ. At the level of the cell, the concentration of metabolites, transcripts and proteins can vary spatially and temporally.

Differentiating the importance of each of these possible sources of variability on morphogenesis output has been tackled in a study on *Drosophila* wings, which concluded that the variability at the level of a monoclonal population or at the level of an organism depended on the genetic background of the population: specific genes had the specific role to ensure reproducibility of wings sizes at the level of the individual (Debat and Peronnet, 2013).

Similarly, the cells behavior in one organ can vary; and even at the cellular scale, the concentration of proteins and the gene expression levels can vary over time and space. The variability of cell behavior is important for some aspects of development. For example, in leaves, stomata and trichomes are distributed along the surface of the leaf, in a specific pattern. The emergence of such pattern is granted by the variability of behaviors at the cellular scale (Greese et al., 2012). However, studying variability using mutants can be misleading, because the measured variability can be due to incomplete penetrance instead of an actual increase in variability: an allele has an incomplete penetrance when not all individuals carrying the mutation show the mutant phenotype. One way to distinguish between regulation of variability and incomplete penetrance is to also compare mutant and wild-type means: similar means indicate that the gene regulates variability (Raj et al., 2010).

1.1.2 Sources of variability

The observed variability in shape and behavior has diverse origins. For example, the differences observed between individuals of a polyclonal population are likely to be linked to genetic variability. The specific genes involved in a variable phenotypic trait can be determined using Quantitative Trait Loci (QTLs).

On another hand, the differences between individuals of the same population can also be due to them growing in different environments. However, organs in the same individual develop in the same environment and share the same genotype, for example hands show differences of about 1% in length (Palmer, 1996). This measured fluctuating asymmetry is a metric of developmental stability.

The perturbations studied during development usually refer to several processes such as thermal noise at the molecular level, random variation of the rates of biological processes impacting

cell-to-cell communication, rates of cell growth or division (Palmer, 1996). Depending on what characteristic of the organisms and what source of perturbation is tested, the perturbations can be internal or external, e.g. for the development of a flower, the environmental variability is external whereas the cell scale variability is internal (Masel and Siegal, 2009). One question often addressed in the studies on variability is whether the cellular response is different for an internal or an external source or perturbations (Meiklejohn and Hartl, 2002). Moreover, the cellular response can also differ depending on the kind of environmental perturbation: when exposed to temperature or starvation, different species of *Caenorhabditis* nematode reacted differently, indicating the intricate response of developmental systems to environment (Braendle and Félix, 2008). At an even smaller scale, gene expression itself is noisy, leading to variability in time and between cells in bacteria (McAdams and Arkin, 1999) and eukaryotic cells (Blake et al., 2003).

1.1.3 What should vary but actually does not

Given all the possible aspects of life that can vary, how is it possible that two hands, or two leaves are so similar? Only a few studies focused on this paradox.

During the development of the early embryo, many steps of cell differentiation rely on the sensing of morphogen gradients. Any stochastic variation of morphogen concentration in this gradient needs to be buffered for a robust development. In particular, in *Drosophila*, the embryo development strongly relies on Bicoid gradient. The Bicoid gradient is very variable, it is sensitive to environmental factors such as temperature, the total amount of mRNA in the embryo, and the precise amount of protease. However, the limit of the cells differentiating, detected by their expression of *hunchback* along this gradient is strikingly precise (Houchmandzadeh et al., 2002). How the organisms produce such a reproducible limit from a variable input is not resolved. In *Drosophila*, development is robust against environmental variation (temperature), and protein quantities, but changes in the topology of the regulatory network have large impacts (Houchmandzadeh et al., 2002, von Dassow et al., 2000).

In plants, phyllotaxis is the regular arrangement of lateral organs in plants. It has been an interest for scientists and scholars since the ancient Greeks, and many properties have been understood as quite robust and reproducible over species. However, how such robustness is achieved is not understood. The phyllotaxis is set up at the shoot apical meristem of the plant, where the positioning of organs is determined by inhibitory fields, which in turn depend on variable processes such as morphogen diffusion. Despite much progress in the identification of molecular regulators of organogenesis and possible self-organized properties at the tissue scale (e.g. Reinhardt et al. (2003)), how the temporal and spatial robustness of the inhibitory fields is produced is still a mystery (Mirabet et al., 2012, Vernoux et al., 2011).

Because gene expression is noisy (Blake et al., 2003, McAdams and Arkin, 1999), and because the environment varies, many phenotypic characteristics should vary. Morphogenesis stability is the main example that it does not vary nearly as much as it should.

1.1.4 Buffering mechanisms

Development is robust against environmental and genetic variation. This robustness in the development is often referred to as canalization (Wagner and Altenberg, 1996), and the mechanisms allowing such robustness have been the focus of many studies.

Gene networks allow the activity of genes to be backed up by other genes, granting a robustness against genetic variation: if the activity of one gene is impaired, another gene or set of genes is likely to be able to fill its function (Hartman et al., 2001). Moreover, comparing *Drosophila* populations, the most robust ones against genetic perturbations were also the most robust against environmental perturbations (Stearns et al., 1995).

Topology is an important feature in gene regulatory networks: negative feedback loops can increase robustness of the outcome of the regulatory network, as has been demonstrated in yeast (Howell et al., 2012). In particular, the microRNA miR-7 acts in several feedforward and feedback loops during *Drosophila* development, buffering the involved genetic networks against environmental variation (Li et al., 2009). MicroRNAs are likely to function in other pathways as well, such as the control of mRNA transcript copy number, and the degradation of impaired mRNA transcripts (Ebert and Sharp, 2012). Moreover, some genes have been demonstrated to specifically increase robustness. The chaperonin Hsp90 is a heat shock protein, and largely stabilizes morphogenetic pathways, degrading misshaped proteins. When the Hsp90 protein is active, it allows other mutations to cryptically accumulate; Hsp90 activity degrading the impaired proteins.

The identification of such genes is critical for a full understanding of robustness (Masel and Siegal, 2009). When Hsp90 is compromised, for example by a temperature increase, the cryptic mutations get expressed, leading to alterations of cells behaviors that can be more important than those predicted by only the loss of Hsp90 (Rutherford and Lindquist, 1998). Moreover, Hsp90 is present in all organisms and has been identified in *Arabidopsis thaliana*; where the mutant also presents developmental robustness defects, demonstrating the importance of such buffering mechanisms (Queitsch et al., 2002). Another protein with a large impact on robustness has been described in *Arabidopsis thaliana*, *AtCHR23*, which is a chromatin remodeler. This protein has diverse regulates diverse functions of the cell, and when mutated, the plants have a more variable growth in roots, hypocotyls and leaves (Folta et al., 2014).

Most of the time, the proteins involved in robustness have pleiotropic roles in the cell: protein modification (such as chaperonin), chromatin modeling, DNA integrity, RNA elongation, response to stimuli (Levy and Siegal, 2008), and as we will see in chapter 2, reactive oxygen species regulator. These genes are at the crosses of different pathways and are hubs in the genetic network of the cells (Cooper et al., 2006, Levy and Siegal, 2008).

To determine which genes have an impact on robustness, one can also use quantitative trait loci (QTLs). Indeed, QTLs are originally used to map a measured quantity to genetics, but the variability of such quantity can also be mapped to genetics using the same method (Hall et al., 2007, Ordas et al., 2008). Genes have been identified in *Arabidopsis thaliana* which im-

pact developmental robustness: for example, the *ERECTA* gene would be responsible for the robustness of the number of rosette leaves (Hall et al., 2007). However, the robustness of organ size has never been addressed in plants (Boukhibar and Barkoulas, 2015, Lempe et al., 2013).

1.1.5 Spatiotemporal averaging as a buffering mechanism

One way to increase robustness is to average stochastic fluctuations in space and time.

Indeed, it has been shown in a theoretical study that averaging protein concentration in space, by diffusion, enhanced the precision of gene expression patterns by smoothing out bursts of expression (Erdmann et al., 2009). Similarly, in *Schizosaccharomyces pombe* the membrane-bound pom1p protein displays a noisy concentration distribution along the cell, but the temporally averaged distributions were much smoother. In this case, it was shown that the smoothening of the protein distribution was due to the clustering of the proteins (Saunders et al., 2012).

Temporal averaging is also used by bacteria to sense shallow chemical gradients. Indeed, when a chemical gradient is shallow, the stochastic receptor-ligand interactions can exceed the slight gradient signal. To establish the orientation of the gradient, the bacteria sense the chemical concentration in several positions and then stabilizes towards the averaged maximum (Dyer et al., 2013). Spatiotemporal averaging has been shown to play an important role in the robustness of morphogen gradient positional precision. Indeed, in *Drosophila* embryo, the antero-posterior axis is determined by a gradient of Bicoid concentration, which generates cell differentiation, classically detected by the expression of *hunchback*. This gradient is highly sensitive to environmental variability (Houchmandzadeh et al., 2002), however the limit of the cells expressing *hunchback* is strikingly reproducible. Using a mutant displaying a more flat Bicoid gradient, He et al. (2010) showed that the robustness of the wild-type gradient sensing was due to time and spatial averaging. Another way to smooth protein concentration is intrinsic to the different time scales between the biological processes gene activation, transcription, mRNA translation and mRNA and protein degradation, which are sufficient to buffer the temporal variability of gene activation and to produce rather smooth concentrations of proteins over time (Paulsson, 2005).

1.1.6 Is variability always detrimental?

At the cellular level, noise of genetic expression can have beneficial effects. Chemical compounds increasing expression noise in HIV positive cells but where HIV is latent could, when coupled with reactivating drugs, achieve much more efficient results than the reactivating drugs alone (Dar et al., 2014).

Phenotypic plasticity, or the ability of organisms to produce different phenotypes from the same genotype, can be advantageous to a population. Indeed, if the environment changes and a portion of the population dies, the few that were different because of phenotypic stochasticity can proliferate and develop as a new population. Because the survivors have the same genotype as the initial population – if the selection pressure is not too long, the new population has the same

genetical background as the former (Johnston and Desplan, 2010). Similarly, in development and cancer, a cell population can be divided into phenotypic subpopulations. The proportions of each of these subpopulations is determined by stochastic transitions of cells between the states, keeping the proportions constant; even when a subpart of the population is removed (Gupta et al., 2011, Roorda and Williams, 1999, Singh et al., 2013).

Variability at the population level is also useful to interpret signals. For example, the immune NF- κ B pathway is activated in response to the extra-cellular TNF signal. If the TNF signal oscillates, in some cells, the NF- κ B response can synchronize with the TNF input, but only in a given range of frequencies. However, the cell-to-cell variability allows subpopulations of cells to synchronize with different frequencies, allowing the population as a whole to synchronize with a wide range of TNF signal frequencies. In this case, the phenotypic variability of a population of cells is responsible for the ability of the population to respond to an extra-cellular signal (Kellogg and Tay, 2015). Variability can also be a defense mechanism: it has been shown that insect herbivore performance is reduced when the variability of nutritional content of plants is increased (Wetzel et al., 2016).

Robustness against environmental variations is mandatory for a reproducible development in animals and in plants. Nevertheless, the environment carries information, and organisms have to adapt to environmental changes (Abley et al., 2016); this is especially true for plants since they cannot move. Hence, the organisms need to be able to read environmental cues and accordingly tune their behavior. Here it is worth noticing that the reaction of the plants to a given environmental cue must be robust: they "produce variability in a reliable manner" (Abley et al., 2016). Strikingly, the strategies that allow robustness in development are often related to the mechanisms that allow environmental plasticity: network topology, feedback and feedforward loops, pleiotropic genes (Lachowiec et al., 2016). Thus, if the organism is too robust against environmental variability, it will not adapt to environmental variability, ultimately reducing its fitness.

Further than adapting to their environment during their life, robustness and variability have obvious evolutionary implications. In particular, how the robustness in development, or canalization, evolves has been at the center of many studies (Eshel and Matessi, 1998, Gibson and Wagner, 2000, Masel and Bergman, 2003, Pigliucci, 2008, Rice, 1998). These studies demonstrate that the system allows some variability to keep the system evolvable, and that if a system is too robust, it will prevent evolution and ultimately lead to the extinction of the species. It has been theorized that the buffering mechanisms should be a unified mechanism for both genetic and environmental robustness (Meiklejohn and Hartl, 2002).

Here, we focus on the robustness of organ shape and size, which has not been investigated so far. In plants, shape is governed by cell wall mechanical properties. Could the intricate and entangled structure of the cell wall contribute to organ shape reproducibility? To investigate this question, we will introduce the cell wall biochemistry.

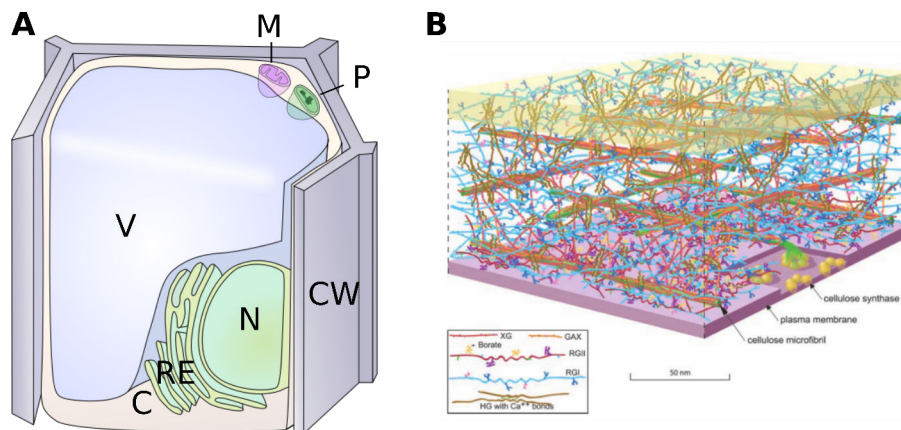


Figure 1.1: The cell is surrounded by the cell wall, which is an intricate structure. (A) Major compartments of a plant cell. V: vacuole, N: nucleus, ER: endoplasmic reticulum, CW: cell wall, M: mitochondrion, P: plastid, C: cytoplasm. (B) The primary cell wall is a complex polysaccharidic structure, composed of cellulose microfibrils, pectin (RGI, RGL, HG) and hemicellulose (XG, GAX), between the cell plasma membrane (at the bottom) and the middle lamella (at the top), separating cell walls of neighboring cells. (from Somerville et al. (2004))

1.2 The cell wall and its regulators

Plant cells are surrounded by an extracellular matrix called the cell wall (see Figure 1.1). Over a plant's life, the chemistry and physical properties of the cell wall change, notably in vasculature, to support the increasing weight of the above tissue and maintain the stature of the plant against gravity. The newly synthesized cell wall, or secondary cell wall, is stiffer and characterized by the presence of lignin. The cells surrounded by secondary cell wall have stopped growing, and their main function is to support the younger tissue. On the other hand, the cells belonging to the young, growing tissue are surrounded by the much softer primary cell wall.

My project is focused on organ growth, thus I will focus on the primary cell wall only.

1.2.1 The composition and biosynthesis of the cell wall

Cell wall composition

In *Arabidopsis thaliana* leaves, the primary cell wall is composed by pectic polysaccharides (42% of the wall), hemicellulose (24%), cellulose (14%) and proteins (14%) (Zabackis et al., 1995) (see Figure 1.2), but the cell wall also contains other components such as callose, notably involved in the regulation of plasmodesmata opening.

Cellulose is an unbranched homopolysaccharide, composed of β -D-glucopyranose units linked by 1,4-glycosidic bonds (OSullivan, 1997) (see Figure 1.3). Between 18 and 36 chains assemble via hydrogen bonds into a cellulose microfibril, forming the crystalline cellulose I (OSullivan, 1997). The spatial organization of the cellulose microfibrils can be studied using X-ray scattering, and several types of crystallized cellulose have been described (Newman et al., 2013).

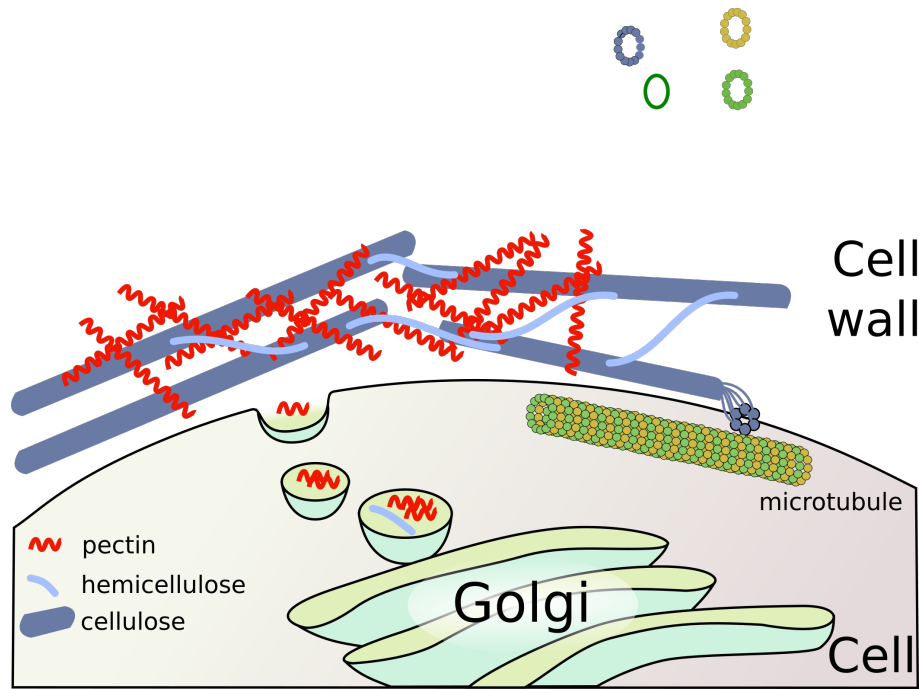


Figure 1.2: Simplified view of the cell wall. The main components are pectin, hemicellulose and cellulose. Pectin and hemicellulose are produced in the Golgi and exocytosed in the cell wall, whereas cellulose is synthesised directly at the plasma membrane, following microtubule orientations.

Hemicellulose is a family of diverse polysaccharides. It contains all the molecules with equatorial β -1,4-linkages, but the sugars can be different from glucose, such as xylose and mannose, and they often carry side-chains (Scheller and Ulvskov, 2010). The main hemicelluloses are xylan (made of xylose), xyloglucan (made of glucose), mannan (made of mannose) and glucomannan (made of mannose and glucose) (Scheller and Ulvskov, 2010) (see Figure 1.4). Hemicellulose backbone can form hydrogen bonds with the cellulose microfibrils (Park and Cosgrove, 2015). Interestingly, mutants of regulators of xyloglucan biochemistry change the growth patterns in plants (Miedes et al., 2013), whereas the mutant depleted of all xyloglucan *xtt1/xtt2* shows only a mild phenotype (Park and Cosgrove, 2012).

Pectins also constitute a diverse and compound family of polysaccharides. The main pectin polysaccharides in *Arabidopsis thaliana* leaves are homogalacturonan (23% of the cell wall), rhamnogalacturonan I (11%), and rhamnogalacturonan II (8%) (Zabackis et al., 1995). Homogalacturonan are linear chains of α -1,4-linked D-galacturonic acid; rhamnogalacturonan I has a backbone composed of repeating disaccharide α -D-galacturonic acid- α -L-rhamnose, linked to various side chains; and rhamnogalacturonan II has a backbone composed of α -1,4-linked D-galacturonic acid, associated with various side chains (Vincken, 2003).

No links between pectins and other components of the cell wall have been documented, however indirect evidence suggest that pectin and cellulose may directly interact (Ralet et al., 2016, Wang and Hussey, 2015). However, Rhamnogalacturonan II molecules can be covalently bound

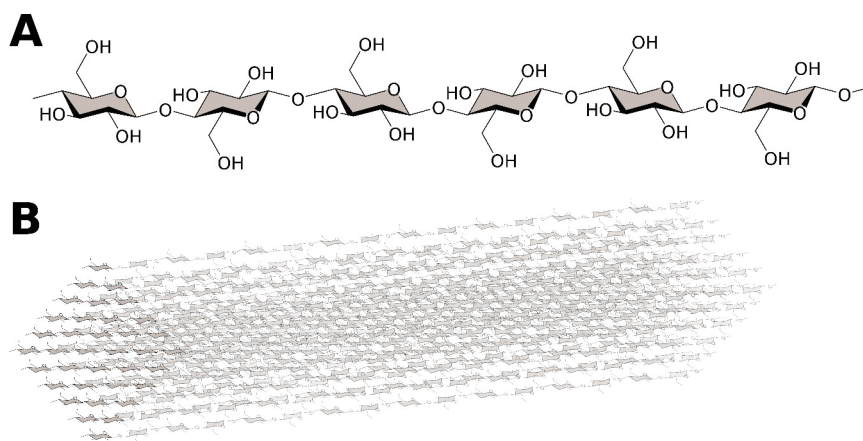


Figure 1.3: Cellulose molecular composition. (A) Cellulose is composed of β -D-glucopyranose units linked by (1 \rightarrow 4) glycosidic bonds. (B) A cellulose microfibril is composed of between 18 and 36 chains. Inspired by Park and Cosgrove (2015).

by borate diester bridges on specific sites (Mazurek and Perlin, 1963, O'Neill et al., 2004) (see Figure 1.5), and homogalacturonan and rhamnogalacturonan II backbones can also be non-covalently linked by calcium bridges (Grant et al., 1973), according to the "egg-box" model, thus forming a gelified structure, stiffer than the free form of pectin (Fraeye et al., 2010) (see Figure 1.5).

Proteins can take up to 14% of the dry mass of the cell wall (Zablackis et al., 1995). The large variety of proteins in the cell wall adds another layer of complexity and an exhaustive overview of the cell wall proteins has yet to be established (Albenne et al., 2014). Nonetheless, the cell wall proteins can be distinguished between the regulatory enzymes, which modify the other components of the cell wall, and the structural proteins (Showalter, 1993).

The structural proteins of the cell wall are the hydroxyproline-rich glycoproteins (HRGPs) or extensins, the arabinogalactan proteins (AGPs), the glycine-rich proteins (GRPs), the proline-rich proteins (PRPs), and proteins that have a mixture of these domains (Carpita et al., 1996, Cassab, 1998). Extensins are the most abundant and the most studied structural proteins (Cassab, 1998): they are involved in cell recognition pathways, e.g. in the mating system of *Chlamydomonas*, and in the growth of the pollen tube during pollinization of maize in particular (Cassab, 1998). Extensins are composed of a succession of hydrophobic and hydrophilic motifs of highly modified amino acids (Fry, 1986), which can be linked together by extensin peroxidase (Fry, 1986, Schnabelrauch et al., 1996), forming sheets of extensin (Epstein and Lamport, 1984). They can also be linked to other molecules of the cell wall, but neither the mechanisms nor the nature of the links are known (Cassab, 1998, Fry, 1986, Qi et al., 1995). Extensin accumulation is associated with the end of cell growth (Cassab, 1998, Ye and Varner, 1991), in accordance with the increase of cell wall tensile strength due to the formation of an extensin-cellulose network (Cassab, 1998). I will not study this proteic complex during my PhD project. The other cell wall proteins are

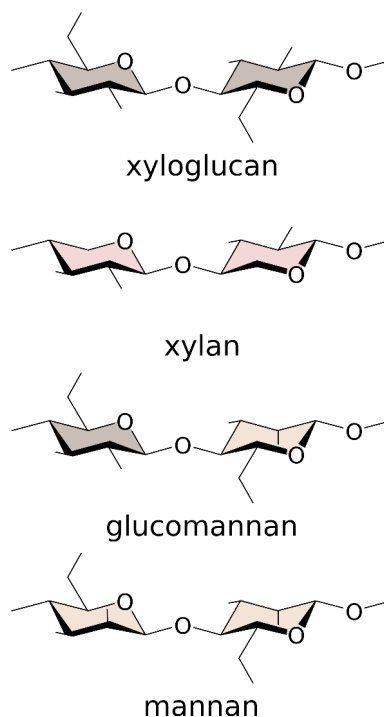


Figure 1.4: Molecular composition of the backbones of the four main hemicellulose subtypes. The side-chains are not represented, and are linked to any carbon of the glycans. After Scheller and Ulvskov (2010).

enzymes modifying the surrounding polysaccharides and proteins. The roles and means of action of these enzymes will be developed in the section 1.2.2.

Lignin is synthesized as a part of the secondary cell wall, so it is not in the focus of this project. Lignin is formed by phenylalanine altered side-chain modifications such as oxidation, and linked together in the cell wall, forming a macromolecule (Boerjan et al., 2003, Fraser and Chapple, 2011). Lignin also covalently links to other components of the cell wall such as cellulose and hemicellulose (Pérez et al., 2002), thus making the cell wall much stronger.

Callose is composed by glucose residues linked together through β -1,3-linkages. It has many regulatory roles, but is not present in high proportion in the cell wall. In particular, it regulates the opening of plasmodesmata, small channels allowing cell-to-cell symplasmic communication (Levy et al., 2007, Roy et al., 1997, Turner et al., 1994). It is also the most prominent physical defense in fungal infection resistance, forming a plug (Aist, 1976), and is found in specific structures such as the cell plate in dividing cells, pollen mother cell walls and pollen tubes (Jacobs et al., 2003).

Because the cell wall is so intricate, this presentation of the cell wall components is not exhaustive, and deciphering exactly which component interacts with which and how is very challenging. The mechanical link between cellulose microfibrils, in particular, plays an important role in the growth of the cell wall. The original view of the cell wall as a tethered network, where cellulose microfibrils are linked by hemicelluloses, has been recently challenged by the 'hot spot' view, where cellulose microfibrils are directly linked in such hot spots via hemicellulose-cellulose

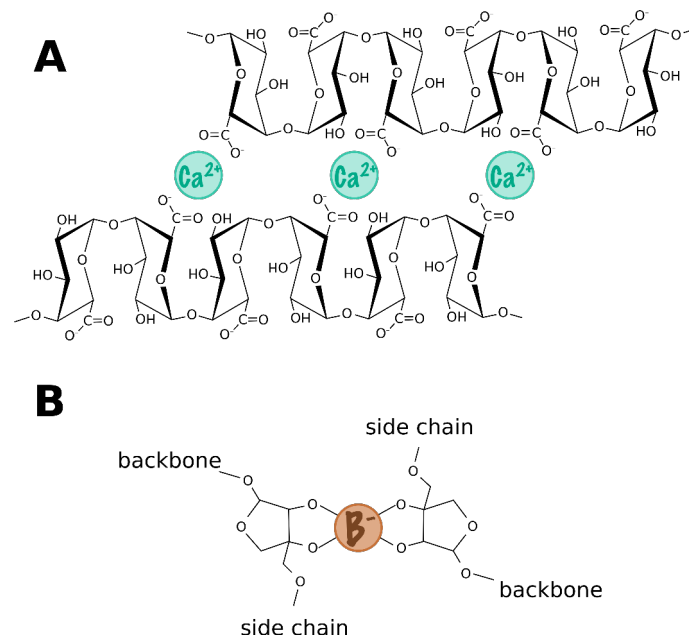


Figure 1.5: Cross-linking of pectin molecules. (A) Homogalacturonan and rhamnogalacturonan II backbones can be linked by Calcium ions on their non-methylesterified residues. (B) Rhamnogalacturonan II side-chains can be covalently bound through borate diester bridges forming via L-fucose residues. After Vincken (2003)

amalgams (Cosgrove, 2016), but determining the exact relationship between the biochemical components remains a challenge.

Cell wall biosynthesis

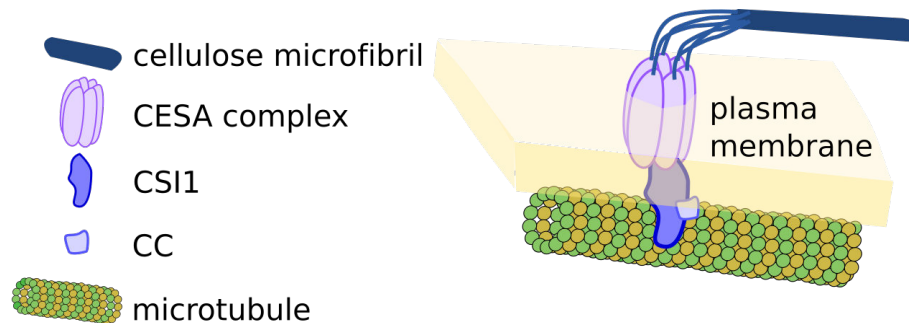


Figure 1.6: Schematic representation of cellulose synthesis. Cellulose synthesis takes place at the plasma membrane, by CESA complexes, which are linked to the microtubules via the Cellulose Synthase Interacting protein CSI1 associated with the Companion of Cellulose Synthase (CC) proteins.

Cellulose is secreted in the membrane *via* cellulose synthase (CESA) complexes, each one synthesizing one chain of cellulose (Somerville, 2006). *Arabidopsis thaliana* genome encodes for at least 9 isoforms of the cellulose synthase. It is known that the CESA complex requires 3 isoforms of CESA proteins in similar amounts, but the exact stoichiometry is not known (Gonneau et al., 2014, Hill et al., 2014). CESA complexes are linked to the cortical microtubule network via

the Cellulose Synthase Interacting (CSI) proteins (Bringmann et al., 2012, Li et al., 2012) and the Companion of Cellulose Synthase (CC) proteins (Endler et al., 2015) (see Figure 1.6). The cortical microtubules array orientation is the result of the auto-organization of the individual microtubules, permitted by a few interaction rules (Wasteney and Ambrose, 2009), and is also controlled by the cell (Sedbrook and Kaloriti, 2008). The microtubule array and its regulation will be detailed in section 1.2.2.

Most of the other components are synthesized in the cell endoplasmic reticulum and in the golgi apparatus, where specific enzymes synthesize and modify the polysaccharides (Geisler et al., 2008, Lerouxel et al., 2006, Mohnen, 2008, Scheller and Ulvskov, 2010) (see Figure 1.2). The exocytosis of the vesicles containing cell wall material is also tightly regulated, as has been shown for the pectin exocytosis (Anderson et al., 2012). Polysaccharide maturation can also take place directly in the cell wall, for example xyloglucan are hydrolyzed in the cell wall (Scheller and Ulvskov, 2010).

1.2.2 The extension of the plant cell wall

The regulation of cell wall biochemistry is central to cell size regulation. The softening of the cell wall has diverse causes, indirect such as the effect of hormones and secondary signals, or direct with the action of specific molecules such as reactive oxygen species and calcium ions, and regulatory proteins.

Mechanical properties of cell wall components

Both turgor pressure and cell wall mechanical properties influence cell growth, but the cell wall has been the most studied so far. The role of turgor pressure will be discussed in the section 1.3.1, here the cell wall biochemistry is detailed.

The stiffness of the cell wall ranges from 10MPa to 10GPa (Boudaoud, 2003, Keckes et al., 2003, Milani et al., 2011, Mirabet et al., 2011). However, the stiffness of the isolated major components of the cell wall are very different: cellulose is the stiffest component (the stiffness is about 100GPa), whereas hemicellulose (40MPa) and pectin (10-200MPa) are much softer (Mirabet et al., 2011).

Cell growth is oriented by the anisotropy of the mechanical properties. The only structure in the cell wall that is strongly anisotropic geometrically and mechanically is the cellulose microfibril: it is the stiffest material in the cell wall, and its deposition often leads to the formation of parallel arrays, thus reinforcing the mechanical anisotropy of the wall: the cell wall is stiffer in the preferential direction of cellulose microfibrils, and softer in the other direction (Kerstens et al., 2001). Because the force driving the growth is isotropic, generated by the internal pressure, the resulting deformation is anisotropic and depends on cellulose preferential orientation in the cell wall (Baskin, 2005).

The cell wall stiffness and anisotropy directly influence the growth. Moreover, the stiffness and

the anisotropy of the cell wall can be regulated by the cell, via the action of hormones, other signaling molecules, mechanical stress, and direct modulators. The roles of these actors are discussed here; the physical aspects of growth are discussed section 1.3.

Phytohormones

Auxin was the first phytohormone showed to impact cell growth and cell wall mechanical properties, its addition causing cell growth (Kutschera and Schopfer, 1986), by both a decrease of the cell wall pH, and downstream transcriptional effects (Fendrych et al., 2016). Auxin regulates many genes at the transcriptional level, including regulators of the cell wall (Abel and Theologis, 1996), but has also direct effects on the cell wall via the activation of H⁺-ATPase, decreasing the pH in the cell wall, which has various effects including the activation of many cell wall remodelers (Rayle and Cleland, 1992).

All the other plant hormones have also been shown to impact cell growth: abscissic acid (Kutschera and Schopfer, 1986), gibberellins (de Lucas et al., 2008), brassinosteroids (Sánchez-Rodríguez et al., 2017, Wolf et al., 2012b), and ethylene (Burg, 1973), but the exact pathways are not fully uncovered. For all phytohormones, even if they have an effect on cell wall mechanical properties and ultimately on growth, they also have pleiotropic effects, and distinguishing which effect has which cause can be very tricky.

Signaling molecules

Reactive oxygen species (ROS) are universal secondary signals in plants and animals (Gilroy et al., 2014). In particular, ROS are important secondary messengers in wound stress signaling, where their production triggers covalent crosslinks between cell wall polysaccharides, ultimately stabilizing the wound (Brisson et al., 1994). ROS also influence plant development in many ways (Foreman et al., 2003, Gapper and Dolan, 2006, Liskay et al., 2003) and are involved in tissue ageing. They can cause both stiffening and softening of the cell wall depending on the circumstances (Schopfer et al., 2002, Xiong et al., 2015).

Calcium is also a secondary messenger involved in many cellular processes (Gilroy et al., 2014, Hepler and Wayne, 1985). In the cell wall, one of its major roles is the non-covalent binding to homogalacturonan backbone to form pectate gels.

Reactive oxygen species and calcium have diverse cellular roles apart from their roles in cell wall mechanical properties, making them difficult to use as tools to modify cell wall mechanical properties, since other properties of the cells will change as well.

Mechanical stresses

The cellular response to mechanical stress has been well established in animal (Bischofs and Schwarz, 2003) and in plant cells (Monshausen and Haswell, 2013), and can lead to modifications of cell shape, behavior, and differentiation. In plants, the origin of mechanical stress is

turgor pressure. No mechanotransduction pathway has been fully described in plants, but putative cell wall sensors have been reported (Ringli, 2010, Wolf et al., 2012a), and the FERONIA receptor-like kinase has been identified during a screen for mutants not responding to external mechanical stimuli (Shih et al., 2014). Building on analogies from the animal and bacterial field, stretch-activated channels could also be mechano-sensors; for instance, the mechanosensitive channel MSL8 in *Arabidopsis* is necessary for pollen tube viability during an hypoosmotic shock (Hamilton et al., 2015); the putative stretch-activated calcium channel MCA1 could have a role in sensing mechanical stimuli in roots (Nakagawa et al., 2007); and the OSCA1 channel is required for osmosensing (Yuan et al., 2014).

Downstream of these mechanosensing pathways, cortical microtubules reorient parallel to maximal tensile stress directions in cells and tissues (Hamant et al., 2008). Whether there is a direct link between the identified mechanosensing pathways and the microtubule reorientation is not known. Moreover, the cellulose deposition follows microtubule orientation, and cellulose is the stiffest component of the cell wall (see the section 1.2.1), hence this reaction to stress allows the cell to resist to mechanical stress, and prevents cell damage. At the single-cell scale, cell geometry prescribes a mechanical stress: the shortest width of the cell bears the highest stress. This leads to the accumulation of transversally aligned microtubules along the smallest widths of the cell. The accumulation of microtubules in turn induces the transversal deposition of cellulose, stiffening the cell wall and preventing the widening of the cell at this location, which hence remains narrow, recruiting even more microtubules. This positive feedback leads to the formation of the so-called puzzle-shaped cells (Sampathkumar et al., 2014).

However, reactive oxygen species, calcium and mechanical signals all have pleiotropic effects, making them difficult tools to investigate the role of cell wall mechanical properties on organ shape robustness.

Wall regulators

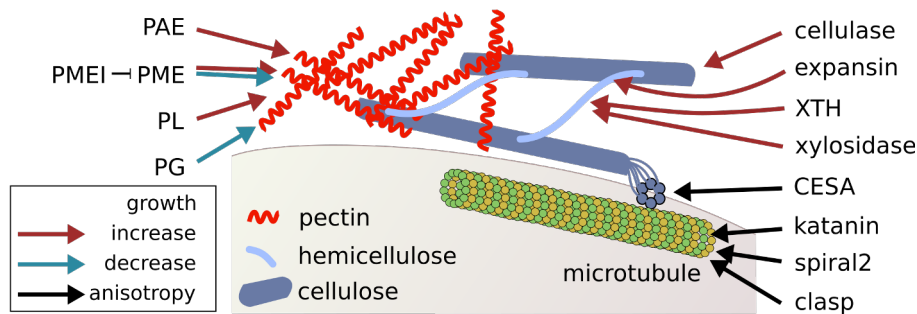


Figure 1.7: Non exhaustive summary of cell wall modifiers. The proteins modify the components pointed by the arrow. A blue arrow means that the presence of this protein is associated with the decrease of growth, a red arrow shows an increase of growth, and a black arrow means that the protein is associated with the control of growth anisotropy. PL: pectate lyase, PG: polygalacturonase, PME: pectin methyl esterase, PME-I: PME inhibitor, XTH: xyloglucan endotransglucosylase/hydrolase.

Direct modifications on the cell wall molecules

Cellulose can be modified by cellulases.

Cellulases, also called endo-1-4- β -glucanases, break the covalent bonds between the glucosidic residues of cellulose but also xyloglucan. The KORRIGAN protein is a cellulase linked to the cellulose synthase complex, and is thought to help the cellulose deposition (Vain et al., 2014), but other cellulases are believed to break cellulose at other locations in the cell wall (Glass et al., 2015). Cellulase activity impacts development: several cellulase mutants are smaller than the wild-type (Glass et al., 2015).

Hemicellulose can be modified by xyloglucan endotransglucosylase/hydrolase or XTH, xylosidases, fucosidases and galactosidases.

XTH enzymes can cut and link xyloglucan chains, with the enzymatic activities endohydrolase and endotransglucosylase, respectively, thus relaxing the stretch in the cell wall (Campbell and Braam, 1999, Rose, 2002). This family of proteins gathers 33 proteins belonging to 3 major phylogenetic groups. This phylogenetic divergence suggests a specialization of the enzymes: members of groups 1 and 2 are thought to mediate exclusively transglucosylation, whereas members of the group 3 could mediate xyloglucan endohydrolysis as well. However, this trend has not been tested for all members of the XTH family and exceptions have been reported (Rose, 2002). Such a large family raises the question whether the genes are redundant or complementary in some way. An expression analysis of the XTH genes showed that they were expressed in different organs at different times in the development, and are differentially regulated by the plant hormones (Yokoyama and Nishitani, 2001), making the proteins not redundant, but rather each very specific. Furthermore, the cell wall mechanical properties are directly softened by XTH activity (Miedes et al., 2011), and XTH directly influence plant growth: the overexpression of XTH increased growth in hypocotyls (Miedes et al., 2013).

Hemicelluloses can also be cleaved by xylosidases. They play a role in plant growth, because the mutants grow smaller siliques whereas the overexpressors siliques are bigger than those of the wild type (Günzl and Pauly, 2011). So far, fucosidases and galactosidases have only been studied in the context of fruit ripening, where they modify hemicellulose side-chains (Lazan et al., 1995, Ranwala et al., 1992).

Cellulose microfibrils and hemicellulose are linked by non-covalent hydrogen bonds. These can be broken by expansins, loosening the cell wall and inducing cell growth; especially in low pH environments (Cosgrove, 1999, Sampedro and Cosgrove, 2005). It has been shown that expansin expression has direct effects on leaf growth: reducing the amount of expressed expansin induced smaller and less extensible leaves, with smaller petiole, whereas increasing the amount of expansin produced lead to the formation of larger leaves with longer petioles (Cho and Cosgrove, 2000).

The pectin network can be modified by endo- or exo-polygalacturonases (PG), pectate lyases (PL), pectin methyl-esterases (PME), pectin acetyl-esterases, and modifications of borate diester and Calcium egg-boxes.

The PGs hydrolyze the homogalacturonan backbone, and the PLs cleave the homogalacturonan

backbone via a β -elimination mechanism (Anderson, 2015). Inducing polygalacturonase activity induced dwarf phenotypes (Capodicasa, 2004), whereas plants with impaired pectate-lyase activity were smaller (Vogel, 2002).

The PME's cleave the methyl groups from the galactose residues of homogalacturonan and rhamnogalacturonan II (Micheli, 2001). These proteins belong to a large family comprising 66 members in *Arabidopsis thaliana* (Pelloux et al., 2007). They are regulated by an equally compound gene family of pectin methylesterase inhibitors (PMEI) (Giovane et al., 2004). The methylesterification of pectins can have two distinct consequences, depending on whether PME's esterify distant pectin residues, or a large number of neighboring residues (Markovič and Kohn, 1984, Micheli, 2001). When PME activity is sparse, the pectin structure associated with the release of protons in the cell wall due to PME activity leads to an increased activity of PG, severing the network and ultimately softening of the cell wall (Micheli, 2001, Moustakas et al., 1991). When PME activity is clustered, a large number of residues in close vicinity display free carboxyl groups, able to interact with calcium ions and establish the stiffer egg-box structures (Goldberg et al., 1996, Micheli, 2001). The interactions between PME and PMEI families are intricate: deciphering the respective roles of each of them during development is a challenge. There are many examples of PME or PMEI mutants both inducing and inhibiting growth, reviewed in Wolf and Greiner (2012) and Peaucelle et al. (2012).

Acetylation can affect both pectin and hemicellulose residues (Nafisi et al., 2015). Only one study focused on the impact of acetylation on growth, where the authors show that acute pectin acetylation defects cause dwarfism (Manabe et al., 2013).

The boron-deficient plants, presenting defects in the borate-diester structures linking rhamnogalacturonan II polysaccharides, are smaller, more fragile than the wild-type, and some cells do not expand properly (Dell and Huang, 1997, O'Neill et al., 2004). In *Arabidopsis* mutant *mur1*, the rhamnogalacturonan II L-Fucose residues are replaced by L-galactose (Reuhs et al., 2004), destabilizing the borate diester bridges; leading to plant dwarfism (O'Neill et al., 2001).

Indirect modifications via the microtubule network

The cellulose orientation depends on the orientation of the cortical microtubule network, itself regulated by microtubule associated proteins (MAPs) (Sedbrook and Kaloriti, 2008). Microtubules have very different roles in the dividing cells and the interphase; many MAPs play roles in microtubule regulation in both cases, but I will focus on the MAPs involved in microtubule network regulation during the interphase.

The interphasic microtubule network consists in an auto-organizing array, which organization depends on MAPs activity and mechanical cues. Moreover, the microtubule array is very dynamic: microtubules grow and shrink continuously. Microtubules also encounter other microtubules at spots called cross-over, and depending on the contact angle, can either depolymerize or zip up to form bundles. Microtubules tend to depolymerize at the edges of the cells if the MAP CLASP is absent (Ambrose et al., 2011, 2007). Ensuing from this behavior, the microtubule array in *clasp* cells is more sensitive to cell shape (Ambrose et al., 2011). The KATANIN protein cuts microtubules at cross-overs, contributing majorly to the microtubule array self-organization.

Although the exact mechanism remains unknown, the KATANIN protein is antagonized by the SPIRAL2 protein at cross-overs. The *katanin* plants hence display less dynamic, more disorganized microtubule arrays (Lindeboom et al., 2013, Stoppin-Mellet et al., 2006), whereas the *spiral2* plants display highly dynamic and aligned arrays (Wightman et al., 2013). The link between microtubule, cellulose deposition, and growth orientation thus explains the mutant phenotypes: *katanin* have round cells and the plants are dwarf (Burk, 2001, 2002), whereas *spiral2* have elongated cells and the plants are taller and thinner than the wild-type (Shoji et al., 2004).

Cells regulate their wall through the coordination of all the processes described in this chapter. Which modifications are required depend on the circumstances and the state of the cell wall, itself monitored by specific proteins called integrity sensors. Wall integrity sensors are not well described yet in plants, but understanding their action could help understand better the cell wall regulation process and possible compensatory mechanisms (Cheung and Wu, 2011).

All the cell wall components are entangled and interact, forming an excessively complex structure, therefore it starts to be studied with a systemic approach (Somerville et al., 2004). My project focuses on one integrated property of the cell wall: its stiffness. To study the effect of cell wall mechanical properties regulation on organ growth, I will use the proteic regulators described in this chapter, which have been shown to have impact on cell wall mechanical properties, but I will not study the precise effect at the cell wall molecular level of these mutations.

1.3 Mechanics and morphogenesis

1.3.1 Turgor pressure and growth

The cell wall biochemistry plays an important role during plant cell growth, since it is an emerging property from the mechanical equilibrium between cell wall and turgor pressure. Only a few studies focused on regulation of turgor pressure during growth, and a full characterization of turgor pressure during growth is yet to be established. Nevertheless, a few examples have shown that turgor pressure can be actively regulated during plant cell growth. Indeed, during lateral root initiation, it is the decrease of turgor pressure in the cortex which allows the emergence of the lateral root. The decrease of turgor pressure in the root cortex is due to the phytohormone auxin which modifies aquaporin activity, in turn impacting turgor pressure (Péret et al., 2012). Furthermore, growing tissues differentially express genes related to turgor pressure such as a tonoplast aquaporin (Ludevid et al., 1992), and they are more permeable than non-growing tissue (Volkov et al., 2007).

But other examples suggest that turgor pressure is not always correlated with growth patterns:: the pollen tube displays growth oscillations without turgor pressure oscillations, showing that the turgor pressure does not influence growth in this context (Proseus et al., 1999), or in other contexts (Beauzamy et al., 2014). Nevertheless, turgor pressure is classically correlated to cell growth, in addition to cell wall mechanical properties (COSGROVE, 1993). Both turgor pressure

and cell wall mechanical properties can be estimated by biological experiments.

1.3.2 Measuring turgor pressure

The classical tool used to measure turgor pressure is the pressure probe. The cell is poked by a pressure probe filled with oil, which displacement can be measured to infer the turgor pressure. This technique furthermore allows to modify the internal pressure, by adding fluid in the cell, which can be used to study the reaction of the cell to higher pressures (Cosgrove, 1985, Franks et al., 2001). The major drawback of the pressure probe technique is that the measured cell dies in the process, but it has long been the only way to estimate turgor pressure in cells, and is nowadays mostly used to assess other less intrusive approaches to measure turgor pressure. In particular, it has been compared to data obtained by micro-indentation. A micro-indenter measures the force necessary to indent a sample, and it is possible to estimate turgor pressure from such measurement without damaging the cell (Lintilhac et al., 2000). The measurements using such technique were in accordance to pressure probe measurements in the same systems (Beauzamy et al., 2016, Wang et al., 2006). The micro-indenter is also simpler to set up, and allows a higher number of experiments to be performed. The main limitation of indentation is that a model is needed to interpret experiments in terms of turgor pressure.

1.3.3 Measuring cell wall stiffness

The cell wall is external, making it reachable to non invasive measurements. Nano- and micro-indentation are the most widely used techniques to measure mechanical properties of the cell wall. The depth of the indentation of a tip into a sample and the force applied to reach this depth are measured, thus allowing the measurement of the sample stiffness. The applied forces and depths can range over several orders of magnitude, especially between a nano-indenter, or atomic force microscope (indentations of 10 to 100nm, forces of 10 to 100nN), and a micro-indenter (indentations of 1 to 10 μ m, forces of 1 to 10 μ N) (Geitmann, 2006, Milani et al., 2013, Routier-Kierzkowska and Smith, 2013, Vogler et al., 2015). Micro-indentation was successfully used to demonstrate the correlation between pollen tube cell wall biochemistry and stiffness (Geitmann and Parre, 2004), and atomic force microscopy was sensitive enough to distinguish cells of different identities in the shoot apical meristem of *Arabidopsis thaliana* (Milani et al., 2011, Peaucelle et al., 2011).

However, a plant tissue is composed of several layers with different mechanical identities: each cell is surrounded by a stiff cell wall, inflated by turgor pressure, which also resists to the indentation. What portion of the stiffness measured by the indenter is due to the turgor pressure, and what portion reflects the cell wall stiffness? Modeling the behavior of a plant like-tissue material under indentation can greatly help distinguish the different stiffnesses at play (Malgat et al., 2016): such approach has been successfully used in different contexts to measure turgor pressure and cell wall stiffness (Felekis et al., 2011, Forouzesh et al., 2013, Hayot et al., 2012, Routier-Kierzkowska et al., 2012). Furthermore, assessing the correct turgor pressure from

indentation data requires taking into account the shape of the cell (Beauzamy et al., 2015, Vogler et al., 2013).

1.3.4 Forces in plants and during morphogenesis

Forces shape cells

Plants have to resist gravity to rise above ground. They can do so thanks to the hydrostatic pressure (turgor pressure) typically ranging from 0.1MPa to 1MPa. It has been observed that when peeling a stem, the external tissue shrinks whereas the internal tissue expands, suggesting that the internal layers are in compression and the external layer under tension (Vandiver and Goriely, 2008). Similarly, cutting a plant tissue leads to a deformation; because it relaxes the forces in the tissue, measuring such deformations can inform on stress patterns. In particular, the widening of a gap means that the original tissue was under tension (Dumais and Steele, 2000). To sum up, the force needed to restore the initial configuration of the cut tissue is equal to the force originally borne by the intact tissue. This approach allows the estimation of the forces at play in a tissue.

At the cellular level, cells are at mechanical equilibrium between the turgor pressure and the stiff cell wall under tension. To evaluate the forces at stake at the cellular level, it is possible to remove the turgor pressure by plasmolysis, the displacement of the cell wall will then convey information on the forces in turgid cells. Turgor pressure results from osmotic pressure, hence it is controlled by the differential of osmolyte concentration between the cell and the outer medium. Hence, it is possible to plasmolyze cells by increasing the outer concentration in osmolytes, reducing the stress due to the turgor pressure and the tension in the cell wall. Comparing plasmolyzed and turgid cells gives information on the tension at play in turgid cell walls (Routier-Kierzkowska et al., 2012). The interplay between turgor pressure and cell wall mechanical properties is at the core of our current understanding of plant cell growth.

Forces and growth

The growth of the plant cell is due to the yielding of the cell wall under the tension generated by turgor pressure. This tension induces deformations of the cell wall, depending on its rheology. In the simplest rheological model, the cell wall is considered purely elastic: it behaves like a spring. In this case, the deformation, or strain ϵ , depends only on the stress σ applied on the string, or the cell wall:

$$\epsilon = \sigma/E$$

where E the stiffness modulus of the cell wall. The principal limitation of this model is that the spring reverts to its original shape when the force is released: such a cell wall does not grow. A more realistic representation of the cell wall is a visco-elastic material. In this case, it behaves like the association of a spring and a damper (see Figure 1.8):

$$\frac{d\epsilon}{dt} = \sigma/\mu + \frac{d\sigma}{dt}/E$$

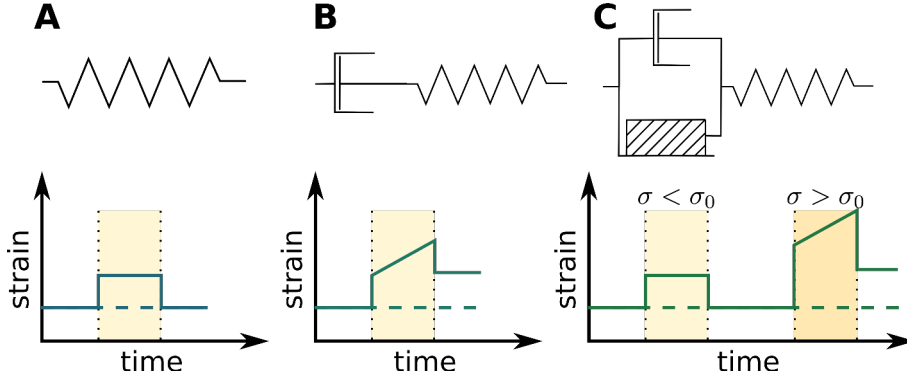


Figure 1.8: Schematics and behaviors of simple rheologies. (A) A pure elastic material behaves like a spring: it returns to its original state when the stress is released. (B) A visco-elastic material behaves like the association of a spring and a damper, and does not revert to its initial state when the stress is released. (C) The behavior of a visco-elasto-plastic material depends on the value of the stress applied: if the stress is smaller than the material-specific threshold σ_0 , it behaves elastically, otherwise it behaves visco-elastically.

where μ is the dynamic viscosity. Here, when the force is released, the material does not revert to its original configuration: this rheology allows cell wall growth. One of the most elaborate rheological model of the cell wall behavior was introduced by Ortega (1985), and proposes that the cell wall behaves as a visco-elasto-plastic material (see Figure 1.8): the cell wall behaves as an elastic material when the stress is lower than a threshold σ_0 , but as a visco-elastic material if the stress is larger:

$$\frac{d\epsilon}{dt} = (\sigma - \sigma_0)/\mu + \frac{d\sigma}{dt}/E$$

Cell wall rheological parameters can be measured, using techniques reviewed in (Milani et al., 2013, Routier-Kierzkowska et al., 2012, Vogler et al., 2015). Depending on the question addressed, one can use one or the other of these rheological model. Note that the rheological parameters of the cell wall can be heterogeneous and/or anisotropic and that these models do not take this into account.

Mechanical forces are omnipresent in plants, and more particularly during morphogenesis; in addition, a growing tissue needs to develop harmoniously integrating all the morphogenetic information over time and space. Models are required to take all actors and their intricate interactions into account.

1.4 Growth of an organ

Despite much progress in developmental biology, we are still far from understanding how organs grow and reach their final size and shape. Growth is associated with a variety of cellular scale phenomena such as cell expansion, cell proliferation, and cell differentiation, as well as cell death and cell migration in the case of animals. These processes occur within the thousands of cells that yield a well defined organ. How these various phenomena are coordinated over time and space to shape a consistent and reproducible organ or organism is still an open question. In this

chapter, we first introduce quantitative descriptions of growth. We then focus on mechanical models of growth; we review types of models and we discuss case studies where such models were used.

1.4.1 Describing morphogenesis

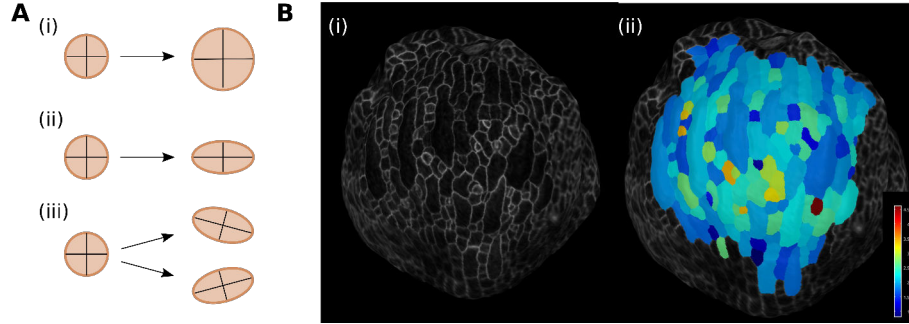


Figure 1.9: Quantifying morphogenesis. (A) Growth can be converted to scalars: (i) growth rate, (ii) growth anisotropy (iii) growth direction. (B) Example of a software developed to quantify growth: (i) image of an *Arabidopsis thaliana* sepal with the membrane tagged, (ii) growth rates quantified over each cell for a 24h interval using MorphGraphX (Barbier de Reuille et al., 2015).

To better understand morphogenesis and reliably compare mutants to wild type and models to experiments, qualitative observations are not sufficient: quantitative measurements are necessary. From an analytical viewpoint, morphogenesis can be dissected as the sum of a small set of elementary transformations. Growth can be decomposed into three parameters: growth rate (differential of area over time), growth anisotropy (ratio between the maximal and the minimal principal directions of growth) and maximal growth direction (see Figure 1.9) (Boudon et al., 2015, Coen et al., 2004, Erickson, 1976, Silk and Erickson, 1979). This conversion from image to quantitative data provides tools to perform statistical analyses and to compare models to experiments in a systematic manner.

Quantifying cell growth

The technical step of quantitative measurements have been facilitated by the development of softwares which segment cells and measure their growth parameters semi-automatically, on 2D surfaces (Barbier de Reuille et al., 2015), and in 3D (Fernandez et al., 2010). These softwares have been used to extract and characterize cell shapes (Lucas et al., 2013, Montenegro-Johnson et al., 2015, Sampathkumar et al., 2013), cell growth (Bringmann and Bergmann, 2017, Kierzkowski et al., 2012, Tauriello et al., 2015) and in the chapter 3, and to compare mutants to wild-type growth (Yang et al., 2016) and in the chapter 2. These cell-based softwares have been used in rather small organs so far (less than a thousand of cells). The growth patterns of bigger organs such as older leafs and flowers are measured at the supracellular level using a continuous description.

Quantifying organ growth

The growth patterns of large organs are measured using methods such as landmark analysis and clonal analysis. It is possible to use landmarks on an organ, and measure the relative displacements of the landmarks over time. Originally, the used landmarks were natural, such as the vein intersections in leaves (Maksymowych, 1959), but also ink drawn grids (Avery, 1933) or set of points (Granier and Tardieu, 1998, Poethig and Sussex, 1985), however, these techniques can be used only on older leaves. Nowadays, more precise methods can be used such as fluorescent microparticles (Remmler and a. G. Rolland-Lagan, 2012, Rolland-Lagan et al., 2014).

On the other hand, it is also possible to use the clonal analysis, consisting in labelling, by expressing a colored marker, groups of cells or single cells and observing their descendants, thus defining growth rate, anisotropy and direction at the level of thousands of cells (Poethig, 1987). Because the tissue deforms during growth, the interpretation of the clonal analysis requires the use of a model (Rolland-Lagan et al., 2003).

In addition, two studies have shown that measuring the leaf contour change over time was sufficient to predict the displacement field of all points inside the leaf (Alim et al., 2016, Mitchison, 2016), because the leaf remains flat all over its development, and because its growth is locally isotropic at later stages of morphogenesis.

In plants, growth is achieved by modulating the mechanical properties of the cell wall. How can we relate the cell wall mechanical properties to the growth? What are the mechanical principles behind plant morphogenesis?

1.4.2 Modeling morphogenesis

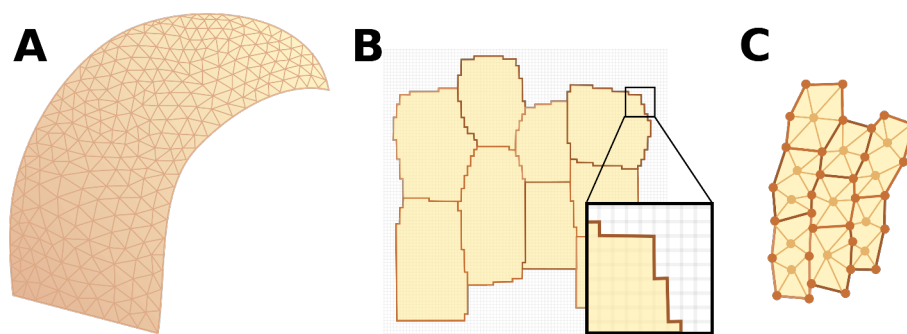


Figure 1.10: Main types of models. (A) Continuous models: the surface of the organ is continuous, usually represented by a triangulated mesh. (B) Cellular Potts model, where the cells are defined on a non-deformable grid. (C) Vertex-based model, the cells are defined by vertices (circles) and their edges with the neighboring cells.

Different types of models

All the models used to describe morphogenesis fall into two main categories: models considering a continuous growing medium and models individualizing each cell.

Continuous models usually describe large organs, comprising thousands of cells, where the cell size is very small compared to the modeled organ size. These models have been used so far to model the morphogenesis of fruits (Cieslak et al., 2016), but more often, flat organs such as

leaves, petals and sepals (e.g. Green et al. (2010) and in chapter 2). The surface of the organ is modeled as a 2D surface evolving in space, where growth is monitored by the mechanical properties of the periclinal cell wall (Holloway and Harrison, 2008), which in flat organs is the thickest and stiffest cell wall, and is thought to restrict the organ growth to the longitudinal direction.

Many models individualize cells, such as the cellular Potts model, and vertex-based model (see Figure 1.10). In the cellular Potts model, cells are defined on a discrete fine grid, and the edges of the cells move depending on a defined set of rules. The cellular Potts model framework is widely used in the animal field, and can have a finer subcellular resolution than vertex-based models, but has been used only once in plants as far as we know, to investigate subcellular localization of auxin in the root (Grieneisen et al., 2007). Indeed, this framework is not suitable for a tissue deforming elastically, and is commonly used to model purely viscous material such as animal cells. Individualizing cells as well, many models are vertex-based (Dupuy et al., 2008, Merks et al., 2011). Cells are then defined by a few points at their edges that can continuously move in space depending on rules such as growth rate and cell wall stiffness. This structure allows each cell to be individualized, defined by its edges and links to neighboring cells. Here, regulatory networks can be defined in each cell, in addition to the communication between cells, and cell division. In this case, cell growth can be influenced by the periclinal cell wall mechanical properties, as in the continuous models, but the anticlinal cell wall can also influence growth (De Vos et al., 2014, Merks et al., 2011, Romero-Arias et al., 2017).

More recently, people started to combine the vertex-based and the continuous approaches, and use the finite element method to implement models where cells were individualized (Boudon et al., 2015, Bozorg et al., 2016), allowing simultaneously the modeling of cell scale behavior (cell division, cell shape), and the consideration of the mechanical properties of the periclinal cell wall at a subcellular resolution. In addition, Boudon et al. (2015) also included for the first time internal cell layers, and showed that they impacted morphogenesis in the shoot apical meristem.

Implementation of growth

Growth can be modeled using two major approaches. In the first type of description, growth rate, direction and anisotropy are specified or inferred from a gene regulatory network at each point in time and space of the simulation, leading to the growth of the whole tissue (Green et al., 2010). In the second type of description, the cell wall mechanical properties such as stiffness and anisotropy are specified or inferred from regulatory networks, and the mechanical equilibrium between the mechanical properties and the turgor pressure defines the current growth rate, or tissue deformation. In this framework, the tissue deformation depends on the tissue rheology, which can be one of the rheologies previously presented: elastic, viscoelastic or visco-elasto-plastic.

1.4.3 Some case studies

Morphogenesis of an isolated plant cell

A first step towards understanding organ morphogenesis is to study cell morphogenesis. A classical system of interest is the pollen tube, an isolated cell displaying a simple tubular shape. During pollination, the pollen lands on the tip of the carpel; followed by the emergence of the pollen tube, which subsequently grows into the carpel reaching the ovule. How a cell can grow in such directional manner has been investigated several times.

Considering the self-similar tip growing cell wall as a stretchable elastic membrane and using large elastic deformation theory, Goriely and Tabor (2003) showed that a lower stiffness at the tip of the tube was sufficient to produce self-similar tip growth, even with no anisotropy of the cell wall mechanical properties. However, the model later developed by Dumais et al. (2006), where the authors considered the cell wall as a viscoelastic material stiffer towards the pollen tube edges, meaning that the material changed shape only when the stress was strong enough; showed that the cell wall anisotropy was mandatory to retrieve self-similar tip growth, except in very few specific cases. In these two studies, the equations were numerically solved based on the circumferential symmetry of the pollen tube, making this modeling framework difficult to export to other systems. More recently, the pollen tube self-similar growth was modeled using the more versatile finite element environment (Fayant et al., 2010). The cell wall was considered as an elastic material, and the loaded configuration was used as the starting geometry for the next loading step. The influence of anisotropy and of the steepness of the gradient of stiffness over the edges of the tube were tested, and the interaction between these two quantities allowed self-similar growth depending on the parameters: a steeper cell wall extensibility gradient was associated with a more isotropic cell wall to produce self-similar growth.

Curving an elongated organ: tropisms

Plants cannot move, but they react to their environment: the stem and root bend towards the light and depending on gravity. The molecular mechanisms involved are relatively well described, and the integration of these mechanisms during growth have been investigated using a vertex-based model. Specifically, the differential localization of auxin transporters from the PIN-FORMED family leads to differential concentrations of auxin, which in turn cause differential growth rates along the transverse axis of roots and hypocotyl (Žádníková et al., 2016), ultimately inducing a bending of the organ (Fozard et al., 2016). These studies focus on the relationship between auxin, cell differential growth, and bending initiation. But they do not explain the bending dynamics until the equilibrium is reached. When only the auxin response to gravity is taken into account, the shoot oscillates around the equilibrium position whereas real shoots do not oscillate around the equilibrium position. However, when the sensing of the local curvature was taken into account, the dynamics of the curving of the stem reproduced the observed behavior,

in the case of both gravitropism (Bastien et al., 2013) and phototropism (Bastien et al., 2015).

Shaping a sheet-like organ

Volvox is a green algae in the form of a spherical sheet of cells with an aperture. One major event in the morphogenesis of Volvox is its inversion: the organism turns inside out. The inversion of the sheet of cells is associated with a sequence of deformations where cells firstly circularly invaginate at the equator, accompanied by the posterior hemisphere which moves into the anterior and inverts as well. Finally, the aperture stretches out over the posterior hemisphere. The deformation of the sheet is associated with cell shape changes, but their role in the sheet inversion remained imprecise. Using high resolution microscopy and modeling the sheet as an elastic material, the authors showed that the shift in the sheet curvature at the equator combined with the contraction of the posterior hemisphere were sufficient to trigger this major morphogenetic event (Höhn et al., 2015).

Plants are composed of two main types of organs: the tubular-shape organs, such as root, stem, hypocotyl, and the sheet-like organs such as leaves and petals. In angiosperms, the shapes of the flat organs are very diverse and can change drastically from one species to another. The underlying regulatory networks are very intricate and predicting the final shape of the petal or the leaf from regulatory networks is impossible without using a model. The Snapdragon corolla, in particular, has a very elaborated, asymmetric shape. The wild-type and several morphogenetic mutants have been successfully modeled using a continuous approach (Green et al., 2010). However, this model does not take into account the fact that at mechanical equilibrium, the cell wall is under tension – since removing the forces applied by the turgor pressure would lead to its deformation. This stress is called residual stress, and can be taken into account or not in the models. Not preserving the residual stress means that the cell wall completely remodels to reach its final size: the cell wall viscosity is prevailing. Even if this view is less realistic (plant tissues are continuously under tension), it is easier to implement and understand, and leads to representative morphogenesis processes (Green et al., 2010). A more realistic point of view is to consider that the cell wall is continuously under residual stress (Boudon et al., 2015). This tension can have dramatic effects on the modeled morphogenesis in specific cases. Indeed, when thin organs display larger growth rates at their edges than in their center, the differential of growth rates leads to a compressive stress at the edges of the organs. If the residual stress was not taken into account, the organ would remain flat. However, taking the residual stress into account leads to the buckling of the edges of the organ (Audoly and Boudaoud, 2003), observed in the petals and leaves of the Lily (Liang and Mahadevan, 2009, 2011). On the other hand, *Arabidopsis thaliana* leaves are flat, thanks to a tight regulation of the growth rates during their growth which have to be locally isotropic (Alim et al., 2016, Mitchison, 2016).

Feedback through mechanical signals

Mechanics are at the core of morphogenesis: the growing cells interact mechanically during morphogenesis, relaxing and creating stresses. Can these mechanical stresses have an impact on cells behavior? The question is then to decipher whether cellulose orients in the stress direction or orthogonally to the strain main direction. The strain maximal direction depends both on the stress and the cell wall mechanical properties, implying that the stress is not necessarily collinear with the strain. Bozorg et al. (2014) did simulations where the mechanical feedback depended on the stress or on the strain. The simulations where the cellulose orientation followed the stress were in accordance with the experimental observations, whereas the simulations where cellulose oriented depending on the strain were less stable and the cellulose orientation was eventually longitudinal instead of the observed transversal orientation.

It has been shown that cells could sense and react to mechanical cues in plants by modifying the orientation of their cortical microtubule networks (Hamant et al., 2008). Furthermore, it is well known that the cortical microtubule network guides the deposition of cellulose microfibrils, which in turn controls the cells growth direction and anisotropy. Consequently, it can be hypothesized that mechanical stress sensing can influence plant morphogenesis. The orientation of cell division, following cortical microtubule orientations in most cells, is also influenced by mechanical cues (Louveau et al., 2016). Cells can also react to mechanical forces to pattern differentiation. For example, during the growth of leaves, the mesenchyme grows faster than the epidermis, thus building compressive stresses in the mesenchyme. The mesenchymal cells then elongate in the direction of the stress, and differentiate into veins. The mechanical feedback induced differentiation is sufficient to produce venation patterns that are similar to the patterns observed in dicotyledon leaves (Corson et al., 2010, Laguna et al., 2008).

Variability and morphogenesis

All the illustrated models so far are deterministic: they describe the expected average behavior of the system. However, the cells in an organ are variable. Modeling the wheat leaf using a cell-based model which takes turgor pressure and water movements into account, Zubairova et al. (2016) showed that turgor pressure was variable between the cells of the wheat leaf, and that this variability correlated with cell identity. The authors suggest that the cells could differentiate depending on the mechanical signals generated by the variable turgor pressure.

Furthermore, taking variability into account in models can be mandatory to understand an observed morphogenetic behavior. The growth of a leaf depends on its venation pattern, because veins are stiffer than mesenchyme. The areas separated by the veins grow at different rates, depending on their sizes and on the sizes of the neighboring veins, which stiffness depends on their thickness. Moreover, when the tissue grows under stretching stress, the venation network reorients towards the direction of the applied stress. Using a vein-based model similar to a vertex-based formulation, Bar-Sinai et al. (2016) showed that the external stress increased the variability of the modeled growth rates of the vein-defined areas. However, the areas growing

under stress were more homogeneous in real leaves. The authors could retrieve such homogeneity only by taking into account a variability of thickness of the veins, and by considering the tissue as an elasto-visco-plastic material.

As a conclusion, modeling morphogenesis improved greatly our understanding of the phenomenon, but a lot remains to be understood, such as the role of mechanical feedback on morphogenesis and the role of variability in morphogenesis.

1.5 Why choosing the sepal as a model system

The sepal of *Arabidopsis thaliana* flowers is an ideal tool to study the influence of mechanical properties on organ shape reproducibility.

The sepal is the most external organ of the flower, and protects the reproductive organs of the plant along their development, its development is synchronized with the development of the other flower organs (Smyth, 1990). A thorough protection of the flower reproductive organs requires a tightly closed flower bud, allowed by a precise control of sepal size and shape. For this reason, the sepal development would be less sensitive to environmental fluctuations than leaves (Roeder, 2010). When the flower opens, the sepal has stopped growing and has reached its final size, allowing an easy determination of the final size of the organ, unlike the leaves for which determining the end of growth is less direct. This will enable a fast and easy assessment of organ size and shape variability.

Moreover, the sepals are highly variable at the cellular scale. Indeed, sepal epidermis displays three major cell types in addition to the ordinary epidermal cell. Stomata, shared by all aerial organs, are small cells allowing gas exchange with the internal tissue. Trichomes are large cells growing out of the epidermis, whose precise function is not determined. Leaves and stems also display trichomes, but sepals are the only flower organs with trichomes. Lastly, giant cells are epidermal cells undergoing up to 4 endoreduplication cycles, making them the largest cells of the epidermis of the sepals (Roeder et al., 2010). In addition, because their formation depends on the fluctuations of the ATML1 transcription factor, their number and pattern are stochastic and vary from sepal to sepal, increasing the inter-individual variability at the cellular level (Meyer et al., 2017).

Furthermore, the sepal has more technical advantages making it an interesting tool for this project: it is external all along its development, allowing live imaging with a confocal microscope, as well as the estimation of its mechanical parameters using atomic force microscopy and indenter (Mosca et al., 2017). The large number of flowers in each plant (more than 60) enables a robust estimation of variability of sepal size and shape with a minimal impact of environment and genetic variability.

The sepal is a relatively recent model for development (Roeder, 2010), so very few informations are available as for its development. However, parallels are often drawn with leaf growth, which has been much more studied (Donnelly et al., 1999, Powell and Lenhard, 2012). Leaf growth is classically divided into two processes: cell division and cell enlargement, which are tightly

regulated over the development of the leaf (Powell and Lenhard, 2012). Many molecular actors have been described contributing to the setting up of these arrest fronts. Sepals are suspected to grow following the same patterns, but it has not been confirmed.

Leaf size control has been intensively studied, and in particular it has been shown that the two distinct processes cell division and expansion interact, by a mechanism called compensation. Indeed, in mutants reducing cell division rate, for example, the expansion phase is stretched so that the cells are larger, and the overall size of the leaf is similar to the wild-types (Horiguchi et al., 2006, Mizukami, 2001, Mizukami and Fischer, 2000). However, how the leaves perceive their size and alter their growth pattern to produce larger or smaller leaves is not understood.

Understanding how sepals regulate their size could also help draw a better insight of the compensation mechanisms.

1.6 Main questions

Arabidopsis thaliana sepal is a great tool to study the influence of mechanical properties in morphogenesis and developmental robustness.

Taking advantage of the perks of the sepals, we first investigated how an increase in the variability of cell wall mechanical properties impacted robustness of morphogenesis.

In a second part, we analyzed how mechanical signals contribute to sepal morphogenesis in parallel to morphogens.

I also investigated whether a component of the cell wall was more responsible for the sepal shape reproducibility, but this will not be detailed in this manuscript (data not shown).

2

Variable Cell Growth Yields Reproducible Organ Development through Spatiotemporal Averaging

UNDERSTANDING HOW ORGANS regulate their size is still a challenge (Vogel, 2013). In particular, it is unknown how the organ achieve such robust shape and size.

Here, we use the sepal as a tool to investigate this question, because they have reproducible size and shape. Therefore, we genetically screened for mutants displaying more variable sepal size and shape. Using a modeling approach, we also investigated the impact of the spatial and temporal variability of mechanical properties on organ shape. With this study, we show that the variability of mechanical properties impacts sepal shape and size stability, and more importantly, that an increase in mechanical properties variability lead to more robust shapes and sizes.

This work was done in a collaboration, where I built the models and solved them numerically and did atomic force microscopy experiments and analyses; and took part in the elaboration of the experiments following the model outcomes, the characterization of mutants of the screen, and in the identification of the *vos1* mutation.

This work was published in Hong et al. (2016), the contents of the article are reproduced in this chapter. Lilan Hong^{1,6}, Mathilde Dumond^{2,5,6}, Satoru Tsugawa^{3,6}, Aleksandra Sapala⁴,

Anne-Lise Routier-Kierzkowska⁴, Yong Zhou^{1,7}, Catherine Chen¹, Annamaria Kiss^{2,5}, Mingyuan

Zhu¹, Olivier Hamant^{2,5}, Richard S. Smith⁴, Tamiki Komatsuzaki³, Chun-Biu Li³, Arezki Boudaoud^{2,5,*}, and Adrienne H.K. Roeder^{1,*}

¹ Weill Institute for Cell and Molecular Biology and Section of Plant Biology, School of Integrative Plant Sciences, Cornell University, Ithaca, NY 14853, USA

² Laboratoire de Reproduction et Développement des Plantes, Université de Lyon, ENS de Lyon, UCBL, INRA, CNRS, 46 Allée d'Italie, 69364 Lyon Cedex 07, France

³ Research Institute for Electronic Science, Hokkaido University, Kita 20 Nishi 10, Kita-ku, Sapporo 001-0020, Japan

⁴ Department of Comparative Development and Genetics, Max Planck Institute for Plant Breeding Research, Carl-von-Linné-Weg 10, 50829 Köln, Germany

⁵ Laboratoire Joliot Curie, CNRS, ENS de Lyon, Université de Lyon, 46 Allée d'Italie, 69364 Lyon Cedex 07, France

⁶ Co-first author

⁷ Present address: Agricultural College, Yangzhou University, Yangzhou 225009, P.R. China

* Correspondence: arezki.boudaoud@ens-lyon.fr

2.1 Summary

Organ sizes and shapes are strikingly reproducible, despite the variable growth and division of individual cells within them. To reveal which mechanisms enable this precision, we designed a screen for disrupted sepal size and shape uniformity in *Arabidopsis* and identified mutations in the mitochondrial i-AAA protease FtsH4. Counterintuitively, through live imaging we observed that variability of neighboring cell growth was reduced in *ftsh4* sepals. We found that regular organ shape results from spatiotemporal averaging of the cellular variability in wild-type sepals, which is disrupted in the less-variable cells of *ftsh4* mutants. We also found that abnormal, increased accumulation of reactive oxygen species (ROS) in *ftsh4* mutants disrupts organ size consistency. In wild-type sepals, ROS accumulate in maturing cells and limit organ growth, suggesting that ROS are endogenous signals promoting termination of growth. Our results demonstrate that spatiotemporal averaging of cellular variability is required for precision in organ size.

2.2 Introduction

Developmental robustness is the ability of an organism to produce the same phenotype regardless of perturbations that occur; for instance, organisms can produce uniformly sized organs despite cellular variability. Within a species, the size of an organ is generally highly reproducible or precise (Lander, 2011). For example, brains of mice vary in size by only about 5% (Williams, 2000), the two arms of a person match in length with an accuracy of 0.2% (Wolpert, 2010), and *Arabidopsis* petals are strikingly uniform (Mizukami, 2001). However, the behavior of cells that make up organs is often variable and unpredictable (Doupé et al., 2010, Gupta et al.,

2011, Meyer and Roeder, 2014, Singh et al., 2013). Equivalent neighboring plant cells grow at markedly different rates in several developing tissues (Armour et al., 2015, Elsner et al., 2012, Kierzkowski et al., 2012, Tauriello et al., 2015, Uyttewaal et al., 2012), although at later stages of development, growth may become more uniform (Zhang et al., 2011a). Similarly, neighboring cells have different constriction rates during *Drosophila* gastrulation (Martin et al., 2009). Thus, how robust organ sizes emerge from the variable growth of cells is a central question in biology. Although signaling pathways regulating organ size and shape have been identified, the mechanism of robustness in size and shape has remained elusive. Screens for mutants with altered organ size have isolated mutants with defects in cell size, cell number, or both (Anastasiou et al., 2007, Andrianakaja et al., 2012, Deprost et al., 2007, Dinneney et al., 2004, Disch et al., 2006, Horiguchi et al., 2005, Karidas et al., 2015, Kawade et al., 2013, Kim and Kende, 2004, Mizukami and Fischer, 2000, Montagne et al., 1999, Nath et al., 2003, Ohno, 2004, Palatnik et al., 2003, Powell and Lenhard, 2012, Ren et al., 2011, Sauret-Güeto et al., 2013, Tumaneng et al., 2012, White, 2006). Although these mutants produce larger or smaller organs, they still tend to produce organs that all have the same size within the same genotype, and thus have little or no effect on robustness. Similarly, mutants disrupting organ shape have been isolated (Cui et al., 2010, Green et al., 2010, Nath et al., 2003, Sauret-Güeto et al., 2013), but little is known about robustness of shape. Mutants with variable size and shape are needed to investigate the mechanism of robustness.

There is persuasive evidence that animals and plants ensure organ size robustness not simply by counting cells or assessing cell size, but by somehow monitoring the overall size of their organs (Day and Lawrence, 2000, Powell and Lenhard, 2012). Plant and animal organs with reduced cell divisions often undergo “compensation,” whereby the cells enlarge to produce almost normally sized organs (Horiguchi and Tsukaya, 2011, Roeder et al., 2010). For example, plant leaves overexpressing a cyclin-dependent kinase inhibitor have significantly reduced cell numbers yet still grow to relatively normal size through increased cell expansion (De Veylder et al., 2001, Ferjani et al., 2007, Hemerly et al., 1995, Kawade et al., 2010). Similarly, inhibition of cell division in *Drosophila* imaginal disks promotes cell enlargement to produce a normally sized wing (Colombani et al., 2012, Garelli et al., 2012, Neufeld et al., 1998, Vallejo et al., 2015, Weigmann et al., 1997). Nevertheless, how growing organs sense their size and know when to stop growth remains a mystery (Vogel, 2013).

Arabidopsis floral organs, particularly sepals, allow robustness in organogenesis to be assessed within a single plant. Each flower has four sepals with the same size; individual plants can produce more than 100 flowers, allowing a statistical assessment of organ size within an individual organism, which generally cannot be done in animals. Sepals are the outermost leaf-like floral organs, making them accessible for imaging throughout development. The consistent size and shape of sepals is required to enclose and protect the developing reproductive organs, maintaining an effective barrier against the external environment. In addition, the size of floral organs is relatively insensitive to environmental effects, allowing us to focus on intrinsic mechanisms. Finally, there is considerable variability in both cell growth and cell cycle within developing

sepals (Qu et al., 2014, Roeder et al., 2010, 2012, Schiessl et al., 2012, Tauriello et al., 2015). Thus, sepals are a good model system for studying how robust organ size and shape arises from cellular variability.

Plant cells grow through the irreversible, turgor pressuredriven extension of their cell walls. These walls are composed of a polymer matrix of cellulose, hemicellulose, and pectins as well as heavily glycosylated proteins. Cellulose microfibrils are the major structural reinforcements and orient cellular growth (COSGROVE, 1993, Somerville et al., 2004). Pectins affect cell wall stiffness, which is fairly heterogeneous within a cell and between cells, but is critical for the growth rate of cells and consequently for morphogenesis (Chebli et al., 2012, Milani et al., 2011, Peaucelle et al., 2011, 2008). Cell-wall stiffness inversely correlates with growth rates (Bassel et al., 2014, Milani et al., 2011). Computational modeling enables the prediction of morphogenesis from cell-wall mechanics, gene activity, or both (Boudon et al., 2015, Coen et al., 2004, Green et al., 2010, Kennaway et al., 2011, Kuchen et al., 2012, Roeder et al., 2011, Sassi et al., 2014, Sauret-Güeto et al., 2013).

In this study we have used molecular genetics, live imaging, and computational modeling to disentangle the links between cellular variability and organ precision. In contrast to previous mutant screens for increased or decreased average organ size, we screened for mutants that disrupted the robustness of sepal size and shape. We characterized the *variable organ size and shape 1* (*vos1*) mutant, ascribing its phenotype to the overaccumulation of reactive oxygen species (ROS). Our key conclusion is that spatiotemporal averaging of cellular variability promotes robustness in organ shape.

2.3 Results

2.3.1 *vos1* Mutants Have Increased Variability in Sepal Size and Shape

To investigate how plants maintain organ size and shape regularity, we screened for mutants with disrupted sepal uniformity within an individual plant and isolated a mutant that we named *variable organ size and shape 1* (*vos1*; Figure 2.1A). In this screen, we isolated six alleles of *vos1* (see Experimental Procedures, Section 2.5), with similar phenotypes, indicating that this gene is essential for maintaining sepal uniformity. Wild-type *Arabidopsis* flowers have uniform sepal sizes (mean \pm SD 1.23 ± 0.10 mm², n = 68, all four sepals from each flower were included in the analysis; Figures 2.1A, 2.1C, 2.1D, and 2.8D). In contrast, *vos1* mutants have sepals of different sizes within the same flower, failing to form an effective barrier to protect the inner developing reproductive organs (Figures 2.1A, 2.1C, 2.1D, and 2.8D). Thus, *vos1* sepals have a decreased average area and increased variance in area (Figure 2.1C; mean \pm SD 0.85 ± 0.27 mm², n = 68, $p < 0.001$). Different *vos1* flowers from the same inflorescence also show great variability (Figures 2.8A and 2.8B).

Similarly, *vos1* sepals have irregular shapes (Figures 2.1A and 2.8B). We quantified variability in sepal shape (S2), independent of size (Figure 2.1E; see Experimental Procedures, Section 2.5).

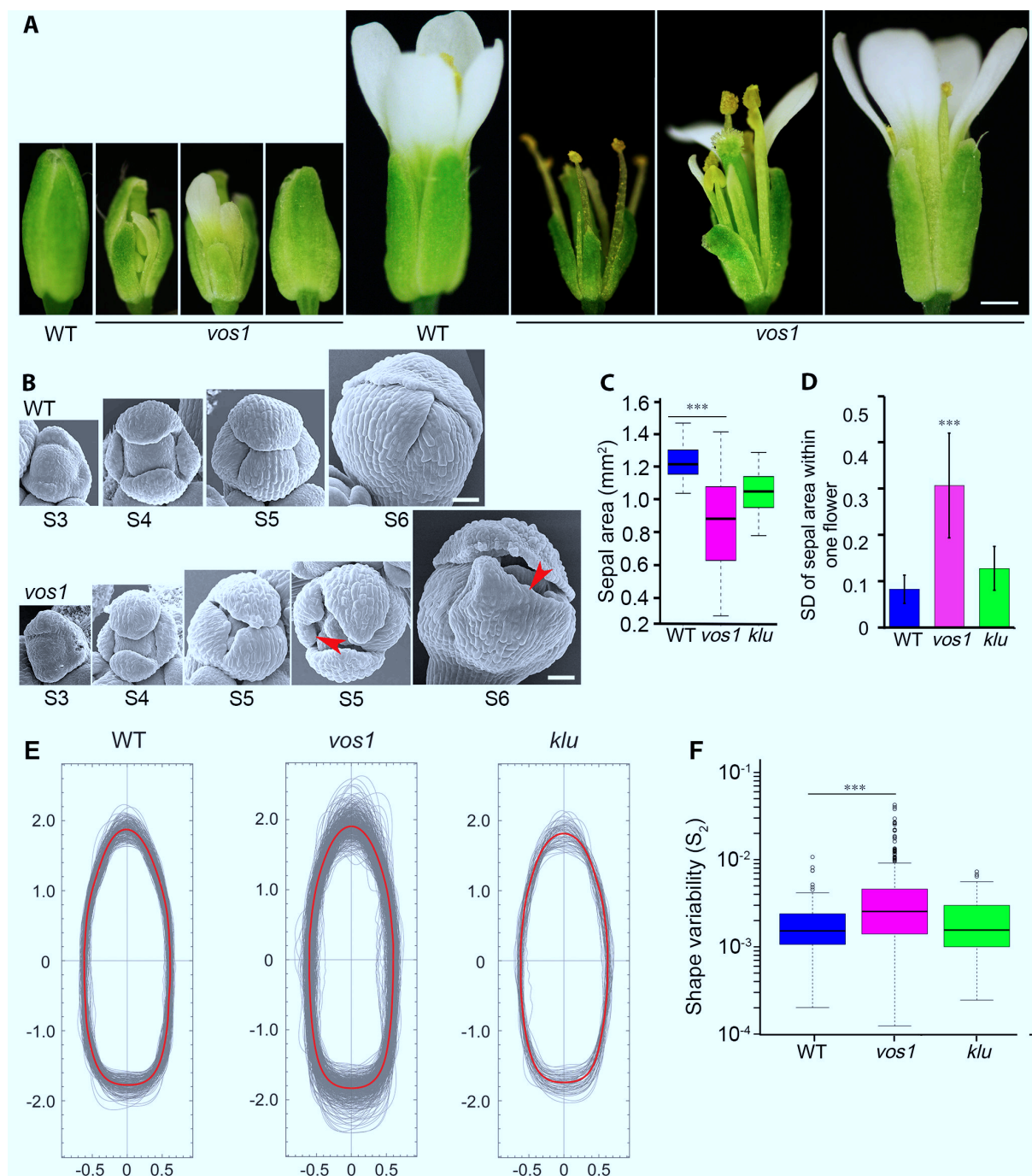


Figure 2.1: *vos1* Mutants Have Increased Variability in Sepal Size and Shape

(A) Wild-type (WT) and *vos1* flowers from single plants (some *vos1* with irregular sepals, some *vos1* with normal) before flower opening at stage 12 (left) and at maturity (stage 14; right).

(B) Scanning electron micrographs show that sepal primordia (stages 3–4 [S3–S4]) form normally in *vos1* mutants. The *vos1* sepal variability phenotype (arrowheads) starts at stage 5 (S5) and intensifies as the flower grows (S6–S7).

(C) Compared with WT, *vos1* has decreased median sepal area (stage 14) and increased variance in area. Not all organ size mutants show increased variability as exemplified by *klu*. * * * $p < 0.001$, significant difference in variance from WT (f test). $n = 68$ for WT and *vos1*, $n = 67$ for *klu*.

(D) Mean SD of sepal area within one flower is increased in *vos1* compared with WT and *klu*. * * * $p < 0.001$, significant difference in mean SD (t test), error bars representing the SD of the mean SD of the sepal area within one flower. $n = 17$ for WT and *vos1*, $n = 14$ for *klu*.

(E) *vos1* mutants have variable organ shape as well as size. Superimposed outlines of mature stage 14 sepals from WT, *vos1*, and *klu* were normalized by size to reveal differences in shape. The variation is the difference between the median outline (red) and that of the individual sepals (gray).

Figure 2.1: (F) Sepal shape variability S2 (squared deviation of sepal outlines): *vos1* has increased sepal shape variance, while *klu* has sepal shape variance similar to that of WT. * * * $p < 0.001$ (t test). $n = 215$ for WT, $n = 518$ for *vos1*, $n = 66$ for *klu* in (E) and (F).

For the boxplots, the box extends from the lower to upper quartile values of the data, with a line at the median, and the whiskers extend past 1.5 of the interquartile range. Scale bars represent $500\ \mu\text{m}$ in (A) and $30\ \mu\text{m}$ in (B). See also Figure 2.8.

The median shape variability S2 for *vos1* (median \pm SE 0.0042 ± 0.0004 , $n = 518$) was significantly increased compared with wild-type (median \pm SE 0.0025 ± 0.0001 , $n = 215$; Figure 2.1F). In *vos1*, defects in organ regularity are also often observed in petals, stamens, carpels, and leaves (Figures 2.1A and 2.1A–2.1C). We focus on the sepal phenotypes, which are representative of the defects seen in other organs.

To confirm that the decreased regularity in *vos1* sepals was not a concomitant effect of decreased sepal area, we analyzed the *kluh* (*klu*) mutant, which has smaller leaves (Anastasiou et al., 2007); *klu* sepals had smaller areas, but the variance in areas was indistinguishable from wild-type (Figures 2.1C, 2.1D, and 2.8D; mean \pm SD $1.05 \pm 0.13\ \text{mm}^2$, $n = 67$). Likewise, shape variability in *klu* sepal was similar to that in wild-type (Figures 2.1E and 2.1F; S2 = 0.0026 ± 0.0003 [median \pm SE], $n = 66$). We also examined a number of mutants known to affect organ size and did not observe any obvious decrease in sepal size uniformity (Figure 2.8E). Therefore, *vos1* mutants disrupt a distinct mechanism maintaining organ regularity, and loss of regularity is not a side effect of decreased organ size.

We next determined when during development the irregularity in *vos1* mutant sepals first occurs. In wild-type flowers, the sepal primordia became visible at stage 3 and grew to completely cover the bud at stage 6 (Figure 2.1B; Smyth (1990)). *vos1* sepals exhibited normal primordia at stages 3 and 4 (Figure 2.1B), indicating that the irregular sepals are not due to a defect in primordium initiation. The loss of sepal uniformity in *vos1* started to become visible at stage 5: some flowers had normal sepals, while others had irregular sepals (arrows in Figure 2.1B). Heterogeneity in shape intensified as *vos1* sepals grew. Gaps appeared between the *vos1* sepals, in contrast to the tightly closed sepals of wild-type flowers from stage 6 onward, suggesting that the *vos1* mutation affects the protective function of the sepals (Figure 2.1B).

2.3.2 Mechanical Modeling Shows that Spatiotemporal Averaging of Cellular Variability Can Produce Organ Regularity

Given previous observations that sepal cells are variable in growth and cell cycle (Roeder et al., 2012, Tauriello et al., 2015), we turned to computational modeling to understand the link between organ robustness and cellular variability and how this link might be disrupted in *vos1* sepals. We built a continuous, tissue-scale, mechanical model of sepal growth (Figure 2.2A and Movie S1; see Experimental Procedures, Section 2.5), as such models are sufficient to investigate how local regulation of growth determines organ shape (Coen et al., 2004, Green et al., 2010,

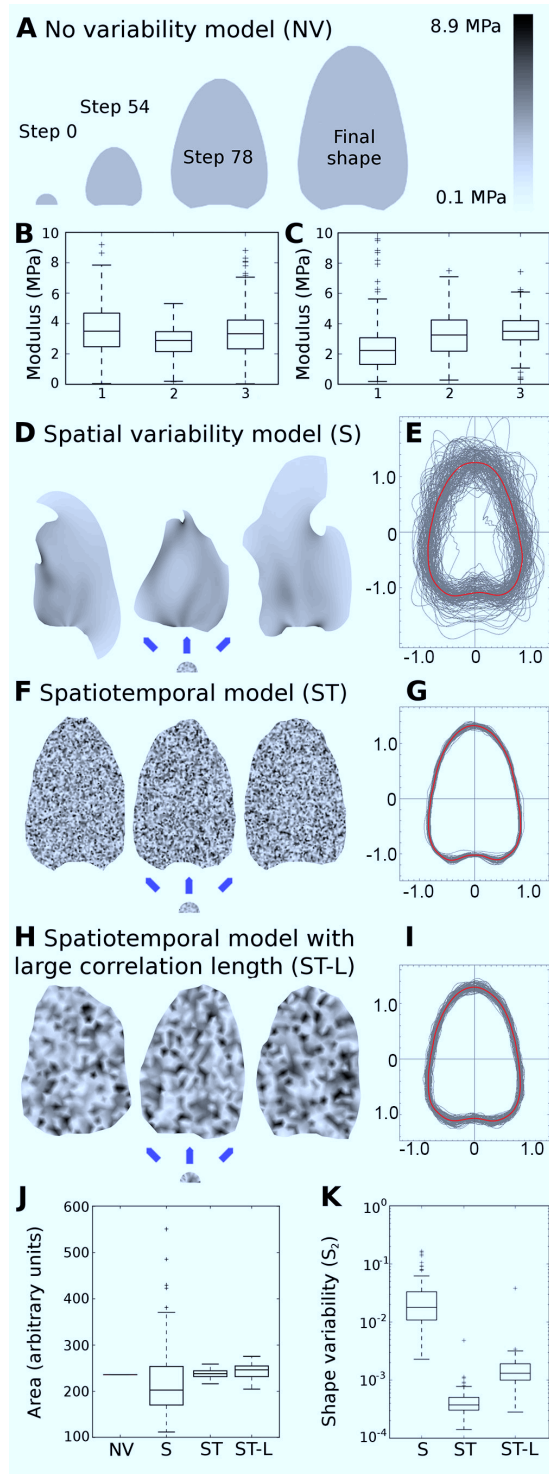


Figure 2.2: A Mechanical Model of Sepal Morphogenesis Predicts that Spatiotemporal Averaging of Local Variability in Growth Generates Robust Organ Shapes

(A) Examples of simulation steps of the model of sepal growth. A continuous, tissue-scale, mechanical model was implemented with transverse anisotropy in stiffness and with no variability of mechanical properties (NV).

(B and C) AFM measurements. Cell-wall mechanical properties are variable in the wild-type sepals (B) and the *vos1* sepals (C).

(D–K) Three models with variability in stiffness. Simulations are initialized from a half-disc-shaped sepal primordium shown below the simulated final states (D, F, H) with a random distribution of elastic moduli deduced from AFM. The modulus is represented by a grayscale heatmap: black is rigid, whereas white is flexible. (D) The spatial variability model (S) results in misshapen sepals. Stiffness persists throughout growth. Thus flexible regions (in light colors) grow protrusively while stiff areas (dark) grow little. Three replicates starting from different stiffness configurations in the primordium are shown. (E) Normalized outlines showing variability in shape for 140 simulations of type S. (F) Robust sepal shape arises from the spatiotemporal variability model (ST). At each time frame, each element selects a new stiffness from the probability distribution. Three replicates are shown. (G) Normalized outlines showing variability in shape for 100 simulations of type ST. (H) Sepal shapes are less robust with decreased local spatial variability (ST-L), i.e., when the correlation length is increased in the model otherwise identical to (F). This model mimics the decrease in local spatial variability (V_{area}) observed in *vos1* mutants (Figures 2.4D–2.4F). (I) Normalized outlines showing variability in shape for 100 simulations of type ST-L. (J) Simulated sepal area (a.u., initial area ~ 1) and (K) shape (S_2) variability with no variability (NV), spatial variability (S), spatiotemporal variability (ST), or spatiotemporal variability with a long correlation length (ST-L). Spatial variability alone leads to lack of robustness in final shape, while spatiotemporal variability yields more precise size (J) and shape (K). Longer correlation length leads to more variable sepals in size (J) and shape (K). The statistics are obtained over 100 replicates (simulation runs).

For the boxplots, the box extends from the lower to upper quartile values of the data, with a line at the median, and the whiskers extend past 1.5 of the interquartile range. See also Figure S2 and Movies S1, S2, S3, S4, and S5.

Hervieux et al., 2016, Kennaway et al., 2011, Kuchen et al., 2012, Sauret-Güeto et al., 2013). We created a two-dimensional model because epidermal cells largely control the rate of growth in plant organs (Kutschera and Niklas, 2007, Savaldi-Goldstein et al., 2007). In our mechanical model, we input variability in stiffness to mimic cellular heterogeneity of

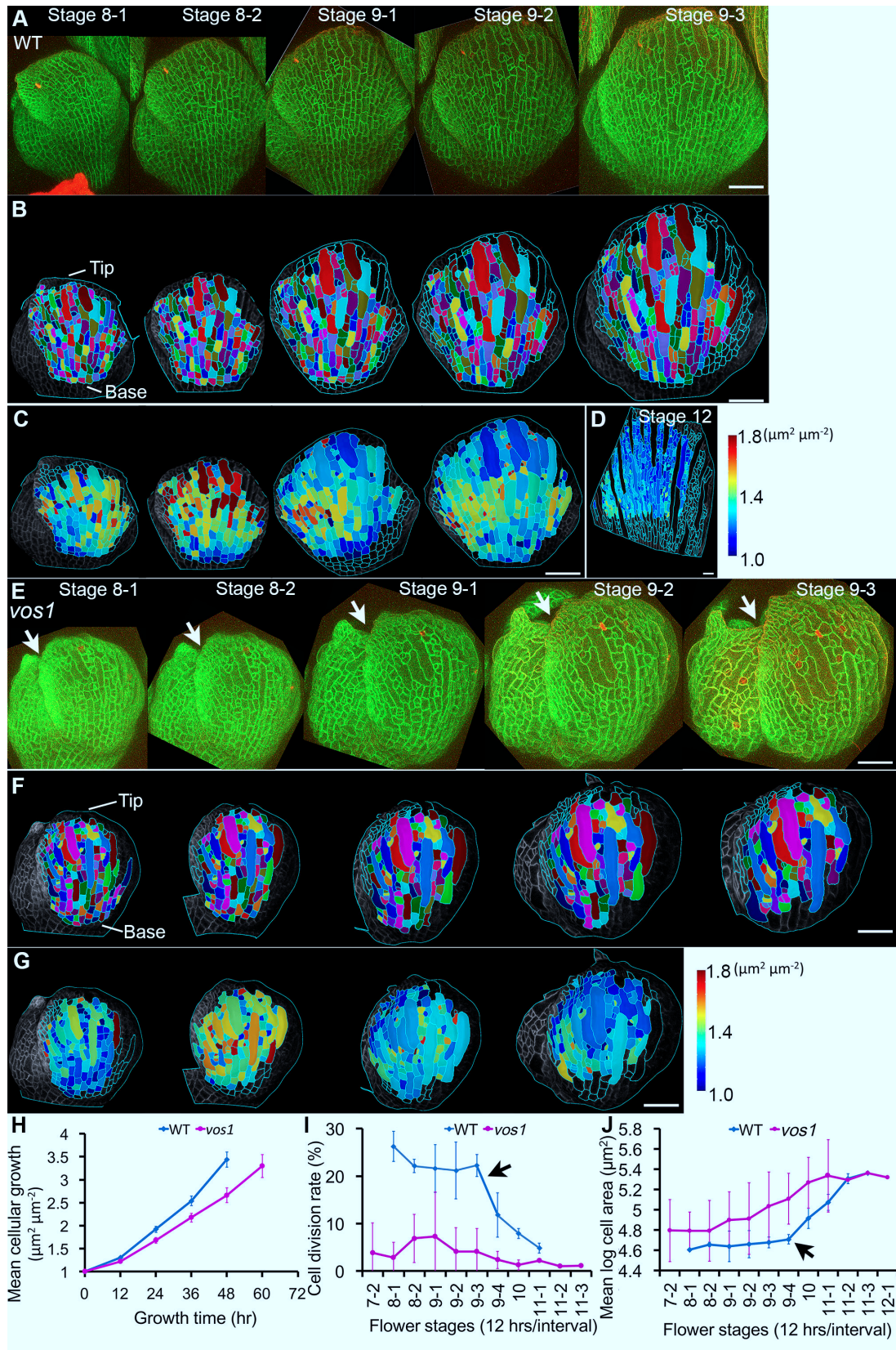


Figure 2.3: *vos1* Sepals Mature Earlier Than Wild-Type

Figure 2.3: (A and E) Confocal stack maximum-intensity projection images of wild-type (WT) (A) and *vos1* (E) flowers in which the epidermal cells are marked with a plasma membrane marker (green; ATML1::mCitrine-RCI2A). Arrows indicate the gaps between sepals that emerge in the mutant due to variability in sepal sizes. Flowers are staged based on their width. Each substage lasts for 12 hrs.

(B and F) WT (B) and *vos1* (F) sepals from images (A) and (E) are segmented into cells, and lineages are tracked with MorphoGraphX. Cells derived from the same mother cell at the starting time point are marked with the same color labels.

(C and G) Heatmap of the cellular areal growth rate in WT (C) and *vos1* (G) sepals. The growth rate is calculated as the ratio of the cell area at the later time point to the cell area at the earlier time point (displayed on the earlier time point).

(D) Heatmap of the cellular areal growth rate in a WT sepal at stage 12, which shows much lower growth rate compared with WT sepals at earlier stages.

(H) Average growth of cell areas calculated as the ratio with the cellular area at the starting time point. Each data point is mean \pm SD. Total $n = 705$ for WT and $n = 472$ for *vos1*.

(I) Cell division rate represented by the percentage of cells that divide in the corresponding growth interval. Initially WT cell division rates are high, but decrease when the sepal matures (arrow), while *vos1* mutant division rates remain low.

(J) Average logarithmic areas of cells for developing sepals. Note that in WT, the average log area stays constant until the maturation phase when the average log area increases (arrow), while average log area increases throughout the mutant growth. $n = 5$ biological repeats for each genotype in (I) and (J), mean \pm SD.

Scale bars, 50 μ m. See also Figure 2.10.

the tissue. To assign parameters, we measured the stiffness of wild-type sepal epidermal cells with atomic force microscopy (AFM) and found significant spatial variability in stiffness (Figures 2.2B, 2.2C, 2.9A, and 2.9B). In the model, organ growth ceased after the size reached a threshold (see Experimental Procedures, Section 2.5). We first made a model with high spatial variability in stiffness of the sepal primordium based on our AFM data (“spatial variability model,” S). Because in the model stiffness determined growth rate, softer regions grew more and stiffer regions grew less. All simulation runs produced misshapen organs, and size and shape were highly variable between the runs (Figures 2.2D and 2.2E; Movie S2). This suggested that some mechanism must mitigate spatial variability of individual cells for regularly sized organs to be possible.

In our next model, we maintained the spatial variability in stiffness, but allowed each region to randomly change stiffness in time (“spatiotemporal variability model,” ST). In each time frame of the model, stiffness was randomly selected from the same distribution as in the first model. As the stiffness varied in space and time, the simulation produced correspondingly variable growth rates (Figures 2.9D and 2.9E); however, the spatiotemporal variability model generated sepals with regular sizes and shapes over all simulation runs (Figures 2.2F, 2.2G, 2.2J, and 2.2K; Movie S3). In essence, the temporal variability allowed the differences in stiffness to average in time; a high stiffness at one time was effectively counterbalanced by a low stiffness earlier or later in growth such that the sepal grew more like a model with uniform stiffness (“non-variable model,” NV; Figures 2.2A and 2.2J; Movie S1). Likewise, a stiff spot next to a softer spot can somewhat counterbalance each other in growth. We call this combined phenomenon spatiotemporal averaging. We also explored models with intermediate levels of temporal variability and found that a relatively low temporal variability is sufficient to yield robust shapes (Figures 2.9C and 2.9G; Movie S4). Thus, although these initial models represent extreme cases (neither wild-

type nor mutant), they demonstrate the fundamental principle that adding temporal variability over spatial variability produces regular organs through spatiotemporal averaging.

2.3.3 Reduced Local Spatial Variability in the Cell Growth of *vos1* Sepals Underlies Irregular Sepal Shape

Next, we tested whether defects in spatiotemporal averaging could explain the reduced regularity of *vos1* sepal shapes. To do so, we analyzed cell growth variability through live imaging of wild-type and *vos1* sepals (Cunha et al., 2012, Roeder et al., 2010). The same flower was imaged every 12 hrs (Figures 2.3A and 2.3E; arrows indicate gaps). We focused our analysis on the epidermis because epidermal cells largely control the rate of organ growth in plants (Kutschera and Niklas, 2007, Savaldi-Goldstein et al., 2007). MorphoGraphX software (Barbier de Reuille et al., 2015) was used to calculate growth rates and cell division rates (Figures 2.3B, 2.3F, and 2.10A–2.10D; $n = 405$ cell lineages in wild-type sepals and 524 cell lineages in *vos1* mutant sepals; see Experimental Procedures, Section 2.5). The sepal matures from tip to base (Hervieux et al., 2016, Roeder et al., 2010). Initially, the tip of the wild-type sepal had a high growth rate, then cell growth and cell division progressively slowed from the tip downward (Figures 2.3C and 2.10E). *vos1* mutant sepals also exhibited slower growth descending from tip to base as in wild-type (Figure 2.3G); however, growth rates decreased in *vos1* mutants more quickly than in wild-type (see below).

For spatiotemporal averaging to occur, growth of wild-type sepal cells should be variable in both time and space. We quantified the temporal variability in growth by calculating the change in a cell’s growth (in area) between two consecutive 12-hr time intervals (D_{area} ; Figures 2.4A and 2.4C; see Experimental Procedures, Section 2.5). We quantified the local spatial variability in growth (in area) by calculating the differences in growth rates among neighboring cells (V_{area} ; Figures 2.4D and 2.4F). For wild-type cells, the growth rate was highly variable in both space and time during stages 8–9 of sepal development (Figures 2.4A, 2.4C, 2.4D, and 2.4F). Thus, wild-type sepal cells exhibit both spatial and temporal variability in growth.

In contrast, local spatial growth variability (V_{area}) was substantially decreased in *vos1* mutants. The growth rate of each cell was more similar to its neighbors in *vos1* than in wild-type ($V_{area} = 5.32\%$ for *vos1* versus 7.69% in wild-type, $p < 10^{-6}$ [permutation test]; see Experimental Procedures, Section 2.5; Figures 2.4E and 2.4F). Temporal variability in growth (D_{area}) of *vos1* cells partially overlapped with wild-type ($D_{area} = 6.94\%$ for *vos1* versus 8.37% for wildtype, $p < 10^{-6}$ [permutation test]; Figures 2.4B and 2.4C), suggesting that temporal variability in cell areal growth was only slightly altered in the *vos1* mutant. Therefore, contrary to our initial model, the *vos1* mutant sepal cells exhibit much less spatial variability and similar temporal variability in growth.

To understand the mechanistic basis for reduced spatial variability in *vos1*, we examined the local spatial variability in cell-wall stiffness of epidermal cells using AFM. In both wildtype and *vos1* sepals we observed subcellular variability in stiffness (Figure 2.4G). We quantified local

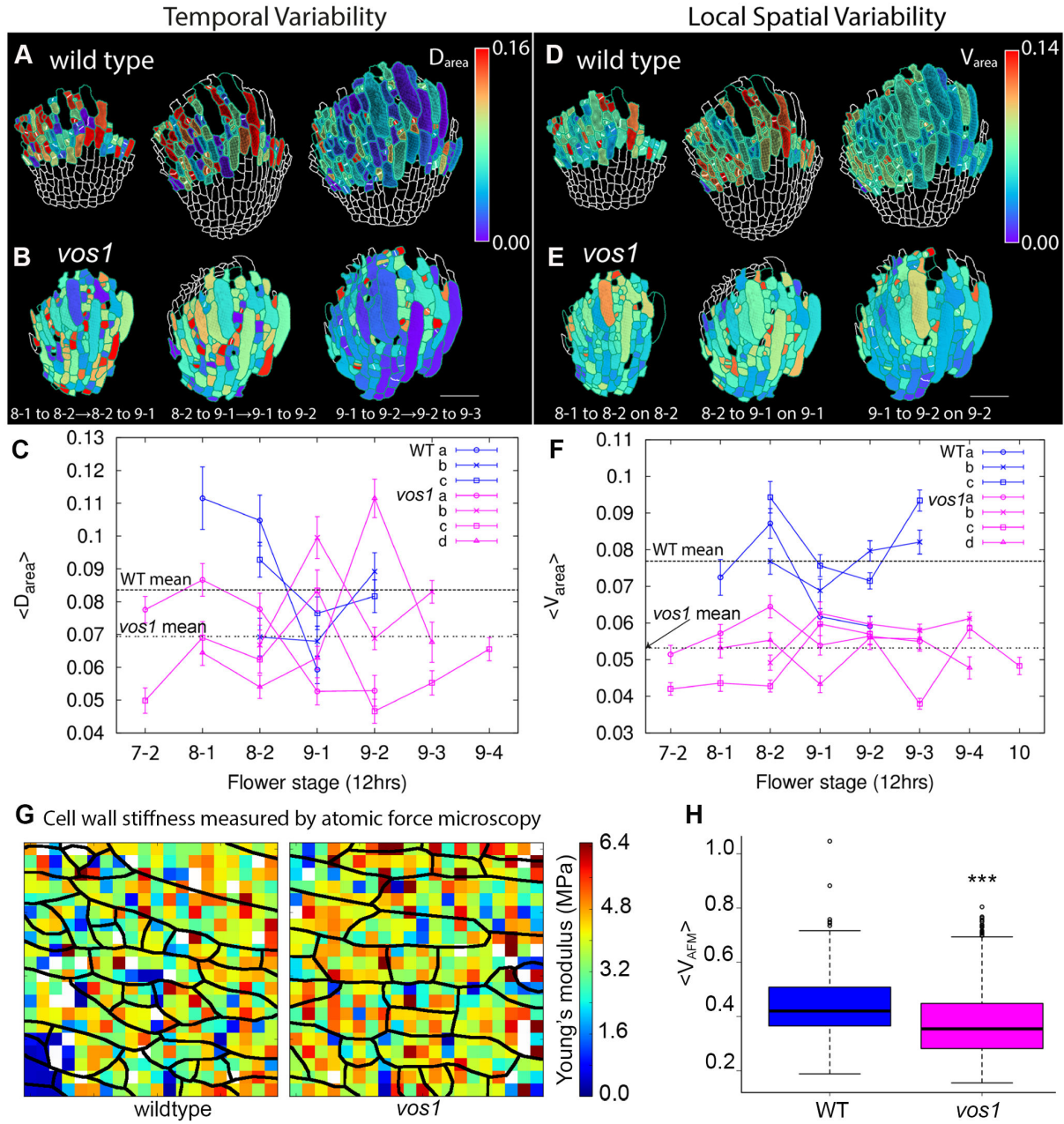


Figure 2.4: Spatial Variability of Cell Growth Rates in Area Is Decreased in *vos1*

(A–C) Temporal variation of the cell growth rate (D_{area} ; heatmap with high variability in red and low variability in blue) is similar in wild-type (WT) and *vos1* sepals. Equivalent cells (defined by the proximity of differentiated stomata) outlined in green are analyzed for WT (A) and *vos1* (B) flowers at stages 8 and 9. Additional nonequivalent WT cells at the base of the sepal are outlined in white. Consecutive 12-hr growth intervals are analyzed; for example, 8-1 to 8-2 → 8-2 to 9-1 means that the growth rate during the 12-hr interval from stage 8-1 to 8-2 is compared with growth rate during the 12-hr interval from stage 8-2 to stage 9-1.

(C) Graph plotting the average temporal variability of the growth rates ($\langle D_{area} \rangle$ signifies the average of D_{area} over cells) in each sepal epidermis at each time point. Three WT flowers (a–c, blue) and four *vos1* mutant flowers (a–d, magenta) are shown. Dotted black lines indicate the average temporal variability for all cells at all time points (WT 8.37%; *vos1* 6.94%). The WT and mutant data partially overlap and only slight differences of temporal variability ($\langle D_{area} \rangle$) are detected ($p < 10^{-6}$, permutation test). The error bars represent the SE. Scale bar represents 50 μm .

Figure 2.4: (D–F) Local spatial variation in the cell growth rate (V_{area} ; heatmap with high variability in red and low variability in blue) is decreased in *vos1* sepals. Flowers are the same as in (A)–(C). The 12-hr interval analyzed is specified by stages. For example, 8-1 to 8-2 on 8-2 is the 12-hr interval from stage 8-1 to stage 8-2 displayed on the sepal cells at stage 8-2.

(F) Graph plotting the average spatial variability in growth rate among neighboring cells ($\langle V_{area} \rangle$ signifies the average of V_{area} over cells) for all the cells of each sepal at each floral stage imaged. Dotted black lines indicate the average spatial variability for all cells at all time points (WT 7.69%; *vos1* 5.32%). Note that *vos1* flowers tend to have decreased spatial variability (lower $\langle V_{area} \rangle$; $p < 10^{-6}$, permutation test). The error bars represent the SE. Scale bar represents 50 μm .

(G and H) Local spatial variation in the cell-wall stiffness is decreased in *vos1* sepals. (G) Cell-wall stiffness of WT and *vos1* sepals at stage 10 measured by AFM is displayed as a heatmap with stiff points in red and soft points in blue. Cells are outlined in black based on topology maps. Each square represents one measurement point, which is 5 μm from the next measurement. (H) Graph plotting the average spatial variability in cell-wall stiffness ($\langle V_{AFM} \rangle$) for WT and *vos1* sepals. Note that *vos1* sepals have decreased spatial variability in cell-wall stiffness (lower V_{AFM}) compared with WT.

*** $p < 0.001$ (t test). $n = 8$ for WT and $n = 9$ for *vos1*.

For the boxplots, the box extends from the lower to upper quartile values of the data, with a line at the median, and the whiskers extend past 1.5 of the interquartile range. See also Figure 2.11.

stiffness variability (V_{AFM}) in a 35-by-35- μm square, by analogy with the calculation of V_{area} (see Experimental Procedures, Section 2.5). Compared with wild-type, *vos1* had a substantial decrease in local spatial variability of stiffness ($V_{AFM} = 37.3\%$ for *vos1* versus 43.7% for wild-type, $p < 10^{-15}$ [t test]; Figure 2.4H). This result is consistent with the decreased local spatial variability in growth rates observed in *vos1*.

Our model prediction that reducing temporal variability produces irregular sepals does not explain our observations in *vos1*. Instead, the growth and AFM analysis in *vos1* suggest that the lower level of spatial variability inhibits sepal shape robustness, which we tested in our next model. Reducing local spatial variability means that neighboring cells are more correlated. Therefore, in the model we increased the correlation length of stiffness (the distance over which the stiffness is similar). We maintained temporal variation as in the spatiotemporal variability model. The simulated sepals from this “spatiotemporal variability model with low spatial variability” (ST-L) were less regular in shape than the simulated sepals produced by the ST model (Figures 2.2H–2.2K and Movie S5). They were also somewhat more variable in size than those produced by the initial spatiotemporal variability model (Figure 2.2J). Although the ST-L model increases size variability, it does not reproduce the extent of sepal size variation or the smaller average size of *vos1* sepals compared with wild-type. Thus, size and shape regularity can be partly uncoupled. An additional mechanism must contribute to sepal size variability in *vos1*, which we discuss below. To conclude, our revised model confirms that decreased local spatial variability can lead to irregularity of sepal shape. Thus, counterintuitively, we find that the higher level of local spatial variability found in wild-type sepals actually promotes sepal shape robustness.

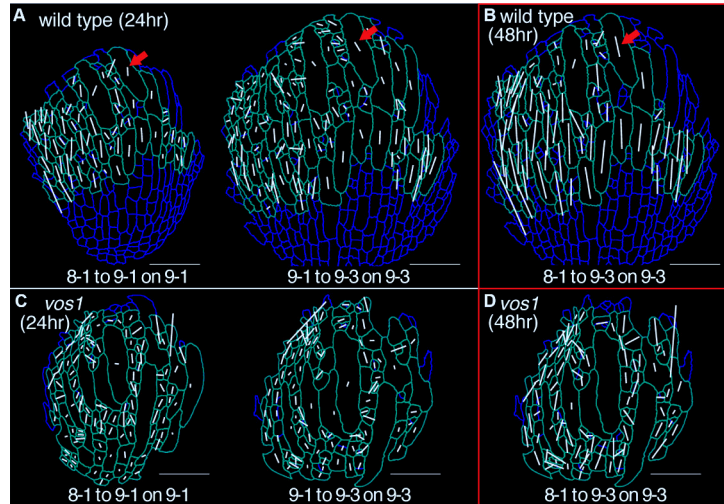


Figure 2.5: High Local Spatial Variability of Cellular Growth Promotes Organ Regularity

(A and C) The principal direction of growth in the maximal growth direction (PDG_{max} ; white line) of the wild-type (A) and *vos1* (C) sepal cells calculated for each 24-hr interval show spatial and temporal variations (e.g., red arrows). Equivalent cells outlined in green are analyzed for wild-type and *vos1*. Only cells in which the growth is anisotropic are considered (maximum growth minus minimum growth >10%); PDG_{max} is not shown for cells growing isotropically where the direction is not well defined.

(B and D) PDG_{max} of wild-type cells calculated for the cumulative growth from 0 to 48 hrs (B) become much more coordinated across the sepal (e.g. red arrow), indicating that the plant is temporally averaging the variations seen at 24 hrs in (A). In contrast, the *vos1* sepal cells (D) show less temporal averaging of variability than wild-type, as the PDG_{max} for the cumulative 48-hrs growth are not aligned.

See also Figure 2.12.

2.3.4 Wild-Type Sepals Undergo Spatiotemporal Averaging of the Principal Direction of Growth, Resulting in Regularity, which Is Disrupted in *vos1* Mutants

To further explore how spatiotemporal averaging produces regular sepal shapes from variable cellular growth, we examined the principal directions of growth (PDGs) (Dumais and Kwiatkowska, 2002). Here we show only the vector in the direction maximal of growth, PDG_{max} . Cells growing isotropically (nearly equally in all directions) were excluded from analysis because in this case the PDGs become arbitrary. The PDG_{max} provide a visual indication of the coordination of growth directions between nearby cells and their overall alignment with the growth of the organ. In wild-type sepals, the PDG_{max} of cells during short 24-hr growth intervals showed varied orientations (Figure 2.5A) in space and in time (Figure 2.5A, arrows), consistent with the spatial variability in cellular growth. We tested whether spatiotemporal variability averages to produce regular growth by examining PDGs calculated for longer time intervals. Over intervals of 48 hrs, we found that the PDG_{max} were highly aligned in the tip base axis of the sepal (Figure 2.5B, arrow), indicating that the spatial and temporal variability averages lead to regularity of plant growth. In the *vos1* mutant sepal cells, the PDG_{max} were also spatially and temporally variable over 24-hr intervals; however, the PDG_{max} of *vos1* mutant cells calculated for the cumulative

growth over 48 hrs were not well aligned with each other, indicating that *vos1* mutants are defective in the spatiotemporal averaging of growth direction (Figures 2.5C and 2.5D). Averaging was still defective over longer time intervals in *vos1* (Figure 2.12A). The reduced spatiotemporal averaging of variability in growth direction might explain the irregular shape of mutant sepals.

2.3.5 *vos1* Is a Mutant of the FtsH4 Mitochondrial Protease

Genetic analysis and map-based cloning revealed that the *vos1* phenotype is caused by recessive mutations in the FtsH4 gene (Figures 2.6A and 2.13A). Hence, we renamed the *vos1* mutant *ftsh4-5*; the *ftsh4-5* mutation causes a premature stop codon in the FtsH4 protein. *FtsH4* encodes an AAA-ATPase metalloprotease in the FtsH family ((Janska et al., 2010, Sakamoto et al., 2003, Urantowka et al., 2005) FtsH proteases play key roles in quality control of membrane proteins in prokaryotic organisms and organelles of bacterial origin (i.e., mitochondria and chloroplasts) by eliminating abnormal membrane proteins and by promoting assembly of oxidative phosphorylation complexes (Ito and Akiyama, 2005). There are four FtsH proteases in *Arabidopsis* mitochondria: FtsH3, FtsH4, FtsH10, and FtsH11. Based on their topology in the membrane, FtsH4 and FtsH11 are classified as i-AAA proteases, which face the intermembrane space (Figure 2.13B), unlike matrix-facing m-AAA proteases FtsH3 and FtsH10 (Heazlewood et al., 2004, Sakamoto et al., 2003, Urantowka et al., 2005). Although phylogenetically related, FtsH4 and FtsH11 are functionally divergent, with their mutations affecting different aspects of plant growth (Gibala et al., 2009, Wagner et al., 2011, Zhang et al., 2014). They form independent homo-oligomeric i-AAA protease complexes in mitochondria, and FtsH11 is localized in both mitochondria and chloroplasts (Urantowka et al., 2005). FtsH4 is the only i-AAA protease required for the proper assembly and stability of oxidative phosphorylation complexes in *Arabidopsis* mitochondria (Kolodziejczak et al., 2007). Because the premature stop codon in *ftsh4-5* leads to the deletion of both the AAA-ATPase domain and the metalloprotease domain of FtsH4, *ftsh4-5* is likely to be a null mutant. Notably, from our screen, we isolated six *ftsh4* mutants. Although these had different mutations in FtsH4, all the alleles had variable sepal size phenotypes similar to that of *ftsh4-5* (Figures 2.6A and 2.13A).

FtsH4 homologs are highly conserved in *Escherichia coli*, yeast, humans, and *Arabidopsis* (Figure 2.13A). We rescued the variable sepal size phenotype of *ftsh4-5* mutants by transgenically expressing YME1, the yeast homolog of FtsH4; this demonstrated that the biochemical function of FtsH4 is conserved between eukaryotic kingdoms (Figures 2.6F and 2.6G).

2.3.6 The Increased Irregularity in *ftsh4* Sepals Is Caused by Increased ROS Levels

Building on the well-established role of FtsH4 homologs at the molecular and organelle levels, we focused our analysis on the cell and organ levels. Mutations in *FtsH4* have previously been shown to cause mitochondrial defects, including reduced cristae in mitochondria (Gibala et al., 2009). Mitochondrial defects can lead to increased levels of ROS (Pulliam et al., 2013). In

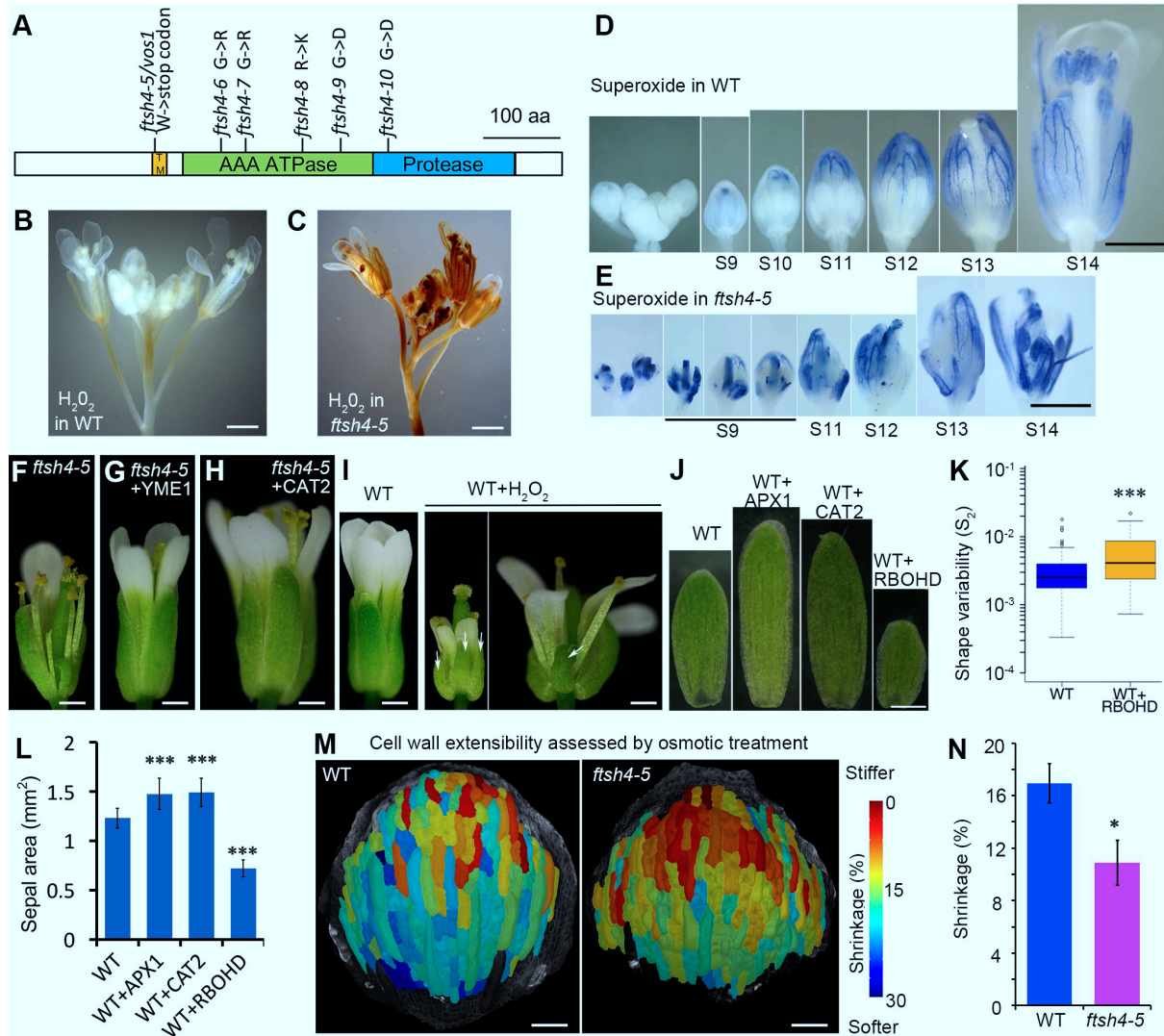


Figure 2.6: Reactive Oxygen Species Regulates Sepal Growth

(A) The protein domains of FtsH4 and the mutation sites of *ftsh4* alleles isolated in our study. The AAA-ATPase domain is shown in green, the protease domain in blue, and the transmembrane (TM) domain in orange.

(B and C) DAB staining for H_2O_2 in WT (B) and *ftsh4-5* (C) inflorescences. *ftsh4-5* mutants have a higher level of H_2O_2 throughout the inflorescences.

(D and E) NBT staining for superoxide in WT (D) and *ftsh4-5* (E) flowers. *ftsh4-5* has higher and more variable level of superoxide in the sepals. S9–S14: flowers at different stages.

(F and G) Expression of the yeast homolog gene of FtsH4 (YME1) in Arabidopsis *ftsh4-5* mutants (F) rescues the variable sepal size phenotype (G). (H) Overexpression of a catalase gene (CAT2), which catalyzes the decomposition of H_2O_2 , in *ftsh4-5* rescues the irregular sepal size and shape phenotype.

(I) Wild-type (WT) flowers treated with 100mM H_2O_2 (WT + H_2O_2) mimics *ftsh4* phenotype, generating sepals of variable sizes. The control WT was mock treated. Arrows show smaller sepals.

(J) WT flowers overexpressing a peroxidase gene (WT + APX1) or CAT2 (WT + CAT2), which both decrease H_2O_2 , have larger mature sepals. WT flowers overexpressing a NADPH oxidase gene (WT + RBOHD), which produce superoxide, have smaller mature sepals, as plotted in (L).

(K) WT + RBOHD flowers have larger variability in mature sepal (stage 14) shape S_2 . WT data were reproduced from Figure 2.1D for comparison. *** $p < 0.001$, significant difference from WT (t test).

Figure 2.6: (L) Area of sepals in (J) confirming that decreasing ROS (WT + APX1 and WT + CAT2) increases sepal size while increasing ROS (WT + RBOHD) decreases sepal size. *** $p < 0.001$, significant difference from WT (t test). Data are mean \pm SD. $n = 68$ for WT, $n = 108$ for WT + APX1, $n = 145$ for WT + CAT2, $n = 69$ for WT + RBOHD.

(M and N) Cell walls are stiffer (had a lower percent shrinkage in osmotic treatments) in *ftsh4-5* sepals than in WT at stages 8–9. In the heatmap, the cells in red have low shrinkage and are stiffer than cells in blue with high shrinkage. (N) Plots of area shrinkage for the whole sepal. * $p < 0.1$, significant difference from WT (t test). Data are mean \pm SD. $n = 3$ for WT and *ftsh4-5*.

For the boxplots, the box extends from the lower to upper quartile values of the data, with a line at the median, and the whiskers extend past 1.5 of the interquartile range. Scale bars represent 1 mm in (B)–(E), 500 μm in (F)–(J), and 50 μm in (M). See also Figures 2.13 and 2.14.

addition, studies of chloroplast FtsH protease mutants have shown that high ROS accumulation is a major cause of morphological defects in leaves (Kato et al., 2009). Thus, we compared ROS levels between wild-type and mutant sepals. ROS include many molecules, with hydrogen peroxide (H_2O_2) and the superoxide radical (O_2^-) as the two major ones (Apel and Hirt, 2004). Using chemical stains specific for these two molecules, we found that *ftsh4-5* mutants have higher levels of both H_2O_2 and O_2^- in their sepals (Figures 2.6B–2.6E).

Remarkably, O_2^- formed a gradient in wild-type sepals that paralleled the wave of cellular maturation from the tip to the base of sepals (Figure 2.6D). High levels of O_2^- were first detectable in the sepal tip of flowers at stage 10, and progressed downward as the sepal grew, finally spreading to the whole sepal when it matured (stage 13; Figure 2.6D). In *ftsh4-5* sepals, O_2^- levels were higher and more variable. High levels of O_2^- were present in very young buds, and were unevenly distributed between different parts of a single sepal and between different sepals within the same flower (Figure 2.6E).

We next tested whether premature and uneven ROS were sufficient to disrupt sepal size uniformity. Wild-type flowers treated with H_2O_2 from early stages mimicked the *ftsh4* phenotype, generating variably sized sepals that were smaller on average (Figure 2.6I). We then decreased ROS levels in *ftsh4-5* by overexpressing *CATALASE 2* (*CAT2*). *CAT2* encodes a peroxideme-tabolizing enzyme with high specificity for H_2O_2 (Mhamdi et al., 2010, Mittler et al., 2004). The transgene restored sepal size uniformity in the *ftsh4* mutant (Figures 2.6F and 2.6H), and transgenic flowers had lower ROS levels (Figure 2.13D). These results indicate that increased ROS levels cause the increased variability and decreased average size of *ftsh4* sepals.

2.3.7 ROS Act as a Growth Regulator in Wild-Type Sepals, Promoting Maturation and Termination of Growth

The pattern of O_2^- accumulation from the tip to the base of the wild-type sepal, coincident with the progressive maturation of the sepal from tip to base (Hervieux et al., 2016, Roeder et al., 2010), raised the question of whether O_2^- acts as an endogenous growth regulator controlling the termination of sepal growth. To test this, we decreased ROS levels in wild-type sepals by

overexpressing either the catalase-encoding gene *CAT2* or the *ASCORBATE PEROXIDASE 1* (*APX1*) gene, which encodes another enzyme that scavenges H_2O_2 in *Arabidopsis* (Davletova et al., 2005, Ishikawa and Shigeoka, 2008, Mittler et al., 2004). Both kinds of transgenic plants had larger sepals than wild-type: 1.20 ± 0.13 -fold for *APX1* (mean \pm SD, $n = 108$) and 1.21 ± 0.12 -fold for *CAT2* (mean \pm SD, $n = 145$; Figures 2.6J and 2.6L). Overexpression of *CAT2* did not abolish the tip-to-base accumulation of O_2^- , but delayed it, consistently with the larger sepal sizes observed (Figure 2.13G). This demonstrated that decreasing the ROS level could promote sepal growth, and suggested that ROS act as endogenous signals to limit wild-type sepal growth. ROS may be general signals promoting a shift from cell division to maturation, as leaves had a similar pattern of O_2^- accumulation from tip to base correlating with the cessation of cell division, and overexpression of *CAT2* produced larger leaves (Figures 2.13C and 2.13E).

2.3.8 *ftsh4* Sepals Exhibit Cellular Characteristics of Maturation Earlier than Wild-Type

To further test whether ROS act as maturation signals, we reexamined the growth of *ftsh4* flowers to determine whether their early increase in ROS correlated with early cellular maturation. Based on wild-type, we defined the region of maturing cells as those with slower growth rates and low cell division which we observed developing from tip to base (Figures 2.3C and 2.10E) (Hervieux et al., 2016, Roeder et al., 2010). Growth rates decreased in *ftsh4* mutants more quickly than in wild-type; growth rates of cells in mutant sepals at stage 9 appeared more similar to maturing cells of wild-type sepals at stage 12 (Figures 2.3D and 2.3G). The average of cellular growth rates over 12 hrs was lower in *ftsh4-5* (mean \pm SD 1.28 ± 0.19 , $n = 472$) than wild-type (mean \pm SD 1.37 ± 0.22 , $n = 705$) (Figure 2.3H). Accordingly, while wild-type cell lineages grew 3.43-fold larger on average in 48 hrs, *ftsh4* mutant cell lineages required 60 hrs to grow 3.3- fold (Figure 2.3H).

Maturation coincided with a shift from rapid cell division to slow cell division in wild-type sepals (Figures 2.3I and 2.10E). In *ftsh4* mutant sepals, the cell division rate remained low, throughout stages 7–11 (Figures 2.3I and 2.10E). Initially cell division and growth were balanced in wild-type sepals, yielding a constant average logarithm of cell area (Figures 2.3J and 2.10G). As cell division decreased, maturation coincided with a general increase in the average logarithm of cell area (Figure 2.3J). In *ftsh4* mutant sepals, the average logarithm of cell area began increasing at an unusually early stage of development (Figures 2.3J and 2.10H). Mature *ftsh4* sepals contained substantially fewer epidermal cells that were larger on average than wild-type sepal cells (Figures 2.10I and 2.10J), consistent with reduced cell division and early entry into cell expansion observed in the developing mutant sepals. In summary, *ftsh4* sepal cells behave like wild-type sepal cells of a later developmental stage, suggesting that *ftsh4* sepals begin maturation too early and that ROS promote cellular maturation in sepals.

2.3.9 *ftsh4* Sepals Are Stiffer Than Wild-Type

One possible mechanism through which ROS may directly slow growth and reduce cellular growth variability is by modifying cell-wall mechanical properties (Barceló and Laura, 2009, Cosgrove, 2005, Lu et al., 2014). ROS may promote cell-wall stiffening by facilitating the formation of crosslinks between wall polysaccharides and glycoproteins (Fry, 2004, Ralph et al., 2004); alternatively, ROS may also loosen the cell wall by cleaving wall polysaccharides (Fry, 1998, Schopfer, 2001, Schweikert et al., 2000). As AFM allowed us to probe only small regions in the center of the sepal, we did not detect any difference in average stiffness between wild-type and *ftsh4* cell walls (Figure 2.4G). We therefore used osmotic treatments to assess the stiffness of the whole sepal (Kierzkowski et al., 2012). Wild-type sepals had a gradient with stiffer cells at the tip (Figures 2.6M and 2.12D), which matched the decreased growth rates of similarly staged sepal tips (compare with Figure 2.3C). Likewise, *ftsh4* flowers showed a gradient with stiffer cells at the tip; however, whole *ftsh4* sepals were stiffer than wild-type sepals (wild-type $17\% \pm 2.6\%$ shrinkage; *ftsh4* $11\% \pm 1.7\%$ shrinkage; mean \pm SD, $n = 3$ sepals of each genotype; Figures 2.6M, 2.6N, and 2.12D). These results are consistent with a scenario in which ROS limit growth in sepals by increasing the number of crosslinks in cell walls.

2.3.10 Reduced Cellular Variability and Spatiotemporal Averaging Correlate with ROS Accumulation in Maturing Wild-Type Sepal Tips

If ROS signals in wild-type sepals promote maturation, and the *ftsh4* phenotype is generated by an overabundance of ROS signal (essentially a gain of function), then we would expect to observe inhibition of spatiotemporal averaging of growth in the tips of wild-type sepals as the ROS signal initiates there. As expected, the maturing tips of wild-type sepals exhibited reduced local spatial variability in growth (Figure 2.11D) and reduced spatiotemporal averaging of PDGs (Figures 2.12B and 2.12C) but no change in temporal variability of growth (Figures 2.11A and 2.11B), compared with the middle of the sepal, where ROS had not yet accumulated. These results are consistent with ROS inhibiting cellular variability and spatiotemporal averaging during wild-type sepal maturation.

2.3.11 Spatiotemporal Averaging Combined with a Maturation Gradient Regulated by ROS Produce Sepal Regularity

Based on our observation that O_2^- accumulates and growth slows from the sepal tip downward (Figures 2.3C and 2.6D), we postulated that ROS act as signals that terminate sepal growth. Therefore, we created an “arrest front” (AF) model, in which we initiate a ROS signal at the tip when the sepal reaches a defined height, with variability in the initiation height (see Experimental Procedures, Section 2.5). The signal propagates down the developing sepal and growth stops when the signal reaches the base (Figure 2.7A). This AF model was initially implemented in the NV model template to examine the effects of variability in arrest front alone. AF models with

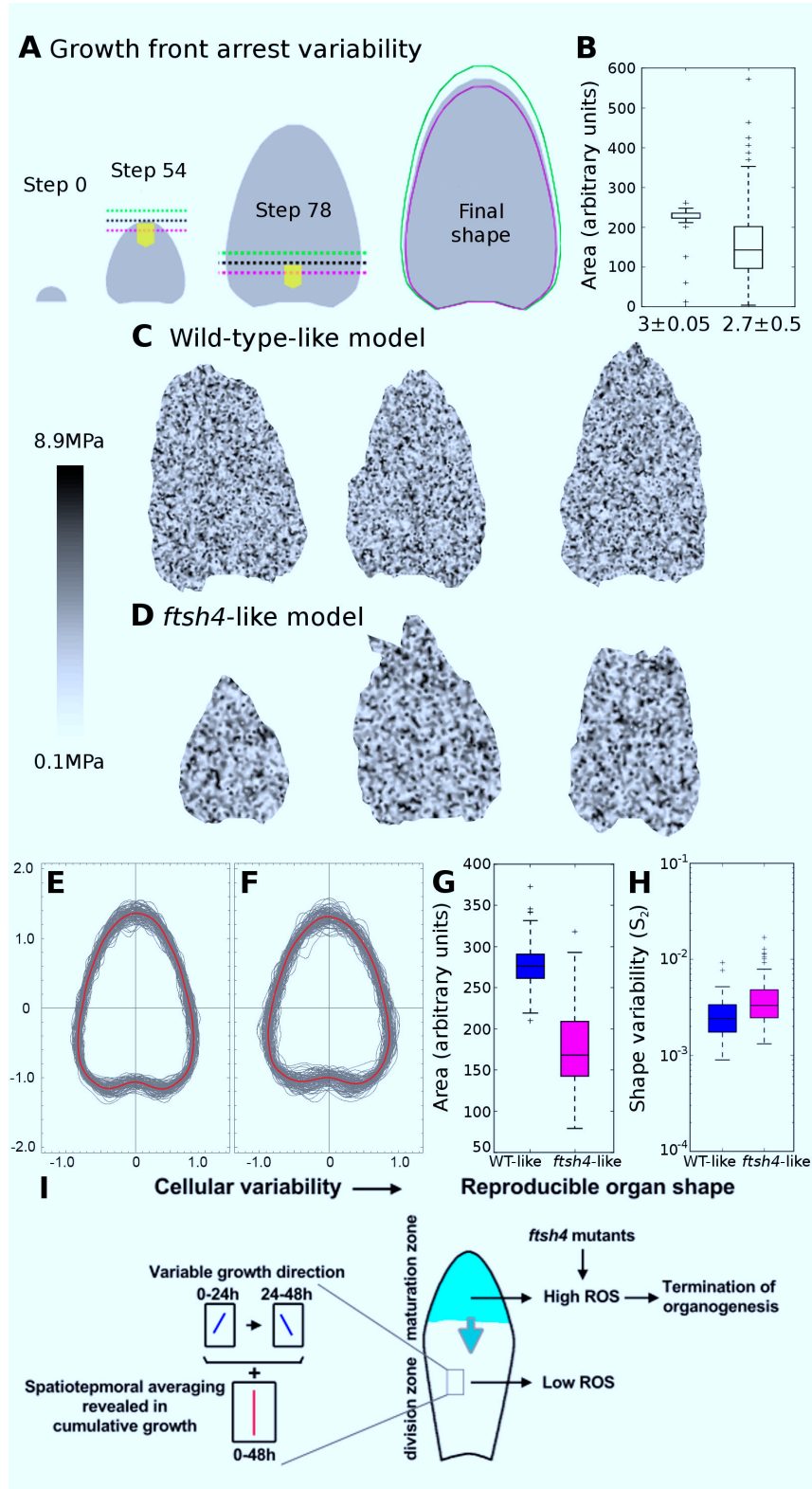


Figure 2.7: Reproducible Organs Arise from Variable Cells

(A and B) Examples of simulation steps of the arrest front model of sepal growth. When the sepal reaches a threshold in length, a front (dotted black line) propagates at constant velocity toward the base, arresting growth when the front reaches the base, which determines the final sepal size and shape. If the height of the threshold is variable, then sepal size is also variable (green high threshold, larger size; magenta low threshold, smaller size). This model was run with uniform stiffness based on the NV model from Figure 2.2A to isolate the effect of the arrest front.

(B) Boxplot of simulated sepal area (a.u., initial area !1) with 470 sets of parameters: arrest front with a little noise on threshold (3.0 ± 0.05), and arrest front with smaller average threshold and enhanced noise on threshold (2.7 ± 0.5) (arrest front follows a Gaussian curve of parameters mean \pm SD).

Figure 2.7: (C–H) The wild-type and *vos1* phenotypes have been reproduced with the model. (C) Three replicates of the wild-type-like model, with parameters: correlation length 1/5, renewal 1/10 (see Figure 2.9), arrest front threshold 3.0 ± 0.08 . (D) Three replicates of the *vos1*-like model, with parameters: correlation length 1/3.5, renewal 1/10, front arrest 2.7 ± 0.15 . (E) Normalized simulated sepal outlines showing shape variability of the wild-type-like model. (F) Normalized simulated sepal outlines showing increased shape variability of the *ftsh4*-like model. (G) Simulated sepal area of the wildtype-like model (WT-like) and the *ftsh4*-like model (*vos1*). Note that the simulated *ftsh4*-like sepal has a smaller median size and larger range than the wild-type-like sepal and is comparable with the real sepal data in Figure 2.1C (mean ratio of area mutant/ wild-type: experimental data = 0.69, model = 0.62; coefficient of variation of wild-type: experimental data = 0.08, model = 0.10; coefficient of variation of mutant: experimental data = 0.32, model = 0.28) (f test, $p < 10^{-6}$). (H) Simulated sepal shape variability of the wild type-like model (WT-like) and the *ftsh4*-like model (t test, $p < 10^{-5}$). Note that the simulated *ftsh4*-like sepal has increased shape variability comparable with the real sepal data in Figure 2.1F (shape variation S_2 for WT sepals: experimental data = 0.00253, model = 0.00242; shape variation S_2 for mutant sepals: experimental data = 0.00423, model = 0.00331). The statistics in (B, G–H) were obtained over 100 replicates (simulation runs).

(I) Conceptual summary. Spatiotemporal averaging of cellular growth variability produces regular organ shapes. For instance, the maximum principal direction of growth (PDG_{max} ; blue line) in a cell may tilt to the left and then later to the right such that the variability averages so that the cumulative growth (red PDG) is highly regular, aligning with other cells, to produce uniform organs. Our data suggest that ROS (aqua) inhibit spatiotemporal averaging while promoting the maturation of cells, reduction of cell division, and termination of growth. ROS accumulate in maturing cells starting at the tip and descending toward the base of the sepal (aqua arrow). Increased, variable, and premature accumulation of ROS in *ftsh4* mutants causes irregular sepal shapes by reducing cellular variability and inhibiting spatiotemporal averaging and irregular sepal sizes by variable initiation of the arrest front.

For the boxplots, the box extends from the lower to upper quartile values of the data, with a line at the median, and the whiskers extend past 1.5 of the interquartile range. See also Movies S1, S4, and S6.

low variability in the initiation height produce robust sepal sizes (e.g., arrest front height 3 ± 0.05 SD in Figure 2.7B), whereas large variability in the arrest front initiation height produced large variation in sepal size (e.g., 2.7 ± 0.5 SD in Figure 2.7B).

However, sepals produced by the AF model did not show any variation in shape. Therefore, to model wild-type sepals, we combined the AF model (ROS arrest front initiation height = 3.0 ± 0.04 SD) with the ST model, which produced robust sepals with little variation in shape (S_2) and size (coefficient of variation, CV), comparable with wild-type sepals (Figures 2.7C, 2.7E, and 2.7G–2.7H compared with Figures 2.1C, 2.1E, and 2.1F; Movie S6). To fit simulation output to experiments, we chose a level of temporal variability corresponding to a renewal value of 10%, meaning that 10% of the mechanical properties are updated from one computational step to the next (Figures 2.9F and 2.9G).

To model *ftsh4* sepals, we combined the AF model initiated with a lower and more variable arrest front reflecting the early and variable accumulation of O_2^- (Figure 2.6E; ROS arrest front initiation height = 2.7 ± 0.15 SD) with a reduced spatiotemporal variability model (ST-L correlation length of 1/3.5). This model reproduced both the size (CV) and shape (S_2) variability of *ftsh4* sepals relative to wild-type (Figures 2.7D–2.7F compared with Figures 2.1C–2.1F; Movie S6). Thus, modeling and experiments together suggest that the size irregularity of *ftsh4* sepals arises primarily from the variable accumulation of ROS, whereas the shape irregularity of *ftsh4* sepal arises from the decreased cellular spatial variability and reduced spatiotemporal averaging. To test this conclusion experimentally, we induced more uniform ROS accumulation in real

sepals. Induction of ectopic expression of an NADPH oxidase, which produces O_2^- , caused the sepals to be uniformly smaller, with variability in sepal size comparable with wild-type sepals (mean \pm SD 0.69 ± 0.10 mm², $n = 69$; Figures 2.6J and 2.6L; compared with wild-type 1.23 ± 0.10 mm²), but sepals were irregular in shape with variability in shape similar to that of *ftsh4* mutants (NADPH oxidase S2 = 0.0041 ± 0.0005 , $n = 69$; *ftsh4* S2 = 0.0042 ± 0.0004 , $n = 518$; wild-type S2 = 0.0025 ± 0.0001 , $n = 215$; mean \pm SE; Figures 2.1F, 2.6K, and 2.13E). This result confirms that the variability of ROS accumulation in *ftsh4* mutants contributes to the irregular sizes, and is consistent with ROS accumulation reducing cellular growth variability and inhibiting spatiotemporal averaging.

2.4 Discussion

We address the key question of how organs can reach precise shapes and sizes despite the variable growth of their cells. We found that organs average variations in cellular growth over space and time to achieve constant morphology. First, using computational simulation, we predicted that robust shapes could emerge from a combination of spatial and temporal variability in a phenomenon termed spatiotemporal averaging. This phenomenon was observed in the cellular growth of wild-type sepals. For example, if a cell’s growth is oriented toward the left at one time point and then toward the right at another time point, the total growth averages to vertical, and aligns with neighboring cells (Figure 2.7I). In this way, organs can maintain robust morphology. We verified this model by screening for mutants in *Arabidopsis* with disrupted organ uniformity (i.e., mutants with differently sized and shaped sepals in the same plant). We identified *ftsh4*, which disrupted regularity in floral organ size and shapes, due to premature and uneven ROS accumulation. First, ROS accumulation inhibited spatiotemporal averaging in *ftsh4* mutants, which caused irregularity primarily in shape. In *ftsh4* mutants the local spatial variability in cell growth decreased. Similarly, model simulations with decreased local spatial variability produced more irregular sepal shapes. Imagine a cell that starts growing awry, e.g., in the “wrong” direction. If local spatial variability is high, its neighbors will not follow it and will somehow compensate for the “wrong” direction. If local spatial variability is low, its neighbors are correlated with this cell and will also grow awry, which can affect overall organ growth. Second, the uneven ROS accumulation in *ftsh4* mutants caused substantial variability in sepal size. Cellular growth in *ftsh4* mutants exhibited many characteristics of sepal cells maturing earlier than in wild-type, suggesting that ROS act as growth regulators promoting maturation (Figure 2.7I). Enzymatically reducing ROS in *ftsh4* mutants restored uniform sepal size and shape, which demonstrated that the abnormal ROS accumulation caused the failure of organ size uniformity in *ftsh4* mutants.

ROS also accumulated in the maturing cells of wild-type sepals, coincident with a wave of arrest propagating from tip to base (Figure 2.7I). Interestingly, ROS accumulation in wild-type sepal tips also inhibited spatiotemporal averaging, but since these cells were already slowing their growth and maturing, this had little effect on sepal regularity. We demonstrated that ROS reg-

ulates wild-type sepal growth by reducing ROS enzymatically in wild-type sepals, which caused the sepals to grow significantly larger than wild-type. Thus, ROS is a key growth regulator that promotes maturation and termination of organ growth while simultaneously inhibiting spatiotemporal averaging. The correct pattern and timing of ROS accumulation in the sepal is required to maintain organ regularity.

2.4.1 Spatiotemporal Averaging as a General Mechanism to Deal with Stochasticity

Growth on the cellular level is highly variable. In plants, such variability is also found for cell-wall stiffness measured with AFM (Milani et al., 2011, Yakubov et al., 2016), consistent with our results on sepals. In addition, experiments and modeling have shown that feedback loops between mechanical stress and plant cell growth orientation can promote heterogeneity in the growth rates and orientations between neighboring cells in *Arabidopsis* (Uyttewaal et al., 2012). In theory, time integration (temporal filtering) can explain the maintenance of robustness in the face of variability originating from random or unpredictable cellular or molecular behaviors (Lander, 2011). In a developmental context, spatiotemporal averaging has been proposed to account for precise distributions of hunchback mRNA in the *Drosophila* embryo despite stochastic hunchback transcription (Little et al., 2013). The use of spatiotemporal averaging to overcome noise in biology at these two different scales (transcript to cell and cell to organ) suggests that it may be a common mechanism ensuring robustness in many biological processes.

Variability on the cellular level could be beneficial to organisms. Unicellular organisms use expression variability to create population heterogeneity, to switch between different physiological states, and to deal with environmental stresses (Blake et al., 2006, Kussell and Leibler, 2005). Expression variability has been proposed to facilitate the evolution of gene regulation (Wolf et al., 2015). Maintenance of growth heterogeneity within the shoot apical meristem has also been proposed to prime cells for differential growth and organogenesis (Uyttewaal et al., 2012). Our results indicate that cellular variability yields consistent organs as the reduced local spatial variability in cellular growth in area of *ftsh4* mutants leads to the production of more variable organs.

The observation that spatiotemporal averaging is decreased in the wild-type sepal tip as ROS accumulate to promote maturation and terminate organ growth suggests that there might be an inherent conflict between terminating organ growth and maintaining regularity through spatiotemporal averaging. In wild-type, this inhibition of spatiotemporal averaging occurs only during maturation when growth slows, so it does not create highly variable shapes as seen in the *ftsh4* mutant, where spatiotemporal averaging is blocked throughout much of sepal development. It may, however, account for the small amount of shape variability in wild-type.

2.4.2 ROS as a Signal that Promotes Cellular Maturation and Growth Arrest

Previous screens for mutations in genes regulating robustness have been done only in yeast (Bauer et al., 2015, Boukhibar and Barkoulas, 2015, Levy and Siegal, 2008, Rinott et al., 2011). These yeast studies show that genes that are master regulators of robustness (also called phenotypic capacitors) encode proteins that are often part of highly connected nodes in the gene regulatory networks. In both plants and animals, ROS form highly connected nodes bridging several signal transduction networks that regulate growth and cell proliferation (Covarrubias et al., 2008, Mittler et al., 2011, Xia et al., 2015).

In addition to the well-established role of ROS in plant stress responses (Choudhury et al., 2013, Perez and Brown, 2014), our work and that of others show that ROS signaling is important for plant development (Foreman et al., 2003, Gapper and Dolan, 2006, Rodriguez et al., 2002). Previous studies have suggested that ROS could affect organ growth through controlling cell division in many organisms (Boonstra and Post, 2004). In mammalian cells and *Drosophila* eye imaginal disks, increasing ROS induces the CDK inhibitors that induce cell-cycle arrest or delay (Owusu-Ansah et al., 2008, Russo et al., 1995). As well as limiting cell proliferation, ROS can also affect cell enlargement. In *Arabidopsis* roots, different types of ROS modulate the balance between cell proliferation and cell elongation creating the characteristic zones of the root meristem, which affect root growth (Reyt et al., 2015, Tsukagoshi et al., 2010). In leaves, reducing ROS levels due to elevated level of antioxidants will delay cell proliferation exit, thus resulting in more cells (Xue et al., 2015). On the other hand, modulating ROS balance in leaves by increasing peroxidase activity will also lead to smaller cells (Lu et al., 2014). Moreover, our dynamic analysis of cell and organ growth reveals that ROS play an important role in organ size and shape robustness through limiting cell division and promoting maturation, as well as through inhibiting spatiotemporal averaging of cellular growth variability.

In yeast, mutating the yeast FtsH4 homolog YME1 results in growth defects (Thorsness and Fox, 1993, Thorsness et al., 1993). Expressing yeast YME1 in *Arabidopsis* rescues the *ftsh4* mutant, suggesting conserved biochemical function across eukaryotes. Our analyses of yeast *yme1* mutants revealed that, under some growth conditions, *yme1* mutants produced higher levels of ROS and had lower proliferation than wild-type (Figure 2.14). These results are consistent with previous studies indicating a role for ROS in inhibiting cell proliferation.

In addition to its signaling role, our osmotic treatments support a role for ROS in directly arresting growth mechanically by stiffening cell walls through the formation of crosslinks between wall polysaccharides and glycoproteins (Barceló and Laura, 2009, Bell et al., 2009, Cosgrove, 2005, Fry, 2004, Lu et al., 2014, Ralph et al., 2004). As cell-wall stiffness controls growth rate, this could explain the reduced spatial variability in the growth rate of the *ftsh4* mutant (Figures 2.4G and 2.4H).

To conclude, the abnormal accumulation of ROS in *ftsh4* mutants disrupts sepal uniformity in two ways. First, it creates a more variable termination signal, causing the sepal to mature early. Second, it inhibits spatiotemporal averaging of cellular variability, resulting in oddly shaped

sepals.

2.5 Experimental procedures

Detailed methods are described in Supplemental Experimental Procedures, Section 2.6.

2.5.1 Plant Material and Treatment

Arabidopsis accession *Col-0* plants are used as wild-type throughout. Mutants were generated by ethyl methanesulfonate mutagenesis. Mutations were isolated using standard map-based cloning (Lukowitz et al., 2000). Allelism tests were conducted between different *ftsh4* alleles. Plants were examined under a dissecting microscope for the sepal phenotype. Flowers were staged according to (Smyth, 1990).

The *YME1* gene, *CAT2* gene, and *APX1* gene full-length cDNA were amplified and LR recombined into the gateway vector pB7WG2. Full-length cDNA of the *RBOHD* gene was used for dexamethasone-inducible expression from the pOp/LhGR expression system (Craft et al., 2005). All of the intermediate and final plasmids used for plant transformation were verified by sequencing. The final constructs were individually transformed into *ftsh4-5* or wild-type plants by *Agrobacterium*-mediated floral dipping.

For H₂O₂ treatment or dexamethasone induction, flowers were dipped into 100 mM H₂O₂ or 5 μ M dexamethasone solution once a day for 7 days.

2.5.2 Microscopy and Image Analysis

Low-magnification whole sepal/flower images were photographed using a dissecting microscope mounted with a camera.

For sepal area and shape measurements, custom Python programs were used to extract the contour and measure the area of each stage 14 sepal. The data were sorted, analyzed, and plotted in Microsoft Excel or the statistical software R. The shape variability was studied by analyzing the sepal's contour points using Fourier decomposition. The contours were normalized with respect to the average radius. The squared deviation of a given contour from the median contour was used to quantify shape variability.

AFM was performed on off-plant stage 10 flowers, using a JPK Nanowizard III atomic force microscope with an extended vertical range of 100 μ m. The cantilevers (SCANASYST-AIR, Bruker) had a nominal spring constant of 7 N/m and a pyramid-shaped tip (tip angle 18°, nominal radius 2 nm). Scanning electron microscopy was performed using a Leica 440 (Roeder et al., 2010).

For live imaging, flowers expressing pAR169 (*pATML1::RCI2A-mCitrine*) were imaged with a Zeiss LSM710 confocal microscope every 12 hrs. MorphoGraphX was used to segment individual cells, track cell lineages, and calculate cell area and PDGs. The spatial and temporal variability in the growth of cell area used the consecutive areas of the cells with the same lineage, based

on the area calculated in MorphoGraphX.

Sepal stiffness was measured by treating stage 8–9 sepals with 0.4 M NaCl solution for 30 min, imaging the cell wall with a Leica SP8 confocal microscope, and calculating the cell shrinkage in MorphoGraphX.

In situ detection of H_2O_2 and O_2^- was carried out by 3,3'-diaminobenzidine and nitroblue tetrazolium staining, respectively.

2.5.3 Computational Modeling

A continuous mechanical model for sepal morphogenesis was built, based on a model previously developed for fission yeast (Bonazzi et al., 2014). Only surface cell walls were modeled, yielding a two-dimensional material with a prescribed distribution of elastic modulus, E . Morphogenesis occurred by successive increments in area. The model was implemented in Freefem++ (Hecht, 2012) and the results were analyzed using Python scripts.

2.6 Supplemental Experimental Procedures

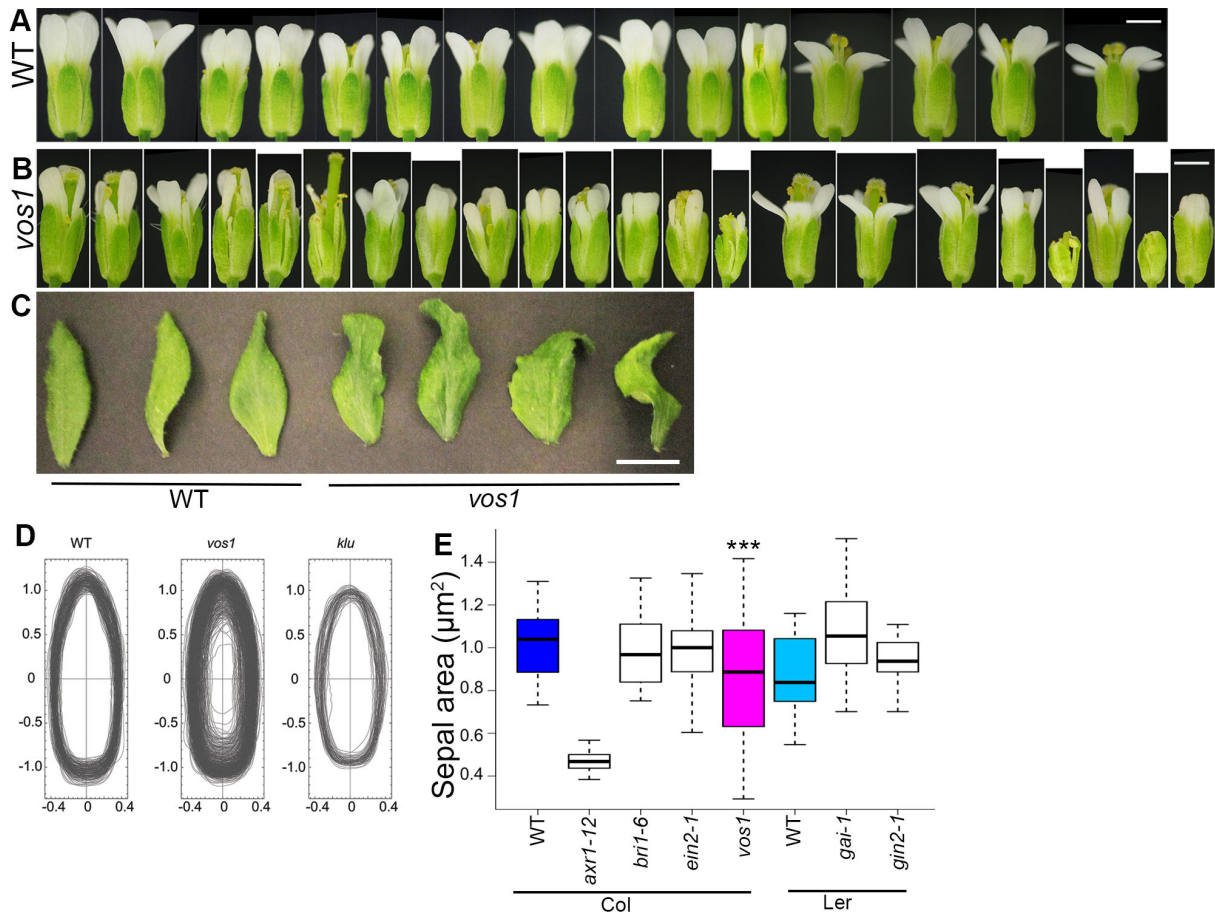


Figure 2.8: *vos1* mutants have increased variability in sepal size and shape, related to Figure 2.1

(A) Flowers taken sequentially from the same WT inflorescence have similar sepals. (B) Flowers sequentially from the same *vos1* inflorescence (the lower row) have irregular sepal shape and size. Note that the *vos1* phenotype does not become progressively more irregular. (C) *vos1* mutants have more twisted cauline leaves than WT. (D) Outlines of WT, *vos1* and *klu* sepals revealing both size and shape variability (equivalent to Fig. 2.1E except that the sepals are not normalized by area). (E) Areas of mature stage 14 sepals from WT (blue and light blue), *vos1* (magenta; data reproduced from Fig. 2.1C for comparison) and hormone signaling mutants (white), showing that most mutants affecting organ size do not increase variance in area. *axr1-12*, *bri1-6* and *ein2-1* are in the Col (Columbia, blue) background. *gai-1* and *gin2-1* are in the Ler (Landsberg *erecta*, light blue) background. *** $p < 0.001$, significant difference in variance from WT (F test). In boxplots, the box extends from the lower to upper quartile values of the data, with a line at the median, and the whiskers extend past 1.5 of the interquartile range. Scale bars: 1 mm in A and B, 1 cm in C.

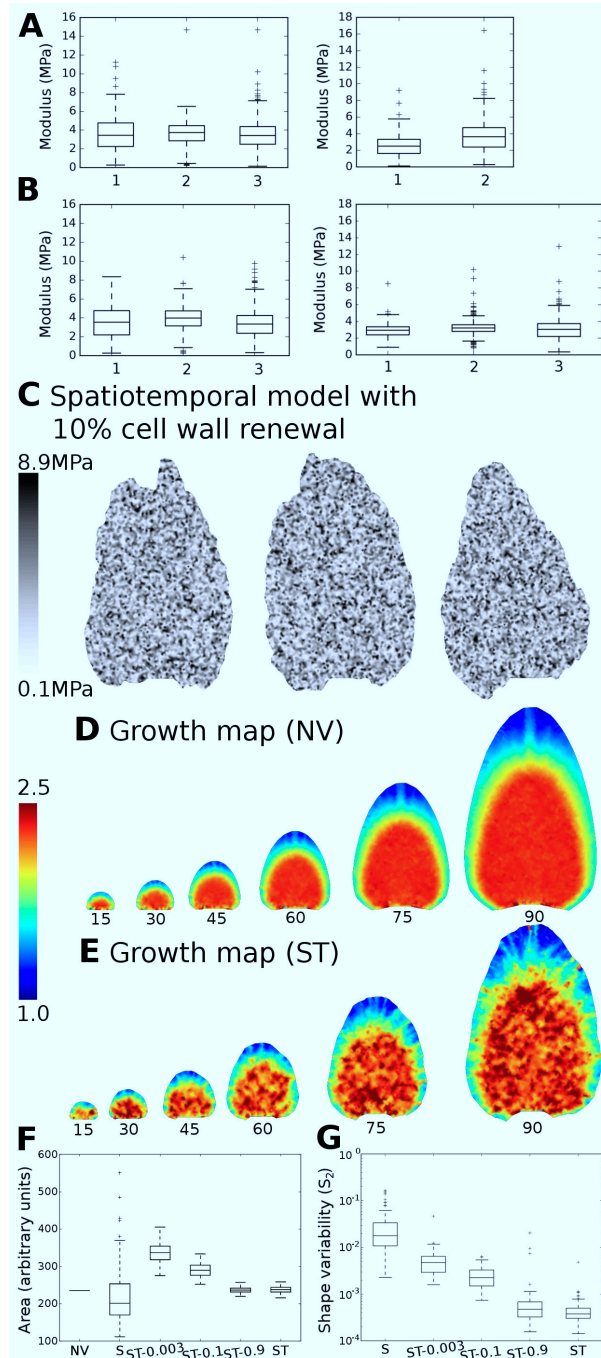


Figure 2.9: A mechanical model of sepal morphogenesis predicts that spatiotemporal averaging of local variability in growth generates robust organ shapes, related to Figure 2.2

(A, B) Additional AFM measurements of wild-type (A) and *vos1* (B) sepals. Each box corresponds to one sepal and each plot to a separate batch of experiments. (C) Example of a model with intermediary temporal variability, in which mechanical properties are partially renewed: At each time point and at each vertex, mechanical properties are replaced by a weighted average of the properties at the previous step and of random properties following similar probability distribution functions. Here, the weight of the random modulus is 10% (ST-0.1) so that 90% of the previous properties are kept. (D-E) Typical heat maps of the growth rates in simulations. Growth is computed every 15th step, as an integration of growth over the 15 previous steps. (D) No variability model (NV). (E) Spatiotemporal variability model (ST). (F-G) Simulated sepal area (F) and shape (G) with the same models as in Figure 2K, with different levels of renewal: 0% (S), 0.3% (ST-0.003), 10% (ST-0.1), 90% (ST-0.9) and 100% (ST).

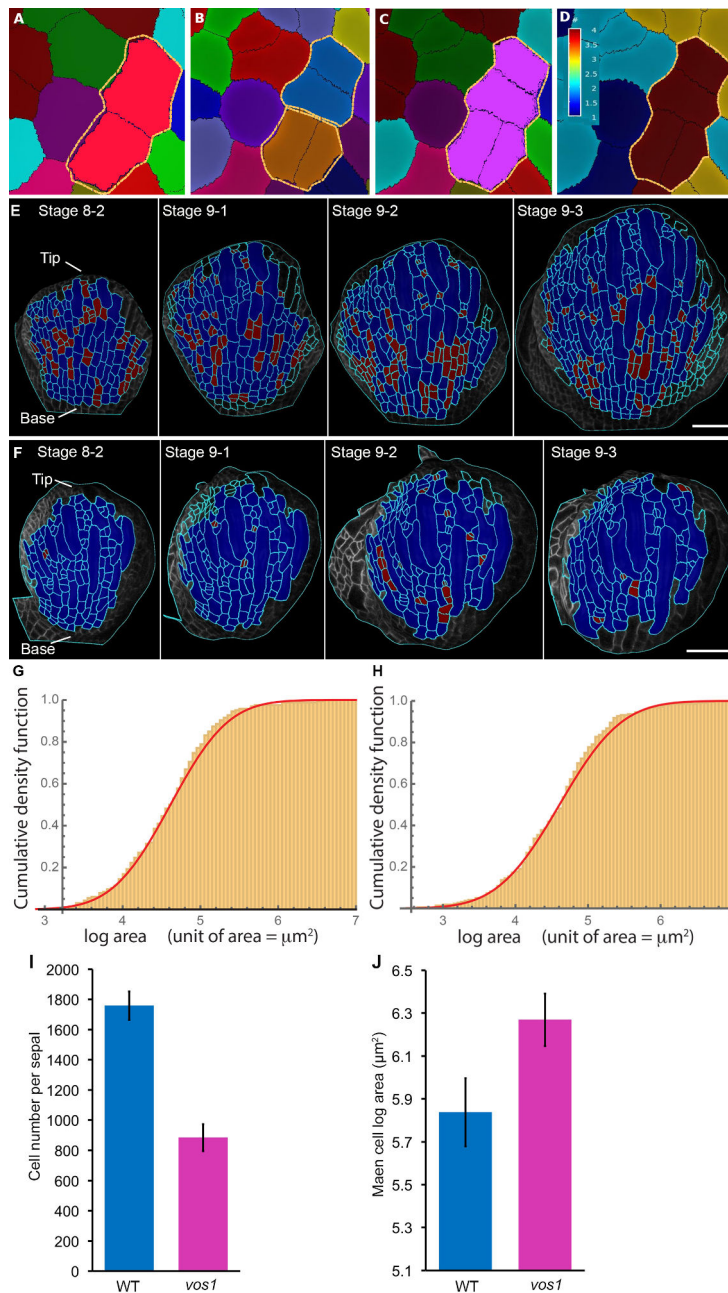


Figure 2.10: Cell lineage tracking and cell area analysis on sepal epidermis, related to Figure 2.3

(A-D) The Multi Step Lineage Tracking (MSLT) tool tracks cell lineages over multiple consecutive time points (T0, T1, T2). Daughter cells of one cell have the same color and are marked with yellow line. (A) Cell lineage generated between T0 and T1, cells in red are daughters of a single cell at T0. (B) Lineage of the corresponding cells generated between T1 and T2. Both the upper cell and lower cell divide to make two daughter cells (blue, upper; brown, lower). (C) Using the MSLT it is possible to generate cell lineages between T0 and T2, showing that all 4 purple daughter cells in T2 descended from a single cell at T0. (D) Heat map of cell proliferation between T0 and T2. Color scale represents number of cells originating from one parent cell, i.e. brown color indicates 4 daughters at T2 descended from 1 cell at T0. (E-F) Spatial maps of cell division in WT (E) and *vos1* (F) sepals. Flowers were staged based on their width. Each sub-stage lasts for 12 hours. The cells that have divided in the previous 12-hour sub-stage are marked in red. The WT sepal had active cell proliferation throughout the sepal at stage 8. Then the cells progressively exited from proliferation from the tip downward. *vos1* mutant sepals have low cell division rate throughout stages 8 and 9. Scale bars: 50 μm in E and F. (G-H) The logarithm of cell area in (G) WT and (H) *vos1* sepals at stage 8-1 follows normal distribution (red lines show the normal distribution fit). $n = 166$ in E, and 220 in F. (I) Total number of cells in mature WT and *vos1* sepals (stage 13). (J) Average of the logarithm of cell area for WT and *vos1* sepals at stage 13. Mature *vos1* sepals have fewer cells while with larger cell area. $n = 4$ biological repeats for each genotypes in I and J, mean \pm SD.

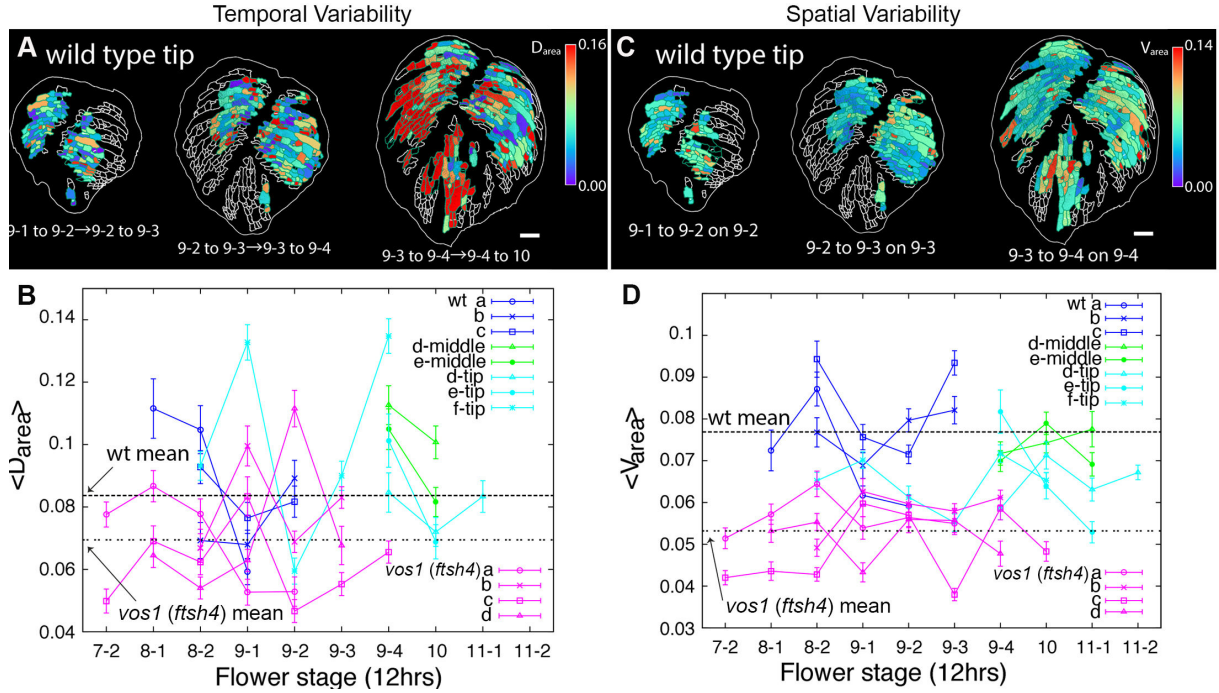


Figure 2.11: Spatial variability of cell growth rates in area is decreased in maturing cells at the wild type-sepal tip, related to Figure 2.4

(A) Temporal variation of the cell growth rate in area (D_{area} , see materials and methods for details) of the tip part of a wild-type sepal, where the cells are maturing. The images were taken such that the top of the flower is shown revealing the tips of three sepals. In comparison flowers in Fig. 2.4 were imaged from the side. Variability is displayed as a heat map with high variability in red and low variability in blue. Consecutive 12-hour growth intervals were analyzed; for example, 8-1 to 8-2 \rightarrow 8-2 to 9-1 means that the growth rate during the 12-hour interval from stage 8-1 to 8-2 was compared to growth rate during the 12-hour interval from stage 8-2 to stage 9-1. (B) Graph plotting the average temporal variability of the areal growth rates ($\langle D_{area} \rangle$ = the average of D_{area}) in each sepal epidermis. The $\langle D_{area} \rangle$ plots from Fig. 2.4C are reproduced here (wild type a-c and *vos1* a-d), for comparison to the wild-type tip data. We divided the sepals of two wild-type flowers imaged at relative later stages (flower d and e) into the middle and tip (defined based on the differentiation of stomata). Wild-type flower f is the flower shown in A and only the tip is available for analysis. Note that for all flowers, the average temporal variability $\langle D_{area} \rangle$ plots largely overlap suggesting there is little difference between the middle and the tip parts of the wild-type sepals. (C) Local spatial variation in the cell growth rate in area is decreased in the tip of a wild-type sepal. Local spatial variability was quantified by calculating the differences in growth rates for a cell and all of its neighbors (V_{area}) in the tip of wild type sepals for each 12-hour interval of growth (see Experimental Procedures for details). Variability is displayed as a heat map with high variability in red and low variability in blue. (D) Graph plotting the average spatial variability in areal growth rate between a cell and its neighbors ($\langle V_{area} \rangle$) for all the cells of each sepal at each floral stage imaged. The $\langle V_{area} \rangle$ plots from Fig. 2.4F are reproduced here (wild type a-c and *vos1* a-d), for comparison to the wild-type tip and middle data. Flowers shown in panels C and D are the same as in panels A and B. The maturing tip cells of wild type sepals have lower $\langle V_{area} \rangle$ than the middle cells in the later stage wild-type sepals.

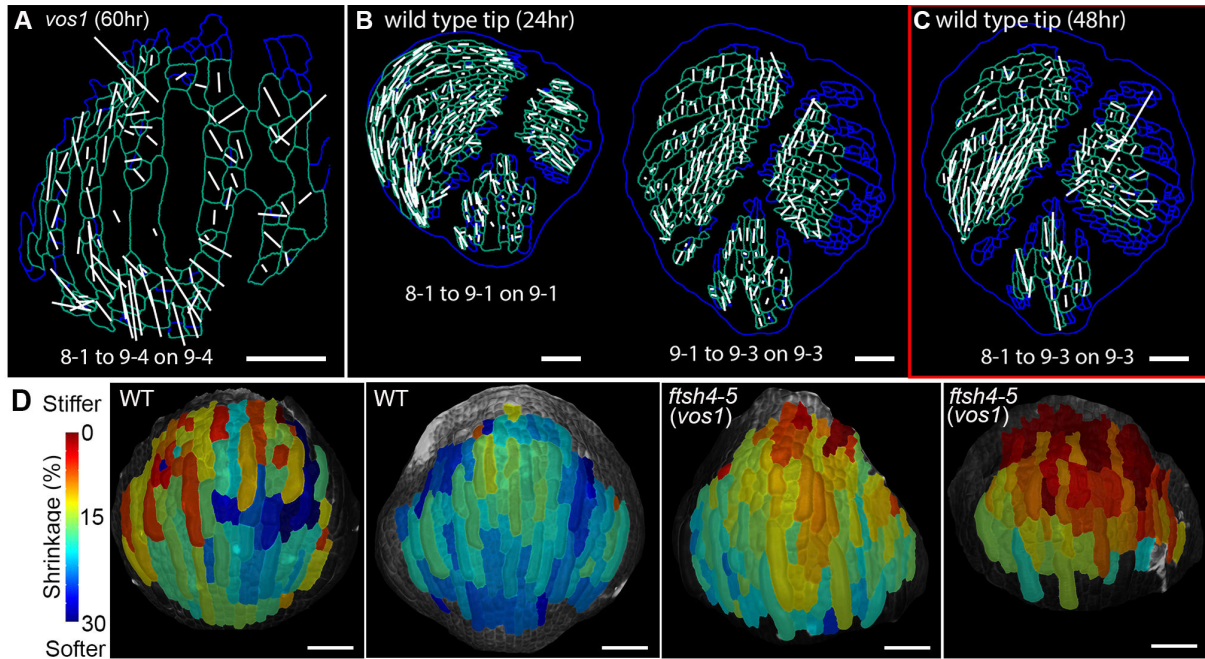


Figure 2.12: *vos1* sepal and wild-type sepal tip show less temporal averaging of variability in the cell growth directions and lower cell wall extensibility, related to Figure 2.5

(A) The integrated growth directions of *vos1* sepal cells over 60 hours. The axes show the maximal growth directions (PDGs; white line) of the cells, with the length of the axes indicating the magnitude of the growth in that direction. The PDGs were mapped on the ending time point of the growth interval. Note that even after 60 hours the maximal growth directions are not well aligned. (B) The PDGs of cells on the tip part of a wild-type sepal, calculated for each 24-hour interval of growth (stages at the bottom). Flower is the same as that shown in Figures S4A and S4C. (C) The PDGs of the sepal tip cells calculated for the cumulative growth from 0 to 48 hours. The tip sepal cells show less temporal averaging of variability than cells in the middle of wild-type sepals, as the PDGs integrated for 48 hours are less aligned (compared with Figure 5B). (D) Cell wall extensibility in wild type and *ftsh4-5* (*vos1*) sepals at stages 8-9. Cell wall extensibility was measured by calculating the change in area (% shrinkage) of the sepal epidermal cell region after osmotic treatment. Area shrinkage for each cell region was shown in heatmaps on the segmented images. The greater the shrinkage the more extensible the cell wall. In the heatmaps, the cells in red have low extensibility/shrinkage and cells in blue have high extensibility/shrinkage. Note that the sepal tips are less extensible than the middle part of the sepal. Scale bars represent 50 μm .

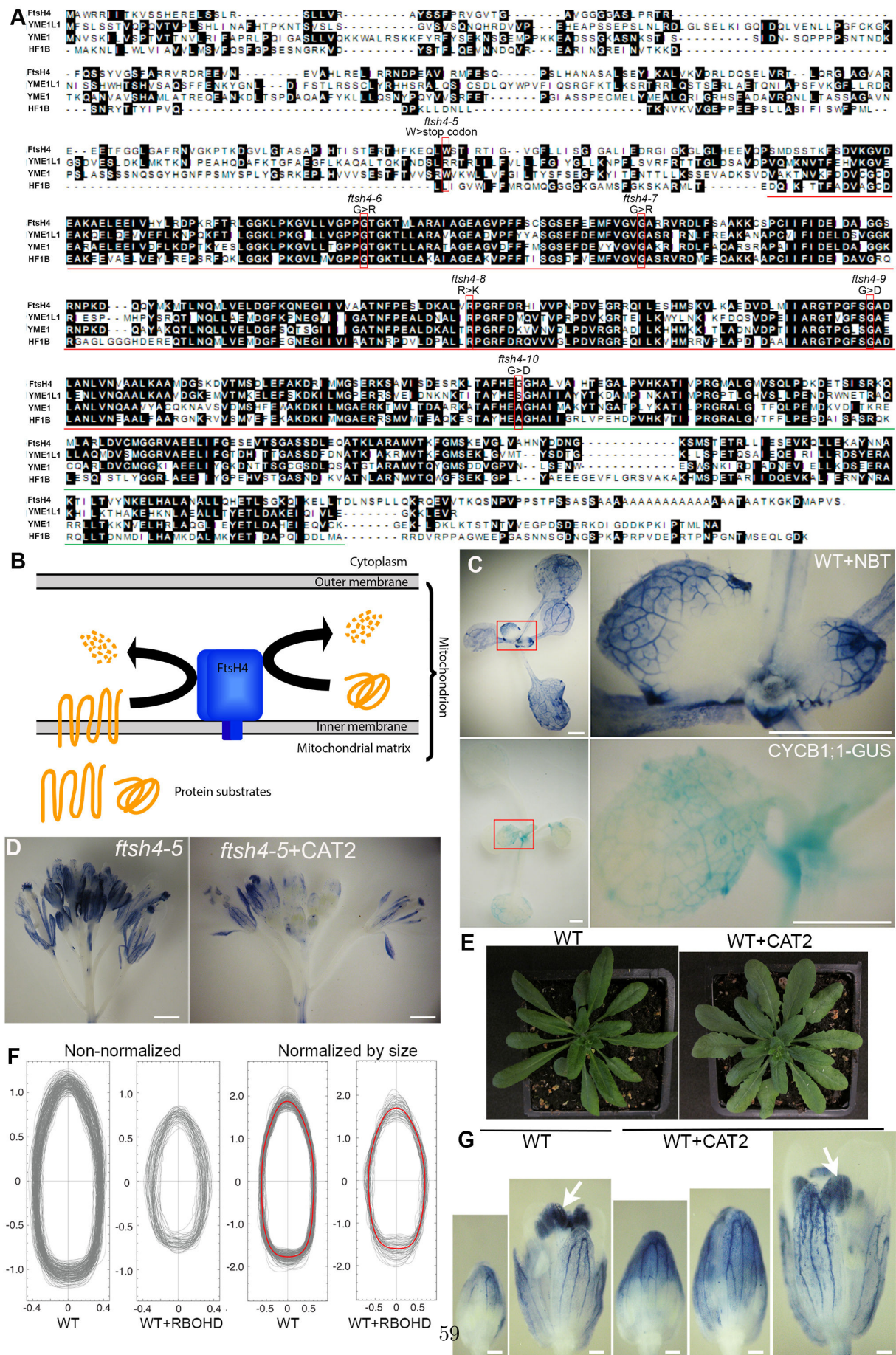


Figure 2.13: *FtsH4* mutations increases ROS and leads to variable sepals, related to Figure 2.6

Figure 2.13: (A) Full-length protein alignment of FtsH4 homologs from *Arabidopsis* (FtsH4), human (*Homo sapiens*, YME1L1), yeast (*Saccharomyces cerevisiae*, YME1), and *E. coli* (*Escherichia coli*, HF1B). Sequences were aligned using the CLUSTAL W program. Conserved amino acid residues are shaded in black. The residues of the ATPase domain are highlighted in red, and the protease domain in green. The mutation sites for different *ftsH4* alleles isolated in this research are marked in red boxes, with the allele names and the amino acid changes labeled. (B) The intra-mitochondrial localization and function of FtsH4 proteins. (C) The superoxide distribution detected by NBT staining (upper panel) anticorrelates with cell division activity indicated by CYCB1;1-GUS expression (lower panel) in young wild-type leaves. Images on the right are magnifications of the red boxed regions in the left images. Similar to sepals, superoxide accumulates on the tip of the young leaves, where the cells have low cell division activity, and spreads toward the base as leaves grow. (D) NBT staining for superoxide in flowers showing that overexpressing a catalase gene *CAT2* in *ftsH4-5* (*ftsH4-5*+*CAT2*) reduced superoxide level in the sepals, as the much lighter staining in *ftsH4-5*+*CAT2* sepals indicates. (E) Wild-type plants overexpressing *CAT2* (WT+*CAT2*) have larger and more expanded leaf blades. (F) Outlines (grey) of mature stage 14 sepals from WT and WT plants overexpressing a NADPH oxidase gene *RBOHD* (WT+*RBOHD*), showing decreased size and increased variation in shape. Outlines on the right have been normalized by sepal size and the median contours for each genotypes are shown in red revealing the difference in shape. WT data were reproduced from Fig. 1E for comparison. (G) Wild-type plants overexpressing *CAT2* (WT+*CAT2*) have a similar but delayed superoxide gradient in sepals, which progresses downward as sepals mature. Although the overall pattern of progressive accumulation of superoxide from the tip to the base of the sepal is the same in WT and WT+*CAT2*, at a given sepal size, superoxide accumulation has progressed further down the WT sepal than the WT+*CAT2* sepal. In stage 14 flowers, stamens are strongly stained with NBT (arrows). To clearly visualize the superoxide accumulation pattern, flowers were stained for a longer time than flowers in D. Scale bars = 1 mm in C and D, 200 μ m in G.

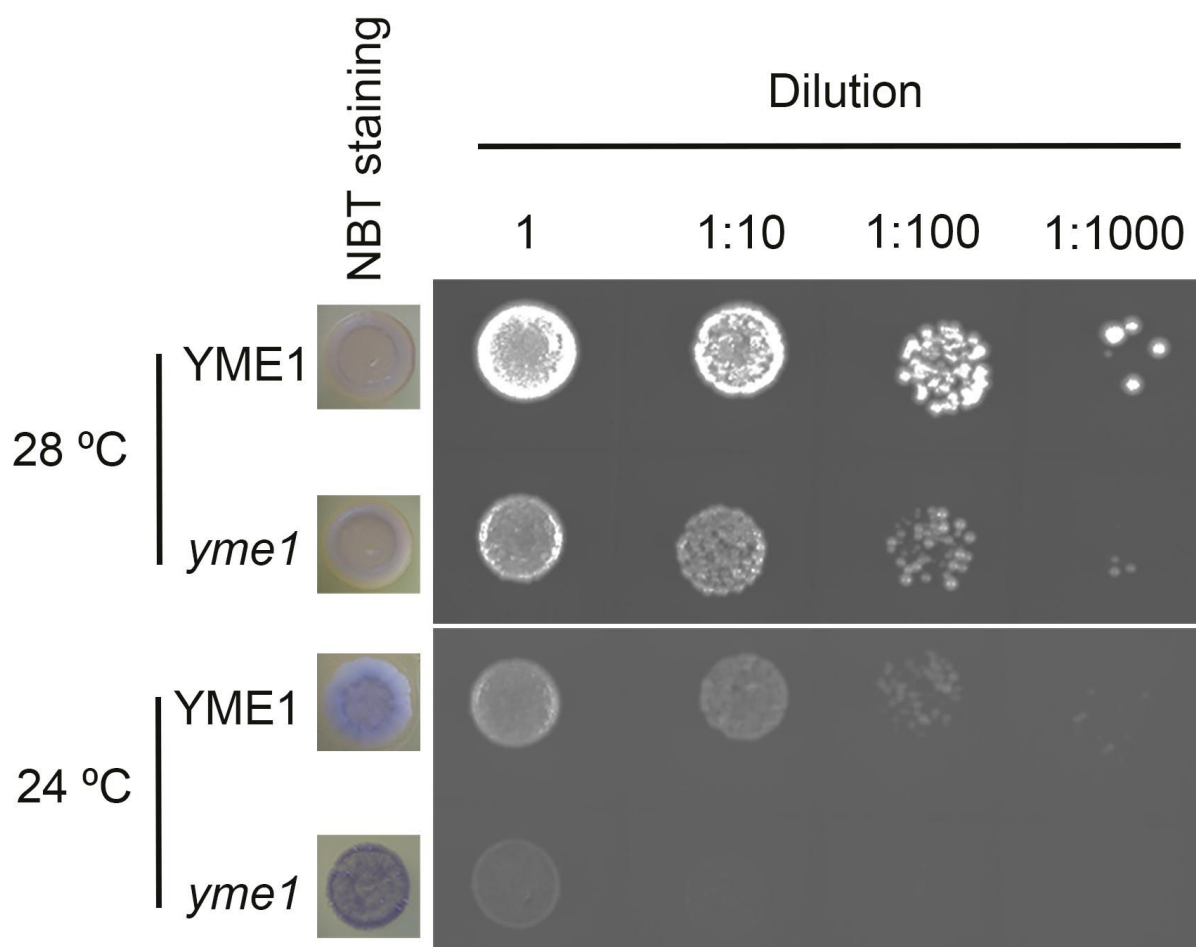


Figure 2.14: FtsH4 homolog YME1 affects growth rate and ROS production in yeast, related to Figure 2.7

Growth assay of wild-type yeast (YME1) and *yme1* mutant (*yme1*) at optimal temperature 28°C or low temperature 24°C and NBT staining for superoxide level of yeasts growing at 24°C. Upper row, yeasts growing at 28°C. Lower row, yeasts growing at 24°C. *yme1* mutants have similar growth rate and superoxide level when growing at 28°C. When growing at 24°C, *yme1* mutants produce higher superoxide and have lower proliferating activity.

Supplemental Experimental Procedures

Mutations and genotyping

Arabidopsis accession *Col-0* plants are used as wild type (WT) in this study. WT seeds were mutagenized with 0.3% ethyl methanesulfonate in 10 ml 0.02% Tween 20 for 24 hours. M2 plants (plants in the second generation after mutagenized plants were self-fertilized) were examined under a dissecting microscope for the variable sepal size phenotype. Mutants of interest were crossed with a Landsberg *erecta* accession plant to generate mapping populations. Mutations were isolated using standard map-based cloning (Lukowitz et al., 2000). The *ftsh4-5* mutation contains a G to A change at base 543 of the coding sequence of *FtsH4*, which generates a premature stop codon. The *ftsh4-5* mutation can be PCR-genotyped by amplifying with primers oLH168 and oLH169 (sequences listed in Primer Table) at 55°C annealing temperature, followed by digesting the product with *NcoI* to produce a 103-bp wild-type product or a 124-bp mutant product. *ftsh4-5* plants were backcrossed three times to wild-type *Col-0* plants prior to further analysis. Allelism tests were conducted between *ftsh4-5* and *ftsh4-6* (a G to A change at base 808 of the CDS, resulting in G to R change in amino acid residues), between *ftsh4-5* and *ftsh4-7* (a G to A change at base 910 of the CDS, resulting in G to R change in amino acid residues), and between *ftsh4-5* and *ftsh4-8* (a G to A change at base 1142 of the CDS, resulting in R to K change in amino acid residues). All alleles failed to complement *ftsh4-5*, establishing that the variable sepal size phenotype is due to the mutation in the *FtsH4* gene. Another two alleles, *ftsh4-9* (a G to A change at base 1289 of the CDS, resulting in G to D change in amino acid residues) and *ftsh4-10* (a G to A change at base 1463 of the CDS, resulting in G to D change in amino acid residues), were also isolated in the screen.

Flower stage

Flowers were staged according to (Smyth et al., 1990).

Sepal area measurements

Sepals dissected from stage 14 flowers were flattened between two slides and photographed on a black background using a dissecting microscope mounted with a camera. Custom Python programs (Data File S1) were used to extract each sepal's contour from the sepal photos and to measure sepal's area. Briefly, images were segmented using the watershed method. Contours were extracted and aligned along their longest axis determined by a principal component analysis of the contour points. Images and contours were smoothed on a scale of diameter 25μm. The data were sorted, analyzed and plotted in Microsoft Excel or the statistical software R.

Quantification of shape variability

The shape variability is studied by analyzing the sepal's contour points, $(x_1, y_1), \dots, (x_N, y_N)$ where N is the number of contour points, using Fourier methods (Data File S1). In order to remove the translational degree of freedom, the contours are first centered at the center of mass of the contour points, $(x_c, y_c) = (\frac{1}{N} \sum_{i=1}^N x_i, \frac{1}{N} \sum_{i=1}^N y_i)$. The radial distance $r(\theta)$ of the contour points from the center can then be obtained as a function of the polar angle θ . Since $\theta = 0$ is so far defined arbitrarily, we remove the rotational degree of freedom with the help of the polar Fourier transformation as $r(\theta) = r_0 + \sum_{n=1}^{n_{max}} c_n \cos(n(\theta + \phi_n))$. Here $r_0 = \frac{1}{2\pi} \int_0^{2\pi} r(\theta) d\theta$ is the average

radius of the contour, n_{\max} is chosen to be large enough such that the Fourier series well describe the fluctuations in $r(\theta)$, and ϕ_n specifies the angular phase of the n th Fourier mode. To fix the orientation of the contour, we choose the convention that $\phi_2 = 0$ for the second harmonic. The second harmonic is used to fix the orientation since $r_{2nd}(\theta) = r_0 + \cos(2(\theta + \phi_2))$ represents a shape close to an ellipse, and setting $\phi_2 = 0$ implies that $\theta = 0$ is defined by the long axis of the ellipse-like shape. With the translation and orientation fixed, the non-normalized (in size) contours for each genotype are then plotted as shown in Figures S1D and S6F .

To further compare the contours independent of the sepal size, we consider the normalized contours with respect to the average radius, defined by $r_{norm}(\theta) = r(\theta)/r_0 = 1 + \sum_{n=1}^{n_{\max}} \frac{c_n}{r_0} \cos(n(\theta + \phi_n))$, with $\phi_2 = 0$. The normalized contours are plotted in Figures 1E and S6F in the main text. For each genotype, we also evaluate the “median” normalized contour, denoted by $\tilde{r}_{norm}(\theta)$, (red line in Figures 1E and S6F) that is defined by the median radius at each angle from the set of contours belonging to the same genotype. To quantify shape variability, we consider the squared deviation of a given contour $r_{norm,\alpha}(\theta)$ ($\alpha = 1, 2, \dots, N_{contour}$) from the median contour, $S_2 = \frac{1}{2\pi} \int_0^{2\pi} (r_{norm,\alpha}(\theta) - \tilde{r}_{norm}(\theta))^2 d\theta$. Here $N_{contour}$ is the number of sepal contours for the genotype under consideration. The median of S_2 from the set of contours of the same genotype provides us with a statistical measure of shape variability. The median, instead of the mean, is used in our analysis since it is relatively insensitive to the effects of outliers. We also note that the main reason to introduce Fourier analysis here is to remove the translation, orientation and size effects in the evaluation of shape variability. The box plots in Figures 1F and 6K give the S_2 of the different genotypes studied in this research.

Permutation test to check if two populations have the same statistics

We use the permutation test, which does not require the knowledge of the underlying distribution functions, to test if the statistics of two populations are the same (Data File S1). Suppose we have two populations, $\{x_1, \dots, x_M\}$ and $\{y_1, \dots, y_N\}$ with finite sizes M and N , respectively, and we want to test if these two populations have the same, e.g. median, with the presence of sampling errors. Let us denote the observed medians be \tilde{x} and \tilde{y} , respectively, and assume $\tilde{x} \geq \tilde{y}$ without loss of generality. In order to tell if the two medians are different, we consider the observed difference $\Delta = \tilde{x} - \tilde{y}$. One expects that if Δ is very large, it is more likely that the medians are different. To have a sense what value of Δ is big enough for us to draw a statistical conclusion, we compare the observed Δ with the cases when the medians are the same as follows: The two populations are joined to form a single population with size $M+N$, and the ordering of the elements is permuted. After the permutation, the medians of the first M elements and the last N elements, denoted by $\tilde{x}_{permute}$ and $\tilde{y}_{permute}$, respectively, are evaluated to obtain the permuted difference $\Delta_{permute} = \tilde{x}_{permute} - \tilde{y}_{permute}$. The above permutation is then carried out many times, e.g., 1000 times, to construct the distribution of $\Delta_{permute}$. Since $\tilde{x}_{permute}$ and $\tilde{y}_{permute}$ come out from the same population, the expectation value of $\Delta_{permute}$ should be zero and the distribution of $\Delta_{permute}$ represents the possible fluctuations in the value of $\Delta_{permute}$ due to finite sampling. Finally, the observed difference Δ is compared with the distribution of $\Delta_{permute}$ to obtain the one-sided p -value, which is defined as the percentage of $\Delta_{permute}$ having values larger than the observed Δ . A small p -value therefore implies that the observed Δ is large and it is more likely to have $\tilde{x} > \tilde{y}$. We declare that $\tilde{x} > \tilde{y}$ is statistical significant if the p -value is less than 5%.

SEM observation

Scanning electron microscopy was performed as described using a Leica 440 (Roeder et al., 2010).

Cell division activity analysis by GUS staining

Cell division activity in young leaves was assayed using the CYCB1-GUS transgenic line having the *CYCB1;1* promoter and the destruction box fused to the reporter *uidA* gene (Colón Carmona et al., 1999). GUS staining was performed as described (Sessions et al., 1999). In brief, seedlings were stained with staining solution (50 mM sodium phosphate buffer pH 7.0, 0.2% Triton-X-100, 10mM potassium ferrocyanide, 10mM potassium ferricyanide, 1mM X-gluc) overnight at 37 °C. The stained tissue was dehydrated and cleared with an ethanol series. GUS-stained seedlings were imaged with a digital camera mounted on a dissecting microscope.

Live imaging of sepal development

Live imaging of plants expressing pAR169 (pATML1::RCI2A-mCitrine) was conducted according to procedures in (Cunha et al., 2012; Roeder et al., 2010), except that plants were imaged every 12 hours. Three-dimensional optical stacks were collected with a Zeiss 710 confocal laser scanning microscope using a $\times 20$ water-immersion objective. The depth of z-sections was set to 0.5 μm for accurate curvature analysis. Samples were excited with an argon laser (488 nm), and data were collected in the yellow fluorescent protein (505 to 545 nm) channel. The resulting confocal stacks were converted from the LSM format to TIFF image stacks using FIJI (<http://fiji.sc/Fiji>) and imported into MorphoGraphX (Barbier de Reuille et al., 2015). The YFP stack was loaded into the software, and the stack was processed (Gaussian blur, edge detect, and fill holes) to obtain a sharp outline of the sepal abaxial surface. The surface was fit with a polygonal mesh using 5 μm cubes, and subsequently the mesh was subdivided and smoothed three times to $\sim 500,000$ vertices. YFP signal marking the plasma membrane was projected perpendicularly onto the surface from 4 to 8 μm depth within the stack, using the surface as measure 0 μm . Individual cells in the images were manually seeded and segmented using the watershed algorithm. For single growth intervals, cell lineage was defined manually by matching mother and daughter cell labels. For analyzing growth over several time points, progeny information between single time points was combined using 'Multi-step lineage tracking' (MSLT). MSLT is a script written in Python programming language which enables tracking cell clones over any permutation of time points in a time lapse imaging series in an automated way (Figures S3A-S3D; Data File S1). Heatmaps were generated to visualize the areal growth rate (defined as the cell lineage area at the second time point divided by cell area at the first time point). The values for each cell in the heatmaps were exported and analyzed with Microsoft Excel to calculate the mean of the logarithm of cell area, cellular area growth rate, and cell division rate for each sepal. The cell division rate for a sepal was calculated as the ratio of the number of cells that divided in the 12-hour growth interval to the total cell number at the beginning of that growth interval for the observed regions of the sepal.

Both wild-type and *vos1* flowers were developmentally staged by their flower width because flower width is minimally affected in *vos1* (Figures 1B, S1A, and S1B) (Smyth et al., 1990). Our SEM data (Figure 1B) showed that *vos1* sepal size irregularity appeared at relatively late stages, so flowers at stages 7 to 11 were used for imaging.

For mature sepal cell number and cell area measurements, sepals dissected from stage 14 flowers expressing pAR169 (*pATML1::RCI2A-mCitrine*) were imaged with a Zeiss 710 confocal laser scanning microscope using a $\times 20$ water-immersion objective. The stack images were

processed in MorphoGraphX to segment individual cells and calculate cell area, using the above mentioned procedures.

Detection and measurements of ROS

In situ detection of H₂O₂ and O₂⁻ were carried out as described previously (Dutilleul et al., 2003), with minor modifications. For H₂O₂ detection, inflorescences were vacuum-infiltrated (three cycles of 5 min) with 0.1% (w/v) DAB in 10 mM sodium phosphate buffer (pH 4)/Tween-20 (0.05% v/v) and incubated in the dark (covered with aluminum foil) at room temperature overnight. For O₂⁻ detection, inflorescences or seedlings were vacuum-infiltrated and incubated in 0.1% (w/v) NBT in 50 mM sodium phosphate buffer (pH > 6.8)/ 0.05% Tween-20 (v/v) for 90 min at room temperature in dark. After reaching the optimal staining state, stained samples were removed from the staining solution and cleared by boiling in acetic acid:glycerol:ethanol (1:1:3, v/v/v) solution. The clearing solution was replaced once after the boiling. After clearing, samples (sometimes individual flowers were detached from the inflorescence if necessary) were photographed against a white background using a dissecting microscope mounted with a camera.

Transgenic plants

The *YME1* gene, *CAT2* gene, and *APX1* gene full-length cDNA were first PCR amplified and cloned into pENTR/D-TOPO vectors (Invitrogen) as described in the manual, using primer pairs listed in Primer Table. The resultant vectors were LR recombined into the gateway vector pB7WG2 (Karimi et al., 2002) to generate three final constructs p35S::*YME1*, p35S::*CAT2* and p35S::*APX1*. All of the intermediate and final constructs were verified by sequencing. The three final constructs were individually transformed into *ftsh4-5* plants by *Agrobacterium*-mediated floral dipping. Seedlings about one week after germination were selected with 100 µg/mL Basta. Surviving plants were genotyped (primer sequences listed in Primer Table) and observed for sepal size phenotype.

For the overexpression of the *RBOHD* gene, the pOp/LhG4 inducible trans-activation system was used (Craft et al., 2005). The *RBOHD* gene full-length cDNA were first PCR amplified, using primer pairs listed in Primer Table, and cloned into a pBJ36-6xOPpro plasmid after the 6xOP promoter, resulting in plasmid pBJ36-6xOPpro:*RBOHD*. The 6xOPpro:*RBOHD* fragment from this plasmid was digested and cloned together with fragment 35Spro:GR-LhG4 (digested from the pBJ36-GR-LhG4) into the pMOA34 plasmid, to generate the pMOA34-6xOPpro:*RBOHD*-35Spro:GR-LhG4 construct. This final construct was transformed into wild-type plants by *Agrobacterium*-mediated floral dipping. Seeds were selected on 1/2MS medium with 50 µg/mL hygromycin. Surviving plants were transplanted to soil and genotyped (primer sequences listed in Primer Table). After the transgenic plants started bolting, the inflorescences were treated with a solution containing 5 µM dexamethasone (Sigma-Aldrich), 0.1% v/v ethanol and 0.01% v/v Silwet L-77, once every day for seven days. The flowers at stage 14 on these treated inflorescences were used for sepal size and shape analyses.

Primer Table: Primers used in this study.

Name	Primers	Description
oLH168	AGAAAGGACTCACTTTAAAGAACAGCCATG	5' primer for <i>fish4-5</i> genotyping
oLH169	TCCTCTGTCCTCGATAAGAGCTCC	3' primer for <i>fish4-5</i> genotyping
oLH266	CACCATGAACGTTTCAAAAATACTTGTG	5' primer for amplifying <i>YME1</i> CDS and genotyping p35S::YME1
oLH267	TCATGCATTTAACATTGTAGGAA	3' primer for amplifying <i>YME1</i> CDS
oLH248	CACCATGGATCCTTACAAGTATCGTCCAG	5' primer for amplifying <i>CAT2</i> CDS
oLH249	TTAGATGCTTGGTCTCACGTTTCAG	3' primer for amplifying <i>CAT2</i> CDS
oLH233	CACCATGACGAAGAACTACCCAACCGTG	5' primer for amplifying <i>APX1</i> CDS
oLH234	CACACACACACAGAGCATACGTC	3' primer for amplifying <i>APX1</i> CDS
oLH275	TCTTCAACCTGTTGGACGTATG	5' primer for genotyping p35S::CAT2
oLH281	GATGGGCTTATCTGACAAAGACATT	5' primer for genotyping p35S::APX1
oAR424	GGAGAAAAATAGAGAGAGATAG	3' primer for genotyping p35S::YME1, p35S::CAT2 and p35S::APX1
oLH237	ATGAAAATGAGACGAGGCAATTC	5' primer for amplifying <i>RBOHD</i> CDS
oLH238	CTAGAAGTTCTCTTTGTGGAAGTC	3' primer for amplifying <i>RBOHD</i> CDS
oLH232	CACACACACACAGAGCATACGTC	5' primer for genotyping pMOA34-6xOPpro:RBOHD-35Spro:GR-LhG4
oAR315	CTACGTGTTCCGCTTCCTTTAG	3' primer for genotyping pMOA34-6xOPpro:RBOHD-35Spro:GR-LhG4

Computational modeling

We built a continuous mechanical model for sepal morphogenesis (Data File S1), starting from a model previously developed for fission yeast (Bonazzi et al., 2014). Only surface cell walls are modeled, yielding a two-dimensional medium with a prescribed distribution of elastic modulus, E . Morphogenesis occurs by successive increments in area: the rest shape at step n is inflated by turgor pressure, P , leading to a new equilibrium shape, which is then used as a rest shape for the next step, $n+1$. At each step, the equilibrium configuration is found using the finite element method and the sepal is remeshed so as to keep a roughly constant mesh size. The model was implemented in Freefem++ (Hecht, 2012) and the results were analyzed using Python scripts. There are about 1500 epidermal cells in the *Arabidopsis* sepal (Roeder et al., 2010) and there are on average about 6 triangular elements per cell in the final model, which enables us to describe a cell with a complex shape and to allow some level of heterogeneity within one cell. In the present study, we accounted for three new ingredients: mechanical anisotropy, growth arrest front, and variable properties, as detailed hereafter.

Mechanical anisotropy was introduced to obtain a higher expansion rate along the y axis than the x axis, corresponding respectively to the proximo-distal and medio-lateral axes of the sepal. We thus used the generalized Hooke's law linking the stress tensor σ and the strain tensor ε through the elasticity matrix,

$$\begin{pmatrix} \sigma_{xx} \\ \sigma_{yy} \\ \sigma_{xy} \end{pmatrix} = \begin{pmatrix} A_1 & B & 0 \\ B & A_2 & 0 \\ 0 & 0 & C \end{pmatrix} \begin{pmatrix} \varepsilon_{xx} \\ \varepsilon_{yy} \\ \varepsilon_{xy} \end{pmatrix},$$

where $A_1 = (1 - \nu)E/((1 + \nu)(1 - 2\nu))(1 + \alpha/2)$, $A_2 = (1 - \nu)E/((1 + \nu)(1 - 2\nu))(1 - \alpha/2)$, $B = \beta\sqrt{A_1A_2}$, $C = E/(1 + \nu)$, E being the reduced elastic modulus, ν the reduced

Poisson's ratio, α the mechanical anisotropy, and β a non-dimensional modulus ($\beta < 1$ for the elasticity matrix to be well-defined) (Landau and Lifshitz, 1986).

The starting configuration is always a semi-disk of radius 1.1. When the sepal reaches a length L , a front propagates proximally by a distance d per simulation step. The simulations are arrested when this front reaches the basis.

We considered variability of either the arrest front or the elastic modulus. In the former case, L is a random Gaussian variable of mean M_L and standard deviation S_L . In the latter, E is a random Gaussian variable, of mean M_E and standard deviation S_E , defined at each vertex and each time step; in order to avoid abnormally low stiffness, E is redrawn when it is smaller than T_E . In the case of pure spatiotemporal variability, the distribution of E is reset at each time step. In the case of pure spatial variability, the distribution of E is set in the initial configuration and then inherited throughout time: Following each remeshing, the value of modulus at a given vertex is interpolated from the previous mesh using the *adaptmesh* function of Freefem++.

In the intermediate case of partial renewal, the value of modulus E_n at step n is computed from the interpolated value E_{n-1} at step $n-1$, $E_n = (1-m) E_{n-1} + e$, where e is a random variable, of mean $M_E - (1-m) M_{n-1}$ and standard deviation $\sqrt{(S_E^2 - (1-m)^2 S_{n-1}^2)}$, where M_{n-1} and S_{n-1} are the mean and the standard deviation of the elastic modulus at step $n-1$ in the whole sepal. (E_n was also redrawn when smaller than T_E .) The renewal parameter m is such that $0 < m < 1$, $m = 0$ corresponding to no renewal and $m = 1$ to full renewal; $m=0.1$ (corresponding to 10% renewal) was used for the wild-type-like and the *ftsh4*-like models.

In the simulations shown here, we used $P = 0.5$ MPa, $E = 3.27$ MPa (estimated from AFM), $\nu = 0.48$, $\alpha = 0.2$, $\beta = 0.5$, $L = 3$, $d = 0.05$. The parameters for the random variables were $M_L = 3$ or 2.7 , $S_L = 0.05$ or 0.5 , $M_E = 3.27$ MPa, $S_E = 2.7$ MPa, $T_E = 0.1$ Mpa. The size of the mesh was $1/1.5$, $1/5$, and $1/3.5$ corresponding to high (ST), low (ST-L), and *ftsh4*-like local variability, respectively. In addition, we explored a range of other values and found the same qualitative results.

Atomic force microscopy (AFM)

Stage 10 flowers were dissected off the stem and then put in a Petri dish containing solid growth medium as described (Fernandez et al., 2010). The flowers were oriented with abaxial sepals facing upward and covered with a water drop for measurements. Atomic force microscopy was performed as described in (Milani et al., 2013), with minor modifications. We used a JPK Nanowizard AFM with an extended stage enabling a vertical range of 100 μ m, which was required because of the bumpiness of the sepal surface. The cantilevers (SCANASYST-AIR, Bruker Inc.) had a nominal spring constant of 7N/m and a pyramid-shaped tip (tip angle 18°, nominal radius 2 nm). Each cantilever was calibrated by using indentation on sapphire and thermal tune, in water. Areas of about 100 μ m x 100 μ m in the center of the sepal were first scanned to obtain sample topography, then approach and retraction were performed on a square grid of 20x20 equally separated points, with two measurements at each point, yielding 800 curves per sepal. Approach and retract velocity was 5 μ m/s. Maximal depths ranged from 100 to 200 nm, in order to obtain curves that are mostly sensitive to cell wall mechanics. Force curves were fitted to the Hertz-Sneddon equation as in (Milani et al., 2013); fits with coefficient of determination smaller than 0.95 (about 20% of the

data) were discarded. We thus obtained effective elastic moduli that quantify cell wall mechanics around each point of the grid.

Osmotic treatments measuring sepal stiffness

All flowers except for one of stage 8-9 were dissected off the inflorescence. The sample was incubated in water containing 0.1% PPM (Plant Cell Technology) for 1-2 hours and stained in 0.1% Propidium Iodide solution (Sigma-Aldrich) for 15 minutes. The sample was immobilized in ½ MS medium in such a way that the end of the stem was stuck in the medium and the flower remained above the surface of the medium covered in water and the first confocal stack was taken. The water was then removed and the sample was incubated in NaCl (Roth) solution for 30 minutes. Confocal stacks were taken directly before and after NaCl treatment.

The concentration of osmolyte in which epidermal cell plasmolysis can be observed was determined by conducting the osmotic treatment procedure on *Col-0* flowers in NaCl concentrations ranging from 0.2 M to 1 M. PI was used to visualize the cell wall and pUBQ10::myrYFP marker donated by Raymond Wightman was used to visualize the plasma membrane. In this marker line YFP is N-terminally modified with a short myristoylated and probably acetylated peptide. The optimal NaCl concentration for which plasma membrane was visibly detached from the cell wall while maintaining good image quality was 0.4 M for both *Col-0* and *ftsh4* sepals.

For confocal imaging SP8 microscope with water immersion long working distance objective (HCX APO 40x/0.8, Leica) was used. Images were collected at 605-664 nm for PI (excitation at 524 nm, argon laser) and 520-550 nm for YFP (excitation at 488 nm, argon laser).

Images from before and after the osmotic treatment were segmented in MorphoGraphX. Giant cells were segmented individually while small cells were clustered in groups which shape roughly resembled the shape of giant cells. Change in cell area (% shrinkage) was calculated and displayed on the segmented images as heat map. When cells are placed in hypertonic solutions (high salt), water flows out of the cell decreasing the turgor pressure; the shrinkage of the cell is an indication of the cell wall elastic properties, with stiffer cells shrinking less.

Analysis of spatiotemporal variability in the growth of cell area

The growth of cell area was based on the quantification of area in MorphographX (Barbier de Reuille et al., 2015). In this analysis (Data File S1), we used the consecutive areas of the cells with same lineage. If the mother cell divided during the time interval, the areas of all daughter cells were summed in order to calculate the corresponding areal growth rate. The areas of the parent cell and all the daughter cells were denoted by A_x and A_y , respectively. Then, the areal growth rate was defined as $AGR = (A_y/A_x)/\Delta t$ where Δt is the time interval of the consecutive time frames. In order to calculate the local spatial variability in the areal growth rate among neighboring cells, we defined the areal growth rate for the cell of interest (labelled f) as $AGR(f)$ and for neighboring cells surrounding cell f as $AGR(i)$ where $i = 1, 2, \dots, N$ (N is the number of neighbors of cell f). Then, the difference of the areal growth rates among neighboring cells was defined as $V_{area} =$

$\frac{1}{N} \sum_{i=1}^N \frac{|AGR(f) - AGR(i)|}{|AGR(f) + AGR(i)|}$. The areal growth rates with cumulative probability $p(V_{\text{area}}) > 0.95$ were taken as outliers.

In order to calculate the temporal variation of the areal growth rate, we defined the areal growth rate for the cell of interest at the current time frame as $AGR^{(t)}$ and the areal growth rate for the same cell at the next time frame as $AGR^{(t+\Delta t)}$. If the cell of interest has divided into m cells, we obtain m different quantities of the type $AGR^{(t+\Delta t)}$. The temporal variation of the areal growth rate for the same cell lineages between consecutive growth intervals was then defined as $D_{\text{area}} = \frac{|AGR^{(t)} - AGR^{(t+\Delta t)}|}{|AGR^{(t)} + AGR^{(t+\Delta t)}|}$. In this case, the areal growth rates with cumulative probability $p(D_{\text{area}}) > 0.95$ were taken as outliers.

Accession Numbers

FtsH4/VOS1, AT2G26140; *CAT2*, AT4G35090; *APX1*, AT1G07890; *RBOHD*, AT5G47910; *FtsH3*, AT2G29080; *FtsH10*, AT1G07510; *FtsH11*, AT5G53170; *YME1L1*, AJ132637; *YME1*, DQ333030; *HF1B*, NP_417645

Supplemental References

Barbier de Reuille, P., Routier-Kierzkowska, A.L., Kierzkowski, D., Bassel, G.W., Schüpbach, T., Tauriello, G., Bajpai, N., Strauss, S., Weber, A., Kiss, A., et al. (2015). MorphoGraphX: A platform for quantifying morphogenesis in 4D. *eLife* 4, e05864.

Bonazzi, D., Julien, J.-D., Romao, M., Seddiki, R., Piel, M., Boudaoud, A., and Minc, N. (2014). Symmetry breaking in spore germination relies on an interplay between polar cap stability and spore wall mechanics. *Dev Cell* 28, 534–546.

Colón Carmona, A., You, R., Haimovitch Gal, T., and Doerner, P. (1999). Spatio-temporal analysis of mitotic activity with a labile cyclin–GUS fusion protein. *Plant J* 20, 503–508.

Craft, J., Samalova, M., Baroux, C., Townley, H., Martinez, A., Jepson, I., Tsiantis, M., and Moore, I. (2005). New pOp/LhG4 vectors for stringent glucocorticoid-dependent transgene expression in *Arabidopsis*. *Plant J* 41, 899–918.

Cunha, A., Tarr, P.T., Roeder, A.H.K., Altinok, A., Mjolsness, E., and Meyerowitz, E.M. (2012). Computational analysis of live cell images of the *Arabidopsis thaliana* plant. *Methods Cell Biol.* 110, 285–323.

Donnelly, P.M., Bonetta, D., Tsukaya, H., Dengler, R.E., and Dengler, N.G. (1999). Cell cycling and cell enlargement in developing leaves of *Arabidopsis*. *Dev Biol* 215, 407–419.

Fernandez, R., Das, P., Mirabet, V., Moscardi, E., Traas, J., Verdeil, J.-L., Malandain, G., and Godin, C. (2010). Imaging plant growth in 4D: robust tissue reconstruction and lineaging at cell resolution. *Nat Methods* 7, 547–553.

Gonzalez, N., Vanhaeren, H., and Inzé, D. (2012). Leaf size control: complex coordination of cell division and expansion. *Trends Plant Sci* 17, 332–340.

Hecht, F. (2012). New development in FreeFem++. *J Numer Math* 20, 251–266.

Karimi, M., Inzé, D., and Depicker, A. (2002). GATEWAY™ vectors for *Agrobacterium*-mediated plant transformation. *Trends Plant Sci* 7, 193–195.

Landau, L.D., and Lifshitz, E.M. (1986). *Theory of Elasticity* (Oxford: Pergamon Press).

Lukowitz, W., Gillmor, C.S., and Scheible, W.R. (2000). Positional cloning in *Arabidopsis*. Why it feels good to have a genome initiative working for you. *Plant Phys* 123, 795–805.

Milani, P., Braybrook, S.A., and Boudaoud, A. (2013). Shrinking the hammer: micromechanical approaches to morphogenesis. *J Exp Bot* 64, 4651–4662.

Roeder, A.H.K., Chickarmane, V., Cunha, A., Obara, B., Manjunath, B.S., and Meyerowitz, E.M. (2010). Variability in the control of cell division underlies sepal epidermal patterning in *Arabidopsis thaliana*. *PLoS Biol* 8, e1000367.

Sessions, A.A., Weigel, D.D., and Yanofsky, M.F.M. (1999). The *Arabidopsis thaliana* *MERISTEM LAYER 1* promoter specifies epidermal expression in meristems and young primordia. *Plant J* 20, 259–263.

Smyth, D.R., Bowman, J.L., and Meyerowitz, E.M. (1990). Early flower development in *Arabidopsis*. *Plant Cell* 2, 755–767.

3

A Mechanical Feedback Restricts Sepal Growth and Shape in Arabidopsis

IT IS CLASSICALLY ADMITTED that morphogenesis is the result of morphogen activity. Morphogens thus impose growth rates and directions to the cells of a tissue, the interaction of the cellular growth thus leading to the final organ shape. In plants, morphogens modulate cell growth by modulating wall mechanical properties. However, the wall mechanical properties can be modified by other means, in particular, cells react to their physical environment: one best characterized reaction is the alignment of microtubules against maximal tensile stress, in turn changing the cellulose microfibrils orientation and the cell wall mechanical properties.

Here, using mutants affected in the efficiency of this mechanical response and modeling, we demonstrate that mechanical feedback does indeed influence the growth pattern of the sepal. In addition, trichome emergence is correlated with an alignment of the microtubule network around the trichome. Whether trichome growth induces morphogenetic changes in sepals have been studied in a submitted paper (see the Appendix5.1), where the modeling framework I designed is used to test if mechanical feedback strength associated with trichome emergence could trigger sepal shape modifications.

This work was done in a collaboration, where I built the models and solved them numerically, and took part in the elaboration of the experiments and the writing of the article. A mechanical

feedback restricts sepal growth and shape in Arabidopsis

Nathan Hervieux¹, Mathilde Dumond¹, Aleksandra Sapala², Anne-Lise Routier-Kierzkowska², Daniel Kierzkowski², Adrienne H.K. Roeder³, Richard S. Smith², Arezki Boudaoud^{1,*}, Olivier Hamant^{1,*}

¹ Plant Reproduction and Development lab, INRA, CNRS, ENS Lyon, UCB Lyon 1, 46 allée d'Italie, 69007 Lyon, France

² Department of Comparative Development and Genetics, Max Planck Institute for Plant Breeding Research, Carl-von-Linné-Weg 10, 50829 Köln, Germany

³ Weill Institute for Cell and Molecular Biology and Section of Plant Biology, School of Integrative Plant Sciences, Cornell University, Ithaca, NY, 14853 USA

Correspondence : olivier.hamant@ens-lyon.fr, arezki.boudaoud@ens-lyon.fr

3.1 Summary

How organs reach their final shape is a central yet unresolved question in developmental biology. Here we investigate whether mechanical cues contribute to this process. We analyze the epidermal cells of the Arabidopsis sepal, focusing on cortical microtubule arrays, which align along maximal tensile stresses and restrict growth in that direction through their indirect impact on the mechanical anisotropy of cell walls. We find a good match between growth and microtubule orientation throughout most of the development of the sepal. However, at the sepal tip, where organ maturation initiates and growth slows down in later stages, microtubules remain in a configuration consistent with fast anisotropic growth, i.e. transverse, and the anisotropy of their arrays even increases. To understand this apparent paradox, we build a continuous mechanical model of a growing sepal. The model demonstrates that differential growth in the sepal can generate transverse tensile stress at the tip. Consistently, microtubules respond to mechanical perturbations and align along maximal tension at the sepal tip. Including this mechanical feedback in our growth model of the sepal, we predict an impact on sepal shape that is validated experimentally using mutants with either increased or decreased microtubule response to stress. Altogether this suggests that a mechanical feedback loop, *via* microtubules acting both as stress sensor and growth regulator, channels the growth and shape of the sepal tip. We propose that this proprioception mechanism is a key step leading to growth arrest in the whole sepal in response to its own growth.

3.2 Introduction

A central and still unresolved question in developmental biology is how organs reach reproducible size and shape (Vogel, 2013). Evidence that organ size is controlled by intrinsic signals has been accumulating over the years. This was nicely demonstrated by Twitty and Schwind

in 1931 (Vogel, 2013): grafting the limb bud from a large salamander onto a small salamander results in the growth of a large limb on a small salamander. In most organisms including plants, the size and shape of organs is highly characteristic and varies little between individuals. In plants, evidence that organ size is tightly controlled is illustrated by the concept of compensation. Leaves with a reduced cell number can reach their normal size by increasing the rate or duration of the cell expansion phase (Hisanaga et al., 2015, Horiguchi et al., 2006). However, the associated mechanisms are unknown. The control of organ size and shape involves the tight regulation of growth arrest, in addition to other variables, such as the number of cells recruited to the new organ primordium and the expansion and division rate of those cells. While morphogen gradients are involved in the growing phase of organs, they have also been proposed to be involved in growth arrest: morphogens become diluted as growth occurs, and beyond a certain threshold of concentration, they may not promote growth anymore. This provides an interesting geometrical negative feedback loop in which shape and distance determines growth arrest (Jaeger et al., 2008, Kuchen et al., 2012, Wartlick et al., 2011).

Mechanical signals have been proposed to act as a means to inform the genetic control of development by providing a mechanism to probe an organ’s developing size and shape (e.g. (Hamant et al., 2008, Shraiman, 2005)). In the wing imaginal disc of *Drosophila melanogaster*, cells grow uniformly despite the gradient of the growth promoting factor Dpp emanating from the center of the disc (Hufnagel et al., 2007, Schluck et al., 2013, Shraiman, 2005). A simple stress feedback on growth has been proposed to explain this disconnect between observed growth and the morphogens controlling it (Aegerter-Wilmsen et al., 2007, LeGoff et al., 2013, Shraiman, 2005). Dpp promotes growth of the central cells, causing compressive stresses locally, while also causing tensile stresses in the surrounding cells at the periphery of the disc. Beyond a certain threshold, compression is proposed to trigger an arrest of cell proliferation, whereas tensile stress enhances proliferation. The observed synchrony in cell division and growth in the wing disc is consistent with this hypothesis (Aegerter-Wilmsen et al., 2007, Hufnagel et al., 2007, Schluck et al., 2013, Shraiman, 2005). Yet, the role of mechanical forces in organ size is still debated. In particular, *dpp* concentration in the wing disc also scales with disc size (Wartlick et al., 2011), opening the possibility that both morphogen dilution and mechanical compression contribute to growth arrest.

In plants mechanical stress and strain drive growth (Lockhart, 1965), providing a pervasive passive feedback on growth. The strongest evidence for active mechanical feedback in plants involves the cortical microtubules, which orient along maximal tensile stress directions (Green and King, 1966, Hamant et al., 2008, Williamson, 1990). Since the cortical microtubules guide the trajectories of cellulose synthase (Paredez et al., 2006) that orient the deposition of cellulose microfibrils, this feedback directly controls the direction of maximal stiffness in cell walls (Baskin, 2005, Landrein et al., 2013). Cellulose restricts wall expansion in the direction of the microfibrils, and thus likely plays a key role in growth arrest and in channeling final shape. An analysis of tension and microtubule patterns in the jigsaw puzzle shaped pavement cells supports such a scenario at the single cell scale (Sampathkumar et al., 2014). Using the

Arabidopsis sepal as a model system, we show that this mechanism also operates at the organ level.

3.3 Results

3.3.1 The abaxial sepal exhibits a stereotypical growth pattern

The sepal is the outermost organ in the flower; out of the four sepals in each flower, the abaxial sepal is the farthest from the stem axis. Because the final size and shape of this organ is relatively insensitive to environmental conditions, the contribution of intrinsic signals in its final shape can be analyzed more easily, making it an ideal system to investigate the role of mechanical signals in shaping organs.

To analyze cellular growth in the wild type sepal, we performed time lapse imaging of the abaxial sepal expressing a fluorescent plasma membrane marker. We used MorphoGraphX (Barbier de Reuille et al., 2015) to segment cells in the epidermis for each time point and analyze their growth properties. We chose 24-hour intervals, which reduced variability when compared with 6 hour intervals reported previously (Tauriello et al., 2015). A stereotypical pattern of growth could be observed (Figure 3.1A and B, Figure 3.5, n=3 long time sequences). Using the staging defined in (Smyth, 1990), we observed that, from the initiation of the primordium until stage 6, both growth rate (Figure 3.1A) and growth anisotropy (Figure 3.1B) were very high at the sepal tip and lower towards the base. The direction of maximal growth was along the longitudinal axis of the growing sepal (Figure 3.1B). Then, between stage 6 and 7, growth rates were greatly reduced at the sepal tip while maintaining a relatively fast anisotropic growth at the lateral margin. From stage 7, a region of isotropic, relatively fast growth appeared around the center of the sepal and gradually proceeded towards its base in later stages (Figure 3.1B). Cell proliferation followed global gradients in growth rates as well as reflected the appearance of stomata lineages (Figure 3.1C).

3.3.2 The tip of the sepal exhibits a stereotypical cortical microtubule pattern

To examine the molecular basis of this growth pattern, we next analyzed the microtubule behavior during sepal growth. We used a transgenic line expressing both a membrane marker (LTI6b-2xmCherry) under the control of the UBQ10 promoter and a microtubule marker (GFP-MBD) under the control of the CaMV35S promoter.

As shown in other tissues (e.g. (Landrein et al., 2013, Shaw, 2013, Wasteneys and Ambrose, 2009)), we found that the cortical microtubule (CMT) network is dynamic over time and space (Figure 3.2, Figure 3.6). We focused our analysis on regions and stages where the growth pattern exhibited marked changes in order to draw more clear-cut correlations. Before stage 6, CMT orientation was consistent over several cell files, perpendicular to the longitudinal axis

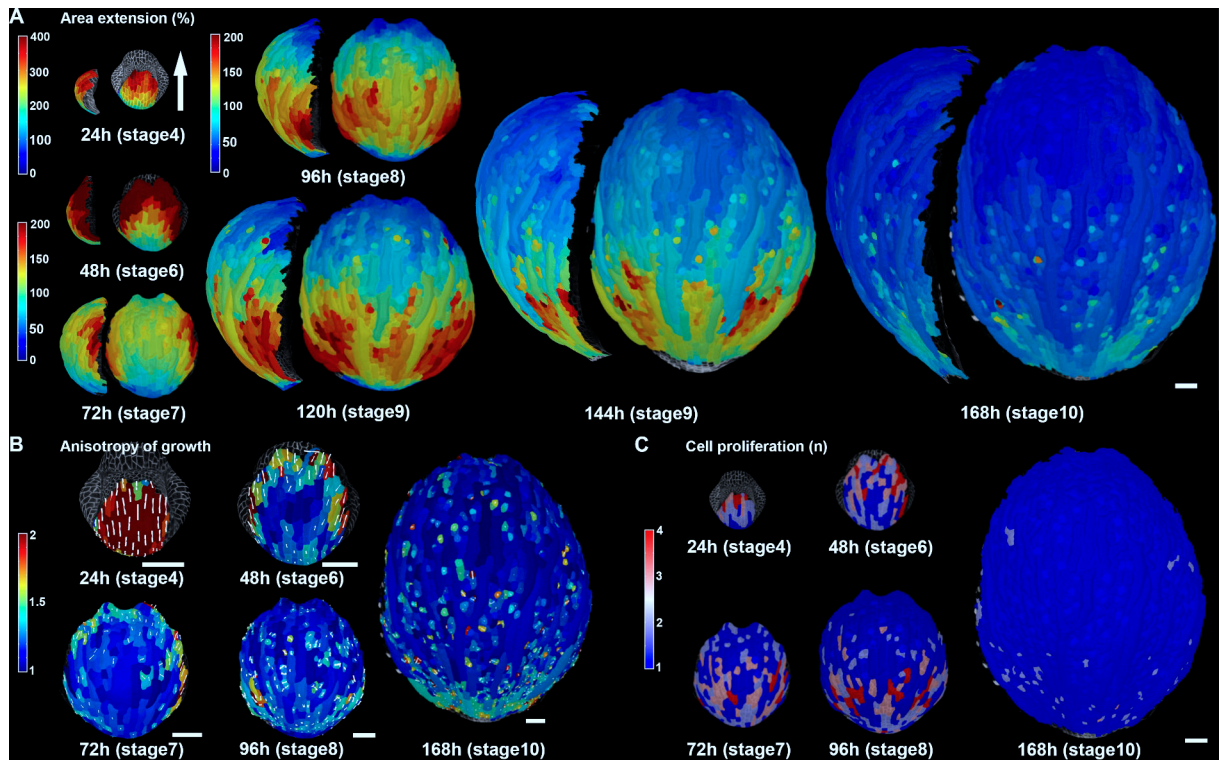


Figure 3.1: Growth analysis for a time-lapse series of an abaxial sepal growing for 168 hours

The white arrow shows the apico-basal axis of the sepal (the tip of the arrow corresponds to the distal tip of the sepal) for all images. (A) Heat map of areal expansion (in %) over consecutive 24-hour intervals, displayed on the second time point (see also Figure 3.5). Developmental stage of the flower was assigned at each time point as in Smyth (1990). Each time point is displayed from the side (left) and from the top (right). Note that the same magnification is used for all stages. Note that averaged growth data are represented: averaging is a similar approach to the Tauriello displacement field (Tauriello et al., 2015) and has a similar effect, i.e. smoothing out the noise to identify underlying trends. (B-C) Images of selected time points from the image sequence displayed in (A). (B) Anisotropy of growth calculated as deformation in maximal growth direction (Principal Growth Direction, PDG_{max}) divided by deformation in minimal growth direction (PDG_{min}). White bars represent direction of maximal growth for cells displaying growth anisotropy above 20%. (C) Cell proliferation over 24 hours displayed for selected time points. Color scale: number of daughter cells that arose from a single cell within the previous 24 hours. Scale bars 50 μm. See also Figure 3.5.

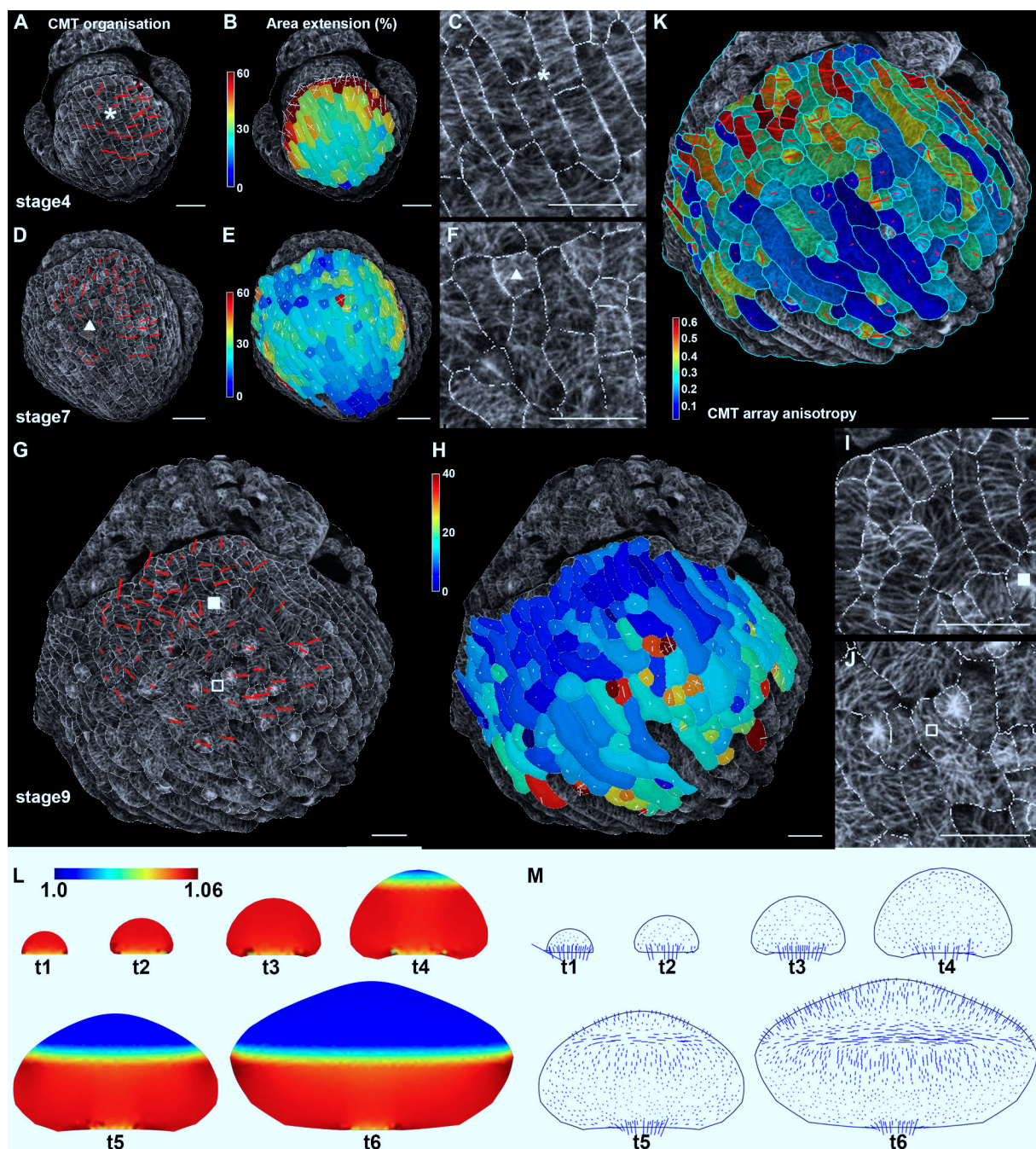


Figure 3.2: A stereotypical growth and cortical microtubule pattern prescribed a mechanical stress pattern at the tip

(A, D and G) CMT organization at the surface of the abaxial sepal (see also Figure 3.6). The direction and length of the red bars indicate the average orientation and anisotropy of CMTs in each cell, respectively. (B, E and H) Heat map of areal expansion (%) over 24-hour intervals displayed on the first time point. Principal directions of growth (PDGs) are indicated in white for expansion and in red for shrinkage. (C, F and I, J) Details of CMT organization in regions highlighted with a white symbol in (A, D and G) respectively. (K) Heat map of the anisotropy of CMT arrays presented in (G). Scale bar 20 μm . (L and M) Mechanical simulation of a growing sepal (successive time points), without any mechanical feedback. Areal growth rates (L) as well as stress direction and magnitude (M) are represented. Scale is identical for all time points in the simulation. See also Figure 3.6.

of the sepal (Figure 3.2A-C, $n>10$). This orientation is also consistent with the predominant longitudinal growth direction at that stage (see Figure 3.1B), compatible with the role of CMTs in guiding cellulose deposition, and thus in channeling growth direction. Then, at stage 7, when growth became more isotropic, we observed that the CMT network also became more isotropic (Figure 3.2D-F, $n>10$), again consistent with a scenario in which growth direction mainly depends on CMTs. At stage 9, the correlation between CMT orientation and growth was however only partially maintained (Figure 3.2G and H, $n>10$): whereas isotropic growth in the center of the sepal correlated with isotropic CMT orientations (Figure 3.2J), CMTs in several cell layers at the slow isotropically growing tip were well aligned, tangentially to the sepal edge (Figure 3.2I). Importantly, microtubule arrays at the tip became more anisotropic, even though growth became slower and more isotropic (Figure 3.2K). Proximal and side views of growing sepals provided consistent patterns (Figure 3.6C and D).

It is well established that CMTs orient according to cell geometry, i.e. along the longitudinal axis of the cell, when growth stops in the hypocotyl (Lloyd, 2011). As CMTs remain predominantly transverse at the tip (Figure 3.2I), we next explore whether that CMT behavior at the tip may be better explained by a supracellular cue (Hamant et al., 2008, Jacques et al., 2013, Sampathkumar et al., 2014).

3.3.3 The sepal growth pattern prescribes a mechanical stress pattern

Many supracellular cues may be involved in prescribing such a specific microtubule behavior at the sepal tip. Here we investigated whether growth-derived mechanical stress may be one of these cues. CMTs have indeed been found to orient along maximal tensile stress direction in meristem, cotyledons and immature seeds (Creff et al., 2015, Hamant et al., 2008, Sampathkumar et al., 2014).

To test this hypothesis, we built a continuous two-dimensional mechanical model of the sepal that accounts for the surface walls of the epidermis and we aimed at simulating stage 7 onwards. The simulations were initialized with a half-disk shape. At a given time point, the system is assumed to be elastic and the elastic modulus increases from the basis to the tip of the sepal so as to mimic stiffening associated with maturation; as we observed a sharp decay in growth rate at the tip of sepals from stage 8 onwards, we assumed the extent of the gradient to be bigger than the initial size of the simulated sepal and the increase in stiffness to be 10-fold. The base of the sepal is fixed and turgor pressure is applied perpendicularly to the remainder of the boundary; equilibrium displacements are computed using the finite element method (for details, see Experimental procedures), yielding an equilibrium shape with a greater area than the initial shape. Growth is modeled incrementally: the equilibrium shape of the previous step is taken in the following step as the initial shape to which turgor is applied again (Kuchen et al., 2012). This leads to a succession of configurations with increasing area (Figure 3.2L), simulating sepal growth. As expected from the gradient in stiffness (Bassel et al., 2014, Lockhart, 1965), we

observed a distal region with reduced growth rates, and that covered more and more of the simulated sepal (Figure 3.2L). As spatial differences in growth rate can induce mechanical stress, we examined the orientation of the main stress (Figure 3.2M) and found a pattern of transverse tensile stress at the proximal part of the stiff region.

To test whether the emergence of such a stress pattern depends on the model design, we also developed a model variant in which elastic properties are constant over the whole sepal and differential growth is instead implemented by a gradient in plastic properties. The corresponding simulations provided qualitatively similar results, i.e. transverse tensile stress at the border between the more or less plastic regions (Figure 3.7B and C).

These results thus provide a scenario in which a growth gradient can generate transverse tensile stress at the border between the two growing domains. In turn these stresses may coordinate cell behavior. Interestingly, this predicted pattern of stress matches the transverse orientation of CMTs at the sepal tip (see Figure 3.2G, I and K). Therefore, these data are consistent with the following scenario: first, CMTs channel the sepal growth direction; then, as a growth gradient appears, tensile stresses are building up at the tip of the sepal, which in turn would lock the CMTs in a tangential orientation at the tip, restricting radial growth of the sepal at the tip.

3.3.4 CMTs align along maximal tensile stress in growing sepals

To test this hypothesis, we performed mechanical perturbations and checked whether CMTs would align along the new stress pattern.

First, we performed compression experiments. Young floral buds were placed under a coverslip for 3 hours, and microtubule orientation was recorded before and after compression (Figure 3.3A-I, $n=6$). As observed in cotyledons with the same set-up (Sampathkumar et al., 2014), we found that CMTs became hyperbundled in the compressed part of the sepal (Figure 3.3E), while CMTs in the non-compressed sides of the sepal seemed unaffected (Figure 3.3F). The response was reversible, demonstrating that the microtubule hyperbundling response was not caused by cell death (Figure 3.3H).

To further test the impact of mechanical stress on sepal shape, we next induced a transient phase of isotropic growth by depolymerizing CMTs in the sepal and observe the resulting sepal shape and microtubule behavior. We reasoned that such a treatment should enhance growth rate in the sepal transverse direction, when compared to the untreated sepal, and thus the anisotropy and magnitude of mechanical stress at the tip.

Sepals were treated with $20\mu\text{g/ml}$ oryzalin for 3 hours, and this was sufficient to deplete most of the microtubules for a period of 24 hours (Figure 3.3J-N, $n=10$). As observed in the shoot apical meristem, this did not impact the pattern of growth rate (Hamant et al., 2008): the tip of the sepal still experienced slow growth after oryzalin treatment (Figure 3.3M). As expected, oryzalin treatment also amplified growth isotropy in the sepal (Figure 3.3K and M). CMTs

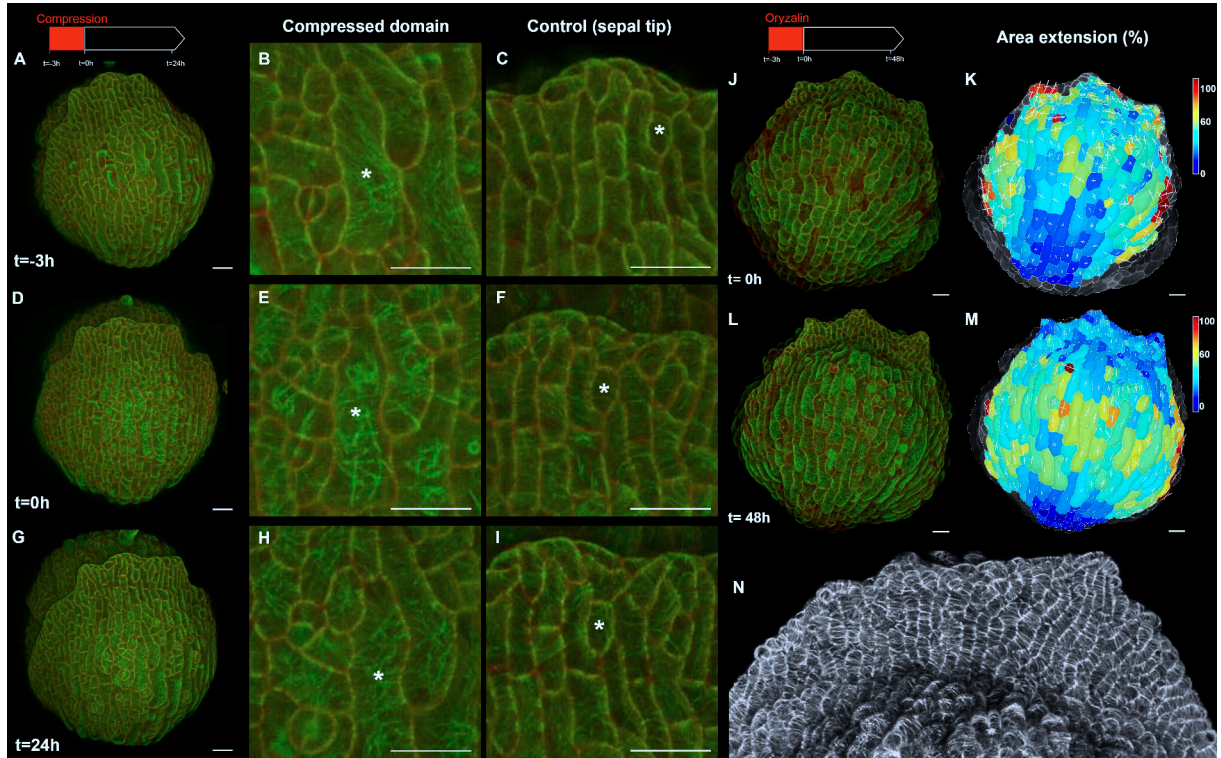


Figure 3.3: CMTs align along maximal tensile stress in growing sepals

(A to I) Compression of abaxial sepal results in the reversible apparent bundling of CMTs. A white star is added to ease the observation of cell lineage in the different time-points. (A, D and G) Live imaging of an abaxial sepal before (A) and after compression (D and G). (B, E and H) Close-up of CMT apparent bundling response in the compressed domain. (C, F and I) Close-up of the CMT behavior in the uncompressed domain (control). (J to N) Effect of oryzalin treatment on CMT orientation and growth pattern. (J and L) Live imaging of abaxial sepal after oryzalin treatment. (K and M) Heat map of areal expansion (%) over 24 hours interval displayed on the first time point. Principal directions of growth (PDGs) are indicated with expansion in white and shrinkage in red. (N) Close-up of the tip of the abaxial sepal 48h after oryzalin treatment showing a supracellular CMT alignment at the tip. Scale bar 20 μm . See also Figure 3.7.

did repolymerize in this context, and the first aligned CMT arrays could be observed 48 hours after oryzalin treatment. Strikingly, CMTs followed a clear-cut supracellular alignment at the tip and isotropic orientations in the center of the sepal (Figure 3.3N), matching the predicted pattern of stress.

Altogether, these data are consistent with CMTs aligning with maximal tensile stress in the sepal, as shown in other tissues. A scenario in which CMT align at the sepal tip along growth-derived stress is thus plausible.

3.3.5 A mechanical feedback may channel sepal shape

To test whether such a mechanical feedback would be sufficient to affect sepal shape, we incorporated such a hypothesis in our sepal growth model. Because of the similarities between the plastic and elastic model presented above, in the following, we concentrated our efforts on

the growth model that is based on a gradient of elastic properties. We assumed the material to be mechanically anisotropic, so as to represent the anisotropy of cellulose arrays in the cell wall, high anisotropy corresponding to high alignment of cellulose microfibrils and the orientation of the stiffest direction to the main orientation of microfibrils. In order to account for the orientation of CMTs according to stress and the subsequent cellulose synthesis, we assumed that, at each step, the direction of the stiffest direction aligns with the direction of maximal stress in the previous step, and that the level of mechanical anisotropy is an increasing Hill-like function of the stress anisotropy (Figure 3.7A, see Experimental procedures); the level of feedback can be modulated through the two parameters of this Hill-function (sharpness s of response and maximal response α_M). We found that moderate levels of feedback yielded unstable, noisy sepal shapes, consistently with growth heterogeneity observed in a cellular model with similar hypotheses (Uyttewaal et al., 2012). As CMTs exhibit supracellular patterns, we reasoned that such a feedback would contribute to sepal shape only if microtubules primarily respond to the stronger supracellular stress pattern, and less to the local stress pattern, as shown previously in cotyledons (Sampathkumar et al., 2014). Therefore, we assumed that mechanical anisotropy depends on the stress field averaged over the whole sepal. Such spatial averaging may reflect the time it takes for the wall mechanical anisotropy to change and would also account for the stabilization of microtubule orientation by tension (Hamant et al., 2008, Sampathkumar et al., 2014). This yielded more regular shapes. In all cases, mechanical stress was transverse at the proximal part of the slowly growing region, close to the front with the fast growing region (Figure 3.4B, E and H). Promoting feedback strength led to increased mechanical anisotropy in the transverse orientation in the upper part of the sepal (Figure 3.4C, F and I). As feedback strength increased, we found that the tip became more and more triangular (Figure 3.4A, D and G; see Figure 3.2L for no feedback at all). For higher feedback level, we found that the tip was sharper and the sepal was narrower (Figure 3.4G). The predicted pattern of mechanical anisotropy is comparable to observed CMT alignment at the very tip of the sepal, when a sharp growth gradient appears with the tip slowing down its growth (see Figure 3.2G-I). At later stages however, the CMT pattern looks more heterogeneous. Such noisy patterns may in part reflect local heterogeneities in growth rates, and thus in mechanical stress.

To check whether the main conclusion from the simulations depend on the choice of parameters, we tested different types of gradients in model variants: a larger linear gradient, a quadratic gradient, a sigmoid gradient and a double gradient was implemented and although simulations provided quantitatively different results, they were all qualitatively similar: when the feedback strength increased, the tip became more triangular and the sepal became narrower (Figure 3.7). Altogether this confirms that growth-derived stress may impact sepal shape.

To test these conclusions experimentally, we used two mutants impaired in microtubule dynamics to modify the response of the sepal cells to mechanical perturbations. The CMT response to stress depends on katanin-driven microtubule severing activity (Sampathkumar et al., 2014, Uyttewaal et al., 2012). First, we verified that mutants with reduced microtubule severing activity slowed down their CMT response to mechanical stress in the sepal. To do so, we

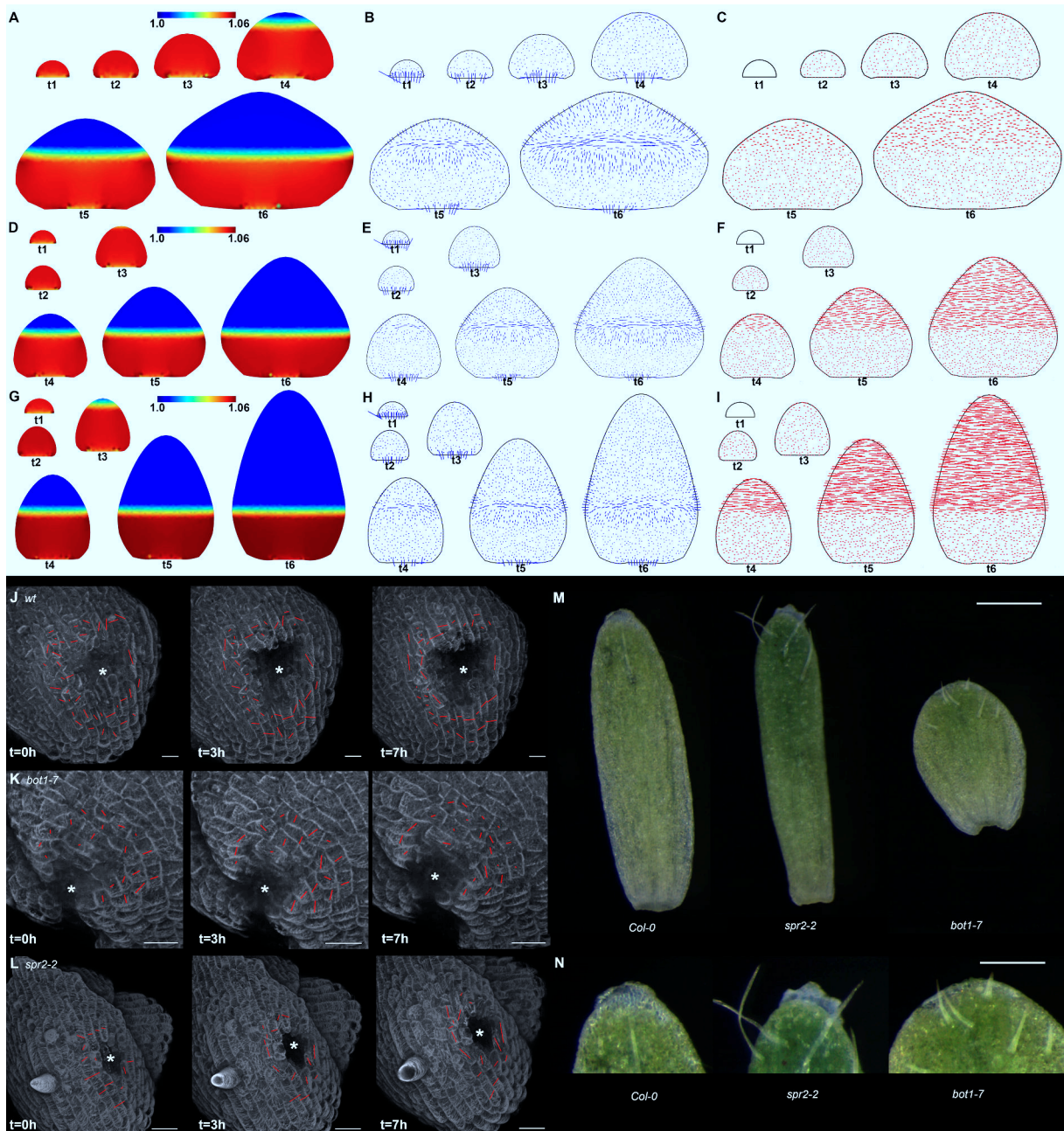


Figure 3.4: A mechanical feedback may channel sepal shape

(A-C) Mechanical simulation of a growing sepal, with a weak mechanical feedback on growth direction ($s = 6, \alpha_M = 2$). The areal growth rate (A), the stress direction and magnitude (B) and the resulting mechanical anisotropy (C) are represented. Scale is identical for all time points. (D-F) Mechanical simulation of a growing sepal, with a moderate mechanical feedback on growth direction ($s = 20, \alpha_M = 2$). The areal growth rate (D), the stress direction and magnitude (E) and the resulting mechanical anisotropy (F) are represented. Scale is identical for all time points. (G-I) Mechanical simulation of a growing sepal, with a strong mechanical feedback on growth direction ($s = 20, \alpha_M = 3.5$). The areal growth rate (G), the stress direction and magnitude (H) and the resulting mechanical anisotropy (I) are represented. Scale is identical for all time points. (J-L) Live imaging of CMT response after mechanical ablation in different genotypes. (J) Ablation induces a circumferential orientation of microtubule arrays around the site of ablation in WT. (K) The CMT response to ablation is slower in the *bot1-7* mutant. (L) The CMT response to ablation occurs earlier in the *spr2-2* mutant: a full CMT reorientation was visible as early as 3 hours after ablation. The direction and the length of the red bars indicate the average orientation and anisotropy of CMTs in each cell, respectively. Scale bar $20 \mu\text{m}$. (M and N) Mature sepals in the wild-type (*Col-0*), *bot1-7* and *spr2-2* mutants. Scale bar 1 mm. (N) Close-up of the tip of mature sepals in the corresponding genotype. Scale bar 0.5 mm. See also Figure 3.8.

performed large-scale ablations in the *bot1-7* katanin allele. As expected, a circumferential reorientation of the CMTs could be detected 3 hours after ablation in the WT (Figure 3.4J, $n>10$; Figure 3.8A), whereas the CMT reorientation was slower and less obvious in the *bot1-7* mutant (Figure 3.4K, $n>10$). To further test the conclusions of the model, we also required a mutant with an increased microtubule response to mechanical stress. SPIRAL2/TORTIFOLIA was proposed to prevent microtubule severing at the site of crossing over (Buschmann et al., 2004, Shoji et al., 2004, Wightman et al., 2013); thus, in a *spr2* mutant, we would expect an enhanced response to mechanical perturbations because microtubule severing and dynamics is promoted. As predicted, CMT array were oriented circumferentially around the ablation in *spr2-2*. Interestingly, this happened earlier than in the WT as full CMT reorientation was accomplished as early as 3 hours after ablation (Figure 3.4L, $n=8$). Note that cells with well aligned CMTs tend to reorient their CMT arrays more slowly than cells with more random CMT orientations in the wild type, consistent with the promotion of CMT reorganization by crossovers (see e.g. (Atkinson et al., 2014, Sambade et al., 2012, Vineyard et al., 2013, Zhang et al., 2013)). This differential response was observed in response to mechanical perturbations in meristematic cells with different microtubule patterns before ablation (Uyttewaal et al., 2012). Although CMTs were well aligned in all cells of the *spr2-2* sepals before ablation (Figure 3.4L, left panel), CMTs still reoriented faster than the wild type, thus further confirming that this mutant exhibits an increased microtubule response to mechanical stress. Altogether, this provides a series of genotypes in which the effects of an enhanced (*spr2-2*) or reduced (*bot1-7*) mechanical feedback on CMT can be analyzed.

We also noticed that the sepal shapes of *bot1-7* and *spr2-2* seem to support our model’s prediction, that modulating the response of CMTs to mechanical stress should affect the final shape of the tip (Figure 3.4M and N, $n>10$). While the tip was smooth and rounded in *bot1-7*, the tip of *spr2-2* sepals formed triangular shapes, which is consistent with a hyper-response of CMTs at the tip, as predicted by our model (compare Figure 3.4A, D, G with Figure 3.4M and N).

We also observed that *spr2-2* sepals were narrower than *bot1-7*. While this is consistent with our model predictions, because of the complexity and heterogeneity of such a large tissue, it is likely that other players are also involved. In particular, in addition to the regulators of cellulose deposition and associated mechanical feedback, sepal shape also relies on large-scale biochemical gradients. Although the presence of a genetic “polarizer” remains to be formally demonstrated in such tissues (Cui et al., 2010, Green et al., 2010), it may add another layer of complexity to this picture, potentially adding robustness to sepal shapes in parallel to the mechanical feedback described here (Figure 3.8B-D). Altogether, our results show that the modulation of the microtubule response to mechanical stress can affect the shape of the sepal tip, consistent with a role of mechanical signals in channeling organ shape.

3.4 Discussion

Our study suggests that differential growth during sepal development generates a stress pattern that feeds back on CMT orientation and further channels the growth pattern, notably at the sepal tip. Albeit at a different scale, this result echoes the work conducted on shoot apical meristems, where it was shown that differential growth between adjacent cells also generates mechanical conflicts that in turn further promotes the maintenance of growth heterogeneity and the competence to generate marked differential growth during organogenesis (Uyttewaal et al., 2012). We propose that the microtubule-tension feedback operating at the tip of the sepal functions as a shape sensing mechanism: by resisting tangential tension, microtubules hinder further transverse expansion of the sepal; this may be the first step leading to growth arrest at the tip. Interestingly, in the shoot meristem, the domain that exhibits such a strong supracellular microtubule alignment is predicted to be under high tensile stresses. In that domain, cells grow at a very low rate and mostly in the direction of maximal stress (Burian et al., 2013), consistent with a scenario in which cells end up reducing their growth by resisting the increasing maximal stress.

Note that we considered the growth of the abaxial sepal, independent from the contact of its neighbours. It is possible that other organs within the flower, and most notably the opposing adaxial sepal, adds another mechanical input, by further restricting the expansion of the abaxial sepal. This type of mechanical constraint within the developing leaf bud was proposed to play a role in shaping folded leaves (Couturier et al., 2012, 2009, 2011).

There is now accumulating evidence that mechanical signals play a key role in controlling cell division, cell polarity and cell fate in animal single cells (Dalous et al., 2008, Engler et al., 2006, Houk et al., 2012, Minc et al., 2011, Swift and Discher, 2014, Théry et al., 2007, Verkhovsky et al., 1999). This also implies that mechanical signals largely contribute to shaping individual cells. Although this remains to be fully shown, mechanical signals also seem to shape plant cells (e.g. (Lynch and Lintilhac, 1997, Sampathkumar et al., 2014)). The contribution of mechanical signals in shaping multicellular objects is more difficult to tackle because of the added complexity, notably in animal tissues where cells can migrate/intercalate and because growth can be very fast during the main morphogenetic events of embryogenesis. Yet, mechanical forces have been involved in promoting major multicellular shape changes, notably in *Drosophila* (Aigouy et al., 2010, Collinet et al., 2015, Lecuit et al., 2011, Pouille et al., 2009), *Ciona* (Sherrard et al., 2010), Zebrafish (Brunet et al., 2013, Heckel et al., 2015) or *Caenorhabditis* (Zhang et al., 2011a). However, the role of forces in tissues does not seem to be restricted to the channeling of existing morphogenetic events, as they have been proposed to trigger growth arrest through their shape-sensing role (Aegerter-Wilmsen et al., 2007, Hufnagel et al., 2007, Shraiman, 2005) and even to initiate major developmental steps, such as mesoderm differentiation (Brunet et al., 2013, Desprat et al., 2008, Farge, 2003). Here we take advantage of the relatively simpler mechanics of plant tissues to show that supracellular mechanical signals do contribute to the formation of organs with consistent shapes, through a microtubule-based growth restriction

process and in parallel to morphogens, despite heterogeneity at the individual cell level. As shown for organ polarity in which mechanical stress has been involved both in plants and animals (Aigouy et al., 2010, Kuchen et al., 2012), we thus propose that mechanical signals act as organ shape sensing factors across kingdoms, triggering growth arrest and generating organs with reproducible shapes.

3.5 Experimental procedures

3.5.1 Plant material and growth conditions

For growth analysis, we used the *pUBQ10::myrYFP* line kindly provided by Raymond Wightman. In this line, myrYFP corresponds to a YFP which is N-terminally modified with a short peptide that is myristoylated and probably acylated (R. Wightman, unpublished). Plants were grown in long day conditions (Vlad et al., 2014). The *p35S::GFP-MBD* (WS-4) and *p35S::GFP-TUA6* were described previously (Hamant et al., 2008, Ueda et al., 1999). The membrane reporter line *pUQ10::Lti6b-2xmCherry* (Col-0) was kindly provided by Yvon Jaillais. The *botero1-7* katanin mutant allele was previously isolated by Bichet et al. (2001) and described in Uyttewaal et al. (2012). The *spiral2-2* mutant allele was previously described in Shoji et al. (2004). For mechanical perturbations and microtubule alignment analysis, plants were grown on soil in a phytotron in short day conditions (8h/16h light/dark period) for 4 weeks and then transferred to long day conditions (16h/8h light/dark period).

3.5.2 Live imaging of the growing abaxial sepal

1 to 2 cm long main inflorescence stems were cut from the plant. To access young buds, the first 10 to 15 flowers were dissected out and the stem was then kept in an apex culture medium (Hamant et al., 2014) supplemented with BAP 900 $\mu\text{g/L}$. 24 hours after dissection, the young buds were imaged with a SP8 Laser-Scanning Confocal Microscope (Leica) using a long distance 25x or 40x water dipping objective (NA: 0.95). During time-lapse imaging plants were kept in $\frac{1}{2}$ MS medium (Vlad et al., 2014) and imaged every 24 hours for up to 8 days. Flowers were dissected at the end of the time-lapse series to determine their growth stage based on internal organs (Smyth, 1990).

3.5.3 Mechanical perturbations

All experiments were performed on dissected apices as described above. Ablations were performed manually using a small needle, as in Uyttewaal et al. (2012). Compression was achieved by placing a coverslip on top of the flower for 3h; the coverslip was then removed carefully for

imaging as in Sampathkumar et al. (2014). Oryzalin treatment were achieved by immersed dissected plants in an aqueous solution containing oryzalin at 20µg/ml for 3h, then washed twice with water, as in Hamant et al. (2008).

3.5.4 Image analysis

Images were processed with MorphoGraphX 3D image analysis software (Barbier de Reuille et al., 2015). Stages of flower growth were determined in the time-lapse series using MorphoGraphX clipping planes to examine internal organs in cross section. In order to better visualize the general growth patterns, the areal growth maps displayed in Figure 3.1 show the growth averaged for each cell and its immediate neighbors, weighted by cell area.

3.5.5 Computational Modeling

We built a continuous mechanical model for sepal morphogenesis, starting from a model previously developed for fission yeast (Bonazzi et al., 2014). Only surface cell walls are modeled, yielding a two-dimensional medium with a prescribed distribution of mechanical properties. Morphogenesis occurs by successive increments in area: the rest shape at step n is inflated by turgor pressure, P , leading to a new equilibrium shape, which is then used as a rest shape for the next step, $n+1$. At each step, the equilibrium configuration is found using the finite element method and the sepal is remeshed so as to keep a roughly constant mesh size. The model was implemented in Freefem++ (Hecht, 2012) and the results were analyzed using Python scripts. In the present study, we accounted for three new ingredients: mechanical anisotropy, mechanical feedback, and gradient in mechanical properties, as detailed hereafter.

Mechanical anisotropy was introduced to account for cellulose fibrils locally more oriented in direction a ; the coordinate system (a, b) may vary spatially. We used the generalized Hooke's law linking the stress tensor σ and the strain tensor ϵ through the elasticity matrix C^1 ,

$$\begin{pmatrix} \sigma_{aa} \\ \sigma_{bb} \\ \sigma_{ab} \end{pmatrix} = C^1 \begin{pmatrix} \epsilon_{aa} \\ \epsilon_{bb} \\ \epsilon_{ab} \end{pmatrix}, C^1 = \begin{pmatrix} A_1 & B & 0 \\ B & A_2 & 0 \\ 0 & 0 & 0 \end{pmatrix},$$

where $A_1 = (1 - \nu)E/((1 + \nu)(1 - 2\nu))(1 + \alpha/2)$, $A_2 = (1 - \nu)E/((1 + \nu)(1 - 2\nu))(1 - \alpha/2)$, $B = \beta\sqrt{A_1 A_2}$, and $C = A/(1 + \nu)$, E being the reduced elastic modulus, ν the reduced Poisson's ratio, α the mechanical anisotropy, and β a non-dimensional modulus ($\beta < 1$ for the elasticity matrix to be well defined). Note that $A_1 > A_2$, meaning that direction a is stiffer than direction b , consistent with the mean orientation of cellulose microfibrils.

To incorporate the mechanical feedback, we first compute the eigenvalues (σ_1 and σ_2 , $\sigma_1 > \sigma_2$) and corresponding eigenvectors (v_1 and v_2) of the stress tensor. In the next step, we set direction

$a = v_1$ and the mechanical anisotropy $\alpha = 2\alpha_M[1 + \exp[-s(\sigma_1 - \sigma_2)/(\sigma_1 + \sigma_2)]] - \alpha_M$. These two equations are similar to previous work (Bozorg et al., 2014). They mean that the next-stiffest direction matches the maximal stress orientation, whereas anisotropy varies between 0 for isotropic stress and its maximal value α_M when the stress is highly anisotropic; s quantifies the steepness of the response to stress.

The starting configuration is always a semi-disk of radius 1.1. In order to account for the observed growth gradient at later stages, we assume a low value of modulus, $E = Y_m E$, in the proximal region delimited by a line at a distance d_m from the sepal basis, a high value of the modulus, $E = Y_M E$, in the distal region delimited by a line at a distance d_M from the sepal basis, and a distance-based linear interpolation of the two values of modulus between these two lines.

We also tested quadratic and sigmoid interpolations of the two values of the modulus, as well as the use of two linear elasticity gradients, with the second one remaining at the tip of the sepal ($d_m^1 = 3$, $d_M^1 = 4$, $d_m^2 = 2$ from the tip, $d_M^2 = 1$ from the tip, $Y^1 = 0.1$ at the bottom, $Y^2 = 0.5$ in the middle, $Y^3 = 1$ at the tip). We also considered the possibility of a molecular polarizer biasing growth toward the longitudinal direction in the proximal region, i.e., before the elasticity gradient. We defined a new elasticity matrix C^2 in addition to the previously defined C^1 , with parameters $E = 3.27$ MPa and $A_1 - A_2 = 0.6$ MPa, and a new parameter γ , such that $C = (1 - \gamma)C^1 + \gamma C^2$. (Thus, γ represents the relative strength of the molecular polarizer.) $\gamma_1 = 0.75$ in the proximal region and $\gamma_2 = 0$ in the distal region. To test whether the observed shapes were due to the artificial increase of the modulus, we also implemented a version where the observed growth gradient was reproduced through differential plasticity (at each time step, a fraction p of the displacement field is kept as a permanent deformation accounting for growth), with no elasticity gradient, where $p_m = 1$ and $p_M = 0.1$.

In the simulations shown here, we used $p = 0.5$ MPa, $E = 3.27$ MPa, $\nu = 0.48$, $\beta = 0.5$, $\alpha_M = 2$ or 3.5 , $s = 6$ or 20 , $Y_m = 0.1$, $Y_M = 1$, $d_m = 3$, $d_M = 4$, and $d_m = 1$, $d_M = 5$ to test for longer gradient. The dimensionless size of the mesh was $1/5$. In addition, we explored a range of other values and found the same qualitative results.

3.6 Supplemental Experimental Procedures

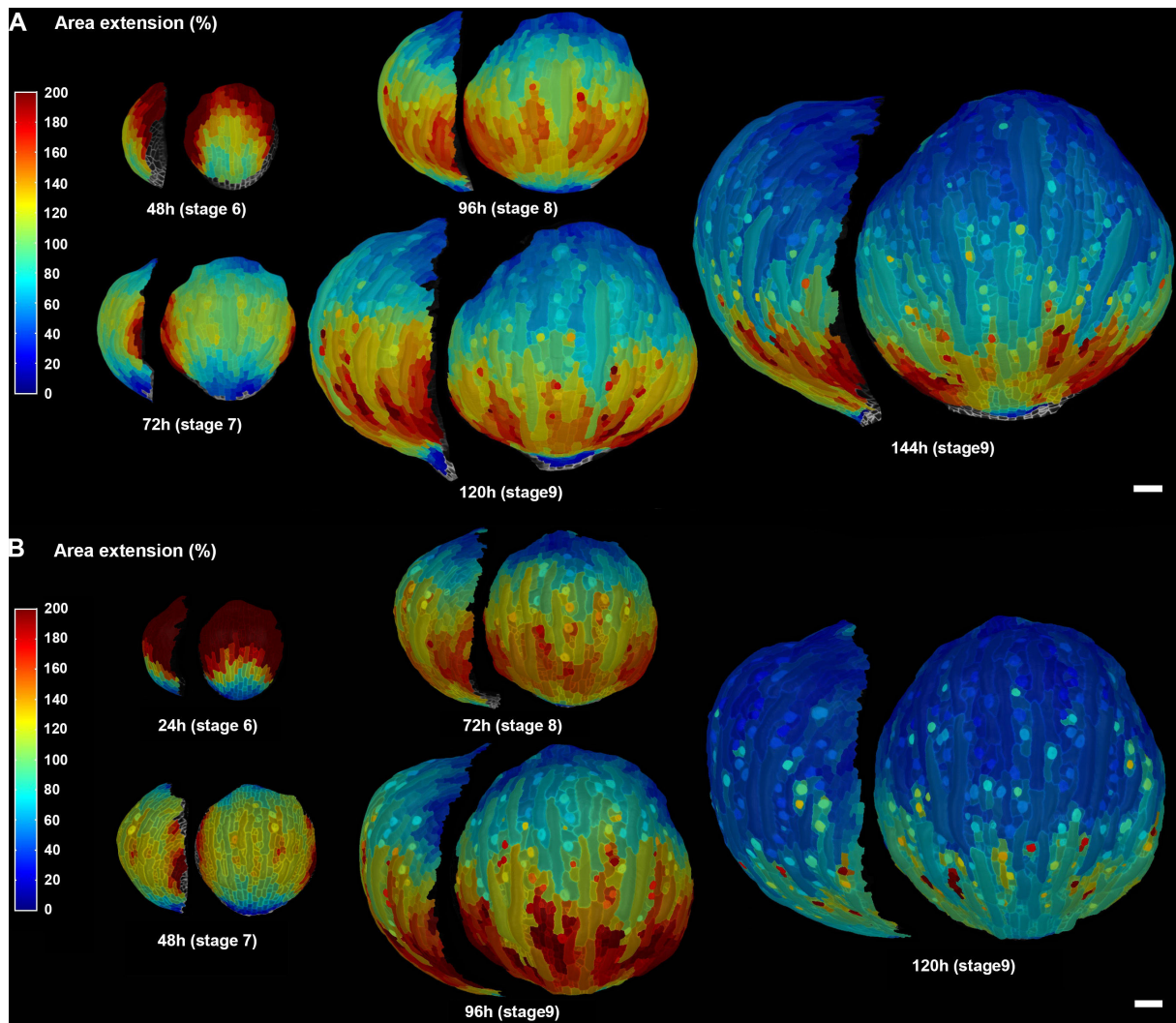


Figure 3.5: Live imaging of two abaxial sepals, related to Figure 3.1

The sepals are viewed from the side (left) and from the top (right). Color scale represents area extension over 24-hour intervals as in Figure 1. Scale bar 50 μm .

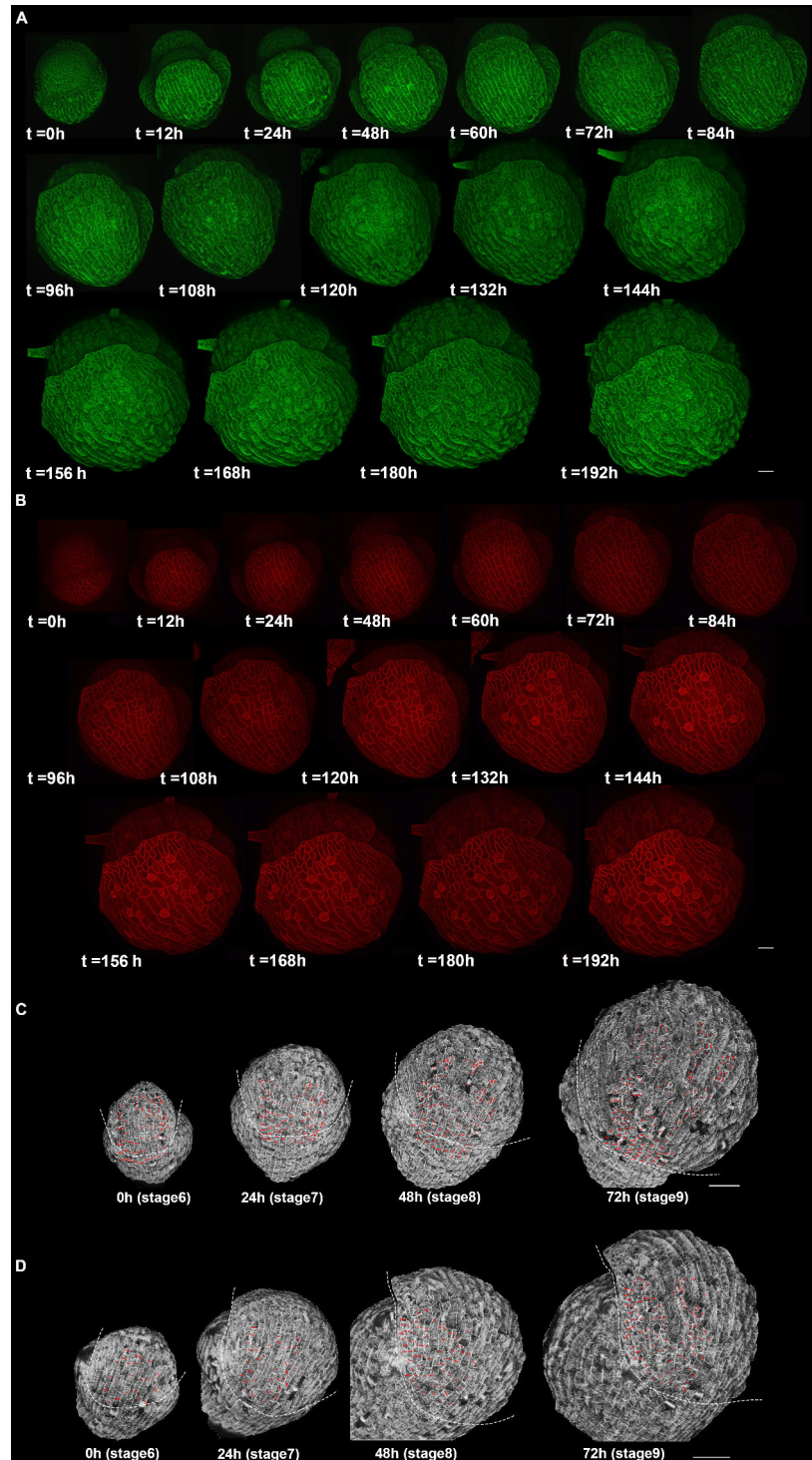


Figure 3.6: Microtubule and cell shapes during sepal growth, related to Figure 3.2

(A) Live imaging CMT behavior at the surface of the abaxial sepal. CMTs were labeled using a *p35S::GFP-MBD* construct. (B) Live imaging of cell shapes at the surface of the same abaxial sepal. Cell contours were labeled using a *pUBQ10::Lti6b-2xmCherry* construct. (C-D) CMT organization at the surface of abaxial sepals, imaged from a proximal (C) and side (D) viewpoints. The direction and length of the red bars indicate the average orientation and anisotropy of CMTs in each cell, respectively. The dashed white line indicates the base and side of the sepal. Scale bar 20 μm

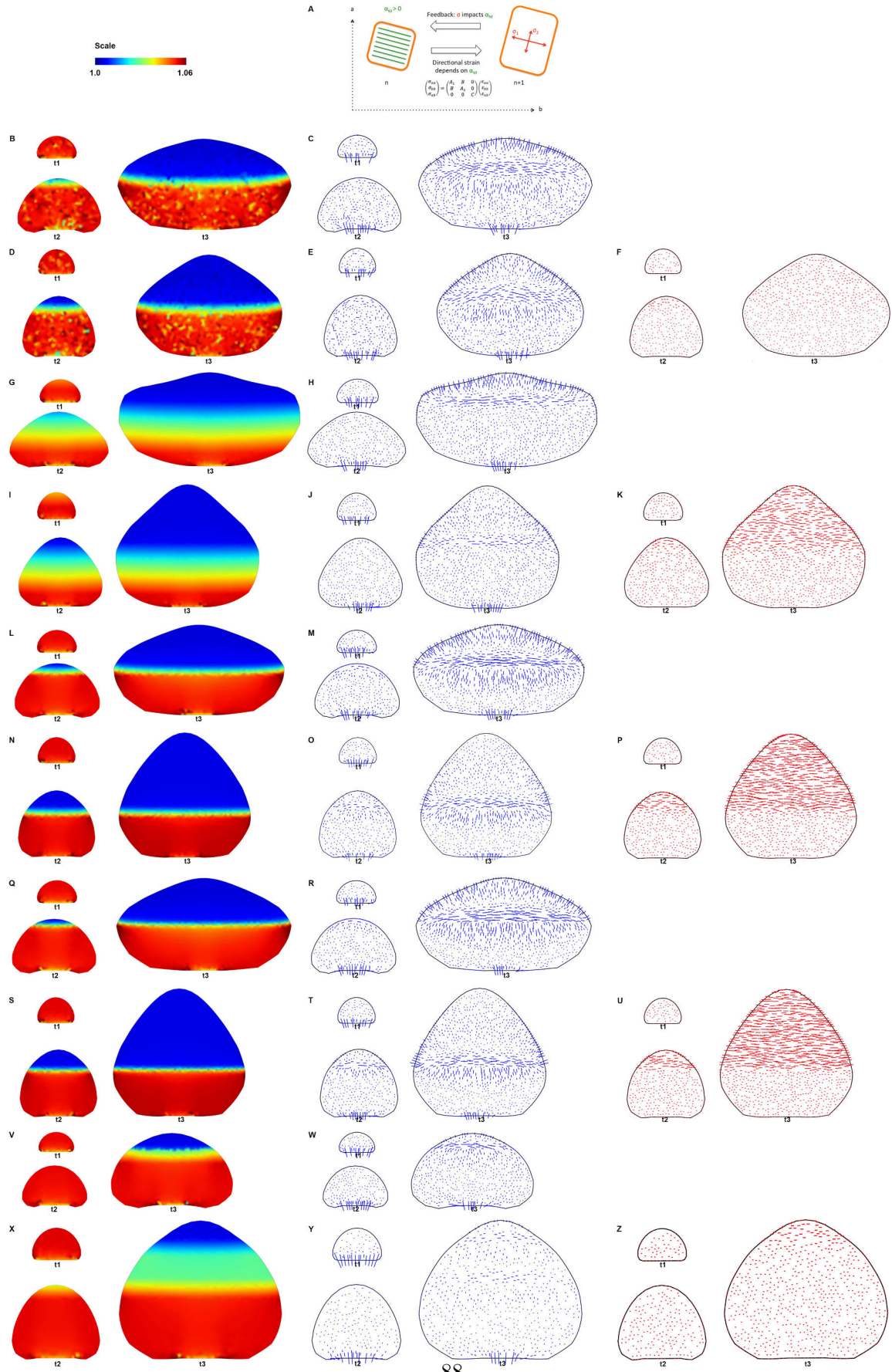


Figure 3.7: Mechanical models of a growing sepal, related to Figure 3.3

Figure 3.7: (A) Implementation of the microtubule - tension feedback in the model. Scale is identical for all time points. The areal growth rate (left column) and the stress direction and magnitude (blue lines, central column) are represented in all simulations. The mechanical anisotropy resulting from the mechanical feedback is represented (red lines, right column). (B-C) Mechanical simulation of a growing sepal with a gradient in plastic properties, and constant elastic properties, without a mechanical feedback on mechanical anisotropy. (D-F) Same as (B-C), with a mechanical feedback ($s = 20$, $\alpha_M = 2$). (G-H) Mechanical simulation of a growing sepal with a large linear gradient in elastic properties without a mechanical feedback on mechanical anisotropy. (I-K) Same as (G-H), with a mechanical feedback ($s = 20$, $\alpha_M = 2$). (L-M) Mechanical simulation of a growing sepal with a quadratic gradient in elastic properties without a mechanical feedback on mechanical anisotropy. (N-P) Same as (G-H), with a mechanical feedback ($s = 20$, $\alpha_M = 2$). (Q-R) Mechanical simulation of a growing sepal with a sigmoid gradient in elastic properties without a mechanical feedback on mechanical anisotropy. (S-U) Same as (Q-R), with a mechanical feedback ($s = 20$, $\alpha_M = 2$). (V-W) Mechanical simulation of a growing sepal with a two-step gradient in elastic properties without a mechanical feedback on mechanical anisotropy. (X-Z) Same as (V-W), with a mechanical feedback ($s = 20$, $\alpha_M = 2$).

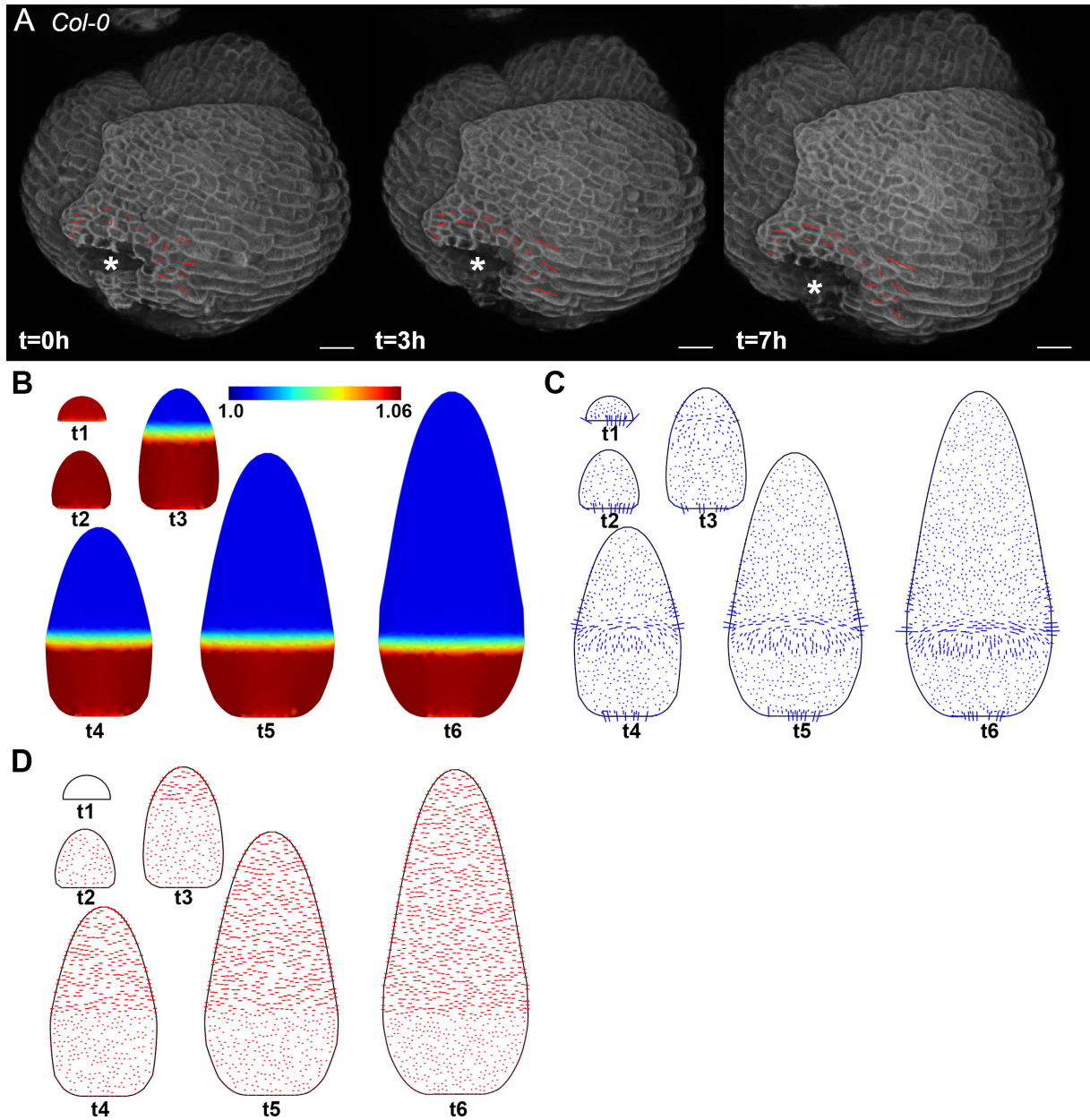


Figure 3.8: A mechanical feedback may channel sepal shape, related to Figure 3.4

(A) Live imaging of CMT response after ablation in the *p35S::GFP-TUA6* line. Ablation induces a circumferential orientation of microtubule arrays around the site of ablation, as observed in the *p35S::GFP-MBD* line. (B-D) Mechanical simulation of a growing sepal with a gradient in elastic properties, with a mechanical feedback on mechanical anisotropy and with a polarizer biasing growth towards the longitudinal direction of the sepal at the lower end. The areal growth rate (B), the stress direction and magnitude (C) and the mechanical anisotropy resulting from the mechanical feedback ($s = 20$, $\alpha_M = 2$) (D) are represented.

4

Discussion

During this project, I showed that the variability of cell wall mechanical properties could lead to organ shape reproducibility in the context of *Arabidopsis thaliana* sepal morphogenesis, and that morphogenesis depended not only on morphogen regulation, but also on the sensing of mechanical cues in the growing organ.

4.1 Variability may have beneficial effects during development

Variability is classically considered deleterious for development, environmental noise leading to lack of developmental robustness and defects in the grown organism. However, variability can be beneficial: for instance, bacteria use variability of gene expression to build population heterogeneity, thus enabling the population to resist to environmental stresses (Blake et al., 2003, Kussell and Leibler, 2005). In this project, I additionally showed that mechanical properties are highly variable in space. If, as it was previously considered, this variability was deleterious for sepal morphogenesis, a mutant displaying more variable organ shape should also display more variable mechanical properties, or any cellular characteristic. To our surprise, however, we established that a mutant with more variable sepal shapes had actually less variable mechanical properties, thus leading us to the conclusion that an increased small scale variability yielded robust shapes. This behavior is permitted by the spatiotemporal averaging of growth. Indeed, an equilibrium rises between the fast growing and the slow growing areas, and as long as the distinct areas are small enough, and changing rapidly enough in time, the growth integrated over time is smooth, even if the differences between areas are high. If the properties do not change fast enough, growth differences become too high to be smoothed-out over time, and if the areas are too large, the differential amount of growth is, as well, too large to be smoothed-out over time, which is what happens in the *vos1* mutant.

Similar spatiotemporal averaging have been shown to improve robustness in diverse systems implying interpreting a fluctuating signal such as in *Drosophila* development (Little et al., 2013, Reeves et al., 2012), bacteria chemoattraction (Dyer et al., 2013, Saunders et al., 2012) and to smooth gene expression in general (Erdmann et al., 2009).

Even if the tackled question in this project is different: how to robustly develop instead of how to robustly read a fluctuating signal, spatiotemporal averaging is in both cases key to smooth

variations and produce reproducible results.

An obvious advantage of having a system that is robust to small scale variations is that this system is much more robust to chance. Indeed, in a system sensitive to very small variability, any stochastic variation or modification of the system would have large consequences. For example, if sepals were characterized by a constant stiffness, if a small area is by chance twice as soft as the rest of the organ, the grown sepal would likely be highly deformed. A naturally variable system will not be as strongly impacted by such modification. Therefore, increasing variability at small scale can be a noticeably effective way to increase robustness in a system.

4.2 Morphogens act in parallel to mechanical signals during morphogenesis

The consensus so far was that morphogenesis is channeled by morphogens, their concentrations and gradients defining growth rates and directions. However, during this project, we showed that morphogenesis could be influenced by mechanical sensing, in parallel to morphogen concentrations and gradients.

4.2.1 Mechanical sensing influences morphogenesis

It has been shown previously that mechanosensing influences cell shape and cytoskeleton behavior (Dalous et al., 2008, Houk et al., 2012, Théry et al., 2007), division orientation (Minc et al., 2011), and cell fate (Engler et al., 2006). In plants, because of the tight link between cytoskeleton and cell wall deposition, cell wall mechanical properties are also ultimately impacted (Hamant et al., 2008, Jacques et al., 2013, Lynch and Lintilhac, 1997, Sampathkumar et al., 2014). In the presented study, modifying the mechanical sensing of cells changed organ shape, meaning that shape is not fully defined by morphogen concentrations and gradients. This result is strengthened by the fact that the presence of trichomes also impact the final shape of the organs, by modifying the mechanical landscape of the sepal (see the Appendix). These studies are still pioneer and this observation needs to be backed up, but this radically new way of appreciating morphogenesis could open new horizons where organs can sense their own shape and modify their growth in consequence, thus fine-tuning their shape to any non-canonical event.

4.2.2 Cell wall sensing could play a role in compensation

We described a process where morphogenesis changes during growth depend on growth output, which is a first step towards understanding compensation. Indeed, compensation is the name given to morphogenesis processes which give rise to phenotypes surprisingly close to the wild-type. For example, a mutant with smaller cells should have smaller leaves than the mutant; but when measured, its leaves were not as small as expected, because the cells had divided more times than in the wild-type. Such behavior was also recorded for mutants displaying larger

cells, and fewer and more cells, which then divide less, or display larger or smaller cells, respectively (Hisanaga et al., 2015). How can the organs sense that they do not have the right size, and change their growth accordingly? Mechanosensing could be this missing link, sensing the size of the developing organ, and altering its morphogenesis to rescue any growth defect. Indeed, it has been shown in other organisms that mechanical sensing had an impact on organ shape and size determination during *Drosophila* wing development (Aegerter-Wilmsen et al., 2007, Hufnagel et al., 2007, Lecuit and Lenne, 2007, LeGoff et al., 2013, Schluck et al., 2013), *C. elegans* development (Zhang et al., 2011b), and that mechanical sensing influenced tumor size (Low et al., 2014, Zeng and Hong, 2008). Consistent with our results, mechanical cues have also been shown to play roles in growth arrest through their shape-sensing roles in *Drosophila* wing discs (Aegerter-Wilmsen et al., 2007, Hufnagel et al., 2007, Shraiman, 2005).

However, the means of mechanical sensing are as not well known in plants as in animals, where the YAP/TAZ family is a well described family of mechanosensors (Dupont et al., 2011). As far as we know, three putative mechanosensors have been identified in plants: the receptor-like kinase FERONIA (Shih et al., 2014) and a previously unknown plasma membrane protein MCA1 (Nakagawa et al., 2007) have been shown to play a role in the transduction of mechanical signals: the mutants show altered Ca^{2+} signalling and reduced touch-specific genes activation in response to mechanical stimuli, as well as the previously unknown plasma membrane protein OSCA1, implied in osmosensing (Yuan et al., 2014).

It would be interesting to directly study the interaction between compensation and mechanical sensing by combining mutants displaying compensation and mutants showing mechanosensing defects, which would help deciphering whether mechanosensing really plays a role in the compensation phenomenon.

4.3 Mechanics and robustness of morphogenesis

With these studies on the influence of the variability of cell wall mechanical properties on shape robustness, and the influence of mechanical feedback on organ shape, the question on how cell wall biochemistry and mechanical feedback influence organ shape reproducibility naturally surface.

4.3.1 Cell wall biochemistry and robustness

During my PhD project, I also investigated whether cell wall biochemistry could influence sepal shape robustness (data not shown). To do so, I did a screen directed towards cell wall modifiers expressed during sepal development to see if one or the other cell wall components had a stronger impact. The cell wall modifiers I tested impacted biosynthesis and regulation of cellulose, hemicellulose and pectin. Because cellulose deposition greatly depends on the interphasic microtubule array, I also tested the influence of microtubule associated proteins on sepal shapes. The mutants were purchased from NASC (Scholl et al., 2000), and genotyped with the

help of my Masters student Justine Chabredier. For each studied mutant, I dissected around 60 abaxial sepals of stage 13 (early opened flowers) over 6 plants, flattened them and took pictures. The pictures were then analyzed to extract morphological information such as length, width, area and perimeter of each sepal, using the same procedure as in Hong et al. (2016). I then compared the mutant sepals to the same amount of sepals from wild-type plants. To reduce the environmental effect, I took control pictures along with every mutant I analyzed. I analyzed more than 130 mutants and took over 10,000 pictures, with the help of the engineer in the team Nelly Dubrulle.

Preliminary results of this study showed that the mutants impacted in cellulose orientation were more likely to display reduced robustness of sepal shape than the other mutants. However, this study does not allow to determine whether pectin and hemicellulose mutants were not more variable than the wild type due to the underlying structure of the cell wall and because pectin and hemicellulose have radically different roles compared to the cellulose; or because the gene families are more redundant, thus explaining the lack of variability phenotype by a compensation from the other genes of the same family.

The *csi1* mutant, affecting cellulose orientation, was selected to be further investigated. The CSI1 protein, also called POM2, links the cellulose synthase complexes to the microtubule, thus leading the cellulose deposition along the microtubules (Bringmann et al., 2012). The mutant displays altered phyllotactic patterns due to the lack of guidance of cellulose deposition by the microtubules (Landrein et al., 2013). A further study of this mutant will, in particular, help linking the variability at smaller scale and the organ shape robustness.

4.3.2 Mechanosensing and robustness

We established that the strength of the mechanical feedback had an influence on sepal shape. Does mechanical feedback influence organ shape robustness? The screen presented in the previous part included the two mutants used to study the influence of mechanical feedback on organ shape: *katanin* and *spiral2*. Both mutants displayed different organ shape and size variability compared to the wild-type, indicating that mechanical feedback could influence organ shape robustness. Furthermore, mechanical feedback loops promote heterogeneity of growth rates and orientations between neighboring cells in the shoot apical meristem of *Arabidopsis thaliana*: differential growth generates mechanical conflicts, which in turn promote growth heterogeneity, and the ability to generate differential growth during morphogenesis (Uyttewaal et al., 2012).

The importance of mechanosensing on robustness in plants have been further demonstrated through the thorough study of the mechanosensor FERONIA. The *feronia* mutant lacks calcium signaling in response to mechanical perturbations, impairing biological responses to mechanical stimuli. The mutant displays root developmental defects: growth is more spatiotemporally variable in *feronia* plants, meaning that FERONIA-linked signalling regulates growth, in response to external as well as internal mechanical cues (Shih et al., 2014). However, the sepal size and shape of the mutant were not significantly more variable than those of the wild-type.

4.4 General conclusion

This work allowed to consider plant morphogenesis with a new light, by both stepping back from the morphogens, and showing that variability could actually enhance reproducibility, which was not previously considered. Moreover, the large amount of collected data on sepal shapes on that many mutants has a lot of work to offer, especially in the more precise analysis of shapes, and in the more thorough study of the different mutants phenotypes – which are for now grouped depending on the impacted cell wall component.

Understanding better the intricate interplay between mechanical properties, mechanical feedback and organ shape robustness and compensation is still a challenge, but this work opens new insights on these questions.

Bibliography

- Abel, S. and Theologis, A. (1996). Early Genes and Auxin Action. *Plant Physiology*, 111(1):9–17.
- Abley, K., Locke, J. C. W., and Leyser, H. M. O. (2016). Developmental mechanisms underlying variable, invariant and plastic phenotypes. *Annals of Botany*, 0:1–16.
- Aegerter-Wilmsen, T., Aegerter, C. M., Hafen, E., and Basler, K. (2007). Model for the regulation of size in the wing imaginal disc of *Drosophila*. *Mechanisms of Development*, 124(4):318–326.
- Aigouy, B., Farhadifar, R., Staple, D. B., Sagner, A., Röper, J.-C., Jülicher, F., and Eaton, S. (2010). Cell flow reorients the axis of planar polarity in the wing epithelium of *Drosophila*. *Cell*, 142(5):773–786.
- Aist, J. R. (1976). Papillae and Related Wound Plugs of plant cells. *Annu. Rev. Phytopathol.*, 14:145–163.
- Albenne, C., Canut, H., Hoffmann, L., and Jamet, E. (2014). Plant Cell Wall Proteins: A Large Body of Data, but What about Runaways? *Proteomes*, 2:224–242.
- Alim, K., Armon, S., Shraiman, B. I., and Boudaoud, A. (2016). Leaf growth is conformal. *Physical Biology*, 13(5):05LT01.
- Ambrose, C., Allard, J. F., Cytrynbaum, E. N., and Wasteneys, G. O. (2011). A CLASP-modulated cell edge barrier mechanism drives cell-wide cortical microtubule organization in *Arabidopsis*. *Nature Communications*, 2(may):430.
- Ambrose, J. C., Shoji, T., Kotzer, A. M., Pighin, J. a., and Wasteneys, G. O. (2007). The *Arabidopsis* CLASP gene encodes a microtubule-associated protein involved in cell expansion and division. *The Plant cell*, 19(9):2763–2775.
- Anastasiou, E., Kenz, S., Gerstung, M., MacLean, D., Timmer, J., Fleck, C., and Lenhard, M. (2007). Control of plant organ size by KLUH/CYP78A5-dependent intercellular signaling. *Developmental cell*, 13(6):843–856.
- Anderson, C. T. (2015). We be jammin’: an update on pectin biosynthesis, trafficking and dynamics. *Journal of experimental botany*, 67(2):495–502.

- Anderson, C. T., Wallace, I. S., and Somerville, C. R. (2012). Metabolic click-labeling with a fucose analog reveals pectin delivery, architecture, and dynamics in Arabidopsis cell walls. *Proceedings of the National Academy of Sciences*, 109(4):1329–1334.
- Andriankaja, M., Dhondt, S., DeBodt, S., Vanhaeren, H., Coppens, F., DeMilde, L., Mühlenbock, P., Skirycz, A., Gonzalez, N., Beemster, G. T. S., and Inzé, D. (2012). Exit from Proliferation during Leaf Development in Arabidopsis thaliana: A Not-So-Gradual Process. *Developmental Cell*, 22(1):64–78.
- Apel, K. and Hirt, H. (2004). Reactive oxygen species: metabolism, oxidative stress, and signal transduction. *Annu. Rev. Plant Biol.*, 55:373–399.
- Armour, W. J., Barton, D. A., Law, A. M., and Overall, R. L. (2015). Differential Growth in Periclinal and Anticlinal Walls during Lobe Formation in Arabidopsis Cotyledon Pavement Cells. *The Plant Cell*, 27(9):2484–2500.
- Atkinson, S., Kirik, A., and Kirik, V. (2014). Microtubule array reorientation in response to hormones does not involve changes in microtubule nucleation modes at the periclinal cell surface. *Journal of experimental botany*, 65(20):5867–5875.
- Audoly, B. and Boudaoud, A. (2003). Self-Similar Structures near Boundaries in Strained Systems. *Physical Review Letters*, 91(8):86105.
- Avery, G. S. (1933). Structure and Development of the Tobacco Leaf. *American Journal of Botany*, 20(9):565–592.
- Bar-Sinai, Y., Julien, J.-D., Sharon, E., Armon, S., Nakayama, N., Adda-Bedia, M., and Boudaoud, A. (2016). Mechanical Stress Induces Remodeling of Vascular Networks in Growing Leaves. *PLOS Computational Biology*, 12(4):e1004819.
- Barbier de Reuille, P., Routier-Kierzkowska, A.-L., Kierzkowski, D., Bassel, G. W., Schüpbach, T., Tauriello, G., Bajpai, N., Strauss, S., Weber, A., Kiss, A., Burian, A., Hofhuis, H., Sapala, A., Lipowczan, M., Heimlicher, M. B., Robinson, S., Bayer, E. M., Basler, K., Koumoutsakos, P., Roeder, A. H., Aegerter-Wilmsen, T., Nakayama, N., Tsiantis, M., Hay, A., Kwiatkowska, D., Xenarios, I., Kuhlemeier, C., and Smith, R. S. (2015). MorphoGraphX: A platform for quantifying morphogenesis in 4D. *eLife*, 4:1–20.
- Barceló, A. R. and Laura, V. G. R. (2009). *Reactive oxygen species in plant cell walls*. Springer.
- Baskin, T. I. (2005). Anisotropic expansion of the plant cell wall. *Annual Review of Cell and Developmental Biology*, 21(1):203–222.
- Bassel, G. W., Stamm, P., Mosca, G., Barbier de Reuille, P., Gibbs, D. J., Winter, R., Janka, A., Holdsworth, M. J., and Smith, R. S. (2014). Mechanical constraints imposed by 3D cellular geometry and arrangement modulate growth patterns in the Arabidopsis embryo. *Proceedings of the National Academy of Sciences of the United States of America*, 111(23):8685–90.

- Bastien, R., Bohr, T., Moulia, B., and Douady, S. (2013). Unifying model of shoot gravitropism reveals proprioception as a central feature of posture control in plants. *Proceedings of the National Academy of Sciences of the United States of America*, 110(2):755–60.
- Bastien, R., Douady, S., and Moulia, B. (2015). A Unified Model of Shoot Tropism in Plants: Photo-, Gravi- and Propio-ception. *PLoS Computational Biology*, 11(2):1–30.
- Bauer, C. R., Li, S., and Siegal, M. L. (2015). Essential gene disruptions reveal complex relationships between phenotypic robustness, pleiotropy, and fitness. *Molecular systems biology*, 11(1):773.
- Beauzamy, L., Fourquin, C., Dubrulle, N., Boursiac, Y., Boudaoud, A., and Ingram, G. (2016). Endosperm turgor pressure decreases during early Arabidopsis seed development. *Development*, 143(18):3295–3299.
- Beauzamy, L., Louveaux, M., Hamant, O., and Boudaoud, A. (2015). Mechanically, the Shoot Apical Meristem of Arabidopsis Behaves like a Shell Inflated by a Pressure of About 1 MPa. *Frontiers in plant science*, 6(November):1038.
- Beauzamy, L., Nakayama, N., and Boudaoud, A. (2014). Flowers under pressure: ins and outs of turgor regulation in development. *Annals of Botany*, 114(7):1517–1533.
- Bell, E., Takeda, S., and Dolan, L. (2009). Reactive oxygen species in growth and development. In *Reactive oxygen species in plant signaling*, pages 43–53. Springer.
- Bichet, A., Desnos, T., Turner, S., Grandjean, O., and Hofte, H. (2001). BOTERO1 is required for normal orientation of cortical microtubules and anisotropic cell expansion in Arabidopsis. *The Plant Journal*, 25(2):137–148.
- Bischofs, I. B. and Schwarz, U. S. (2003). Cell organization in soft media due to active mechanosensing. *Proceedings of the National Academy of Sciences*, 100(16):9274–9279.
- Blake, W. J., Balázsi, G., Kohanski, M. A., Isaacs, F. J., Murphy, K. F., Kuang, Y., Cantor, C. R., Walt, D. R., and Collins, J. J. (2006). Phenotypic consequences of promoter-mediated transcriptional noise. *Molecular cell*, 24(6):853–865.
- Blake, W. J., Kærn, M., Cantor, C. R., and Collins, J. J. (2003). Noise in eukaryotic gene expression. *Nature*, 422(6932):633–637.
- Boerjan, W., Ralph, J., and Baucher, M. (2003). Lignin Biosynthesis. *Annual Review of Plant Biology*, 54(1):519–546.
- Bonazzi, D., Julien, J. D., Romao, M., Seddiki, R., Piel, M., Boudaoud, A., and Minc, N. (2014). Symmetry Breaking in Spore Germination Relies on an Interplay between Polar Cap Stability and Spore Wall Mechanics. *Developmental Cell*, 28(5):534–546.

- Boonstra, J. and Post, J. A. (2004). Molecular events associated with reactive oxygen species and cell cycle progression in mammalian cells. *Gene*, 337:1–13.
- Boudaoud, A. (2003). Growth of Walled Cells: From Shells to Vesicles. *Physical Review Letters*, 91(1):018104.
- Boudon, F., Chopard, J., Ali, O., Gilles, B., Hamant, O., Boudaoud, A., Traas, J., and Godin, C. (2015). A Computational Framework for 3D Mechanical Modeling of Plant Morphogenesis with Cellular Resolution. *PLoS Computational Biology*, 11(1):e1003950.
- Boukhibar, L. M. and Barkoulas, M. (2015). The developmental genetics of biological robustness. *Annals of Botany*, 117(5):699–707.
- Bozorg, B., Krupinski, P., and Jönsson, H. (2014). Stress and strain provide positional and directional cues in development. *PLoS computational biology*, 10(1):e1003410.
- Bozorg, B., Krupinski, P., and Jönsson, H. (2016). A continuous growth model for plant tissue. *Physical Biology*, 13(6):065002.
- Braendle, C. and Félix, M. A. (2008). Plasticity and Errors of a Robust Developmental System in Different Environments. *Developmental Cell*, 15(5):714–724.
- Bringmann, M. and Bergmann, D. C. (2017). Tissue-wide Mechanical Forces Influence the Polarity of Stomatal Stem Cells in Arabidopsis. *Current Biology*, 27(6):1–7.
- Bringmann, M., Li, E., Sampathkumar, A., Kocabek, T., Hauser, M.-T., and Persson, S. (2012). POM-POM2/CELLULOSE SYNTHASE INTERACTING1 Is Essential for the Functional Association of Cellulose Synthase and Microtubules in Arabidopsis. *The Plant Cell*, 24(1):163–177.
- Brisson, L. F., Tenhaken, R., and Lamb, C. (1994). Function of oxidative cross-linking of cell wall structural proteins in plant disease resistance. *The Plant Cell*, 6(December):1703–1712.
- Brunet, T., Bouclet, A., Ahmadi, P., Mitrossilis, D., Driquez, B., Brunet, A.-C., Henry, L., Serman, F., Béalle, G., and Ménager, C. (2013). Evolutionary conservation of early mesoderm specification by mechanotransduction in Bilateria. *Nature communications*, 4.
- Burg, S. P. (1973). Ethylene in plant growth. *Proceedings of the National Academy of Sciences of the United States of America*, 70(2):591–7.
- Burian, A., Ludynia, M., Uyttewaal, M., Traas, J., Boudaoud, A., Hamant, O., and Kwiatkowska, D. (2013). A correlative microscopy approach relates microtubule behaviour, local organ geometry, and cell growth at the Arabidopsis shoot apical meristem. *Journal of experimental botany*, 64(18):5753–5767.

- Burk, D. H. (2001). A Katanin-like Protein Regulates Normal Cell Wall Biosynthesis and Cell Elongation. *the Plant Cell*, 13(4):807–828.
- Burk, D. H. (2002). Alteration of Oriented Deposition of Cellulose Microfibrils by Mutation of a Katanin-Like Microtubule-Severing Protein. *The Plant Cell*, 14(9):2145–2160.
- Buschmann, H., Fabri, C. O., Hauptmann, M., Hutzler, P., Laux, T., Lloyd, C. W., and Schöffner, A. R. (2004). Helical growth of the Arabidopsis mutant *tortifolia1* reveals a plant-specific microtubule-associated protein. *Current Biology*, 14(16):1515–1521.
- Campbell, P. and Braam, J. (1999). Xyloglucan endotransglycosylases: Diversity of genes, enzymes and potential wall-modifying functions. *Trends in Plant Science*, 4(9):361–366.
- Capodicasa, C. (2004). Targeted Modification of Homogalacturonan by Transgenic Expression of a Fungal Polygalacturonase Alters Plant Growth. *Plant Physiology*, 135(3):1294–1304.
- Carpita, N. C., McCann, M. C., and Griffing, L. R. (1996). The Plant Extracellular Matrix : News from the Cell’s Frontier. *The Plant Cell*, 8(9):1451–1463.
- Cassab, G. I. (1998). Plant cell wall proteins. *Annual review of plant physiology and plant molecular biology*, 49(1):281–309.
- Chebli, Y., Kaneda, M., Zerzour, R., and Geitmann, A. (2012). The cell wall of the Arabidopsis pollen tube—spatial distribution, recycling, and network formation of polysaccharides. *Plant Physiology*, 160(4):1940–1955.
- Cheung, A. Y. and Wu, H.-M. (2011). THESEUS 1, FERONIA and relatives: a family of cell wall-sensing receptor kinases? *Current opinion in plant biology*, 14(6):632–41.
- Cho, H.-T. and Cosgrove, D. J. (2000). Altered expression of expansin modulates leaf growth and pedicel abscission in Arabidopsis thaliana. *Proceedings of the National Academy of Sciences*, 97(17):9783–9788.
- Choudhury, S., Panda, P., Sahoo, L., and Panda, S. K. (2013). Reactive oxygen species signaling in plants under abiotic stress. *Plant signaling & behavior*, 8(4):e23681.
- Cieslak, M., Cheddadi, I., Boudon, F., Baldazzi, V., Génard, M., Godin, C., and Bertin, N. (2016). Integrating Physiology and Architecture in Models of Fruit Expansion. *Frontiers in Plant Science*, 7(November):1–19.
- Coen, E., Rolland-Lagan, A.-G., Matthews, M., Bangham, J. A., and Prusinkiewicz, P. (2004). The genetics of geometry. *Proceedings of the National Academy of Sciences*, 101(14):4728–4735.
- Collinet, C., Rauzi, M., Lenne, P.-F., and Lecuit, T. (2015). Local and tissue-scale forces drive oriented junction growth during tissue extension. *Nature cell biology*, 17(10):1247.

- Colombani, J., Andersen, D. S., and Léopold, P. (2012). Secreted peptide Dilp8 coordinates *Drosophila* tissue growth with developmental timing. *Science*, 336(6081):582–585.
- Cooper, T. F., Morby, A. P., Gunn, A., and Schneider, D. (2006). Effect of random and hub gene disruptions on environmental and mutational robustness in *Escherichia coli*. *BMC Genomics*, 7(1):237.
- Corson, F., Henry, H., and Adda-Bedia, M. (2010). A model for hierarchical patterns under mechanical stresses. *Philosophical Magazine*, 90(1-4):357–373.
- Cosgrove, D. J. (1985). Cell wall yield properties of growing tissue : evaluation by in vivo stress relaxation. *Plant physiology*, 78(2):347–356.
- COSGROVE, D. J. (1993). Wall extensibility: its nature, measurement and relationship to plant cell growth. *New Phytologist*, 124(1):1–23.
- Cosgrove, D. J. (1999). Enzymes and other agents that enhance cell wall extensibility. *Annual Review of Plant Physiology and Plant Molecular Biology*, 50(1):391–417.
- Cosgrove, D. J. (2005). Growth of the plant cell wall. *Nature Reviews Molecular Cell Biology*, 6(11):850–861.
- Cosgrove, D. J. (2016). Catalysts of plant cell wall loosening. *F1000Research*, 5(0):1–13.
- Couturier, E., Brunel, N., Douady, S., and Nakayama, N. (2012). Abaxial growth and steric constraints guide leaf folding and shape in *Acer pseudoplatanus*. *American journal of botany*, 99(8):1289–1299.
- Couturier, E., Du Pont, S. C., and Douady, S. (2009). A global regulation inducing the shape of growing folded leaves. *PloS one*, 4(11):e7968.
- Couturier, E., Du Pont, S. C., and Douady, S. (2011). The filling law: a general framework for leaf folding and its consequences on leaf shape diversity. *Journal of theoretical biology*, 289:47–64.
- Covarrubias, L., Hernández-García, D., Schnabel, D., Salas-Vidal, E., and Castro-Obregón, S. (2008). Function of reactive oxygen species during animal development: passive or active? *Developmental biology*, 320(1):1–11.
- Craft, J., Samalova, M., Baroux, C., Townley, H., Martinez, A., Jepson, I., Tsiantis, M., and Moore, I. (2005). New pOp/LhG4 vectors for stringent glucocorticoid-dependent transgene expression in *Arabidopsis*. *The Plant Journal*, 41(6):899–918.
- Creff, A., Brocard, L., and Ingram, G. (2015). A mechanically sensitive cell layer regulates the physical properties of the *Arabidopsis* seed coat. *Nature Communications*, 6.

- Cui, M.-L., Copsey, L., Green, A. a., Bangham, J. A., and Coen, E. (2010). Quantitative control of organ shape by combinatorial gene activity. *PLoS biology*, 8(11):e1000538.
- Cunha, A., Tarr, P. T., Roeder, A. H. K., Altinok, A., Mjolsness, E., and Meyerowitz, E. M. (2012). Computational analysis of live cell images of the *Arabidopsis thaliana* plant. *Methods Cell Biol*, 110:285–323.
- Dalous, J., Burghardt, E., Müller-Taubenberger, A., Bruckert, F., Gerisch, G., and Bretschneider, T. (2008). Reversal of Cell Polarity and Actin-Myosin Cytoskeleton Reorganization under Mechanical and Chemical Stimulation. *Biophysical Journal*, 94(3):1063–1074.
- Dar, R. D., Hosmane, N. N., Arkin, M. R., Siliciano, R. F., and Weinberger, L. S. (2014). Screening for noise in gene expression identifies drug synergies. TL - 344. *Science (New York, N.Y.)*, 344 VN -(6190):1392–1396.
- Davletova, S., Rizhsky, L., Liang, H., Shengqiang, Z., Oliver, D. J., Coutu, J., Shulaev, V., Schlauch, K., and Mittler, R. (2005). Cytosolic ascorbate peroxidase 1 is a central component of the reactive oxygen gene network of *Arabidopsis*. *The Plant Cell*, 17(1):268–281.
- Day, S. J. and Lawrence, P. A. (2000). Measuring dimensions: the regulation of size and shape. *Development*, 127(14):2977–2987.
- de Lucas, M., Davière, J.-M., Rodríguez-Falcón, M., Pontin, M., Iglesias-Pedraz, J. M., Lorrain, S., Fankhauser, C., Blázquez, M. A., Titarenko, E., Prat, S., de Lucas, M., Davière, J.-M., Rodríguez-Falcón, M., Pontin, M., Iglesias-Pedraz, J. M., Lorrain, S., Fankhauser, C., Blázquez, M. A., Titarenko, E., and Prat, S. (2008). A molecular framework for light and gibberellin control of cell elongation. *Nature*, 451(7177):480–484.
- De Veylder, L., Beeckman, T., Beemster, G. T. S., Krols, L., Terras, F., Landrieu, I., Van Der Schueren, E., Maes, S., Naudts, M., and Inzé, D. (2001). Functional analysis of cyclin-dependent kinase inhibitors of *Arabidopsis*. *The Plant Cell*, 13(7):1653–1668.
- De Vos, D., Vissenberg, K., Broeckhove, J., and Beemster, G. T. S. (2014). Putting Theory to the Test: Which Regulatory Mechanisms Can Drive Realistic Growth of a Root? *PLoS Computational Biology*, 10(10):e1003910.
- Debat, V. and Peronnet, F. (2013). Asymmetric flies. *Fly*, 7(2):70–77.
- Dell, B. and Huang, L. (1997). Physiological response of plants to low boron. *Plant and Soil*, 193:103–120.
- Deprost, D., Yao, L., Sormani, R., Moreau, M., Leterreux, G., Nicolai, M., Bedu, M., Robaglia, C., and Meyer, C. (2007). The *Arabidopsis* TOR kinase links plant growth, yield, stress resistance and mRNA translation. *EMBO reports*, 8(9):864–870.

- Desprat, N., Supatto, W., Pouille, P.-A., Beaurepaire, E., and Farge, E. (2008). Tissue deformation modulates twist expression to determine anterior midgut differentiation in *Drosophila* embryos. *Developmental cell*, 15(3):470–477.
- Dinney, J. R., Yadegari, R., Fischer, R. L., Yanofsky, M. F., and Weigel, D. (2004). The role of JAGGED in shaping lateral organs. *Development*, 131(5):1101–1110.
- Disch, S., Anastasiou, E., Sharma, V. K., Laux, T., Fletcher, J. C., and Lenhard, M. (2006). The E3 Ubiquitin Ligase BIG BROTHER Controls Arabidopsis Organ Size in a Dosage-Dependent Manner. *Current Biology*, 16(3):272–279.
- Donnelly, P. M., Bonetta, D., Tsukaya, H., Dengler, R. E., and Dengler, N. G. (1999). Cell cycling and cell enlargement in developing leaves of Arabidopsis. *Developmental biology*, 215(2):407–19.
- Doupé, D. P., Klein, A. M., Simons, B. D., and Jones, P. H. (2010). The Ordered Architecture of Murine Ear Epidermis Is Maintained by Progenitor Cells with Random Fate. *Developmental Cell*, 18(2):317–323.
- Dumais, J. and Kwiatkowska, D. (2002). Analysis of surface growth in shoot apices. *The Plant Journal*, 31(2):229–241.
- Dumais, J., Shaw, S. L., Steele, C. R., Long, S. R., and Ray, P. M. (2006). An anisotropic-viscoplastic model of plant cell morphogenesis by tip growth. *Int. J. Dev. Biol.*, 50:209–222.
- Dumais, J. and Steele, C. (2000). New Evidence for the Role of Mechanical Forces in the Shoot Apical Meristem. *Journal of plant growth regulation*, 19:7–18.
- Dupont, S., Morsut, L., Aragona, M., Enzo, E., Giulitti, S., Cordenonsi, M., Zanconato, F., Le Digabel, J., Forcato, M., Bicciato, S., Elvassore, N., and Piccolo, S. (2011). Role of YAP/TAZ in mechanotransduction. *Nature*, 474(7350):179–183.
- Dupuy, L., MacKenzie, J., Rudge, T., and Haseloff, J. (2008). A system for modelling cell-cell interactions during plant morphogenesis. *Annals of Botany*, 101(8):1255–1265.
- Dyer, J. M., Savage, N. S., Jin, M., Zyla, T. R., Elston, T. C., and Lew, D. J. (2013). Tracking shallow chemical gradients by actin-driven wandering of the polarization site. *Current Biology*, 23(1):32–41.
- Ebert, M. S. and Sharp, P. A. (2012). Roles for MicroRNAs in conferring robustness to biological processes. *Cell*, 149(3):505–524.
- Elsner, J., Michalski, M., and Kwiatkowska, D. (2012). Spatiotemporal variation of leaf epidermal cell growth: a quantitative analysis of Arabidopsis thaliana wild-type and triple cyclinD3 mutant plants. *Annals of Botany*, 109(5):897–910.

- Endler, A., Kesten, C., Schneider, R., Zhang, Y., Ivakov, A., Froehlich, A., Funke, N., and Persson, S. (2015). A Mechanism for Sustained Cellulose Synthesis during Salt Stress. *Cell*, 162(6):1353–1364.
- Engler, A. J., Sen, S., Sweeney, H. L., and Discher, D. E. (2006). Matrix Elasticity Directs Stem Cell Lineage Specification. *Cell*, 126(4):677–689.
- Epstein, L. and Lamport, D. T. A. (1984). An intramolecular linkage involving isodityrosine in extensin. *Phytochemistry*, 23(6):1241–1246.
- Erdmann, T., Howard, M., and Ten Wolde, P. R. (2009). Role of spatial averaging in the precision of gene expression patterns. *Physical Review Letters*, 103(25):2–5.
- Erickson, R. O. (1976). Modeling of plant growth. *Annual review of plant physiology*, 27:407–434.
- Eshel, I. and Matessi, C. (1998). Canalization, genetic assimilation and preadaptation: a quantitative genetic model. *Genetics*, 149:2119–2133.
- Farge, E. (2003). Mechanical Induction of Twist in the Drosophila Foregut/Stomodaeal Primordium. *Current Biology*, 13(16):1365–1377.
- Fayant, P., Girlanda, O., Chebli, Y., Aubin, C.-E., Villemure, I., and Geitmann, A. (2010). Finite element model of polar growth in pollen tubes. *The Plant cell*, 22(8):2579–2593.
- Felekis, D., Muntwyler, S., Vogler, H., Beyeler, F., Grossniklaus, U., and Nelson, B. (2011). Quantifying growth mechanics of living, growing plant cells in situ using microrobotics. *Micro & Nano Letters*, 6(5):311.
- Fendrych, M., Leung, J., and Friml, J. (2016). Tir1/AFB-Aux/IAA auxin perception mediates rapid cell wall acidification and growth of Arabidopsis hypocotyls. *eLife*, 5(September2016):1–18.
- Ferjani, A., Horiguchi, G., Yano, S., and Tsukaya, H. (2007). Analysis of Leaf Development in *fugu* Mutants of Arabidopsis Reveals Three Compensation Modes That Modulate Cell Expansion in Determinate Organs. *Plant Physiology*, 144(2):988–999.
- Fernandez, R., Das, P., Mirabet, V., Moscardi, E., Traas, J., Verdeil, J.-L., Malandain, G., and Godin, C. (2010). Imaging plant growth in 4D: robust tissue reconstruction and lineaging at cell resolution. *Nature methods*, 7(7):547–53.
- Folta, A., Severing, E. I., Krauskopf, J., van de Geest, H., Verver, J., Nap, J.-P., and Mlynarova, L. (2014). Over-expression of Arabidopsis AtCHR23 chromatin remodeling ATPase results in increased variability of growth and gene expression. *BMC plant biology*, 14(1):76.
- Foreman, J., Demidchik, V., Bothwell, J. H. F., Mylona, P., Miedema, H., Torres, M. A., Linstead, P., Costa, S., Brownlee, C., Jones, J. D. G., Davies, J. M., and Dolan, L. (2003).

- Reactive oxygen species produced by NADPH oxidase regulate plant cell growth. *Nature*, 422(6930):442–446.
- Forouzesh, E., Goel, A., MacKenzie, S. A., and Turner, J. A. (2013). In vivo extraction of Arabidopsis cell turgor pressure using nanoindentation in conjunction with finite element modeling. *Plant Journal*, 73(3):509–520.
- Fozard, J. A., Bennett, M. J., King, J. R., and Jensen, O. E. (2016). Hybrid vertex-midline modelling of elongated plant organs. *Interface Focus*, 6(5):20160043.
- Fraeye, I., Colle, I., Vandevenne, E., Duvetter, T., Van Buggenhout, S., Moldenaers, P., Van Loey, A., and Hendrickx, M. (2010). Influence of pectin structure on texture of pectin-calcium gels. *Innovative Food Science and Emerging Technologies*, 11(2):401–409.
- Franks, P. J., Buckley, T. N., Shope, J. C., and Mott, K. a. (2001). Guard cell volume and pressure measured concurrently by confocal microscopy and the cell pressure probe. *Plant physiology*, 125(4):1577–84.
- Fraser, C. M. and Chapple, C. (2011). The phenylpropanoid pathway in Arabidopsis. *Arabidopsis Book*, 9:e0152.
- Fry, S. C. (1986). Cross-Linking of Matrix Polymers in the Growing Cell Walls of Angiosperms. *Annual Review of Plant Physiology*, 37(1):165–186.
- Fry, S. C. (1998). Oxidative scission of plant cell wall polysaccharides by ascorbate-induced hydroxyl radicals. *The Biochemical journal*, 332 (Pt 2(2):507–515.
- Fry, S. C. (2004). Primary cell wall metabolism: tracking the careers of wall polymers in living plant cells. *New Phytologist*, 161:641–675.
- Gapper, C. and Dolan, L. (2006). Control of Plant Development by Reactive Oxygen Species. *Plant Physiology*, 141(June):341–345.
- Garelli, A., Gontijo, A. M., Miguela, V., Caparros, E., and Dominguez, M. (2012). Imaginal discs secrete insulin-like peptide 8 to mediate plasticity of growth and maturation. *Science*, 336(6081):579–582.
- Geisler, D. A., Sampathkumar, A., Mutwil, M., and Persson, S. (2008). Laying down the bricks: logistic aspects of cell wall biosynthesis. *Current Opinion in Plant Biology*, 11(6):647–652.
- Geitmann, A. (2006). Experimental approaches used to quantify physical parameters at cellular and subcellular levels.
- Geitmann, A. and Parre, E. (2004). The local cytomechanical properties of growing pollen tubes correspond to the axial distribution of structural cellular elements. *Sexual Plant Reproduction*, 17(1):9–16.

- Gibala, M., Kicia, M., Sakamoto, W., Gola, E. M., Kubrakiewicz, J., Smakowska, E., and Janska, H. (2009). The lack of mitochondrial AtFtsH4 protease alters Arabidopsis leaf morphology at the late stage of rosette development under short-day photoperiod. *The Plant journal : for cell and molecular biology*, 59(5):685–99.
- Gibson, G. and Wagner, G. P. (2000). Canalization in Evolutionary Genetics: a Stabilizing Theory? *BIOessays*, 22:372–380.
- Gilroy, S., Suzuki, N., Miller, G., Choi, W. G., Toyota, M., Devireddy, A. R., and Mittler, R. (2014). A tidal wave of signals: Calcium and ROS at the forefront of rapid systemic signaling. *Trends in Plant Science*, 19(10):623–630.
- Giovane, a., Servillo, L., Balestrieri, C., Raiola, A., D’Avino, R., Tamburrini, M., Ciardiello, M. a., and Camardella, L. (2004). Pectin methylesterase inhibitor. *Biochimica et biophysica acta*, 1696(2):245–52.
- Glass, M., Barkwill, S., Unda, F., and Mansfield, S. D. (2015). Endo- β -1,4-glucanases impact plant cell wall development by influencing cellulose crystallization. *Journal of integrative plant biology*, 57(4):396–410.
- Goldberg, R., Morvan, C., Jauneau, A., and Jarvis, M. C. (1996). Methyl-esterification, de-esterification and gelation of pectins in the primary cell wall. *Progress in Biotechnology*, 14(C):151–172.
- Gonneau, M., Desprez, T., Guillot, A., Vernhettes, S., and Höfte, H. (2014). Catalytic subunit stoichiometry within the cellulose synthase complex. *Plant physiology*, 166(4):1709–1712.
- Goriely, A. and Tabor, M. (2003). Self-Similar Tip Growth in Filamentary Organisms. *Physical Review Letters*, 90(10):108101.
- Granier, C. and Tardieu, F. (1998). Spatial and temporal analyses of expansion and cell cycle in sunflower leaves. A common pattern of development for all zones of a leaf and different leaves of a plant. *Plant physiology*, 116(3):991–1001.
- Grant, G. T., Morris, E. R., Rees, D. A., Smith, P. J. C., and Thom, D. (1973). Biological interactions between polysaccharides and divalent cations: The egg-box model. *FEBS Letters*, 32(1):195–198.
- Green, A. a., Kennaway, J. R., Hanna, A. I., Bangham, J. A., and Coen, E. (2010). Genetic Control of Organ Shape and Tissue Polarity. *PLoS Biology*, 8(11):e1000537.
- Green, P. B. and King, A. (1966). A mechanism for the origin of specifically oriented textures in development with special reference to Nitella wall texture. *Australian Journal of Biological Sciences*, 19(3):421–438.

- Greese, B., Wester, K., Bensch, R., Ronneberger, O., Timmer, J., Hülskamp, M., and Fleck, C. (2012). Influence of cell-to-cell variability on spatial pattern formation. *IET Systems Biology*, 6(4):143.
- Grieneisen, V. A., Xu, J., Marée, A. F. M., Hogeweg, P., and Scheres, B. (2007). Auxin transport is sufficient to generate a maximum and gradient guiding root growth. *Nature*, 449(7165):1008–1013.
- Günl, M. and Pauly, M. (2011). AXY3 encodes a α -xylosidase that impacts the structure and accessibility of the hemicellulose xyloglucan in Arabidopsis plant cell walls. *Planta*, 233(4):707–19.
- Gupta, P. B., Fillmore, C. M., Jiang, G., Shapira, S. D., Tao, K., Kuperwasser, C., and Lander, E. S. (2011). Stochastic State Transitions Give Rise to Phenotypic Equilibrium in Populations of Cancer Cells. *Cell*, 146(4):633–644.
- Hall, M. C., Dworkin, I., Ungerer, M. C., and Purugganan, M. (2007). Genetics of microenvironmental canalization in Arabidopsis thaliana. *Pnas*, 104(34):13717–13722.
- Hamant, O., Das, P., and Burian, A. (2014). Time-lapse imaging of developing meristems using confocal laser scanning microscope. *Plant Cell Morphogenesis: Methods and Protocols*, pages 111–119.
- Hamant, O., Heisler, M. G., Jonsson, H., Krupinski, P., Uyttewaal, M., Bokov, P., Corson, F., Sahlin, P., Boudaoud, A., Meyerowitz, E. M., Couder, Y., and Traas, J. (2008). Developmental Patterning by Mechanical Signals in Arabidopsis. *Science*, 322(5908):1650–1655.
- Hamilton, E. S., Jensen, G. S., Maksaev, G., Katims, A., Sherp, A. M., and Haswell, E. S. (2015). Mechanosensitive channel MSL8 regulates osmotic forces during pollen hydration and germination. *Science*, 350(6259):438–441.
- Hartman, J. L. I. V., Garvik, B., and Hartwell, L. (2001). Principles for the Buffering of Genetic Variation. *Science*, 1001(2001):1–5.
- Hayot, C. M., Forouzesh, E., Goel, A., Avramova, Z., and Turner, J. A. (2012). Viscoelastic properties of cell walls of single living plant cells determined by dynamic nanoindentation. *Journal of Experimental Botany*, 63(7):2525–2540.
- He, F., Saunders, T. E., Wen, Y., Cheung, D., Jiao, R., Wolde, P. R. T., Howard, M., and Ma, J. (2010). Shaping a morphogen gradient for positional precision. *Biophysical Journal*, 99(3):697–707.
- Heazlewood, J. L., Tonti-Filippini, J. S., Gout, A. M., Day, D. A., Whelan, J., and Millar, A. H. (2004). Experimental analysis of the Arabidopsis mitochondrial proteome highlights signaling and regulatory components, provides assessment of targeting prediction programs, and indicates plant-specific mitochondrial proteins. *The Plant Cell*, 16(1):241–256.

- Hecht, F. (2012). New development in FreeFem++. *Journal of numerical mathematics*, 20(3-4):251–266.
- Heckel, E., Boselli, F., Roth, S., Krudewig, A., Belting, H.-G., Charvin, G., and Vermot, J. (2015). Oscillatory flow modulates mechanosensitive klf2a expression through trpv4 and trpp2 during heart valve development. *Current biology*, 25(10):1354–1361.
- Hemerly, A., de A Engler, J., Bergounioux, C., Van Montagu, M., Engler, G., Inzé, D., and Ferreira, P. (1995). Dominant negative mutants of the Cdc2 kinase uncouple cell division from iterative plant development. *The EMBO journal*, 14(16):3925.
- Hepler, P. K. and Wayne, R. O. (1985). Calcium and Plant Development. *Annual Review of Plant Physiology*, 36(1):397–439.
- Hervieux, N., Dumond, M., Sapala, A., Routier-Kierzkowska, A.-L., Kierzkowski, D., Roeder, A. H., Smith, R. S., Boudaoud, A., and Hamant, O. (2016). A Mechanical Feedback Restricts Sepal Growth and Shape in Arabidopsis. *Current Biology*, 26(8):1019–1028.
- Hill, J. L., Hammudi, M. B., and Tien, M. (2014). The Arabidopsis cellulose synthase complex: a proposed hexamer of CESA trimers in an equimolar stoichiometry. *The Plant Cell*, 26(12):4834–4842.
- Hisanaga, T., Kawade, K., and Tsukaya, H. (2015). Compensation : a key to clarifying the organ-level regulation of lateral organ size in plants. *Journal of Experimental Botany*, pages 1–9.
- Höhn, S., Honerkamp-Smith, A. R., Haas, P. A., Trong, P. K., and Goldstein, R. E. (2015). Dynamics of a Volvox embryo turning itself inside out. *Physical Review Letters*, 114(17):1–5.
- Holloway, D. M. and Harrison, L. G. (2008). Pattern selection in plants: Coupling chemical dynamics to surface growth in three dimensions. *Annals of Botany*, 101(3):361–374.
- Hong, L., Dumond, M., Tsugawa, S., Sapala, A., Routier-Kierzkowska, A.-L., Zhou, Y., Chen, C., Kiss, A., Zhu, M., Hamant, O., Smith, R. S., Komatsuzaki, T., Li, C.-B., Boudaoud, A., and Roeder, A. H. (2016). Variable Cell Growth Yields Reproducible OrganDevelopment through Spatiotemporal Averaging. *Developmental Cell*, 38(1):15–32.
- Horiguchi, G., Ferjani, A., Fujikura, U., and Tsukaya, H. (2006). Coordination of cell proliferation and cell expansion in the control of leaf size in Arabidopsis thaliana. *Journal of Plant Research*, 119(1):37–42.
- Horiguchi, G., Kim, G., and Tsukaya, H. (2005). The transcription factor AtGRF5 and the transcription coactivator AN3 regulate cell proliferation in leaf primordia of Arabidopsis thaliana. *The Plant Journal*, 43(1):68–78.

- Horiguchi, G. and Tsukaya, H. (2011). Organ size regulation in plants: insights from compensation. *Frontiers in Plant Science*, 2.
- Houchmandzadeh, B., Wieschaus, E., and Leibler, S. (2002). Establishment of developmental precision and proportions in the early *Drosophila* embryo. *Nature*, 415(6873):798–802.
- Houk, A. R., Jilkine, A., Mejean, C. O., Boltyanskiy, R., Dufresne, E. R., Angenent, S. B., Altschuler, S. J., Wu, L. F., and Weiner, O. D. (2012). Membrane tension maintains cell polarity by confining signals to the leading edge during neutrophil migration. *Cell*, 148(1-2):175–188.
- Howell, A. S., Jin, M., Wu, C.-F., Zyla, T. R., Elston, T. C., and Lew, D. J. (2012). Negative Feedback Enhances Robustness in the Yeast Polarity Establishment Circuit. *Cell*, 149(2):322–333.
- Hufnagel, L., Teleman, A. A., Rouault, H., Cohen, S. M., and Shraiman, B. I. (2007). On the mechanism of wing size determination in fly development. *Proceedings of the National Academy of Sciences*, 104(10):3835–3840.
- Ishikawa, T. and Shigeoka, S. (2008). Recent advances in ascorbate biosynthesis and the physiological significance of ascorbate peroxidase in photosynthesizing organisms. *Bioscience, Biotechnology, and Biochemistry*, 72(5):1143–1154.
- Ito, K. and Akiyama, Y. (2005). Cellular functions, mechanism of action, and regulation of FtsH protease. *Annu. Rev. Microbiol.*, 59:211–231.
- Jacobs, A. K., Lipka, V., Burton, R. A., Panstruga, R., Strizhov, N., Schulze-Lefert, P., and Fincher, G. B. (2003). An Arabidopsis Callose Synthase, GSL5, Is Required for Wound and Papillary Callose Formation. *The Plant cell*, 15(11):2503–2513.
- Jacques, E., Buytaert, J., Wells, D. M., Lewandowski, M., Bennett, M. J., Dirckx, J., Verbelen, J.-P., and Vissenberg, K. (2013). MicroFilament Analyzer, an image analysis tool for quantifying fibrillar orientation, reveals changes in microtubule organization during gravitropism. *Plant Journal*, 74(6):1045–1058.
- Jaeger, J., Irons, D., and Monk, N. (2008). Regulative feedback in pattern formation: towards a general relativistic theory of positional information. *Development (Cambridge, England)*, 135(19):3175–83.
- Janska, H., Piechota, J., and Kwasniak, M. (2010). ATP-dependent proteases in biogenesis and maintenance of plant mitochondria. *Biochimica et Biophysica Acta (BBA)-Bioenergetics*, 1797(6):1071–1075.
- Johnston, R. J. and Desplan, C. (2010). Stochastic mechanisms of cell fate specification that yield random or robust outcomes. *Annual review of cell and developmental biology*, 26:689–719.

- Karidas, P., Challa, K. R., and Nath, U. (2015). The tarani mutation alters surface curvature in Arabidopsis leaves by perturbing the patterns of surface expansion and cell division. *Journal of Experimental Botany*, 66(7):2107–2122.
- Kato, Y., Miura, E., Ido, K., Ifuku, K., and Sakamoto, W. (2009). The variegated mutants lacking chloroplastic FtsHs are defective in D1 degradation and accumulate reactive oxygen species. *Plant Physiology*, 151(4):1790–1801.
- Kawade, K., Horiguchi, G., and Tsukaya, H. (2010). Non-cell-autonomously coordinated organ size regulation in leaf development. *Development*, 137(24):4221–4227.
- Kawade, K., Horiguchi, G., Usami, T., Hirai, M. Y., and Tsukaya, H. (2013). ANGUSTIFOLIA3 signaling coordinates proliferation between clonally distinct cells in leaves. *Current Biology*, 23(9):788–792.
- Keckes, J., Burgert, I., Frühmann, K., Müller, M., Kölln, K., Hamilton, M., Burghammer, M., Roth, S. V., Stanzl-Tschegg, S., and Fratzl, P. (2003). Cell-wall recovery after irreversible deformation of wood. *Nature Materials*, 2(12):810–813.
- Kellogg, R. A. and Tay, S. (2015). Noise facilitates transcriptional control under dynamic inputs. *Cell*, 160(3):381–392.
- Kennaway, R., Coen, E., Green, A., and Bangham, J. A. (2011). Generation of diverse biological forms through combinatorial interactions between tissue polarity and growth. *PLoS computational biology*, 7(6):e1002071.
- Kerstens, S., Decraemer, W. F., and Verbelen, J.-p. (2001). Cell Walls at the Plant Surface Behave Mechanically Like Fiber-Reinforced Composite Materials 1. *Plant Physiol.*, 127(October):381–385.
- Kierzkowski, D., Nakayama, N., Routier-Kierzkowska, A.-L., Weber, A., Bayer, E. M., Schorderet, M., Reinhardt, D., Kuhlemeier, C., and Smith, R. S. (2012). Elastic domains regulate growth and organogenesis in the plant shoot apical meristem. *Science (New York, N. Y.)*, 335(6072):1096–9.
- Kim, J. H. and Kende, H. (2004). A transcriptional coactivator, AtGIF1, is involved in regulating leaf growth and morphology in Arabidopsis. *Proceedings of the National Academy of Sciences of the United States of America*, 101(36):13374–13379.
- Kolodziejczak, M., Gibala, M., Urantowka, A., and Janska, H. (2007). The significance of Arabidopsis AAA proteases for activity and assembly/stability of mitochondrial OXPHOS complexes. *Physiologia plantarum*, 129(1):135–142.
- Kuchen, E. E., Fox, S., de Reuille, P. B., Kennaway, R., Bensmihen, S., Avondo, J., Calder, G. M., Southam, P., Robinson, S., Bangham, J. A., and Coen, E. (2012). Generation of

- leaf shape through early patterns of growth and tissue polarity. *Science (New York, N.Y.)*, 335(6072):1092–6.
- Kussell, E. and Leibler, S. (2005). Phenotypic Diversity , Population Growth , and Information in Fluctuating Environments. *Science*, 309(September):2075.
- Kutschera, U. and Niklas, K. J. (2007). The epidermal-growth-control theory of stem elongation: an old and a new perspective. *Journal of plant physiology*, 164(11):1395–1409.
- Kutschera, U. and Schopfer, P. (1986). Effect of auxin and abscisic acid on cell wall extensibility in maize coleoptiles. *Planta*, 167(4):527–535.
- Lachowiec, J., Queitsch, C., and Kliebenstein, D. J. (2016). Molecular mechanisms governing differential robustness of development and environmental responses in plants. *Annals of Botany*, 117(5):795–809.
- Laguna, M. F., Bohn, S., and Jagla, E. A. (2008). The Role of Elastic Stresses on Leaf Venation Morphogenesis. *PLOS Computational Biology*, 4(4).
- Lander, A. D. (2011). Pattern, Growth, and Control. *Cell*, 144(6):955–969.
- Landrein, B., Lathe, R., Bringmann, M., Vouillot, C., Ivakov, A., Boudaoud, A., Persson, S., and Hamant, O. (2013). Impaired cellulose synthase guidance leads to stem torsion and twists phyllotactic patterns in arabidopsis. *Current Biology*, 23(10):895–900.
- Lazan, H., Selamat, M. K., and Ali, Z. M. (1995). beta-Galactosidase, polygalacturonase and pectinesterase in differential softening and cell wall modification during papaya fruit ripening. *Physiologia Plantarum*, 95(1):106–112.
- Lecuit, T. and Lenne, P.-F. (2007). Cell surface mechanics and the control of cell shape, tissue patterns and morphogenesis. *Nature reviews. Molecular cell biology*, 8(8):633–644.
- Lecuit, T., Lenne, P.-F., and Munro, E. (2011). Force generation, transmission, and integration during cell and tissue morphogenesis. *Annual review of cell and developmental biology*, 27:157–184.
- LeGoff, L., Rouault, H., and Lecuit, T. (2013). A global pattern of mechanical stress polarizes cell divisions and cell shape in the growing *Drosophila* wing disc. *Development*, 140(19):4051–4059.
- Lempe, J., Lachowiec, J., Sullivan, A. M., and Queitsch, C. (2013). Molecular mechanisms of robustness in plants. *Current Opinion in Plant Biology*, 16(1):62–69.
- Lerouxel, O., Cavalier, D. M., Liepman, A. H., and Keegstra, K. (2006). Biosynthesis of plant cell wall polysaccharides - a complex process. *Current opinion in plant biology*, 9(6):621–30.

- Levy, A., Erlanger, M., Rosenthal, M., and Epel, B. L. (2007). A plasmodesmata-associated β -1,3-glucanase in Arabidopsis. *Plant Journal*, 49(4):669–682.
- Levy, S. F. and Siegal, M. L. (2008). Network Hubs Buffer Environmental Variation in *Saccharomyces cerevisiae*. *PLoS Biology*, 6(11):e264.
- Li, S., Lei, L., Somerville, C. R., and Gu, Y. (2012). Cellulose synthase interactive protein 1 (CSI1) mediates the intimate relationship between cellulose microfibrils and cortical microtubules. *Plant Signaling & Behavior*, 7(7):714–718.
- Li, X., Cassidy, J. J., Reinke, C. A., Fischboeck, S., and Carthew, R. W. (2009). A MicroRNA Imparts Robustness against Environmental Fluctuation during Development. *Cell*, 137(2):273–282.
- Liang, H. and Mahadevan, L. (2009). The shape of a long leaf. *Proceedings of the National Academy of Sciences of the United States of America*, 106(52):22049–54.
- Liang, H. and Mahadevan, L. (2011). Growth, geometry, and mechanics of a blooming lily. *Proceedings of the National Academy of Sciences of the United States of America*, 108(14):5516–5521.
- Lindeboom, J. J., Nakamura, M., Hibbel, A., Shundyak, K., Gutierrez, R., Ketelaar, T., Emons, A. M. C., Mulder, B. M., Kirik, V., and Ehrhardt, D. W. (2013). A mechanism for reorientation of cortical microtubule arrays driven by microtubule severing. *Science*, 342(6163):1245533.
- Lintilhac, P. M., Wei, C., Tanguay, J. J., and Outwater, J. O. (2000). Ball Tonometry: A Rapid, Nondestructive Method for Measuring Cell Turgor Pressure in Thin-Walled Plant Cells. *Journal of Plant Growth Regulation*, 19(1):90–97.
- Liszkay, A., Kenk, B., and Schopfer, P. (2003). Evidence for the involvement of cell wall peroxidase in the generation of hydroxyl radicals mediating extension growth. *Planta*, 217(4):658–667.
- Little, S. C., Tikhonov, M., and Gregor, T. (2013). Precise developmental gene expression arises from globally stochastic transcriptional activity. *Cell*, 154(4):789–800.
- Lloyd, C. (2011). Dynamic Microtubules and the Texture of Plant Cell Walls. In *International review of cell and molecular biology*, volume 287, pages 287–329. Elsevier Inc., 1 edition.
- Lockhart, J. a. (1965). An analysis of irreversible plant cell elongation. *Journal of theoretical biology*, 8(2):264–275.
- Louveaux, M., Julien, J.-D., Mirabet, V., Boudaoud, A., and Hamant, O. (2016). Cell division plane orientation based on tensile stress in *Arabidopsis thaliana*. *Proceedings of the National Academy of Sciences*, 113(30):E4294–E4303.

- Low, B. C., Pan, C. Q., Shivashankar, G. V., Bershadsky, A., Sudol, M., and Sheetz, M. (2014). YAP/TAZ as mechanosensors and mechanotransducers in regulating organ size and tumor growth. *FEBS Letters*, 588(16):2663–2670.
- Lu, D., Wang, T., Persson, S., Mueller-Roeber, B., and Schippers, J. H. M. (2014). Transcriptional control of ROS homeostasis by KUODA1 regulates cell expansion during leaf development. *Nature communications*, 5(May):3767.
- Lucas, M., Kenobi, K., von Wangenheim, D., Voss, U., Swarup, K., De Smet, I., Van Damme, D., Lawrence, T., Peret, B., Moscardi, E., Barbeau, D., Godin, C., Salt, D., Guyomarc’h, S., Stelzer, E. H. K., Maizel, A., Laplace, L., and Bennett, M. J. (2013). Lateral root morphogenesis is dependent on the mechanical properties of the overlaying tissues. *Proceedings of the National Academy of Sciences*, 110(13):5229–5234.
- Ludevid, D., Höfte, H., Himmelblau, E., and Chrispeels, M. J. (1992). The Expression Pattern of the Tonoplast Intrinsic Protein gamma-TIP in *Arabidopsis thaliana* Is Correlated with Cell Enlargement. *Plant physiology*, 100(4):1633–9.
- Lukowitz, W., Gillmor, C. S., and Scheible, W. R. (2000). Positional cloning in *Arabidopsis*. Why it feels good to have a genome initiative working for you. *Plant physiology*, 123(3):795–805.
- Lynch, T. M. and Lintilhac, P. M. (1997). Mechanical Signals in Plant Development : A New Method for Single Cell Studies. *Developmental Biology*, 256:246–256.
- Maksymowych, R. (1959). Quantitative analysis of leaf development in *xanthium pensylvanicum*. *american journal of botany*, 46(9):635–644.
- Malgat, R., Faure, F., and Boudaoud, A. (2016). A Mechanical Model to Interpret Cell-Scale Indentation Experiments on Plant Tissues in Terms of Cell Wall Elasticity and Turgor Pressure. *Frontiers in Plant Science*, 7(September):1351.
- Manabe, Y., Verhertbruggen, Y., Gille, S., Harholt, J., Chong, S.-L., Pawar, P. M.-a., Mellerowicz, E. J., Tenkanen, M., Cheng, K., Pauly, M., and Scheller, H. V. (2013). Reduced Wall Acetylation proteins play vital and distinct roles in cell wall O-acetylation in *Arabidopsis*. *Plant physiology*, 163(3):1107–17.
- Markovič, O. and Kohn, R. (1984). Mode of pectin deesterification by *Trichoderma reesei* pectinesterase. *Experientia*, 40(8):842–843.
- Martin, A. C., Kaschube, M., and Wieschaus, E. F. (2009). Pulsed contractions of an actin–myosin network drive apical constriction. *Nature*, 457(7228):495–499.
- Masel, J. and Bergman, A. (2003). The evolution of the evolvability properties of the yeast prion [PSI⁺]. *Evolution; international journal of organic evolution*, 57(7):1498–1512.

- Masel, J. and Siegal, M. L. (2009). Robustness: mechanisms and consequences. *Trends in Genetics*, 25(9):395–403.
- Mazurek, M. and Perlin, A. S. (1963). Borate complexing by five-membered-ring vic-diols. *Canadian Journal of Chemistry*, 41(7487):4–6.
- McAdams, H. H. and Arkin, A. (1999). It’s a noisy business! Genetic regulation at the nanomolar scale. *Trends in Genetics*, 15(2):65–69.
- Meiklejohn, C. D. and Hartl, D. L. (2002). A single mode of canalization. *Trends in Ecology and Evolution*, 17(10):468–473.
- Merks, R. M., Guravage, M., Inzé, D., and Beemster, G. T. S. (2011). VirtualLeaf: an Open Source framework for cell-based modeling of plant tissue growth and development. *Plant Physiol*, 155(2):656–666.
- Meyer, H. M. and Roeder, A. H. K. (2014). Stochasticity in plant cellular growth and patterning. *Frontiers in plant science*, 5(September):420.
- Meyer, H. M., Teles, J., Formosa-Jordan, P., Refahi, Y., San-Bento, R., Ingram, G., Jönsson, H., Locke, J. C. W., and Roeder, A. H. K. (2017). Fluctuations of the transcription factor ATML1 generate the pattern of giant cells in the Arabidopsis sepal. *eLife*.
- Mhamdi, A., Queval, G., Chaouch, S., Vanderauwera, S., Van Breusegem, F., and Noctor, G. (2010). Catalase function in plants: a focus on Arabidopsis mutants as stress-mimic models. *Journal of Experimental Botany*, 61(15):4197–4220.
- Micheli, F. (2001). Pectin methylesterases: cell wall enzymes with important roles in plant physiology. *Trends in Plant Science*, 6(9):414–419.
- Miedes, E., Suslov, D., Vandenbussche, F., Kenobi, K., Ivakov, A., Van Der Straeten, D., Lorences, E. P., Mellerowicz, E. J., Verbelen, J. P., and Vissenberg, K. (2013). Xyloglucan endotransglucosylase/hydrolase (XTH) overexpression affects growth and cell wall mechanics in etiolated Arabidopsis hypocotyls. *Journal of Experimental Botany*, 64(8):2481–2497.
- Miedes, E., Zarra, I., Hoson, T., Herbers, K., Sonnewald, U., and Lorences, E. P. (2011). Xyloglucan endotransglucosylase and cell wall extensibility. *Journal of Plant Physiology*, 168(3):196–203.
- Milani, P., Braybrook, S. A., and Boudaoud, A. (2013). Shrinking the hammer: micromechanical approaches to morphogenesis. *Journal of experimental botany*, 64(15):4651–62.
- Milani, P., Gholamirad, M., Traas, J., Arnéodo, A., Boudaoud, A., Argoul, F., and Hamant, O. (2011). In vivo analysis of local wall stiffness at the shoot apical meristem in Arabidopsis using atomic force microscopy. *The Plant Journal*, 67(6):1116–1123.

- Minc, N., Burgess, D., and Chang, F. (2011). Influence of cell geometry on division-plane positioning. *Cell*, 144(3):414–426.
- Mirabet, V., Besnard, F., Vernoux, T., and Boudaoud, A. (2012). Noise and robustness in phyllotaxis. *PLoS computational biology*, 8(2):e1002389.
- Mirabet, V., Das, P., Boudaoud, A., and Hamant, O. (2011). The Role of Mechanical Forces in Plant Morphogenesis. *Annual Review of Plant Biology*, 62(1):365–385.
- Mitchison, G. (2016). Conformal growth of Arabidopsis leaves. *Journal of Theoretical Biology*, 408:155–166.
- Mittler, R., Vanderauwera, S., Gollery, M., and Van Breusegem, F. (2004). Reactive oxygen gene network of plants. *Trends in plant science*, 9(10):490–498.
- Mittler, R., Vanderauwera, S., Suzuki, N., Miller, G., Tognetti, V. B., Vandepoele, K., Gollery, M., Shulaev, V., and Van Breusegem, F. (2011). ROS signaling: the new wave? *Trends in Plant Science*, 16(6):300–309.
- Mizukami, Y. (2001). A matter of size: Developmental control of organ size in plants. *Current Opinion in Plant Biology*, 4(6):533–539.
- Mizukami, Y. and Fischer, R. L. (2000). Plant organ size control: AINTEGUMENTA regulates growth and cell numbers during organogenesis. *Proceedings of the National Academy of Sciences of the United States of America*, 97(2):942–947.
- Mohnen, D. (2008). Pectin structure and biosynthesis. *Current Opinion in Plant Biology*, 11(3):266–277.
- Monshausen, G. B. and Haswell, E. S. (2013). A force of nature: Molecular mechanisms of mechanoperception in plants. *Journal of Experimental Botany*, 64(15):4663–4680.
- Montagne, J., Stewart, M. J., Stocker, H., Hafen, E., Kozma, S. C., and Thomas, G. (1999). Drosophila S6 kinase: a regulator of cell size. *Science*, 285(5436):2126–2129.
- Montenegro-Johnson, T. D., Stamm, P., Strauss, S., Topham, A. T., Tsagris, M., Wood, A. T., Smith, R. S., and Bassel, G. W. (2015). Digital Single-Cell Analysis of Plant Organ Development Using 3DCellAtlas. *The Plant Cell*, 27(4):1018–1033.
- Mosca, G., Sapala, A., Strauss, S., Routier-Kierzkowska, A.-L., and Smith, R. S. (2017). On the micro-indentation of plant cells in a tissue context. *Phys. Biol.*, 14:1–11.
- Moustakas, A. M., Nari, J., Borel, M., Noat, G., and Ricard, J. (1991). Pectin methylesterase, metal ions and plant cell-wall extension. The role of metal ions in plant cell-wall extension. *Biochemical Journal*, 279(2):351–354.

- Nafisi, M., Stranne, M., Fimognari, L., Atwell, S., Martens, H. J., Pedas, P. R., Hansen, S. F., Nawrath, C., Scheller, H. V., Kliebenstein, D. J., and Sakuragi, Y. (2015). Acetylation of cell wall is required for structural integrity of the leaf surface and exerts a global impact on plant stress responses. *Frontiers in Plant Science*, 6(July):1–13.
- Nakagawa, Y., Katagiri, T., Shinozaki, K., Qi, Z., Tatsumi, H., Furuichi, T., Kishigami, A., Sokabe, M., Kojima, I., Sato, S., Kato, T., Tabata, S., Iida, K., Terashima, A., Nakano, M., Ikeda, M., Yamanaka, T., and Iida, H. (2007). Arabidopsis plasma membrane protein crucial for Ca²⁺ influx and touch sensing in roots. *Proceedings of the National Academy of Sciences of the United States of America*, 104(9):3639–44.
- Nath, U., Crawford, B. C. W., Carpenter, R., and Coen, E. (2003). Genetic control of surface curvature. *Science (New York, N.Y.)*, 299(5611):1404–7.
- Neufeld, T. P., de la Cruz, A. F. A., Johnston, L. A., and Edgar, B. A. (1998). Coordination of growth and cell division in the Drosophila wing. *Cell*, 93(7):1183–1193.
- Newman, R. H., Hill, S. J., and Harris, P. J. (2013). Wide-Angle X-Ray Scattering and Solid-State Nuclear Magnetic Resonance Data Combined to Test Models for Cellulose Microfibrils in Mung Bean Cell Walls 1. *Plant Physiology*, 163(4):1558–1567.
- Ohno, C. K. (2004). The Arabidopsis JAGGED gene encodes a zinc finger protein that promotes leaf tissue development. *Development*, 131(5):1111–1122.
- O'Neill, M. A., Eberhard, S., Albersheim, P., and Darvill, A. G. (2001). Requirement of borate cross-linking of cell wall rhamnogalacturonan II for Arabidopsis growth. *Science*, 294(5543):846–849.
- O'Neill, M. A., Ishii, T., Albersheim, P., and Darvill, A. G. (2004). RHAMNOGALACTURONAN II : Structure and Function of a Borate Cross-Linked Cell Wall Pectic Polysaccharide. *Review Literature And Arts Of The Americas*, 55(1):109–139.
- Ordas, B., Malvar, R. a., and Hill, W. G. (2008). Genetic variation and quantitative trait loci associated with developmental stability and the environmental correlation between traits in maize. *Genetics research*, 90(5):385–395.
- Ortega, J. K. (1985). Augmented growth equation for cell wall expansion. *Plant physiology*, 79(1):318–320.
- OSullivan, A. C. (1997). Cellulose: the structure slowly unravels. *Cellulose*, 4(3):173–207.
- Owusu-Ansah, E., Yavari, A., Mandal, S., and Banerjee, U. (2008). Distinct mitochondrial retrograde signals control the G1-S cell cycle checkpoint. *Nature genetics*, 40(3):356–361.
- Palatnik, J. F., Allen, E., Wu, X., Schommer, C., Schwab, R., Carrington, J. C., and Weigel, D. (2003). Control of leaf morphogenesis by microRNAs. *Nature*, 425(6955):257–263.

- Palmer, A. R. (1996). Waltzing with Asymmetry. *BioScience*, 46(7):518–532.
- Paredez, A. R., Somerville, C., and Ehrhardt, D. (2006). Visualization of Cellulose Synthase Demonstrates Functional Association with Microtubules. *Science*, 312(2006):1491–1495.
- Park, Y. B. and Cosgrove, D. J. (2012). Changes in cell wall biomechanical properties in the xyloglucan-deficient xxt1/xxt2 mutant of Arabidopsis. *Plant physiology*, 158(1):465–75.
- Park, Y. B. and Cosgrove, D. J. (2015). Xyloglucan and its interactions with other components of the growing cell wall. *Plant and Cell Physiology*, 56(2):180–194.
- Paulsson, J. (2005). Models of stochastic gene expression. *Physics of Life Reviews*, 2(2):157–175.
- Peaucelle, A., Braybrook, S., and Höfte, H. (2012). Cell wall mechanics and growth control in plants: the role of pectins revisited. *Frontiers in Plant Science*, 3(June):121.
- Peaucelle, A., Braybrook, S. A., Le Guillou, L., Bron, E., Kuhlemeier, C., and Höfte, H. (2011). Pectin-Induced Changes in Cell Wall Mechanics Underlie Organ Initiation in Arabidopsis. *Current Biology*, 21(20):1720–1726.
- Peaucelle, A., Louvet, R., Johansen, J. N., Höfte, H., Laufs, P., Pelloux, J., and Mouille, G. (2008). Arabidopsis Phyllotaxis Is Controlled by the Methyl-Esterification Status of Cell-Wall Pectins. *Current Biology*, 18(24):1943–1948.
- Pelloux, J., Rustérucchi, C., and Mellerowicz, E. J. (2007). New insights into pectin methylesterase structure and function. *Trends in Plant Science*, 12(6):267–277.
- Péret, B., Li, G., Zhao, J., Band, L. R., Voß, U., Postaire, O., Luu, D.-T., Da Ines, O., Casimiro, I., Lucas, M., Wells, D. M., Lazzerini, L., Nacry, P., King, J. R., Jensen, O. E., Schäffner, A. R., Maurel, C., and Bennett, M. J. (2012). Auxin regulates aquaporin function to facilitate lateral root emergence. *Nature cell biology*, 14(10):991–8.
- Perez, I. B. and Brown, P. J. (2014). The role of ROS signaling in cross-tolerance: from model to crop. *Frontiers in plant science*, 5.
- Pérez, J., Munos-Dorado, J., de la Rubia, T. D. L. R., and Martinez, J. (2002). Biodegradation and biological treatments of cellulose, hemicellulose and lignin: an overview. *International Microbiology*, 5(2):53–63.
- Pigliucci, M. (2008). Is evolvability evolvable? *Nature reviews Genetics*, 9(1):75–82.
- Poethig, R. S. and Sussex, I. M. (1985). The developmental morphology and growth dynamics of the tobacco leaf. *Planta*, 165(2):158–169.
- Poethig, R. S. L. B. P. B. S. R. . (1987). Clonal analysis of cell lineage patterns in plant development. *Am. J. Bot.*, 74(4):581–594.

- Pouille, P.-A., Ahmadi, P., Brunet, A.-C., and Farge, E. (2009). Mechanical signals trigger Myosin II redistribution and mesoderm invagination in *Drosophila* embryos. *Sci. Signal.*, 2(66):ra16–ra16.
- Powell, A. E. and Lenhard, M. (2012). Control of Organ Size in Plants. *Current Biology*, 22(9):R360–R367.
- Proseus, T. E., Ortega, J. K., and Boyer, J. S. (1999). Separating Growth from Elastic Deformation during Cell Enlargement1. *Plant physiology*, 119(2):775–784.
- Pulliam, D. A., Bhattacharya, A., and Van Remmen, H. (2013). Mitochondrial dysfunction in aging and longevity: a causal or protective role? *Antioxidants & redox signaling*, 19(12):1373–1387.
- Qi, X., Behrens, B. X., West, P. R., and Mort, A. J. (1995). Solubilization and partial characterization of extensin fragments from cell walls of cotton suspension cultures. Evidence for a covalent cross-link between extensin and pectin. *Plant physiology*, 108(4):1691–701.
- Qu, X., Chatty, P. R., and Roeder, A. H. K. (2014). Endomembrane trafficking protein SEC24A regulates cell size patterning in *Arabidopsis*. *Plant physiology*, 166(4):1877–1890.
- Queitsch, C., Sangster, T. a., and Lindquist, S. (2002). Hsp90 as a capacitor of phenotypic variation. *Nature*, 417(6889):618–24.
- Raj, A., Rifkin, S. a., Andersen, E., and van Oudenaarden, A. (2010). Variability in gene expression underlies incomplete penetrance. *Nature*, 463(7283):913–918.
- Ralet, M.-C., Crépeau, M.-J., Vigouroux, J., Tran, J., Berger, A., Sallé, C., Granier, F., Botran, L., and North, H. M. (2016). Xylans provide the structural driving force for mucilage adhesion to the *Arabidopsis* seed coat. *Plant physiology*, 171(1):165–178.
- Ralph, J., Bunzel, M., Marita, J. M., Hatfield, R. D., Lu, F., Kim, H., Schatz, P. F., Grabber, J. H., and Steinhart, H. (2004). Peroxidase-dependent cross-linking reactions of p-hydroxycinnamates in plant cell walls. *Phytochemistry Reviews*, 3(1):79–96.
- Ranwala, a. P., Suematsu, C., and Masuda, H. (1992). The Role of beta-Galactosidases in the Modification of Cell Wall Components during Muskmelon Fruit Ripening. *Plant physiology*, 100(3):1318–25.
- Rayle, D. L. and Cleland, R. E. (1992). The Acid Growth Theory of auxin-induced cell elongation is alive and well. *Plant physiology*, 99(4):1271–1274.
- Reeves, G. T., Trisnadi, N., Truong, T. V., Nahmad, M., Katz, S., and Stathopoulos, A. (2012). Dorsal-Ventral Gene Expression in the *Drosophila* Embryo Reflects the Dynamics and Precision of the Dorsal Nuclear Gradient. *Developmental Cell*, 22(3):544–557.

- Reinhardt, D., Pesce, E.-R., Stieger, P., Mandel, T., Baltensperger, K., Bennett, M., Traas, J., Friml, J., and Kuhlemeier, C. (2003). Regulation of phyllotaxis by polar auxin transport. *Nature*, 426(6964):255–260.
- Remmler, L. and a. G. Rolland-Lagan (2012). Computational Method for Quantifying Growth Patterns at the Adaxial Leaf Surface in Three Dimensions. *Plant Physiology*, 159(May):27–39.
- Ren, M., Qiu, S., Venglat, P., Xiang, D., Feng, L., Selvaraj, G., and Datla, R. (2011). Target of rapamycin regulates development and ribosomal RNA expression through kinase domain in Arabidopsis. *Plant physiology*, 155(3):1367–1382.
- Reuhs, B. L., Glenn, J., Stephens, S. B., Kim, J. S., Christie, D. B., Glushka, J. G., Zablackis, E., Albersheim, P., Darvill, A. G., and O’Neill, M. A. (2004). L-galactose replaces L-fucose in the pectic polysaccharide rhamnogalacturonan II synthesized by the L-fucose-deficient mur1 Arabidopsis mutant. *Planta*, 219(1):147–157.
- Reyt, G., Boudouf, S., Boucherez, J., Gaymard, F., and Briat, J.-F. (2015). Iron-and ferritin-dependent reactive oxygen species distribution: impact on Arabidopsis root system architecture. *Molecular plant*, 8(3):439–453.
- Rice, S. H. (1998). The Evolution of Canalization and the Breaking of Von Baer’s Laws: Modeling the Evolution of Development with Epistasis. *Evolution; international journal of organic evolution*, 52(3):647–656.
- Ringli, C. (2010). Monitoring the Outside: Cell Wall-Sensing Mechanisms. *Plant Physiology*, 153(4):1445–1452.
- Rinott, R., Jaimovich, A., and Friedman, N. (2011). Exploring transcription regulation through cell-to-cell variability. *Proceedings of the National Academy of Sciences*, 108(15):6329–6334.
- Rodriguez, A. A., Grunberg, K. A., and Taleisnik, E. L. (2002). Reactive oxygen species in the elongation zone of maize leaves are necessary for leaf extension. *Plant Physiology*, 129(4):1627–1632.
- Roeder, A. H. (2010). Sepals. *Encyclopedia of Life Sciences*, May:1–6.
- Roeder, A. H. K., Chickarmane, V., Cunha, A., Obara, B., Manjunath, B. S., and Meyerowitz, E. M. (2010). Variability in the control of cell division underlies sepal epidermal patterning in Arabidopsis thaliana. *PLoS biology*, 8(5):e1000367.
- Roeder, A. H. K., Cunha, A., Burl, M. C., and Meyerowitz, E. M. (2012). A computational image analysis glossary for biologists. *Development (Cambridge, England)*, 139(17):3071–80.
- Roeder, A. H. K., Tarr, P. T., Tobin, C., Zhang, X., Chickarmane, V., Cunha, A., and Meyerowitz, E. M. (2011). Computational morphodynamics of plants: integrating development over space and time. *Nature reviews. Molecular cell biology*, 12(4):265–273.

- Rolland-Lagan, A.-G., Bangham, J. A., and Coen, E. (2003). Growth dynamics underlying petal shape and asymmetry. *Nature*, 422(6928):161–3.
- Rolland-Lagan, A.-G., Remmler, L., and Girard-Bock, C. (2014). Quantifying shape changes and tissue deformation in leaf development. *Plant physiology*, 165(June):496–505.
- Romero-Arias, J. R., Hernández-Hernández, V., Benítez, M., Alvarez-Buylla, E. R., and Barrio, R. A. (2017). Model of polar auxin transport coupled to mechanical forces retrieves robust morphogenesis along the *Arabidopsis* root. *Physical Review E*, 95(3):032410.
- Roorda, a. and Williams, D. R. (1999). The arrangement of the three cone classes in the living human eye. *Nature*, 397(6719):520–2.
- Rose, J. K. C. (2002). The XTH Family of Enzymes Involved in Xyloglucan Endotransglucosylation and Endohydrolysis: Current Perspectives and a New Unifying Nomenclature. *Plant and Cell Physiology*, 43(12):1421–1435.
- Routier-Kierzkowska, A.-L. and Smith, R. S. (2013). Measuring the mechanics of morphogenesis. *Current Opinion in Plant Biology*, 16(1):25–32.
- Routier-Kierzkowska, A.-L., Weber, A., Kochova, P., Felekis, D., Nelson, B. J., Kuhlemeier, C., Smith, R. S., Technologies, B., Routier-Kierzkowska, A.-L., Weber, A., Kochova, P., Felekis, D., Nelson, B. J., Kuhlemeier, C., Smith, R. S., and Technologies, B. (2012). Cellular Force Microscopy for in Vivo Measurements of Plant Tissue Mechanics. *Plant Physiology*, 158(April):1514–1522.
- Roy, S., Watada, a. E., and Wergin, W. P. (1997). Characterization of the Cell Wall Microdomain Surrounding Plasmodesmata in Apple Fruit. *Plant physiology*, 114(2):539–547.
- Russo, T., Zambrano, N., Esposito, F., Ammendola, R., Cimino, F., Fiscella, M., Jackman, J., O’Connor, P. M., Anderson, C. W., and Appella, E. (1995). A p53-independent pathway for activation of WAF1/CIP1 expression following oxidative stress. *Journal of Biological Chemistry*, 270(49):29386–29391.
- Rutherford, S. L. and Lindquist, S. (1998). Hsp90 as a capacitor for morphological evolution. *Nature*, 396(6709):336–342.
- Sakamoto, W., Zaltsman, A., Adam, Z., and Takahashi, Y. (2003). Coordinated regulation and complex formation of yellow variegated1 and yellow variegated2, chloroplastic FtsH metalloproteases involved in the repair cycle of photosystem II in Arabidopsis thylakoid membranes. *The Plant Cell*, 15(12):2843–2855.
- Sambade, A., Pratap, A., Buschmann, H., Morris, R. J., and Lloyd, C. (2012). The influence of light on microtubule dynamics and alignment in the Arabidopsis hypocotyl. *The Plant Cell*, 24(1):192–201.

- Sampathkumar, A., Gutierrez, R., McFarlane, H. E., Bringmann, M., Lindeboom, J., Emons, A.-M., Samuels, L., Ketelaar, T., Ehrhardt, D. W., and Persson, S. (2013). Patterning and lifetime of plasma membrane-localized cellulose synthase is dependent on actin organization in Arabidopsis interphase cells. *Plant physiology*, 162(2):675–88.
- Sampathkumar, A., Krupinski, P., Wightman, R., Milani, P., Berquand, A., Boudaoud, A., Hamant, O., Jönsson, H., and Meyerowitz, E. M. (2014). Subcellular and supracellular mechanical stress prescribes cytoskeleton behavior in Arabidopsis cotyledon pavement cells. *eLife*, 3:e01967.
- Sampedro, J. and Cosgrove, D. J. (2005). The expansin superfamily. *Genome Biology*, 6(12):242.
- Sánchez-Rodríguez, C., Ketelaar, K., Schneider, R., Villalobos, J. A., Somerville, C. R., Persson, S., and Wallace, I. S. (2017). BRASSINOSTEROID INSENSITIVE2 negatively regulates cellulose synthesis in Arabidopsis by phosphorylating cellulose synthase 1. *Proceedings of the National Academy of Sciences*, page 201615005.
- Sassi, M., Ali, O., Boudon, F., Cloarec, G., Abad, U., Cellier, C., Chen, X., Gilles, B., Milani, P., Friml, J., Vernoux, T., Godin, C., Hamant, O., and Traas, J. (2014). An Auxin-Mediated Shift toward Growth Isotropy Promotes Organ Formation at the Shoot Meristem in Arabidopsis. *Current Biology*, 24(19):2335–2342.
- Saunders, T. E., Pan, K. Z., Angel, A., Guan, Y., Shah, J. V., Howard, M., and Chang, F. (2012). Noise Reduction in the Intracellular Pom1p Gradient by a Dynamic Clustering Mechanism. *Developmental Cell*, 22(3):558–572.
- Sauret-Güeto, S., Schiessl, K., Bangham, A., Sablowski, R., and Coen, E. (2013). JAGGED controls Arabidopsis petal growth and shape by interacting with a divergent polarity field. *PLoS biology*, 11(4):e1001550.
- Savaldi-Goldstein, S., Peto, C., and Chory, J. (2007). The epidermis both drives and restricts plant shoot growth. *Nature*, 446(7132):199–202.
- Scheller, H. V. and Ulvskov, P. (2010). Hemicelluloses. *Annual Review of Plant Biology*, 61(1):263–289.
- Schiessl, K., Kausika, S., Southam, P., Bush, M., and Sablowski, R. (2012). JAGGED Controls Growth Anisotropy and Coordination between Cell Size and Cell Cycle during Plant Organogenesis. *Current Biology*, 22(19):1739–1746.
- Schluck, T., Nienhaus, U., Aegerter-Wilmsen, T., and Aegerter, C. M. (2013). Mechanical Control of Organ Size in the Development of the Drosophila Wing Disc. *PLoS ONE*, 8(10).
- Schnabelrauch, L. S., Kieliszewski, M., Upham, B. L., Alizedeh, H., and Lamport, D. T. (1996). Isolation of pl 4.6 extensin peroxidase from tomato cell suspension cultures and identification of Val-Tyr-Lys as putative intermolecular cross-link site.

- Scholl, R., May, S., and DH, W. (2000). Seed and molecular resources for Arabidopsis. *Plant Physiology*, 124(4):1477–80.
- Schopfer, P. (2001). Hydroxyl radical-induced cell-wall loosening in vitro and in vivo: implications for the control of elongation growth. *The Plant Journal*, 28(6):679–688.
- Schopfer, P., Liskay, A., Bechtold, M., Frahy, G., and Wagner, A. (2002). Evidence that hydroxyl radicals mediate auxin-induced extension growth. *Planta*, 214(6):821–828.
- Schweikert, C., Liskay, A., and Schopfer, P. (2000). Scission of polysaccharides by peroxidase-generated hydroxyl radicals. *Phytochemistry*, 53(5):565–570.
- Sedbrook, J. C. and Kaloriti, D. (2008). Microtubules, MAPs and plant directional cell expansion. *Trends in Plant Science*, 13(6):303–310.
- Shaw, S. L. (2013). Reorganization of the plant cortical microtubule array. *Current opinion in plant biology*, 16(6):693–697.
- Sherrard, K., Robin, F., Lemaire, P., and Munro, E. (2010). Sequential activation of apical and basolateral contractility drives ascidian endoderm invagination. *Current Biology*, 20(17):1499–1510.
- Shih, H. W., Miller, N. D., Dai, C., Spalding, E. P., and Monshausen, G. B. (2014). The receptor-like kinase FERONIA is required for mechanical signal transduction in Arabidopsis seedlings. *Current Biology*, 24(16):1887–1892.
- Shoji, T., Narita, N. N., Hayashi, K., Asada, J., Hamada, T., and Sonobe, S. (2004). Plant-Specific Microtubule-Associated Protein SPIRAL2 Is Required for Anisotropic Growth in Arabidopsis. *Plant ph*, 136:3933–3944.
- Showalter, A. M. (1993). Structure and Function of Plant Cell Wall Proteins. *The Plant Cell*, 5(January):9–23.
- Shraiman, B. I. (2005). Mechanical feedback as a possible regulator of tissue growth. *Proceedings of the National Academy of Sciences of the United States of America*, 102(9):3318–23.
- Silk, W. K. and Erickson, R. O. (1979). Kinematics of plant growth. *Journal of Theoretical Biology*, 76(4):481–501.
- Singh, A. M., Chappell, J., Trost, R., Lin, L., Wang, T., Tang, J., Wu, H., Zhao, S., Jin, P., and Dalton, S. (2013). Cell-Cycle Control of Developmentally Regulated Transcription Factors Accounts for Heterogeneity in Human Pluripotent Cells. *Stem Cell Reports*, 1(6):532–544.
- Smyth, D. R. (1990). Early Flower Development in Arabidopsis. *The Plant Cell*, 2(8):755–767.
- Somerville, C. (2006). Cellulose synthesis in higher plants. *Annu Rev Cell Dev Biol*, 22:53–78.

- Somerville, C., Bauer, S., Brininstool, G., Facette, M., Hamann, T., Milne, J., Osborne, E., Paredez, A., Persson, S., Raab, T., Vorwerk, S., and Youngs, H. (2004). Toward a Systems Approach to Understanding Plant Cell Walls. *Science (Washington)*, 306(5705):2206–2211.
- Stearns, S. C., Kaiser, M., and Kawecki, T. J. (1995). The differential genetic and environmental canalization of fitness components in *Drosophila melanogaster*. *Journal of Evolutionary Biology*, 8:539–557.
- Stoppin-Mellet, V., Gaillard, J., and Vantard, M. (2006). Katanin’s severing activity favors bundling of cortical microtubules in plants. *Plant Journal*, 46(6):1009–1017.
- Swift, J. and Discher, D. E. (2014). The nuclear lamina is mechano-responsive to ECM elasticity in mature tissue. *J Cell Sci*, 127(14):3005–3015.
- Tauriello, G., Meyer, H. M., Smith, R. S., Koumoutsakos, P., and Roeder, A. H. K. (2015). Variability and constancy in cellular growth of *Arabidopsis* sepals. *Plant Physiology*, page pp.00839.2015.
- Théry, M., Jiménez-Dalmaroni, A., Racine, V., Bornens, M., and Jülicher, F. (2007). Experimental and theoretical study of mitotic spindle orientation. *Nature*, 447(7143):493–496.
- Thorsness, P. E. and Fox, T. D. (1993). Nuclear mutations in *Saccharomyces cerevisiae* that affect the escape of DNA from mitochondria to the nucleus. *Genetics*, 134(1):21–28.
- Thorsness, P. E., White, K. H., and Fox, T. D. (1993). Inactivation of YME1, a member of the ftsH-SEC18-PAS1-CDC48 family of putative ATPase-encoding genes, causes increased escape of DNA from mitochondria in *Saccharomyces cerevisiae*. *Molecular and cellular biology*, 13(9):5418–5426.
- Tsukagoshi, H., Busch, W., and Benfey, P. N. (2010). Transcriptional Regulation of ROS Controls Transition from Proliferation to Differentiation in the Root. *Cell*, 143(4):606–616.
- Tumaneng, K., Russell, R. C., and Guan, K.-L. (2012). Organ size control by Hippo and TOR pathways. *Current Biology*, 22(9):R368–R379.
- Turner, a., Wells, B., and Roberts, K. (1994). Plasmodesmata of maize root tips: structure and composition. *Journal of cell science*, 107 (Pt 1:3351–3361.
- Ueda, K., Matsuyama, T., and Hashimoto, T. (1999). Visualization of microtubules in living cells of transgenic *Arabidopsis thaliana*. *Protoplasma*, 206(1):201–206.
- Urantowka, A., Knorpp, C., Olczak, T., Kolodziejczak, M., and Janska, H. (2005). Plant mitochondria contain at least two i-AAA-like complexes. *Plant molecular biology*, 59(2):239–252.

- Uyttewaal, M., Burian, A., Alim, K., Landrein, B., Borowska-Wykr t, D., Dedieu, A., Peau-
celle, A., Ludynia, M., Traas, J., Boudaoud, A., Kwiatkowska, D., and Hamant, O. (2012).
Mechanical Stress Acts via Katanin to Amplify Differences in Growth Rate between Adjacent
Cells in Arabidopsis. *Cell*, 149(2):439–451.
- Vain, T., Crowell, E. F., Timpano, H., Biot, E., Desprez, T., Mansoori, N., Trindade, L. M.,
Pagant, S., Robert, S., Höfte, H., Gonneau, M., and Vernhettes, S. (2014). The Cellulase
KORRIGAN Is Part of the Cellulose Synthase Complex. *Plant physiology*, 165(4):1521–1532.
- Vallejo, D. M., Juarez-Carreño, S., Bolivar, J., Morante, J., and Dominguez, M. (2015). A brain
circuit that synchronizes growth and maturation revealed through Dilp8 binding to Lgr3.
Science, 350(6262):aac6767.
- Vandiver, R. and Goriely, A. (2008). Tissue tension and axial growth of cylindrical structures
in plants and elastic tissues. *EPL*, 84.
- Verkhovsky, A. B., Svitkina, T. M., and Borisov, G. G. (1999). Self-polarization and directional
motility of cytoplasm. *Current Biology*, 9(1):11–S1.
- Vernoux, T., Brunoud, G., Farcot, E., Morin, V., Van den Daele, H., Legrand, J., Oliva, M.,
Das, P., Larrieu, A., Wells, D., Guedon, Y., Armitage, L., Picard, F., Guyomarc’h, S., Cellier,
C., Parry, G., Koumproglou, R., Doonan, J. H., Estelle, M., Godin, C., Kepinski, S., Bennett,
M., De Veylder, L., and Traas, J. (2011). The auxin signalling network translates dynamic
input into robust patterning at the shoot apex. *Molecular Systems Biology*, 7(1):508–508.
- Vincken, J.-P. (2003). If Homogalacturonan Were a Side Chain of Rhamnogalacturonan I.
Implications for Cell Wall Architecture. *Plant Physiology*, 132(4):1781–1789.
- Vineyard, L., Elliott, A., Dhingra, S., Lucas, J. R., and Shaw, S. L. (2013). Progressive transverse
microtubule array organization in hormone-induced Arabidopsis hypocotyl cells. *The Plant
Cell*, 25(2):662–676.
- Vlad, D., Kierzkowski, D., Rast, M. I., Vuolo, F., Ioio, R. D., Galinha, C., Gan, X., Hajheidari,
M., Hay, A., Smith, R. S., Huijser, P., Bailey, C. D., and Tsiantis, M. (2014). and Loss of a
Homeobox Gene. *Science*, 780(February):780–783.
- Vogel, G. (2013). How Do Organs Know When They Have Reached the Right Size? *Science*,
340(June):1156–1157.
- Vogel, J. P. (2002). PMR6, a Pectate Lyase-Like Gene Required for Powdery Mildew Suscepti-
bility in Arabidopsis. *the Plant Cell Online*, 14(9):2095–2106.
- Vogler, H., Draeger, C., Weber, A., Felekis, D., Eichenberger, C., Routier-Kierzkowska, A. L.,
Boisson-Dernier, A., Ringli, C., Nelson, B. J., Smith, R. S., and Grossniklaus, U. (2013). The
pollen tube: A soft shell with a hard core. *Plant Journal*, 73(4):617–627.

- Vogler, H., Felekis, D., Nelson, B., and Grossniklaus, U. (2015). Measuring the Mechanical Properties of Plant Cell Walls. *Plants*, 4(2):167–182.
- Volkov, V., Hachez, C., Moshelion, M., Draye, X., Chaumont, F., and Fricke, W. (2007). Water permeability differs between growing and non-growing barley leaf tissues. *Journal of Experimental Botany*, 58(3):377–390.
- von Dassow, G., Meir, E., Munro, E. M., and Odell, G. M. (2000). The segment polarity network is a robust developmental module. *Nature*, 406(6792):188–192.
- Wagner, G. P. and Altenberg, L. (1996). Perspective : Complex Adaptations and the Evolution of Evolvability Published by : Society for the Study of Evolution All use subject to <http://about.jstor.org/terms> E VOLUTIION. *Evolution; international journal of organic evolution*, 50(3):967–976.
- Wagner, R., Moon, R., Pratt, J., Shaw, G., and Raman, A. (2011). Uncertainty quantification in nanomechanical measurements using the atomic force microscope. *Nanotechnology*, 22(45):455703.
- Wang, L., Hukin, D., Pritchard, J., and Thomas, C. (2006). Comparison of plant cell turgor pressure measurement by pressure probe and micromanipulation. *Biotechnology Letters*, 28(15):1147–1150.
- Wang, P. and Hussey, P. J. (2015). Interactions between plant endomembrane systems and the actin cytoskeleton. *Frontiers in Plant Science*, 6(June):1–8.
- Wartlick, O., Mumcu, P., Kicheva, A., Bittig, T., Seum, C., Jülicher, F., and Gonzalez-Gaitan, M. (2011). Dynamics of Dpp signaling and proliferation control. *Science*, 331(6021):1154–1159.
- Wasteneys, G. O. and Ambrose, J. C. (2009). Spatial organization of plant cortical microtubules: close encounters of the 2D kind. *Trends in Cell Biology*, 19(2):62–71.
- Weigmann, K., Cohen, S. M., and Lehner, C. F. (1997). Cell cycle progression, growth and patterning in imaginal discs despite inhibition of cell division after inactivation of Drosophila Cdc2 kinase. *Development*, 124(18):3555–3563.
- Wetzel, W. C., Kharouba, H. M., Robinson, M., Holyoak, M., and Karban, R. (2016). Variability in plant nutrients reduces insect herbivore performance. *Nature Publishing Group*, 539(7629):425–427.
- White, D. W. R. (2006). PEAPOD regulates lamina size and curvature in Arabidopsis. *Proceedings of the National Academy of Sciences of the United States of America*, 103(35):13238–43.

- Wightman, R., Chomicki, G., Kumar, M., Carr, P., and Turner, S. R. (2013). SPIRAL2 Determines Plant Microtubule Organization by Modulating Microtubule Severing. *Current Biology*, 23(19):1902–1907.
- Williams, R. (2000). Mapping genes that modulate mouse brain development: a quantitative genetic approach. *Mouse brain development*, pages 21–49.
- Williamson, R. (1990). Alignment of Cortical Microtubules by Anisotropic Wall Stresses. *Australian Journal of Plant Physiology*, 17(6):601.
- Wolf, L., Silander, O. K., and van Nimwegen, E. (2015). Expression noise facilitates the evolution of gene regulation. *Elife*, 4:e05856.
- Wolf, S. and Greiner, S. (2012). Growth control by cell wall pectins. *Protoplasma*, 249(S2):169–175.
- Wolf, S., Hématy, K., and Höfte, H. (2012a). Growth Control and Cell Wall Signaling in Plants. *Annual Review of Plant Biology*, 63(1):381–407.
- Wolf, S., Mravec, J., Greiner, S., and Ho, H. (2012b). Report Plant Cell Wall Homeostasis Is Mediated by Brassinosteroid Feedback Signaling. *Current Biology*, 22:1732–1737.
- Wolpert, L. (2010). Arms and the man: the problem of symmetric growth. *PLoS biology*, 8(9):e1000477.
- Xia, X.-J., Zhou, Y.-H., Shi, K., Zhou, J., Foyer, C. H., and Yu, J.-Q. (2015). Interplay between reactive oxygen species and hormones in the control of plant development and stress tolerance. *Journal of Experimental Botany*, 66(10):2839–2856.
- Xiong, J., Yang, Y., Fu, G., and Tao, L. (2015). Novel roles of hydrogen peroxide (H_2O_2) in regulating pectin synthesis and demethylesterification in the cell wall of rice (*Oryza sativa*) root tips. *New Phytologist*, 206(1):118–126.
- Xue, J., Luo, D., Xu, D., Zeng, M., Cui, X., Li, L., and Huang, H. (2015). CCR1, an enzyme required for lignin biosynthesis in Arabidopsis, mediates the cell proliferation exit for leaf development. *The Plant Journal*, 83(3):n/a–n/a.
- Yakubov, G. E., Bonilla, M. R., Chen, H., Doblin, M. S., Bacic, A., Gidley, M. J., and Stokes, J. R. (2016). Mapping nano-scale mechanical heterogeneity of primary plant cell walls. *Journal of Experimental Botany*.
- Yang, W., Schuster, C., Beahan, C. T., Doblin, M. S., Wightman, R., Meyerowitz, E. M., Yang, W., Schuster, C., Beahan, C. T., Charoensawan, V., Peaucelle, A., and Bacic, A. (2016). Regulation of Meristem Morphogenesis by Cell Wall Synthases in Arabidopsis Article Regulation of Meristem Morphogenesis by Cell Wall Synthases in Arabidopsis. *Current Biology*, pages 1–12.

- Ye, Z.-H. and Varner, J. E. (1991). Tissue-Specific Expression of Cell Wall Proteins in Developing Soybean Tissues. *The Plant Cell American Society of Plant Physiologists*, 3(January):23–37.
- Yokoyama, R. and Nishitani, K. (2001). A comprehensive expression analysis of all members of a gene family encoding cell-wall enzymes allowed us to predict cis-regulatory regions involved in cell-wall construction in specific organs of Arabidopsis. *Plant & cell physiology*, 42(10):1025–1033.
- Yuan, F., Yang, H., Xue, Y., Kong, D., Ye, R., Li, C., Zhang, J., Theprungsirikul, L., Shrift, T., Krichilsky, B., Johnson, D. M., Swift, G. B., He, Y., Siedow, J. N., and Pei, Z.-M. (2014). OSCA1 mediates osmotic-stress-evoked Ca²⁺ increases vital for osmosensing in Arabidopsis. *Nature*, 514(7522):367–371.
- Zabackis, E., Huang, J., Müllerz, B., Darvill, A. C., and Albersheim, P. (1995). Characterization of the Cell-Wall Polysaccharides of Arabidopsis thaliana leaves. *Plant physiology*, 107:1129–1138.
- Žádníková, P., Wabnik, K., Abuzeineh, A., Gallemi, M., Van Der Straeten, D., Smith, R. S., Inzé, D., Friml, J., Prusinkiewicz, P., and Benková, E. (2016). A Model of Differential Growth-Guided Apical Hook Formation in Plants. *The Plant cell*, 28(10):2464–2477.
- Zeng, Q. and Hong, W. (2008). The Emerging Role of the Hippo Pathway in Cell Contact Inhibition, Organ Size Control, and Cancer Development in Mammals. *Cancer Cell*, 13(3):188–192.
- Zhang, D., Grode, K. D., Stewman, S. F., Diaz-Valencia, J. D., Liebling, E., Rath, U., Riera, T., Currie, J. D., Buster, D. W., Asenjo, A. B., Sosa, H. J., Ross, J. L., Ma, A., Rogers, S. L., and Sharp, D. J. (2011a). Drosophila katanin is a microtubule depolymerase that regulates cortical-microtubule plus-end interactions and cell migration. *Nature cell biology*, 13(4):361–70.
- Zhang, F., Wang, Y., Li, G., Tang, Y., Kramer, E. M., and Tadege, M. (2014). STENOFOLIA recruits TOPLESS to repress ASYMMETRIC LEAVES2 at the leaf margin and promote leaf blade outgrowth in Medicago truncatula. *The Plant Cell*, 26(2):650–64.
- Zhang, H., Landmann, F., Zahreddine, H., Rodriguez, D., Koch, M., and Labouesse, M. (2011b). A tension-induced mechanotransduction pathway promotes epithelial morphogenesis. *Nature*, 471(7336):99–103.
- Zhang, Q., Fishel, E., Bertroche, T., and Dixit, R. (2013). Microtubule severing at crossover sites by katanin generates ordered cortical microtubule arrays in Arabidopsis. *Current Biology*, 23(21):2191–2195.
- Zubairova, U., Nikolaev, S., Penenko, A., Podkolodnyy, N., Golushko, S., Afonnikov, D., and Kolchanov, N. (2016). Mechanical Behavior of Cells within a Cell-Based Model of Wheat Leaf Growth. *Frontiers in Plant Science*, 7(December):1–15.

5

Appendix

5.1 Mechanical isolation of rapidly growing cell buffers growth heterogeneity and contributes to organ shape reproducibility

This not finalized article explores the implication of the mechanical response to trichome growth on sepal shape.

I trained a post-doc in the team, Antoine Fruleux, who modified the modeling framework used in chapters 2 and 3 to investigate the impact of trichome development on sepal shape.

Mechanical isolation of rapidly growing cell buffers growth heterogeneity and contributes to organ shape reproducibility

Nathan Hervieux^{1*}, Satoru Tsugawa^{2,5*}, Antoine Fruleux¹, Mathilde Dumond¹, Tamiki Komatsuzaki³, Anne-Lise Routier³, Arezki Boudaoud¹, John C. Larkin⁴, Richard S. Smith³, Chun-Biu Li^{2,5}, Olivier Hamant¹⁺

1 Laboratoire de Reproduction et Développement des Plantes, Université de Lyon, ENS de Lyon, INRA, CNRS, 46 Allée d'Italie, 69364 Lyon Cedex 07, France

2 Research Institute for Electronic Science, Hokkaido University, Kita 20 Nishi 10, Kita-ku, Sapporo 001-0020, Japan

3 Department of Comparative Development and Genetics, Max Planck Institute for Plant Breeding Research, Carl-von-Linné-Weg 10, 50829 Köln, Germany

4 Department of Biological Sciences, Louisiana State University, Baton Rouge, LA 70803-1715, USA.

5 Present address : Department of Mathematics, Stockholm University, 106 91 Stockholm, Sweden

* These authors contributed equally to this work.

+ Author for correspondence: Olivier.hamant@ens-lyon.fr, +33 4 72 72 88 75

Summary

Final organ shapes are highly reproducible despite local growth heterogeneities. The corresponding buffering mechanism is unknown. Here we focus on fast growing trichome cells in the Arabidopsis sepal, a reproducible floral organ. We show *via* computational modeling that rapidly growing cells may distort organ shape. However, the cortical microtubule alignment along growth-derived maximal tensile stress in adjacent cells would mechanically isolate rapidly growing cells and limit their impact on organ shape. *In vivo*, we observed such microtubule response to stress and consistently found no significant effect of trichome number on sepal shape, in WT and lines with trichome number defects. Conversely, modulating the microtubule response to stress in *katanin* and *spiral2* mutant made sepal shape dependent on trichome number, suggesting that, while mechanical signals are propagated around rapidly growing cells, the resistance to stress in adjacent cells mechanically isolate rapidly growing cells, thus contributing to organ shape robustness.

Keywords

Shape reproducibility, growth heterogeneity, mechanical signals, trichome, microtubules, micromechanics, modeling

Introduction

Recent evidence suggests that stochasticity is widespread in cellular and molecular mechanisms (Meyer and Roeder, 2014). Growth is not uniform and neighboring cells can grow at highly different rates, notably in plant tissues (Elsner et al., 2012)(Kierzkowski et al., 2012)(Tauriello et al., 2015)(Uyttewaal et al., 2012). This observation raises the question of how variability and stochasticity observed at the level of each cell composing a tissue can lead to reproducible organ size and shape.

In theory, morphogen gradients may provide a supracellular synchronizing cue within a given region, leading in the end to reproducible shapes (Jaeger et al., 2008; Kuchen et al., 2012; Nelissen et al., 2012). However, even within such regions, adjacent cells can still display high level of growth heterogeneity (Uyttewaal et al., 2012)(Elsner et al., 2012). Thus reproducible shapes in the presence of growth heterogeneity could emerge from the combination of many, partially overlapping, supracellular gradients. While there is evidence that indeed multiple morphogen gradients contribute to morphogenesis, it remains to be shown that such combinations would be sufficient to generate heterogeneity among individual cell. More pragmatically, because patterns of cell growth are not identical between individuals, growth heterogeneity cannot only be the result of a well-choreographed genetic regulation.

Mechanical signals have been proposed to play a central role in the control of organ size and shape. For instance, in organs where cells adhere to each other, differential growth generates mechanical conflicts between neighboring cells that impact final organ shape (Coen and Rebocho, 2016). The accumulation of mechanical stresses was even proposed to trigger growth arrest at the level of the whole organ (Shraiman, 2005). While this proposal is still debated, it may apply to the wing imaginal disc in *Drosophila*, where faster growth in the outer part of the disc compresses internal cells and would provoke an arrest in cell division (Shraiman, 2005)(Aegerter-Wilmsen et al., 2007). In plants, a mechanical conflict emerges between the fast growing center and slow growing tip of the sepal; the resulting transverse tensile stresses at the tip was proposed to channel sepal shape, through an impact of stress on microtubule and cellulose deposition (Hervieux et al., 2016a). While these studies show that mechanical stress can act as supracellular signals, they do not address the link between growth heterogeneity at the cell level and organ size and shape.

In theory, local mechanical conflicts between adjacent cells may add noise to morphogen-derived growth patterns. In that scenario, such random processes would disturb stereotypic development and lead to abnormal individuals in the population. Because organ size and shapes are reproducible, while displaying heterogeneity at the cell level, this suggests instead that either noise is very low or that it is buffered.

On the one hand, it was proposed that a spatiotemporal averaging of cellular growth variability in sepal of *Arabidopsis* leads to precise organ shape. The averaging mechanism requires a reduced production of Reactive Oxygen Species (ROS), and in the simplest scenario does not involve a mechanical feedback (Hong et al., 2016). On the other hand, mechanical feedback from growth onto microtubule behavior has been proposed to amplify differences in growth rate between neighboring cells in the shoot apical meristem of *Arabidopsis* (Uyttewaal et al., 2012). Mechanical feedback would thus not act as buffering mechanism, but would instead increase noise. Reproducibility of organ size and shape thus results from different noise modulation mechanisms.

Here we investigate the relation between local mechanical conflicts and final shape using the *Arabidopsis* sepal as a model system, for its variability in cell type (Roeder et al., 2010) and in cell growth rate (Hervieux et al., 2016a)(Hong et al., 2016)(Tauriello et al., 2015).

Results

Rapidly growing cells induce a circumferential tensile stress pattern in adjacent cells

A local modification of the maximal stress directions in a tissue under tension, by ablating a cell, leads to a circumferential rearrangement of these principal stress directions around the ablation (Hamant et al., 2008)(Sampathkumar et al., 2014). At the level of the tissue each cell grows at its own rate and such growth heterogeneity may affect the local pattern of stress, notably because plant cells are glued to one another through their cell walls. To analyze the impact of rapidly growing cells on their neighbors, we take inspiration from trichomes (i.e. plant hair cells) which exhibit localized rapid growth, leading to their bulging out of the epidermis surface (Hülskamp, 2004). We implemented a mechanical model of a tissue with 3D pressurized cells using the finite element method (FEM). The model construction follows Bassel et al. (Bassel et al., 2014a) and consists of a single layer of 3D cells arranged as a staggered grid of rectangular boxes (Figure 1A). The cell wall was discretized into triangular surface elements, with shared nodes on the walls connecting adjacent cells. We used an isotropic, linearly hyperelastic material model, with a Young's modulus of 300MPa, and a Poisson's ratio of 0.3 (see Methods and Figure 1 – figure supplement 1). In the initial step of the simulation, cells were pressurized with a turgor pressure of 0.5 MPa (Figure 1B). Since all the cells are identical in size and shape, stress patterns are the same in all cells, except for minor differences at the edges due to boundary conditions.

We next explored the impact of a rapidly growing cell on the stress pattern in adjacent cells, taking the trichome as a model system. One hypothesis is that the trichome develops increased turgor pressure (Ruan et al., 2001). To simulate this possibility, we progressively increased the pressure in the central cell of our model and observed the effect on the stress in neighboring cells. A circumferential pattern of stress started to appear for pressures above 3 MPa (Figure 1 – figure supplement 2). A higher pressure in the trichome would also provide an explanation for its increased growth rate, since growth depends on both cell wall relaxation and turgor pressure (Lockhart, 1965)(Ruan et al., 2001)(Cosgrove, 2016).

Using a Lockhart-type growth model described in (Bassel et al., 2014a) we then grew the tissue by expanding the elements' resting shape. At each growth step, the new reference shape of the elements representing the cell wall was computed by multiplying the amount of strain due to turgor

pressure with a fixed growth factor. Higher pressure in the trichome resulted in more stretch in the cell wall, causing faster growth than in the surrounding cells (Figure 1C-D). With the inclusion of growth, the circumferential patterns of stress could be obtained for much lower pressures in the central cell (e.g. 1 MPa) than in the non-growing case (Figure 1 – figure supplement 3).

There is increasing evidence that the epidermis of plant aerial organs are under tension (e.g. (Kutschera and Niklas, 2007)(Sampathkumar et al., 2014)). How this global pattern of stress would impact the local growth-derived stress around rapidly growing cells? Previously published simulation models have shown that when there is global tissue tension, the load borne by an ablated cell is transferred to its neighbors, producing a circumferential pattern of tensile stress around the ablation (Hamant et al., 2008)(Sampathkumar et al., 2014). We reasoned that a more extensible cell wall in the trichome could have a similar effect thus potentially acting in synergy with increased turgor pressure in the trichome cell (see (Ruan et al., 2001). As the trichome grows, tissue tension would be transferred to its neighbors, increasing their stress. We then simulated this scenario by applying tension to the boundary and increasing the growth of the central cell, both by decreasing the cell wall elasticity and by increasing its growth factor (corresponding here to relaxation rate or extensibility (Lockhart, 1965)). Under the conditions we tested, differences in wall mechanical properties alone did not result in a visible mechanical influence between the cells (Figure 1E). When stretching the tissue, a circumferential pattern of stresses emerged around the growing trichome without even requiring any difference in turgor pressure (Figure 1F). When increasing turgor pressure in the central cell, while maintaining the tissue under tension, the circumferential pattern of stress was reinforced (Figure 1G – NEW SIMULATION)

To conclude, increased growth rate in the emerging trichome cell triggers a circumferential tensile stress orientation in adjacent cells and tension in the epidermis would rather reinforce this pattern.

Because trichomes switch from a growth in XY plane to a growth in the Z direction as they bulge out, the pattern of stress would likely not be remain circumferential. To formally demonstrate that hypothesis, we next XXXXXX (transfer the load to the trichome and see the new stress pattern – Figure 1H)

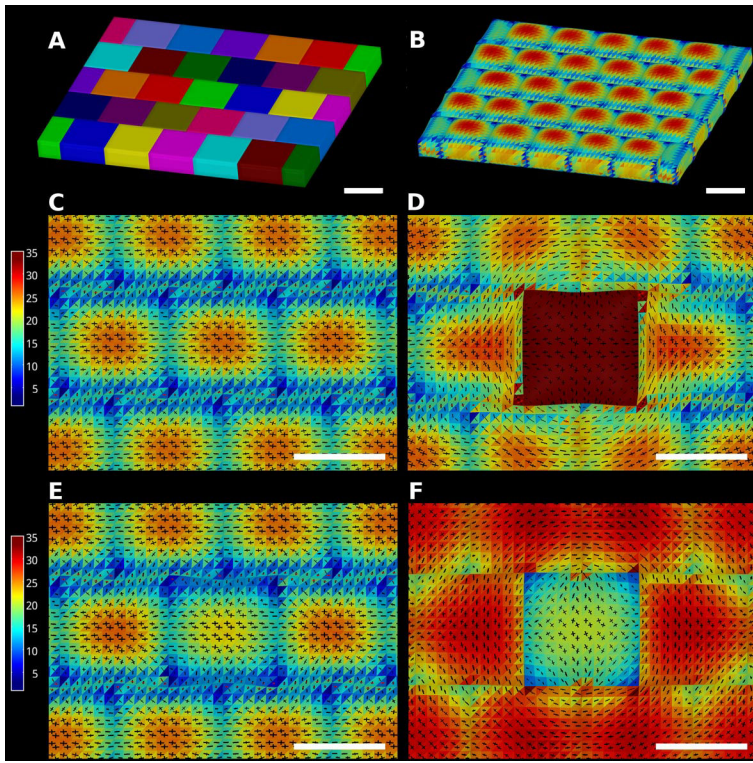


Figure 1. Mechanical simulations of a pressurized cell layer.

(A) Template used for all Finite- Element simulations, colored by cell labels. (B) Internal pressure is applied to the model, causing cell walls to stretch and bulge outwards until a mechanical equilibrium is found. (C-F) Close-up view of the mechanical stresses resulting from different hypotheses. (C) Uniform pressure and mechanical properties within the tissue results in similar stress patterns between cells. Note that local stress is equal in all directions (i.e. isotropic) at the cell centers. (D) Increasing the internal pressure in the central cell to 4 MPa, compared to 0.5 MPa in the other cells, results in a circumferential pattern of stresses around the cell. While the local stress in the circumferential direction slightly increases, the stress in the other direction is decreased but remains non-zero in most places. (E) A softer cell wall in the central cell causes the cell to bulge out more at equilibrium, even when pressure is uniform within the tissue. However, local stresses remain nearly unchanged in the neighboring cells. (F) Circumferential stress patterns become apparent once the whole tissue is stretched and allowed to grow. The fast-growing central cell relaxes stresses faster than its neighbors, resulting in stress concentration around it, similar to an ablated cell. (G) Increasing the internal pressure in the central cell and stretching the whole tissue reinforces the circumferential stress pattern. (H) When the trichome bulges out, the circumferential stress pattern is lost

Crosses: principal directions of stress. Colorbar: sum of local stresses in MPa. Scale bars: (A-B) 40 μm , (C-F) 50 μm .

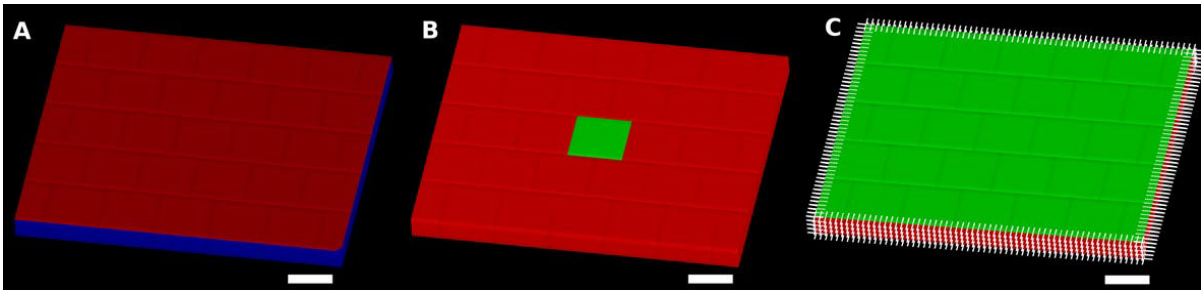


Figure 1 – Figure supplement 1. Material parameters and boundary conditions used for the FEM simulations.

(A) Top and bottom cell walls (red) are assigned a different thickness parameter than anticlinal cell walls (blue). The anticlinal cell walls of two neighboring cells are touching each other and are mechanically coupled, as in real plant tissues. We therefore assigned a thickness of 1 μm to the top and bottom walls, while the anticlinal cell walls belonging to each individual cell are each 0.5 μm thick, summing up to 1 μm for the total thickness. (B) The central cell (green) was assigned different parameters than the rest of the tissue (red), either pressure or cell wall elasticity and growth parameter. (C) Boundary conditions applied to the tissue. Positions of the vertices at the tissue edge (red) were fixed along the directions showed by the white lines. The same directions were used to displace the vertices when stretching the tissue. Scale bars: 40 μm

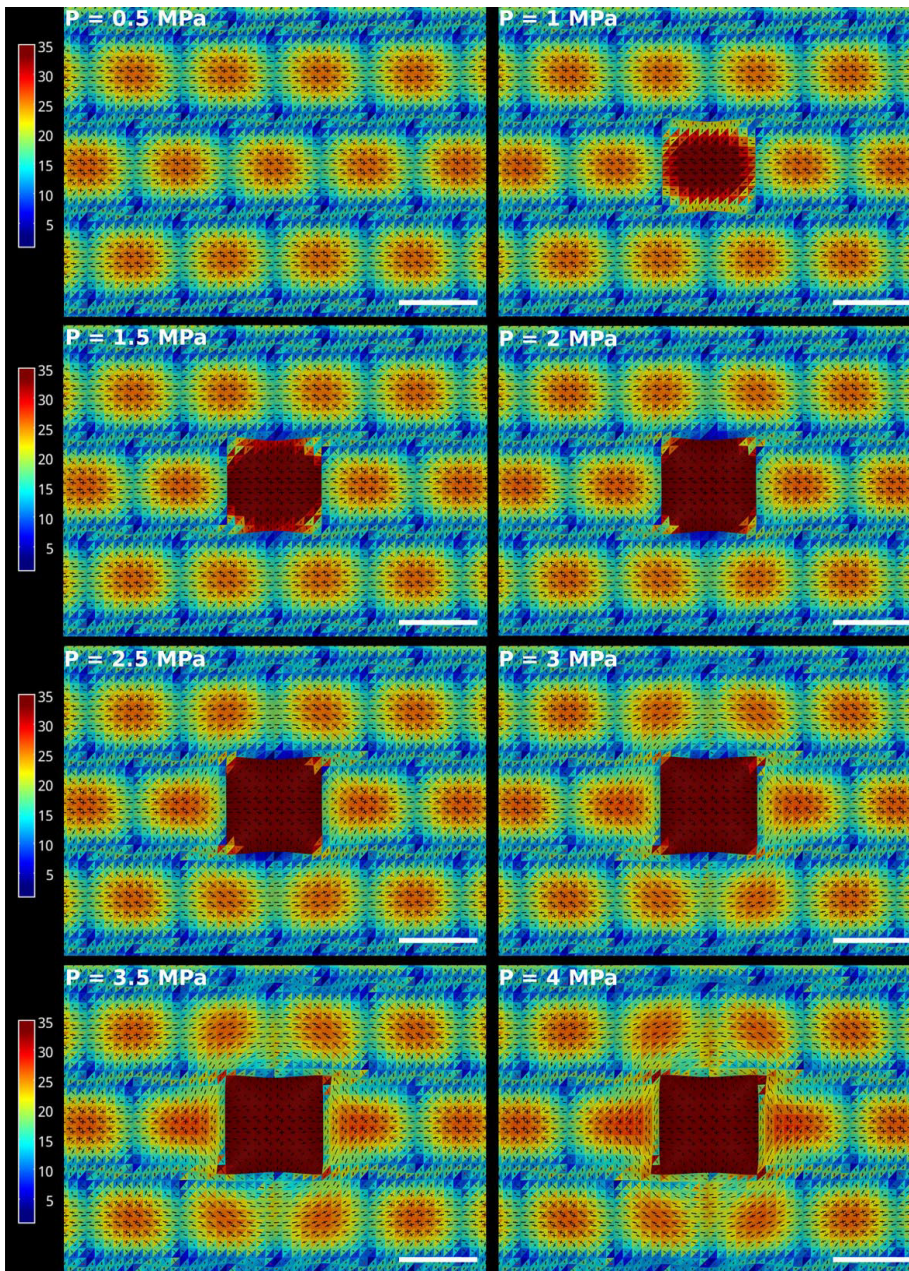


Figure 1 – Figure supplement 2. Effect of increased turgor pressure on stress patterns.

Identical material parameters were assigned to all the cells, while only the pressure of the central cell varied from 0.5 MPa to 4 MPa. Note that a visible circumferential stress pattern occurs from 3 MPa. Turgor pressure of other cells: 0.5 MPa. Material parameters: Young's modulus = 300 MPa, Poisson's ratio = 0.3, Cell wall thickness = 1 μm . No restriction on boundaries. Scale bars: 40 μm

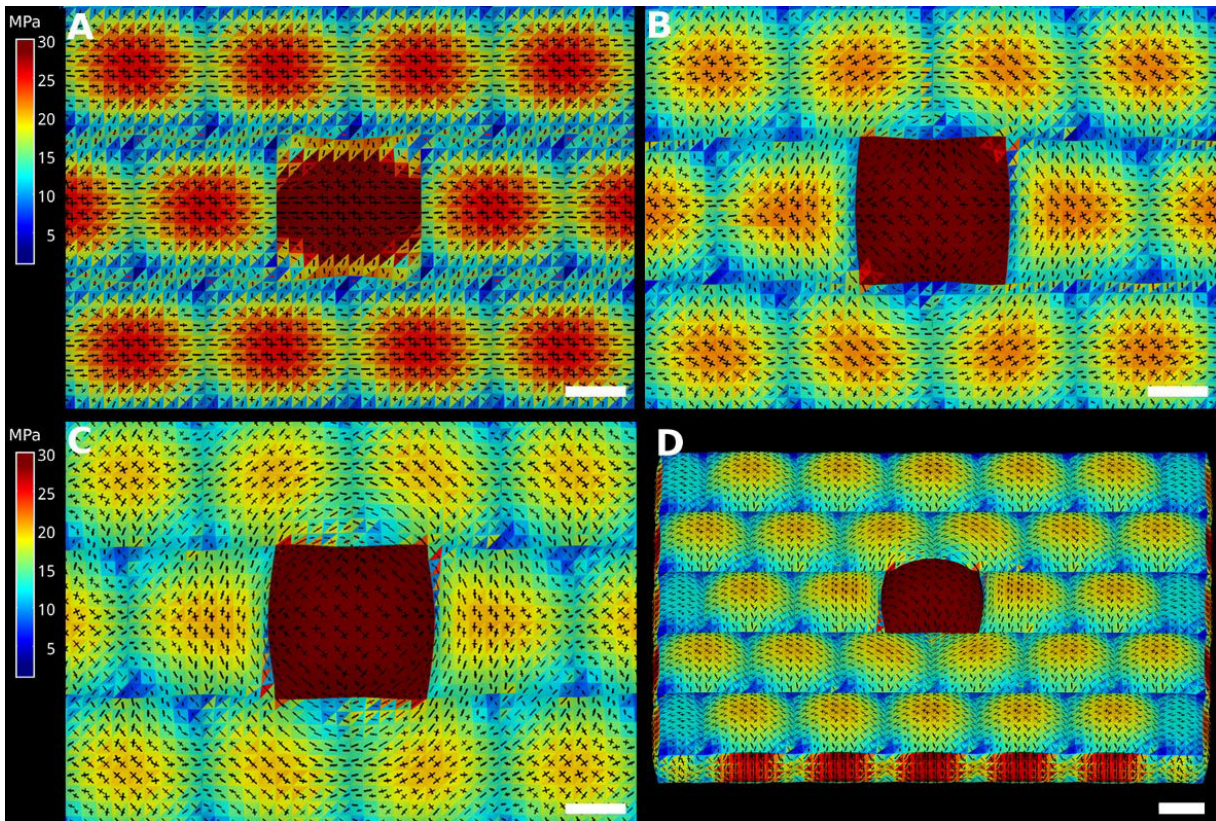


Figure 1 – Figure supplement 3. Effect of increased turgor pressure on stress patterns in a growing tissue.

First step of the simulation is identical to the conditions applied to [Figure S2](#), with internal pressure in the central cell equal to 1 MPa and all the other cells 0.5 MPa. Once mechanical forces are at equilibrium (A), growth was simulated by changing triangles rest length according the amount of elastic deformation they underwent, multiplied by a growth factor. The growth factor was twice as large in the central cell, resulting in this cell bulging into its neighbors and creating a circumferential stress pattern, as visible after 12 (B) and 20 (C) steps of growth simulation. A side view of the tissue shows that the central cell also bulges outward, similar to a trichome cell. Material parameters: Young's modulus = 300 MPa, Poisson ratio's = 0.3, Cell wall thickness = 1 μm , growth factor = 0.1 (0.2 for central cell). No restriction on boundaries. Scale bars: 20 μm

Cortical microtubules reorient along predicted maximal tensile stress around growing trichomes

We next tested this prediction experimentally. We use the abaxial sepal, which is the farthest of the four sepals from the stem axis. Sepals exhibit substantial variability at the cell level (Roeder, 2010), having a wide range of cell sizes and cell identities on the abaxial epidermis, while displaying roughly similar final shapes. Trichomes are one of the cell types present in the abaxial epidermis of the sepal (Figure 2A-D).

First, we confirmed that trichomes grow faster than their neighboring cells in sepals. To do so, we performed time-lapse imaging of emerging trichome on the abaxial sepal expressing a fluorescent plasma membrane marker. We used MorphoGraphX (Barbier de Reuille et al., 2015) to segment cells in the epidermis for each time point and analyze their growth properties. As hypothesized we observed that trichome cells grow approximately twice as fast as their neighbors before they bulge out (Figure 2E-F). Although the number of time points once the trichome starts to elongate along the Z axis (i.e. normal to sepal surface) is low, growth in the XY plane (i.e. tangential to sepal surface) seemed to decrease rapidly at that point.

We next investigated whether this local heterogeneity of growth rate leads to a mechanical conflict and a reorientation of principal stress directions as suggested in our model. Cortical microtubules (CMTs) align with predicted maximal tensile stress after artificial mechanical perturbations, like ablations or compressions, in the sepal (Hervieux et al., 2016a), as well as in shoot meristems (Hamant et al., 2008) and cotyledon pavement cells (Sampathkumar et al., 2014). We thus used a microtubule marker (GFP-MBD) under the control of the CaMV35S promoter to visualize CMTs as a read-out of principal stress directions. The sub-cellular alignment of CMTs was then analyzed from 2.5D extracted cell surfaces (Barbier de Reuille et al., 2015)(Tsugawa et al., 2016).

Qualitatively, we observed that CMTs became circumferential around the trichome during the period of fast trichome growth and this circumferential CMT pattern was then lost after the trichome bulged out (Figure 2G). To quantify this behavior, we used a subcellular nematic tensor-based tool to generate so-called CMT anisotropy segments (CMT segments in short) that represent the orientations and strength of the CMT alignment in a local circle of radius $1\mu\text{m}$ ((Tsugawa et al., 2016), see Methods).

As expected from our qualitative observation and as predicted in our model, we measured a significant bias towards circumferential orientations for CMTs in the first ring around the growing trichome, i.e. between 10 and 20 μm around the center of the trichome before it bulged out (Figure 2H and 3A-C, Figure 3 – figure supplement 1A). Note that this response was less obvious in the outer ring, between 20 and 30 μm , around the center of the trichome (Figure 3D, Figure 3 – figure supplement 1B). Using this method, we could also demonstrate that this circumferential organization disappeared once the trichome bulged out (Figure 3C, Figure 3 – figure supplement 1A). This fits with the tissue tension hypothesis; as trichome growth in the XY plane slows down, it no longer transfers the load to its neighbors and the circumferential stress pattern disappears, as shown in our model (Figure 1H).

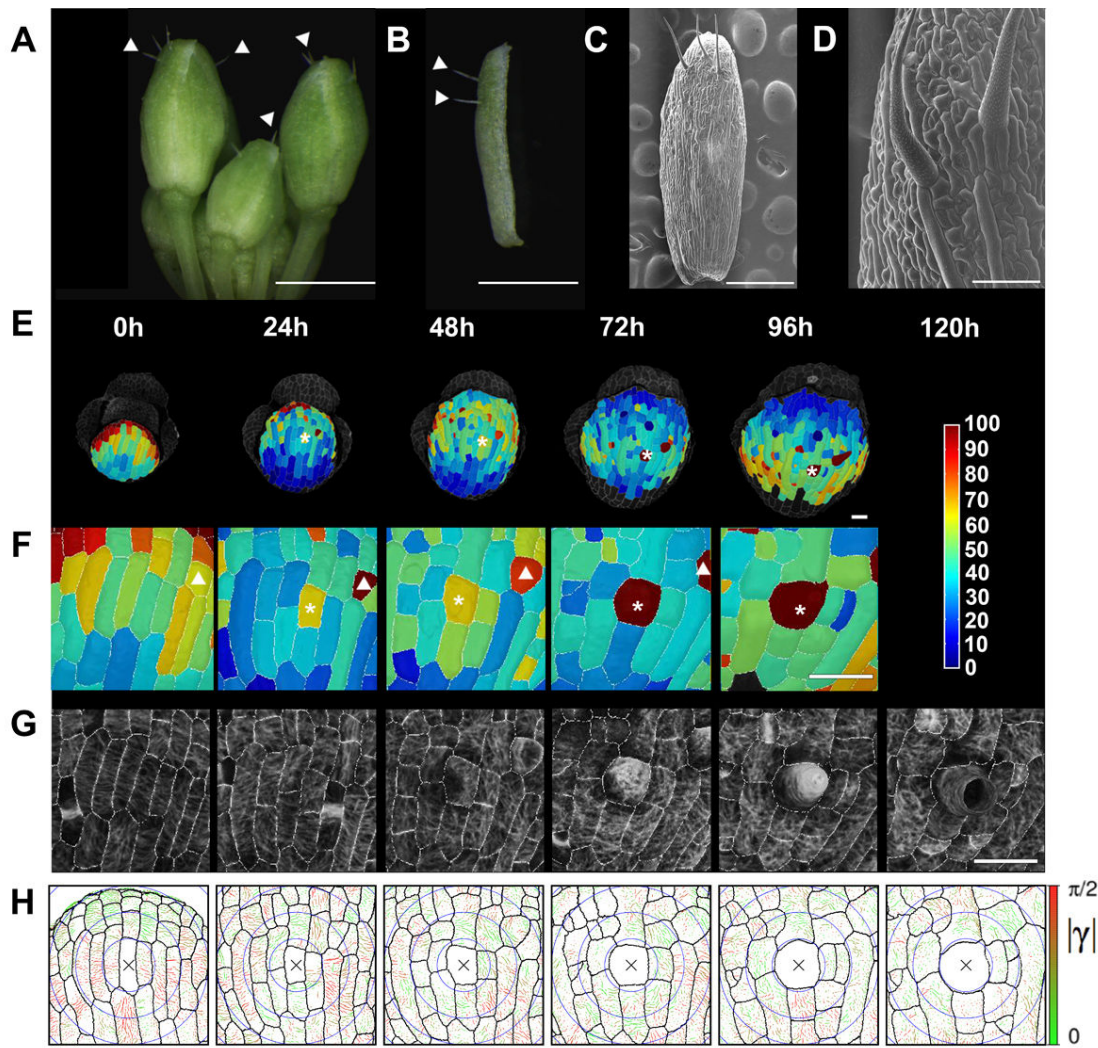


Figure 2. Circumferential CMT orientation around a fast growing trichome in sepals

(A) Trichomes at the surface of floral buds (sepals) Scale bar: 0.5 mm. (B) Trichomes on a dissected abaxial sepal. Scale bar: 0.5 mm (C-D) SEM image of the surface of an abaxial sepal at low (C, scale bar: 300 μ m) and high magnification (D, scale bar: 50 μ m). (E) Heatmap of area extension (%) over 24-hr intervals displayed on the first time point. Scale bar = 20 μ m. (F) Details area extension (%) in regions highlighted with a white symbol in (E). Scale bar = 20 μ m. Note that the cell highlighted with a small triangle is another trichome. (G) Close-up of the CMT organization at the surface of the abaxial sepal around a growing trichome. Scale bar = 20 μ m (H) Results of anisotropy vectors of images shown in (G) See Figure 3A for the definition of angle γ . Note a slight change of inclination between (G) and (H) in order to better visualize anisotropy vectors.

The CMT response to growth-induced stress can be modulated genetically

To further test this response, we next used the *bot1-7*, katanin allele (in WS-4 ecotype), in which CMTs response to mechanical perturbations is slower due to an impaired katanin-driven microtubule-severing activity (Hervieux et al., 2016a)(Sampathkumar et al., 2014)(Uyttewaal et al., 2012). As expected, CMTs around growing trichomes in *bot1-7* was not as clear-cut as in the WT, at least qualitatively. We next quantified the CMT behavior as shown above (see Methods). Although CMTs also became circumferential around a growing trichome in *bot1-7*, the response was slower and weaker during the growing phase of the trichome in the XY plane, when compared to the WT (Figure 3C-D, Figure 3 – figure supplement 1, Figure 3 – figure supplement 2). Also consistent with a slower CMT dynamics and delayed response to stress, a bias towards a circumferential organization was still detected in *bot1-7*, but it appeared after the trichome bulged out (Figure 3C, Figure 3 – figure supplement 1, Figure 3 – figure supplement 2A). The statistical differences between WT and *bot1-7* were confirmed with a permutation test for the probability distribution of the weighted orientations at each time point (see Methods). The p -values for are $p=0.048$ at time -48h, $p < 10^{-15}$ at time -24h, $p < 10^{-15}$ at time 0, $p < 10^{-15}$ at time 24h and $p < 10^{-15}$ at time 48h. The p -values for are $p < 10^{-15}$ at time -48h, $p = 0.21$ at time -24h, $p = 3.0 \times 10^{-4}$ at time 0, $p = 1.0 \times 10^{-4}$ at time 24h and $p < 10^{-15}$ at time 48h. For , the distributions of the weighted orientation are statistically different, except at time -24h.

Taken together these data suggest that the transient reorganization of CMTs around a growing trichome is largely due to a modification of mechanical stress pattern and the ability of CMTs to respond to this perturbation. Furthermore, a tight regulation of CMT dynamics mediated by katanin activity is needed to allow this transient response to occur without delay.

Because our model suggests that local growth heterogeneity may be buffered by the cell response to stress, we next analyzed the impact of the adjacent cell response to stress on local growth pattern. We measured N_{pos} , the number of neighbors growing more slowly than the trichome, before and after the trichome bulged out, and normalized to the total number of neighbors N_{tot} (Figure 3E, see Methods).

In the wild type, N_{pos} decreased rapidly before the trichome bulged out, suggesting that the directional reinforcement of the walls in the cells surrounding a trichome may constrain trichome growth in the XY plane (Figure 3E). To test that hypothesis, we performed the same analysis in the *bot1-7*

mutant, which displayed a delayed microtubule response to stress. As expected, N_{pos} also decreased in *bot1-7*, but with a delay (Figure 3E, $p = 0.0018$ at time -48h, $p = 0.0013$ at time -24h, $p = 0.0038$ at time 0, $p = 0.0008$ at time 24h; the distributions of the averaged proportion of slower neighbors are statistically different between wild type and *bot1-7*). Altogether, these results suggest that while the microtubule response to growth-induced stress is transient in sepal trichomes, it is sufficient to have a local impact on growth.

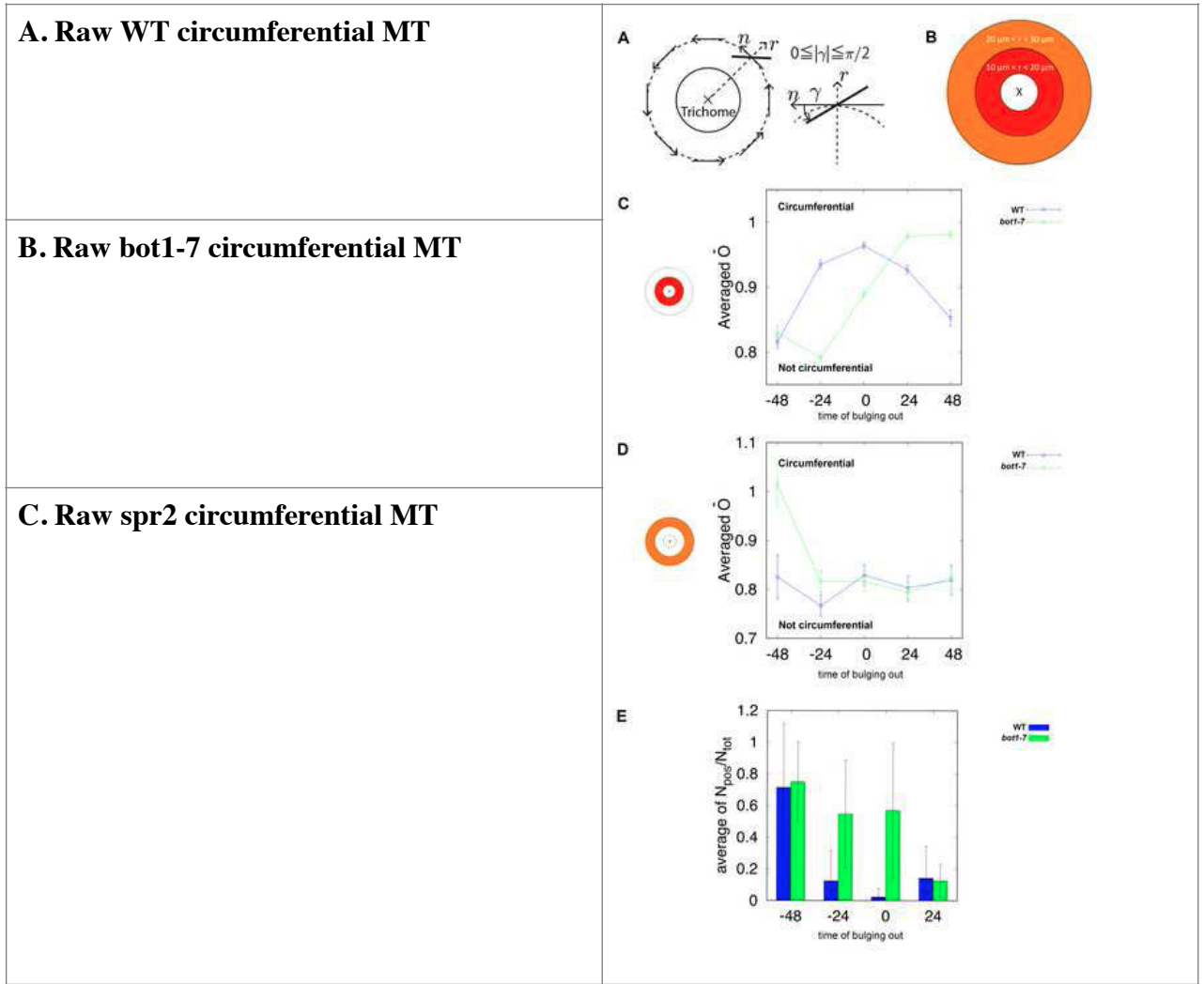


Figure 3. Quantification of the local impact of a fast growing trichome on adjacent cells
(A-C) Close-ups: circumferential CMT alignment around growing trichome cells in WT **(A)**, *bot1-7* **(B)** and *spr2-2* **(C)**. **(D)** Schematic explanation of the angle γ represented in Figure 3H. **(E)** Schematic representation of distance chosen for the analysis. The black cross in the center represents the center of the trichome. **(F-G)** CMT orientation in wild type and *bot1-7*, before and after trichome starts to grow along the Z direction (bulging out) between 10 μ m and 20 μ m **(F)** and between 20 μ m and 30 μ m **(G)** from the center of the trichome. Time is in hours. **(H)** Growth heterogeneity before and after trichome bulges out: N_{tot} is number of total neighbors around trichomes at time t_i ; N_{pos} is the number of neighbors that grow slower than the trichome. The average of the ratio N_{pos}/N_{tot} over all trichomes provides how heterogeneous the growth is around trichome (i.e. the proportion of cases when the trichome grows faster than its neighbours, averaged over all trichomes).

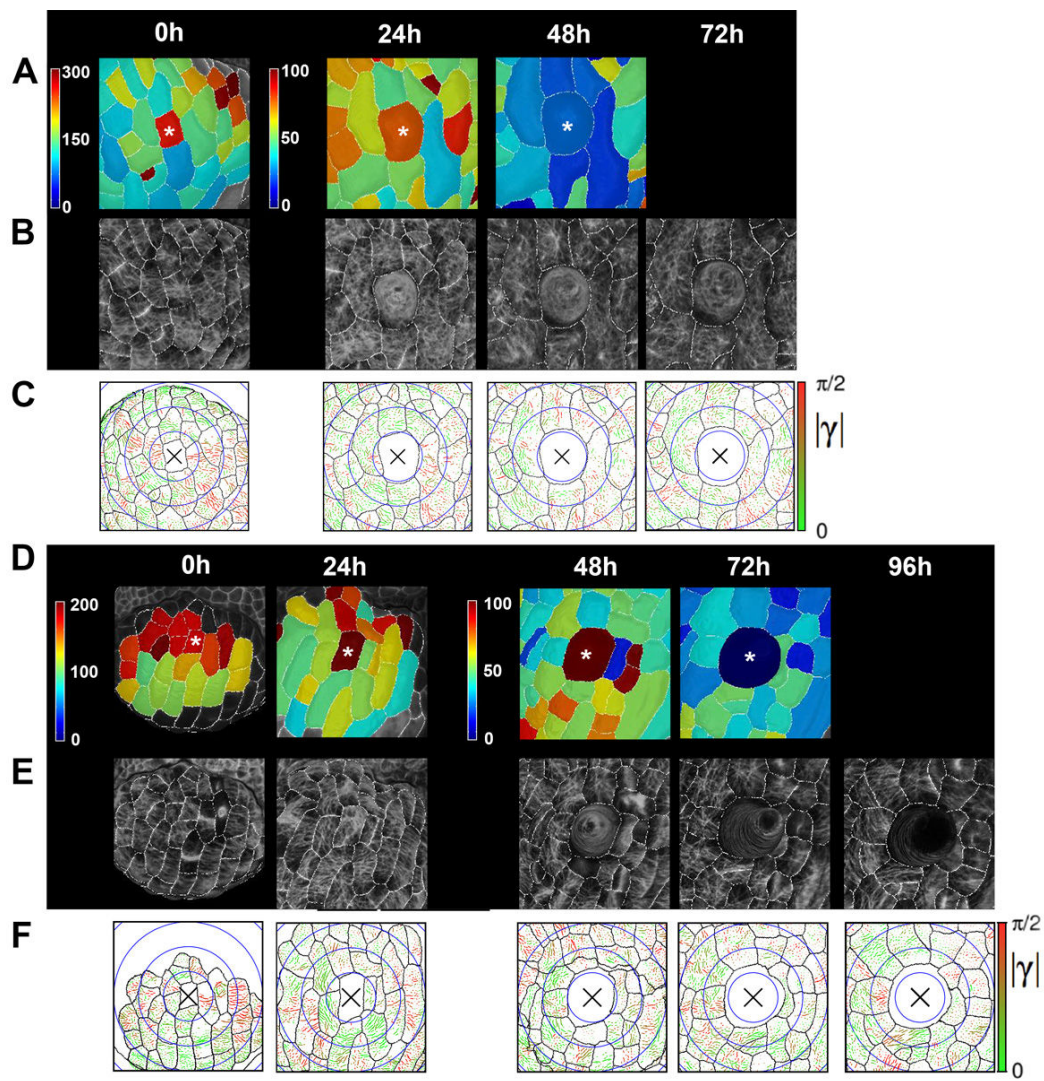


Figure 3 – figure supplement 1. CMT orientation around a fast growing trichome in *bot1-7* (A-C) and *spr2-2* (D-F) sepals

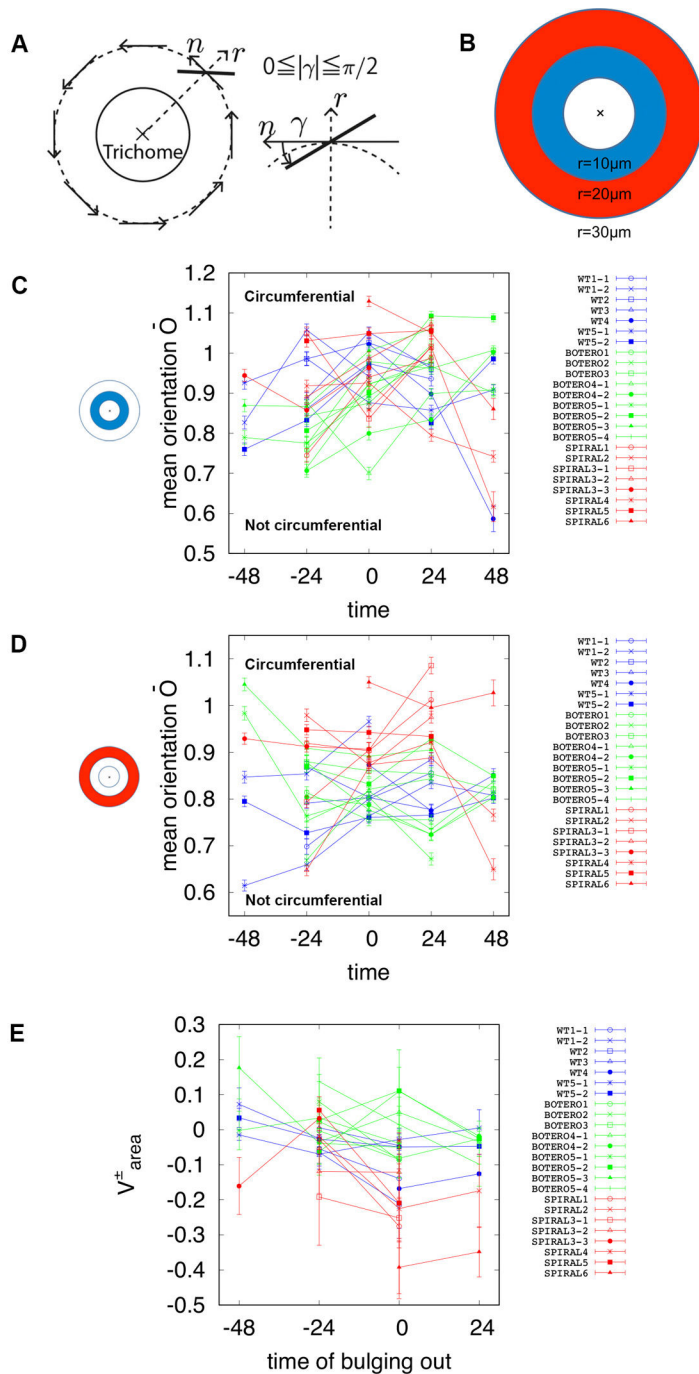


Figure 3 – Figure supplement 2. Kinetics of CMT orientation around a growing trichome.

CMT orientation in wild type, *bot1-7*, and *spr2-2* before and after trichome starts to grow along the Z direction (bulging out) between $10\mu\text{m}$ and $20\mu\text{m}$ (A) and between $20\mu\text{m}$ and $30\mu\text{m}$ (B) from the center of the trichome. #N-i refers to i trichomes on the same sepal N. Time in hours.

Theory: Rapidly growing cells may distort organ shape, depending on the ability of adjacent cells to resist local stress

In an organ with an imposed growth pattern, the addition of noise, i.e. local growth heterogeneity, may in theory affect final organ shape. To test that hypothesis formally, we use a continuous, tissue-scale, finite element model of sepal growth, as in (Hong et al., 2016). Note that such a two-dimensional model matches our focus on the epidermis, and its growth limiting role in shaping organs (Savaldi-Goldstein et al., 2007)(Kutschera and Niklas, 2007).

TEST 1 : No feedback : organ shape reproducibility decreases when trichome number increases

Next, we investigated whether a mechanical resistance of cells adjacent to a rapidly growing cell would limit the impact on organ shape

TEST 2 : Constant feedback : stiff ring around trichomes : organ shape reproducibility becomes less dependent on trichome number

Last, we investigated whether an optimum in buffering exist by modulating the size of the resisting ring around rapidly growing cells.

TEST 3 : Variable feedback : small vs large rings around trichomes : organ shape reproducibility is reached for an optimum in trichome number and ring size

Altogether, these results suggest that while local growth heterogeneities may affect organ shape reproducibility, a mechanical reinforcement in cells neighboring rapidly growing cells can cancel that effect, thus contributing to organ shape reproducibility.

Figure 4. The local response to stress may contribute to organ shape reproducibility

(A) No feedback, variable number of soft cells

(B) Constant ring size, variable ring number

(C) Variable ring size, variable ring number

The cell response to stress modulates the relation between trichome number and sepal shape reproducibility.

Because our model predicts that the mechanical isolation of rapidly growing cells can counteract the impact of rapidly growing cells on organ shape reproducibility, we next analyzed sepal outlines with a previously described pipeline (Hong et al., 2016) and performed a morphometric analysis of the mature sepal shape to detect correlations with the number of trichomes in WT sepals.

In two wild-type ecotypes (*Col-O* and *WS-4*), we did not detect any significant correlation between the number of trichomes and sepal width, length or aspect ratio (Figure 5, $n=197$ *Col-O* sepals and $n=XXXX$ *WS-4* sepals).

To challenge that result, we also analyzed the relation between trichome number and sepal shape reproducibility in two lines (*35SR* and *gl3egl3*) with altered epidermal identity, and notably, in their ability to generate trichomes. Strikingly, even in these genotypes, we could not detect a significant impact of trichome number on sepal shape reproducibility (Figure 5, $n=XXX$ *35SR* sepals, $n=XXXX$ *gl3egl3* sepals).

Because we cannot exclude the possibility that a higher number of trichomes may affect sepal shape, we next investigated whether a reduced response to stress in the katanin mutant would make sepal shape reproducibility dependent on trichome number. Although the effects were weak, we could detect a significant impact of trichome number on sepal shape reproducibility in the *katanin* mutant (Figure 5, $n=431$ *bot1-7* sepals).

To further challenge this result, we conducted the same analysis in the *spiral2* mutant background. SPIRAL2/TORTIFOLIA is present at the sites of microtubule cross-overs and has been proposed to prevent microtubule severing at those sites (Buschmann et al., 2004; Shoji et al., 2004; Wightman et al., 2013). In a *spr2* mutant, severing is thus dramatically increased and microtubule can self-organize more rapidly. Consistently, the *spr2* mutation has recently been shown to promote the CMT response to mechanical perturbations both in shoot meristems and in sepals (Hervieux et al., 2016a) (Louveaux et al., 2016a). We thus reasoned that in a *spr2* mutant background, the CMT alignment around growing trichomes should be enhanced. In *spr2-2* (in *Col-0* ecotype), we observed circumferential CMTs around a growing trichome as expected. Nonetheless, our quantifications did not detect a significant difference between *Col-0* and *spr2-2* in the 10-20 μm ring (Figure 3, Figure 3 –

figure supplement 1, Figure 3 – figure supplement 2). However, when analyzing the more distant cells from the trichome center (20-30 μm ring), a bias towards circumferential CMTs was present in *spr2-2*, whereas this could not be detected in the WT (Figure 3, Figure 3 – figure supplement 1, Figure 3 – figure supplement 2). The CMT circumferential alignment was also more stable in time in *spr2-2* than in the WT, as it was still observed even after the trichome cell budged out, both in the 10-20 μm and 20-30 μm rings from the trichome center (Figure 3, Figure 3 – figure supplement 2). The permutation test was performed between wild type and *spr2-2*. The p-values for are $p < 10^{-15}$ at time -48, $p < 10^{-15}$ at time -24, $p = 0.30$ at time 0, $p = 0.020$ at time 24 and $p = 0.1883$ at time 48. The p-values for are $p < 10^{-15}$ at time -48, $p < 10^{-15}$ at time -24, $p < 10^{-15}$ at time 0, $p < 10^{-15}$ at time 24 and $p = 0.012$ at time 48. The distributions of the weighted orientation are statistically different, except for at time 0 and 48h.

Impact on growth heterogeneity in *spr2* as in WT (Figure 3XXX)

Interestingly, when analyzing sepal shape reproducibility in *spr2-2* mutant, we found it to be dependent on trichome number (Figure 5, Col-0: $n = 189$ Col-0; *spr2-2*: $n = 367$ sepals). We also found that sepal width increased with trichome number (Figure 5). This observation seems consistent with an impact of trichomes on the growth pattern of the sepal (Figure 4C), the circumferential microtubule alignments reducing the bias towards growth along the longitudinal axis of the sepal.

Coming back to our initial question, our results demonstrate that rapidly growing cells can impact the behavior of contiguous cells in sepals, notably through the microtubule response to mechanical signals. The consecutive mechanical isolation then buffers growth heterogeneity and thus contributes to organ shape reproducibility.


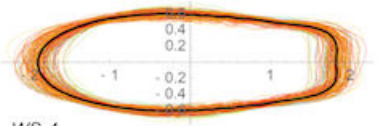
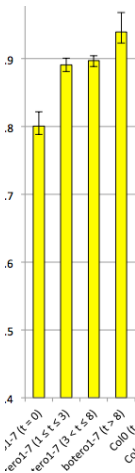
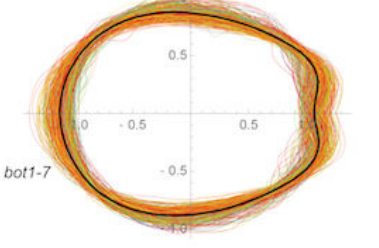
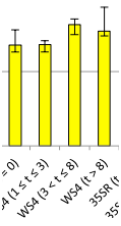
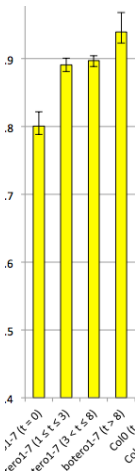
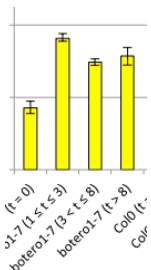
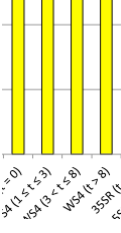
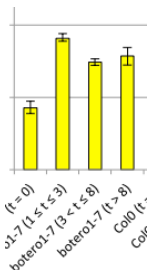
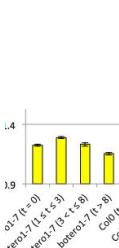
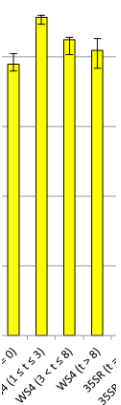
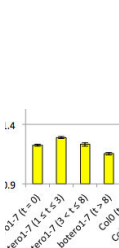
<p>A</p> 	<p>WS-4</p>	<p><i>bot1-7</i></p>	<p>Col-0</p>	<p><i>spr2-2</i></p>	<p><i>35SR</i></p>	<p><i>gl3egl3</i></p>
 <p>WS-4</p>	<p>B. Width</p>					
 <p>bot1-7</p>						
<p>Col-0</p> <p>XXXX</p>	<p>C. Length</p>					
<p><i>spr2-2</i></p> <p>XXXX</p>						
<p><i>35SR</i></p> <p>XXXXX</p>	<p>D. Aspect-ratio</p>					
<p><i>gl3egl3</i></p> <p>XXXXX</p>						

Figure 5. The presence of trichomes does not affect sepal shape and size in WT, *35SR* and *gl3egl3* lines, but impacts sepal shape in *bot1-7* and *spr2-2*

(A) Superimposed outlines of mature stage 14 wild-type (WS-4, Col-0), *bot1-7* (in WS-4), *spr2-2* (in Col-0), *35SR* (in Col-0) and *gl3egl3* (in Col-0) sepals. Outlines were normalized by size to reveal differences in shape. The variation is the difference between the median outline (black) and that of the individual sepals (colored). Colors scale bar represents the number of trichomes for each sepal outline. (B-D) Quantification of width (B), length (C) and aspect ratio (D) in wild-type (WS-4, Col-0), *bot1-7* (in WS-4), *spr2-2* (in Col-0), *35SR* (in Col-0) and *gl3egl3* (in Col-0) sepals, in function of the number of trichomes per sepal (4 classes: no trichome, 1-3 trichomes, 4-7 trichomes, more than 8 trichomes).

Discussion

Our study on sepal trichomes suggests that differential growth between adjacent cells generates a mechanical conflict with neighboring cells, which in turn locally and transiently impacts CMT orientations. Differential growth was already proposed to generate large-scale mechanical conflicts between different regions of a growing sepal (Hervieux et al., 2016a). A global level of growth heterogeneity between adjacent cells had also been proposed to self-maintain through a mechanical feedback on microtubules in shoots apical meristems (Uyttewaal et al., 2012). However, in both of these studies, the local response of cells to differential growth had not been investigated. The novelty of the present study resides in such local analysis: we demonstrate *in silico* and in experiments that two adjacent cells growing at different speed can indeed respond to each other via a mechanical signal; the response of the neighboring cells constrain the rapidly growing cell and prevent it from distorting the tissue (Figure 6). Interestingly in leaves, cells surrounding trichomes are elongated radially, consistent with the circumferential CMT orientation around young trichomes that we observed in sepals (Figure 6 – figure supplement 1).

Averaging variation in cellular growth over space and time is essential to achieve reproducible shape (Hong et al., 2016). Nevertheless, how this spatiotemporal averaging occurs is still unknown. Our results suggest that mechanical feedback could be a mechanism essential for this spatiotemporal averaging. In fact we could argue that the first response of CMTs around a rapidly growing cell occurs in order to restrain the propagation of the mechanical stress: reinforcing the cell wall with oriented cellulose deposition (Paredes 2016) is a way to resist to mechanical stress. Our analysis of growth heterogeneity before and after trichome emergence in wild type and microtubule severing mutants shows that the microtubule response to stress indeed constrains the growth of the trichome.

Note that we only consider the implication of local mechanical feedback. It is possible that other factors such as hormones or small chemical species like ROS could be generated by the emerging trichome and lead to the reorganization of CMTs. For instance, auxin (Sassi et al., 2014) and ROS (Livanos et al., 2014) were shown to affect CMT organization. Nonetheless, our data are consistent with a scenario in which growth-derived mechanical stress is buffered through the optimal response of CMTs, leading to robust organ shapes.

Interestingly, large-scale mechanical signals are likely to contribute to shape reproducibility. In the *feronia* mutant, which is partly impaired in mechanoperception, the root growth pattern exhibits increased variability (Shih et al., 2014). Similarly, neuron growth trajectory depends on the stiffness

of their mechanical environment (e.g. (Sur et al., 2013)). It seems therefore that mechanical signals add robustness to shapes, both *via* large-scale coordinating mechanisms, such as growth-derived tensile stress at the sepal tip, as well as *via* local buffering event, such as the CMT response to fast growing trichomes.

Figure 6. Graphical abstract

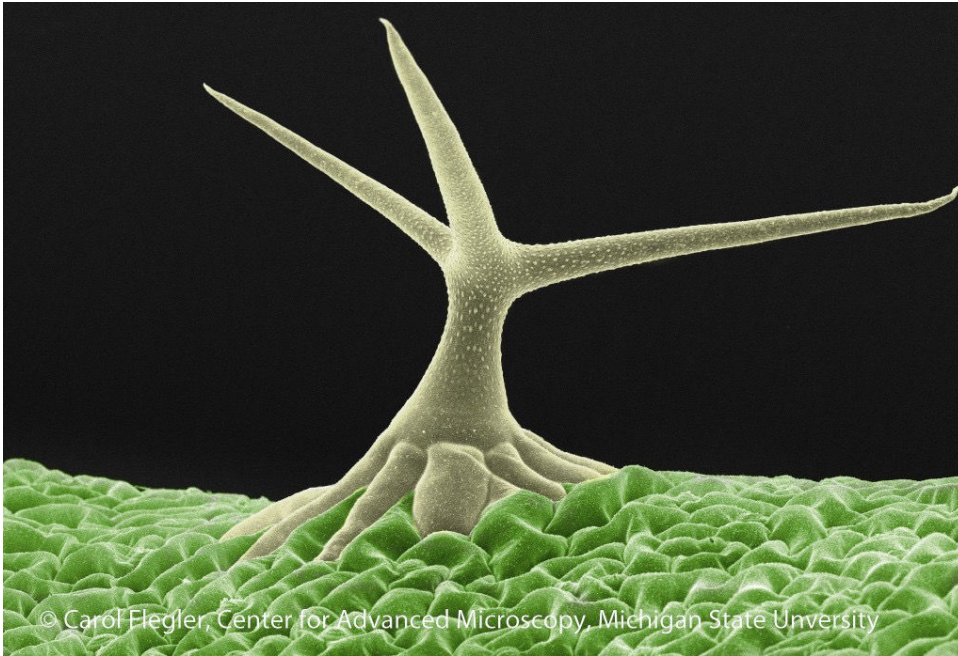


Figure 6 – Figure supplement 1. Radially elongated cells around leaf trichomes
To replace with our own image. John?

Material and methods

Plant Material and Growth Conditions

Plants were grown on soil in a phytotron under short-day conditions (8 hr/16 hr light/dark period) for 4 weeks and then transferred to long-day conditions (16 hr/8 hr light/dark period). The microtubule reporter line *p35S::GFP-MBD* (WS-4) and the membrane reporter line *pUQ10::Lti6b-2xmCherry* (Col-0) were described previously (Hervieux et al., 2016a). The *botero1-7* (katanin loss of function mutant allele) and *spiral2-2* mutants were previously described (Uyttewaal et al., 2012) (Hervieux et al., 2016a).

Live Imaging of the Growing Abaxial Sepal

One- to 2-cm-long main inflorescence stems were cut from the plant. To access young buds, the first 10–15 flowers were dissected out and the stem was then kept in an apex culture medium (Hamant et al., 2014) supplemented with 6-benzylaminopurine (900 mg/L). Twenty-four hours after dissection, the young buds were imaged with an SP8 laser-scanning confocal microscope (Leica) using long-distance 253 (NA 0.95) water-dipping objectives.

SEM observation

Scanning Electron Microscopy images of sepals from stage 14 flowers were acquired using a Hirox mini SEM 3000.

Image Analysis

Images were processed with MorphoGraphX 3D image analysis software (Barbier de Reuille et al., 2015). Cortical microtubules orientation was analyzed as described in (Tsugawa et al., 2016).

Sepal area measurements

Sepals dissected from stage 14 flowers were flattened between two slides and photographed on a black background using a dissecting microscope mounted with a camera. Custom Python programs (Data File S1) were used to extract each sepal's outline from the sepal photos and to measure se-

pal's area. Briefly, images were segmented using the watershed method. Outlines were extracted and aligned along their longest axis determined by a polar Fourier transformation of the outline points (see below for sepal orientation).

Alignment of sepal center and orientation

The alignment of the center and orientation of the sepal allows us to estimate the sepal width and length, and allows comparison of different sepals. Given the sepal's outline points, $(x_1, y_1), \dots, (x_N, y_N)$, where N is the number of outline points, the center of the outline is chosen to be

the center of mass of the outline points, (\bar{x}, \bar{y}) . The radial distance $r(\theta)$ of the outline points from the center is then evaluated as a function of polar angle θ . In order to fix the rotational degree of freedom (orientation), we employ the polar Fourier transformation of the radial distance as $r(\theta) = \sum_{n=0}^{n_{max}} a_n \cos(n\theta - \phi_n)$. Here \bar{r} is the average radius of the outline, n_{max} is chosen to be large enough such that the Fourier series well describe the function $r(\theta)$, and ϕ_n is the angular phase of the n -th Fourier mode. As the second harmonic represents a shape close to an ellipse with perpendicular long and short axes, we fix the orientation of the outline by choosing the convention $\phi_2 = 0$, implying that ϕ_2 corresponds to the long axis of the ellipse-like shape.

For outlines from the wild type with distinct long (tip-to-bottom) and short (side-to-side) axes (see Fig. 4A), there is no ambiguity in fixing the orientation to align the sepal along the long axis, which always corresponds to the tip-to-bottom direction. However, outlines from *bot1-7* are quite round and special care is needed to unambiguously align the sepals. We observe that two dents always appear at the bottom of dissected *bot1-7* sepals (see Figure 5A) that allows us to correctly distinguish the tip-to-bottom direction from the side-to-side direction.

After fixing the sepal orientation, the width is given by the distance between the outline points at $\theta = 0$ and $\theta = \pi$, i.e., width equals to $2r(0)$. Similarly, the length is given by the distance between the outline points at $\theta = \frac{\pi}{2}$ and $\theta = \frac{3\pi}{2}$, i.e., length equals to $2r(\frac{\pi}{2})$.

Computational Modeling

The model construction follows (Bassel et al., 2014b), with some modifications as described below. The tissue template was generated in MorphoGraphX (Barbier de Reuille et al., 2015). It contained 33 cells of dimensions 50x50x20 μm , arranged in 5 rows. Cells were staggered to obtain realistic 3 way junctions. The whole template was divided into 22080 isosceles right triangles with 5 μm long sides. Individual triangles were assigned a thickness either of 0.5 μm or 1 μm , as described in [Figure 1 – figure supplement 1](#). By default, the linearly hyperelastic triangular membrane elements were assigned a Young's modulus = 300 MPa, Poisson's ratio = 0.3 and internal pressure = 0.5 MPa. Tissue boundaries were free unless otherwise specified. We first used static (i.e. non-growing) simulations to test the effects of different parameters on the stress patterns at mechanical equilibrium. The internal pressure of the central cell was increased from 0.5 to 4 MPa by steps of 0.5 MPa, while all other parameters remained as default ([Figure 1](#), [Figure 1 – figure supplement 2](#)). We then tested the effect of softening the cell wall in the central cell by assigning it a Young's modulus = 150 MPa, with an internal pressure of 0.5 MPa ([Figure 1E](#)). For growth simulations, the default growth factor was set to 0.1. Once the equilibrium configuration was found after applying internal pressure, the principal strains were computed for each triangle. The rest lengths of each triangle were then updated by adding the projection of principal strains on the triangles sides, multiplied by the growth factor. A new mechanical equilibrium was found at the end of each growth iteration. We simulated growth in a stretched tissue ([Figure 1F](#)) by restraining degrees of freedoms for displacement at the boundaries ([Figure 1 – figure supplement 1C](#)). Boundary nodes were then displaced in the directions of width and length to simulate a stretch of 20%. The central cell was assigned a Young's modulus = 150 MPa and growth factor = 0.2, while pressure was set to default. A total a 5 growth steps were performed.

CMT orientation around trichomes

We quantified the orientation of CMT segments relative to the trichome as follows. First, we defined the center of the trichome cell as the center of mass of the intersections of the neighboring cells. Second, as depicted in [Figure 3D](#), we defined the x -axis passing through the center of trichome and the center of the CMT segment (thick line segment), and the y -axis that passes through the center of the CMT segment and is perpendicular to the x -axis. By definition, the polar coordinate system (r, θ) is determined by a distance and an angle of the center of the CMT segment from the center of trichome. The x -axis and y -axis are always radial and circumferential, respectively, relative to center of the trichome.

Next we calculated the angle θ_i between the CMT segment i and the $-x$ -axis. The absolute value $|\cos \theta_i|$ represents the degree of circumferential alignment of CMT segments around a trichome ranged from 0 (circumferential) to 1 (radial) (Figure 2D). To investigate the spatial trend of CMT segments, we defined three circles, surrounding the center of the trichome, and with radii of 10, 20 and 30 μm , respectively (Figure 3E). Then we calculated the mean orientation of all CMT segments between two consecutive circles (Figure 3F-G). Note that we use a weighted mean to account for anisotropy of the microtubule arrays: highly anisotropic arrays contribute more to the orientation. The weighted mean orientation around trichome is defined as follows,

where N is the number of CMT segments and w_i is the weight of CMT segment i corresponding to the length of the CMT segment. Randomized orientations should give a mean of $\langle |\cos \theta| \rangle \approx 0.8$ with $N \rightarrow \infty$, circumferential orientations should give a mean superior to 0.8, and radial orientations, a mean inferior to 0.8. Note that we mix all the CMT segments around different trichomes of same genotype together (N are about 1000~3000 segments at each time). The weighted standard deviation is defined as,

The numbers of trichomes are N_{WT} for wild type and $N_{\text{bot 1-7}}$ for *bot 1-7*. The smaller the value of mean orientation $\langle |\cos \theta| \rangle$, the lesser the CMTs orient circumferentially. The CMT segment i satisfies $|\cos \theta_i| > \langle |\cos \theta| \rangle$ in Figure 3F (or in Figure 3G).

Quantification of growth heterogeneity

In order to calculate the growth heterogeneity, we exclude the curvature effect as the trichome bulges in the Z-axis (normal to sepal surface) because the growth of trichome surface area can be twice as much as those of neighboring cells as mentioned in the main text. Therefore, we considered the principal direction of growth (PDG) (Barbier de Reuille et al., 2015)(Goodall and Green, 1986) that describes how much a cell deforms on the XY plane (tangential to sepal surface). The 2×2 deformation matrix summarizes the deformation of the coordinates of "landmark" points in the sepal from the initial to the next time frame. We chose the landmark points as the intersections between neighboring cells. The PDG provides a stretch cross of which the long arm shows the maximum relative extension λ_{max} and the length of the short arm indicates the minimum relative extension λ_{min} .

Then, we can calculate the approximated growth in cell area on the XY plane as follows. We defined l_{max} and l_{min} as the maximum and minimum extension on the XY plane of the trichome at time t_i , and l_{max}^j and l_{min}^j as the maximum and minimum extension on the XY plane of the neighboring cell j of the trichome at time t_i . Then, the growth rate in cell area (AG) on the XY plane is given as:

From these growth rates, we calculate the growth differences between trichome and neighboring cells. Note that the growth difference should be a dimensionless quantity because we want to compare them between different genotypes. Therefore, the normalized growth difference (D_j) between a trichome and neighboring cell j at time t_i can be defined as:

$$D_j(t_i) = (AG^{Tri}(t_i) - AG^j(t_i)) / (AG^{Tri}(t_i) + AG^j(t_i)).$$

The growth variability in cell area (V_{area}) can be evaluated by the average value of D_j over all the neighboring cells:

where N_{tot} is the total number of neighboring cells surrounding a trichome. Since the growth variability quantifies the degree of growth difference between trichome and neighbors, it can be positive if the neighbors grow slower and negative if the neighbors grow faster. If we define the number of slower growing neighbors as N_{pos} in which $N_{pos} > 0$, we can calculate the growth heterogeneity N_{pos} / N_{tot} that describes how many neighboring cells grow slower than the trichome.

Statistical test of CMT orientations and growth heterogeneity

We used the permutation test to compare two data sets of CMT orientations between WT and *bot1-7*, and two data sets of growth heterogeneity between WT and *bot1-7*. The samples are in CMT orientations and the ratio in growth heterogeneity. The null hypothesis is that the means (the weighted mean orientation or the averaged in the main text) of the two data sets have no difference. In the CMT orientation case, for instance between WT and *bot1-7* for the 10-20 μm ring at

time 0, the numbers of data are for WT and for *bot1-7*. The two observed means are (WT)=0.980 and (*bot1-7*)=0.890 and their difference is . We put the two data sets together, and from the mixed distribution, we created the m -times permuted distribution where we randomly picked up the number of data of without replacement. We also define as the rest of the data remaining in the mixed distribution. Then we calculated the permuted difference . After the permutation trials performed times, the p-value is approximated by the percentage where l is the number of trials which satisfy . We used this nonparametric approach because it does not require any knowledge of the distribution of . The significance level of the test was chosen as 0.05.

Author contributions

Conception and design of the work: N.H., J.C.L. and O.H. with inputs from all co-authors. Live imaging and analysis: N.H. Computational analysis of microtubule patterns: S.T. Conception and design of models: R.S.S., A.-L. R, A.F., M.D., A.B. Variability of organ shape analysis: N.H., C.B.L. Writing of the manuscript: N.H., S.T., R.S.S., C.B.L. and O.H. with inputs from all co-authors.

Acknowledgments

We thank Adrienne Roeder for insightful suggestions on this manuscript. This work was supported by Human Frontier Science Program grant RGP0008/2013, the European Research Council (ERC-2013-CoG-615739 “MechanoDevo”), NSF grant MCB 1615782, Bundesministerium für Bildung und Forschung (BMBF e:Bio – Verbundprojekt SystemsX.ch: PlantMechaniX) and by the Cooperative Research Program of "Network Joint Research Center for Materials and Devices" and Grant-in-Aid for Scientific Research on Innovative Areas JP 16H01525 from the Ministry of Education, Culture, Sports, Science and Technology of Japan.

References

- Aegerter-Wilmsen, T., Aegerter, C.M., Hafen, E., and Basler, K. (2007). Model for the regulation of size in the wing imaginal disc of *Drosophila*. *Mech. Dev.* *124*, 318–326.
- Barbier de Reuille, P., Routier-Kierzkowska, A.-L., Kierzkowski, D., Bassel, G.W., Schüpbach, T., Tauriello, G., Bajpai, N., Strauss, S., Weber, A., Kiss, A., et al. (2015). MorphoGraphX: A platform for quantifying morphogenesis in 4D. *eLife* *4*, 05864.
- Bassel, G.W., Stamm, P., Mosca, G., Barbier de Reuille, P., Gibbs, D.J., Winter, R., Janka, A., Holdsworth, M.J., and Smith, R.S. (2014a). Mechanical constraints imposed by 3D cellular geometry and arrangement modulate growth patterns in the *Arabidopsis* embryo. *Proc. Natl. Acad. Sci. U. S. A.* *111*, 8685–8690.
- Bassel, G.W., Stamm, P., Mosca, G., Reuille, P.B. de, Gibbs, D.J., Winter, R., Janka, A., Holdsworth, M.J., and Smith, R.S. (2014b). Mechanical constraints imposed by 3D cellular geometry and arrangement modulate growth patterns in the *Arabidopsis* embryo. *Proc. Natl. Acad. Sci.* *111*, 8685–8690.
- Buschmann, H., Fabri, C.O., Hauptmann, M., Hutzler, P., Laux, T., Lloyd, C.W., and Schaffner, A.R. (2004). Helical growth of the *Arabidopsis* mutant *tortifolia1* reveals a plant-specific microtubule-associated protein. *Curr. Biol.* *14*, 1515–1521.
- Coen, E., and Rebocho, A.B. (2016). Resolving Conflicts: Modeling Genetic Control of Plant Morphogenesis. *Dev. Cell* *38*, 579–583.

- Cosgrove, D.J. (2016). Plant cell wall extensibility: connecting plant cell growth with cell wall structure, mechanics, and the action of wall-modifying enzymes. *J. Exp. Bot.* 67, 463–476.
- Elsner, J., Michalski, M., and Kwiatkowska, D. (2012). Spatiotemporal variation of leaf epidermal cell growth: a quantitative analysis of *Arabidopsis thaliana* wild-type and triple cyclinD3 mutant plants. *Ann. Bot.* 109, 897–910.
- Goodall, C.R., and Green, P.B. (1986). Quantitative Analysis of Surface Growth. *Bot. Gaz.* 147, 1–15.
- Hamant, O., Heisler, M.G., Jonsson, H., Krupinski, P., Uyttewaal, M., Bokov, P., Corson, F., Sahlin, P., Boudaoud, A., Meyerowitz, E.M., et al. (2008). Developmental patterning by mechanical signals in *Arabidopsis*. *Science* 322, 1650–1655.
- Hamant, O., Das, P., and Burian, A. (2014). Time-lapse imaging of developing meristems using confocal laser scanning microscope. *Methods Mol. Biol. Clifton NJ* 1080, 111–119.
- Hervieux, N., Dumond, M., Sapala, A., Routier-Kierzkowska, A.-L., Kierzkowski, D., Roeder, A.H.K., Smith, R.S., Boudaoud, A., and Hamant, O. (2016a). A Mechanical Feedback Restricts Sepal Growth and Shape in *Arabidopsis*. *Curr. Biol. CB*.
- Hervieux, N., Dumond, M., Sapala, A., Routier-Kierzkowska, A.-L., Kierzkowski, D., Roeder, A.H.K., Smith, R.S., Boudaoud, A., and Hamant, O. (2016b). A Mechanical Feedback Restricts Sepal Growth and Shape in *Arabidopsis*. *Curr. Biol.* 26, 1019–1028.
- Hong, L., Dumond, M., Tsugawa, S., Sapala, A., Routier-Kierzkowska, A.-L., Zhou, Y., Chen, C., Kiss, A., Zhu, M., Hamant, O., et al. (2016). Variable Cell Growth Yields Reproducible Organ Development through Spatiotemporal Averaging. *Dev. Cell* 38, 15–32.
- Hülkamp, M. (2004). Plant trichomes: a model for cell differentiation. *Nat. Rev. Mol. Cell Biol.* 5, 471–480.
- Jaeger, J., Irons, D., and Monk, N. (2008). Regulative feedback in pattern formation: towards a general relativistic theory of positional information. *Dev. Camb. Engl.* 135, 3175–3183.
- Kierzkowski, D., Nakayama, N., Routier-Kierzkowska, A.-L., Weber, A., Bayer, E., Schorderet, M., Reinhardt, D., Kuhlemeier, C., and Smith, R.S. (2012). Elastic domains regulate growth and organogenesis in the plant shoot apical meristem. *Science* 335, 1096–1099.
- Kuchen, E.E., Fox, S., de Reuille, P.B., Kennaway, R., Bensmihen, S., Avondo, J., Calder, G.M., Southam, P., Robinson, S., Bangham, A., et al. (2012). Generation of leaf shape through early patterns of growth and tissue polarity. *Science* 335, 1092–1096.
- Kutschera, U., and Niklas, K.J. (2007). The epidermal-growth-control theory of stem elongation: an old and a new perspective. *J. Plant Physiol.* 164, 1395–1409.
- Livanos, P., Galatis, B., and Apostolakos, P. (2014). The interplay between ROS and tubulin cytoskeleton in plants. *Plant Signal. Behav.* 9, e28069.
- Lockhart, J.A. (1965). An analysis of irreversible plant cell elongation. *J. Theor. Biol.* 8, 264–275.
- Louveaux, M., Rochette, S., Beauzamy, L., Boudaoud, A., and Hamant, O. (2016a). The impact of mechanical compression on cortical microtubules in *Arabidopsis*: a quantitative pipeline. *Plant J. Cell Mol. Biol.* 88, 328–342.
- Louveaux, M., Rochette, S., Beauzamy, L., Boudaoud, A., and Hamant, O. (2016b). The impact of mechanical compression on cortical microtubules in *Arabidopsis*: a quantitative pipeline. *Plant J.* n/a – n/a.
- Meyer, H.M., and Roeder, A.H.K. (2014). Stochasticity in plant cellular growth and patterning. *Plant Evol. Dev.* 5, 420.
- Nelissen, H., Rymen, B., Jikumaru, Y., Demuynck, K., Van Lijsebettens, M., Kamiya, Y., Inzé, D., and Beemster, G.T.S. (2012). A local maximum in gibberellin levels regulates maize leaf growth by spatial control of cell division. *Curr. Biol. CB* 22, 1183–1187.

- Roeder, A.H.K., Chickarmane, V., Cunha, A., Obara, B., Manjunath, B.S., and Meyerowitz, E.M. (2010). Variability in the Control of Cell Division Underlies Sepal Epidermal Patterning in *Arabidopsis thaliana*. *PLOS Biol* 8, e1000367.
- Ruan, Y.L., Llewellyn, D.J., and Furbank, R.T. (2001). The control of single-celled cotton fiber elongation by developmentally reversible gating of plasmodesmata and coordinated expression of sucrose and K⁺ transporters and expansin. *Plant Cell* 13, 47–60.
- Sampathkumar, A., Krupinski, P., Wightman, R., Milani, P., Berquand, A., Boudaoud, A., Hamant, O., Jonsson, H., and Meyerowitz, E.M. (2014). Subcellular and supracellular mechanical stress prescribes cytoskeleton behavior in *Arabidopsis* cotyledon pavement cells. *eLife* 3.
- Sassi, M., Ali, O., Boudon, F., Cloarec, G., Abad, U., Cellier, C., Chen, X., Gilles, B., Milani, P., Friml, J., et al. (2014). An auxin-mediated shift toward growth isotropy promotes organ formation at the shoot meristem in *Arabidopsis*. *Curr. Biol. CB* 24, 2335–2342.
- Savaldi-Goldstein, S., Peto, C., and Chory, J. (2007). The epidermis both drives and restricts plant shoot growth. *Nature* 446, 199–202.
- Shih, H.-W., Miller, N.D., Dai, C., Spalding, E.P., and Monshausen, G.B. (2014). The receptor-like kinase FERONIA is required for mechanical signal transduction in *Arabidopsis* seedlings. *Curr. Biol. CB* 24, 1887–1892.
- Shoji, T., Narita, N.N., Hayashi, K., Hayashi, K., Asada, J., Hamada, T., Sonobe, S., Nakajima, K., and Hashimoto, T. (2004). Plant-specific microtubule-associated protein SPIRAL2 is required for anisotropic growth in *Arabidopsis*. *Plant Physiol.* 136, 3933–3944.
- Shraiman, B.I. (2005). Mechanical feedback as a possible regulator of tissue growth. *Proc. Natl. Acad. Sci. U. S. A.* 102, 3318–3323.
- Sur, S., Newcomb, C.J., Webber, M.J., and Stupp, S.I. (2013). Tuning supramolecular mechanics to guide neuron development. *Biomaterials* 34, 4749–4757.
- Tauriello, G., Meyer, H.M., Smith, R.S., Koumoutsakos, P., and Roeder, A.H.K. (2015). Variability and constancy in cellular growth of *Arabidopsis* sepals. *Plant Physiol.*
- Tsugawa, S., Hervieux, N., Hamant, O., Boudaoud, A., Smith, R.S., Li, C.-B., and Komatsuzaki, T. (2016). Extracting Subcellular Fibrillar Alignment with Error Estimation: Application to Microtubules. *Biophys. J.* 110, 1836–1844.
- Uyttewaal, M., Burian, A., Alim, K., Landrein, B., Borowska-Wykret, D., Dedieu, A., Peaucelle, A., Ludynia, M., Traas, J., Boudaoud, A., et al. (2012). Mechanical stress acts via katanin to amplify differences in growth rate between adjacent cells in *Arabidopsis*. *Cell* 149, 439–451.
- Wightman, R., Chomicki, G., Kumar, M., Carr, P., and Turner, S.R. (2013). SPIRAL2 Determines Plant Microtubule Organization by Modulating Microtubule Severing. *Curr. Biol.* 23, 1902–1907.